



SPECTROSCOPIC ANALYSIS OF SCATTERING MEDIA VIA DIFFERENT QUANTIFICATION TECHNIQUES

AUDREY KAH CHING HUONG, B.Eng.

**Thesis submitted to the University of Nottingham for the degree of
Doctor of Philosophy**

FEBRUARY 2012

To our awesome Lord Jesus...

Abstract

This thesis outlines problems in the estimation of concentration value of an absorber present in a medium that is scattering and shortcomings of using the currently available techniques for the characterisation of such a scattering medium. The work describes experiment and analytic techniques used to overcome these problems. This thesis explored experimentally the practicality of using polarisation subtraction technique to minimise the effects of scattering components on the measured data. This work also considered the case when this technique has not been used owing to its limited application, and to that end, the improved linear equation and nonlinear fitting models, and gradient processing method were developed on the basis of the assumed behaviour of how a medium's scattering coefficient changes with wavelength to provide information about the fractional concentration value of an absorber. The performance of these techniques evaluated via simulation showed that linear equation model has the fastest processing speed, nonlinear fitting method is robust to system noise and is able to provide an overall more accurate estimate of value with mean of errors of less than $\pm 1\%$. The gradient processing method has intermediate performances with accuracy of its estimated value improved by about 30% with an increase in the spectral resolution from 1 nm to 0.5 nm. This work concludes that gradient processing method would be employed if accuracy of estimated value, noise robustness and computing time are of concern. However, nonlinear fitting method would be chosen in case high accuracy of the estimated value is required. Both of these methods can be suitably used as complementary techniques to clinical assessment of skin grafts and burnt skin. The simultaneous solution of linear equation model works well if all the measurement parameters are known.

Acknowledgements

I would like to express my heartfelt appreciation to my supervisors Professor John Crowe and Professor Steve Morgan for their generous advice, support and intellectual guidance throughout my years as a research student. Their valuable insights, clear vision and endless help were beyond words.

I am also indebted to Dr. David Morris and Dr. Ian Stockford whose friendship and encouragement were invaluable and who have given me many extremely helpful suggestions throughout these years. I would like to thank Dr. Paul Rodmell for the enlightening discussions from time to time and to all those who shared the same lab with me for their friendship.

I would like to acknowledge my sponsor, Ministry of Higher Education Malaysia for providing me with the financial support.

I would also like to say thank you to my parents and siblings for their endless love and care. Finally, special thanks must go to my husband Xavier Ngu who shared my despair and joy during the course of this work. His endless love, patience and understanding have helped me pull through so many hard times.

Contents

1	Introduction	1
1.1	Motivations	1
1.2	Aims of this thesis	5
1.3	Contributions of this thesis	6
1.4	Structure of this thesis	7
2	Background and literature review	10
2.1	Optical properties of scattering and absorbing media	10
2.1.1	Absorption properties	11
2.1.2	Scattering properties	13
2.2	Temporal Point Spread Function and the derivation of attenuation value	15
2.3	Photon transport model	20
2.3.1	Diffusion approximation	21
2.3.2	Kubelka Munk theory	22
2.3.3	Monte Carlo simulation	23
2.4	Instrumentation for the measurement of optical properties	24
2.4.1	Continuous intensity measurement	25
2.4.2	Time-domain measurement	25
2.4.3	Frequency-domain measurement	26
2.5	Analytic models for obtaining optical coefficients	27
2.5.1	Linear equation model	28
2.5.2	The solution to an inverse problem using a photon transport model	34
2.5.3	Cumulant-based method	35
2.5.4	Power law model	38
2.5.5	Other fitting models	39
2.6	Scattering minimisation techniques	40
2.6.1	Added absorber	40
2.6.2	Spatial filtering	41
2.6.3	Differential polarisation technique	41

2.6.4	Other techniques	44
2.7	Conclusion	45
3	Experimental investigation of polarisation subtraction technique	47
3.1	Introduction	47
3.2	Measurement method and experiment setup	49
3.2.1	Scattering phantoms preparation	49
3.2.2	Description of the experimental system	50
3.3	Modelling of the measurement system and Monte Carlo simulations	54
3.4	Results and analysis	55
3.4.1	Simulation results	56
3.4.2	Measurement results	61
3.5	Conclusion	73
4	Optical examination of scattering media using linear equation model	75
4.1	Introduction	75
4.2	The Modified Lambert Beer law	79
4.2.1	The simulation of attenuation data for demonstration	80
4.2.2	Results and discussion	81
4.2.3	Derivation of error in the estimated value	87
4.3	Investigation of the effects of varying μ'_s on TPSF and attenuation	90
4.3.1	Description of the medium and experimental system	90
4.3.2	Simulation results	93
4.4	The wavelength dependent Modified Lambert-Beer law	96
4.4.1	Results and discussion	101
4.4.2	Strategies for optimal selection of wavelengths	109
4.5	Noise sensitivity investigation	114
4.5.1	Derivation of noise sensitivity of the estimated value	115
4.5.2	The simulation of noisy data for demonstration	117
4.5.3	The selection of optimal wavelengths for practical spectroscopy	120
4.6	Conclusion	129
5	Absorber's fractional concentration estimation via the analysis of attenuation of wavelength pairs	131
5.1	Introduction	131
5.2	Estimation of fractional concentration value using a wavelength pair	133
5.2.1	Deriving the fractional concentration value of an absorber	134
5.2.2	Derivation of error arising from quantisation	135
5.2.3	Demonstration of the technique	137

5.3	Considering a medium with wavelength-invariant μ'_s	142
5.3.1	The selection of wavelength pairs and their attenuation responses	143
5.3.2	The search of the optimal wavelength pairs	144
5.3.3	Grouping the wavelength pairs	146
5.3.4	Results and analysis	147
5.4	Considering a wavelength dependent scattering medium	149
5.4.1	The selection of wavelength pairs and their attenuation responses	153
5.4.2	Processing an attenuation spectrum	156
5.4.3	Results and discussion	160
5.5	Considering a scattering medium with three absorbers	168
5.5.1	Deriving fractional concentration value of different absorbers	168
5.5.2	Gradient response of different wavelength pairs	172
5.5.3	Identifying and storing different wavelength combinations	174
5.5.4	Determining the optimum group of wavelength combinations	176
5.5.5	Demonstration of the technique	177
5.6	The sensitivity analysis and optimum wavelength range	182
5.7	Conclusion	183

6 Nonlinear fitting of attenuation spectrum and its comparison with other techniques 186

6.1	Introduction	186
6.2	The exponential model (Heuristic search-based model)	188
6.3	Relating Heuristic search-based model to cumulant based attenuation model	191
6.3.1	Expressing the TPSF cumulants	191
6.3.2	Considering a medium with wavelength-invariant μ'_s	193
6.3.3	Considering a medium with wavelength dependent μ'_s	194
6.3.4	Deriving parameters of Heuristic-search based model from cumulants	195
6.4	The empirically based model	198
6.5	The search of optimum value of fitting parameters	202
6.5.1	The curve fitting routine	203
6.6	Comparison of the performance of curve fitting models	206
6.6.1	Results and analysis	207
6.7	Comparing the performances of quantification approaches used in this study	209
6.7.1	Result (1) : Error in SO ₂ estimated based on reflectance data	213
6.7.2	Result (2) : Error in SO ₂ estimated based on transmittance data	214
6.7.3	Result (3) : Comparing noise robustness of different techniques	215
6.8	Discussion	219
6.9	Conclusion	222

7	Conclusions and Future work	224
7.1	Conclusion	224
7.2	Future work	229
A	Simultaneous solution to the parameters in Modified Lambert Beer law	230
B	Preparing a scattering phantom	235
C	Monte Carlo simulation of photon propagation direction and polarisation state	238
C.1	Photon propagation direction	238
C.2	Polarisation state of a photon	239
D	Grouping of wavelength combinations for the analysis of a medium with three absorbers	242
E	Solving for the value of fitting parameters using TPSF cumulants	244

Glossary

A	Light attenuation
A_s	Scattering dependent attenuation offset
ΔA	Attenuation difference between a wavelength pair
C	Concentration of an absorber, mol L ⁻¹
ΔC	Concentration change, mol L ⁻¹
c_m	Velocity of light in the medium, mm s ⁻¹
c	Speed of light in vacuum, mm s ⁻¹
D	Diffusion coefficient, mm
d_{ph}	Photon pathlength, mm
$\langle d_{\text{ph}} \rangle$	Mean photon pathlength, mm
f_a	Fractional concentration of an absorber, %
Δf_a	Calculated fractional concentration error, %
G	Approximated attenuation offset
g	Anisotropy factor
COHb	Carboxyhaemoglobin
Hb	Deoxyhaemoglobin
HbO ₂	Oxyhaemoglobin
I_0	Incoming light intensity
I	Detected light intensity
K	Cumulant generating function
κ_n	n^{th} cumulant of a TPSF
M	Moment generating function
m_n	n^{th} moment of a TPSF
mfp	Photon mean free path, mm
m_λ	Gradient of a wavelength pair in A versus wavelength space

$S(t)$	Temporal Point Spread Function, TPSF
$s(t)$	Normalised TPSF
SCO	Percent carbon monoxide in haemoglobin, %
SO ₂	Oxygen saturation, %
Δ SO ₂	Full scale error in calculated oxygen saturation
T	Light transmittance
t	time, s
T_a	Absorbers' total concentration, mol L ⁻¹
T_H	Total hematocrit concentration, mol L ⁻¹
α	Relative specific absorption coefficient, L mm ⁻¹ mol ⁻¹
$\Delta\alpha$	Difference in relative specific absorption coefficient, L mm ⁻¹ mol ⁻¹
ε	Molar extinction coefficient, L mol ⁻¹ mm ⁻¹
$\Delta\varepsilon$	Absorptivity difference, L mol ⁻¹ mm ⁻¹
μ_a	Absorption coefficient, mm ⁻¹
$\Delta\mu_a$	Changes in absorption coefficient, mm ⁻¹
μ_s	Scattering coefficient, mm ⁻¹
μ'_s	Reduced scattering coefficient, mm ⁻¹
μ_t	Total attenuation coefficient, mm ⁻¹
θ_c	Critical angle
λ	Wavelength, nm

Chapter 1

Introduction

1.1 Motivations

In a non-scattering medium, light attenuation changes linearly with the absorption properties of the medium and they are related by the propagation distance of the photons (in a non-scattering case, this is the thickness of the sample), hence the measurement of attenuation gives an estimate of medium's absorption. This relationship is described by the Lambert-Beer law, which will be discussed in section 2.1.1. However, the presence of scattering causes the photons to propagate along random paths. Consequently, uncertainties in the photons' pathlength mean that the sample's absorption properties cannot be accurately estimated using the Lambert-Beer law based on the thickness of the sample.

In addition, scattering also results in an attenuation offset, which is the intensity loss even when the medium has no absorbing substance present. To make things more difficult, the scattering properties of the medium change with measurement wavelength, which causes different attenuation values to be detected even when the absorption of this medium

remains unchanged.

Different approaches towards the characterisation of a scattering sample have been reported in the studies of turbid media over the last few decades. These efforts have mainly revolved around finding a quantitative solution that is inexpensive, fast (i.e. real-time) and effective, as these are highly sought after by industries such as food,¹ clinical (e.g. oximetry,²⁻⁶ bilirubin concentration measurements)⁷, pharmaceutical^{8,9} and also in other research applications, e.g. oceanography.¹⁰ All of the scattering media in these applications share a common characteristic, in that they respond similarly towards the incoming light, and photon migration in these media depends upon the media's properties. The interaction of photons with (absorbing and scattering) particles in the medium modifies the intensity of transmitted or reflected light, promoting a non-invasive means of medium characterisation which makes optical absorption spectroscopy an attractive method to use. An increasingly important and well-known application which exploits this is in the optical clinical diagnostic field, where cancerous cells can be distinguished by analysing the scattered light.¹¹

The measurements and analysis techniques commonly used for optical examination of scattering media include spectroscopic monitoring techniques, the use of photon migration models and analytic models to extract the value of optical parameters (very often this is the fractional concentration value of an absorber, f_a , in a scattering medium that contains at least two light absorbing species). The flow of the optical spectroscopic process can be summarised in Fig. 1.1. This diagram shows that the whole process involves two main stages, namely optical measurement and data analysis. This is underpinned by the use of appropriate photon transport models. Photon transport models are important in terms of validating the performance of a measurement technique, the value of measure-

ment parameters and to provide the reflectance or transmittance spectra to solve an inverse problem. Scattering reduction techniques can be implemented and used with the optical spectroscopic techniques to remove the heavily scattering components of the detected light.

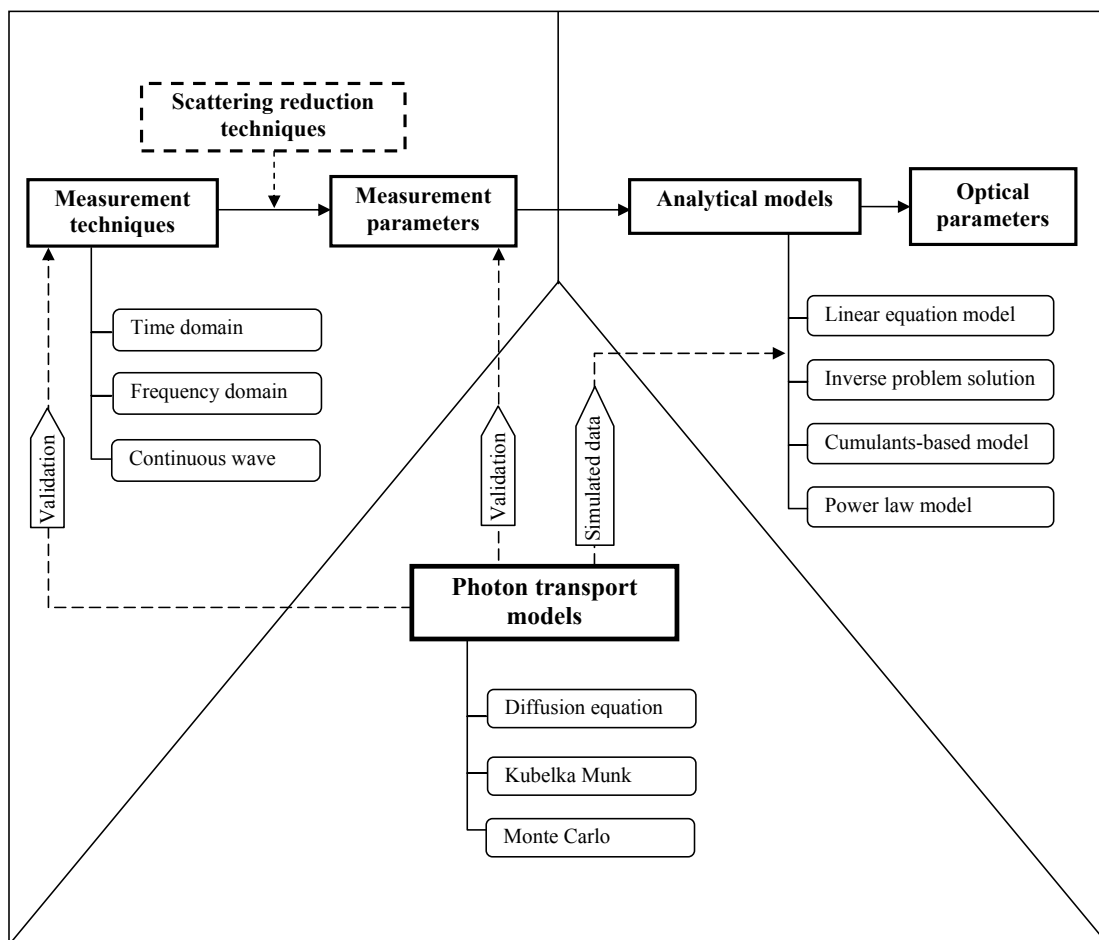


Figure 1.1: Techniques for spectroscopic monitoring and characterisation of a scattering medium.

Even though different techniques and models listed in Fig. 1.1 are available for spectroscopy and analysis of a scattering medium, most of these techniques require extensive

computational processing,¹²⁻¹⁷ bulky and expensive equipments^{18,19} and do not provide real-time characterisation, while others lack robustness or provide limited and poor performance as will be elaborated in the next chapter. This study aims to overcome some of these shortcomings and they are described in section 1.2.

Since there is an increased interest in the spectroscopy of biological tissues for the detection of cancer²⁰ and other diseases (such as diabetes),²¹ oximetry is used in this thesis as an example of application. This work considers oxy- and deoxyhaemoglobin, which are the main light absorbers in blood, as the medium's absorbers whenever the modelling of a scattering phantom for the demonstration of the discussed techniques is required, and the quantified f_a value is given by the fractional concentration of oxyhaemoglobin (or commonly known as blood oxygen saturation, SO_2 , which will be further described in section 2.5.1).

In addition, the reason of this choice is that pulse oximetry, which is a well known instrument used to find SO_2 value owing to its fast processing time and non-invasive nature, has limited application, wherein its performance deteriorates when arterial SO_2 dropped below 70 %. This is because manufacturers (of pulse oximeter) are prohibited to induce extreme hypoxia on volunteers when collecting calibration data for SO_2 measurement.²² This results in poor accuracy of value estimated from extrapolated data. Even though the accuracy of value given by arterial blood gas analyser is not limited to a certain SO_2 range, this is a less popular method due to its invasive character. Various efforts have been made to develop different technique suitably used as an alternative non-invasive means for oximetry. These methods, however, have their own drawbacks. Some of these efforts and methods, and their shortcomings are briefly described as follows:

1. to seek a suitable attenuation model, with the commonly used model is Modified

Lambert Beer law (MLBL). The search of SO_2 value using this model requires either the optimal wavelengths found using brute force method or a fitting routine. Both of these methods can be time consuming.

2. to use either labour-intensive heuristic search method or analytical solution of diffusion equation theory, which succeeded only under certain medium conditions and geometries,²³ to determine a model suitably used to fit to the measured data to extract the value of SO_2 .
3. to use Monte Carlo method or diffusion theory to simulate photon migration in a medium to give a library of pre-measurement data. These data are used to deduce the value of parameters of interest through the fitting of the result to the measured data. Accurate estimation of SO_2 value using this method, however, requires strict knowledge of the medium structure, geometry and its optical properties values.

Further discussion of current state of art of the above mentioned and other techniques that can be used to give an estimate of optical properties values of a scattering medium (e.g. skin tissues) can be found in section 2.5.

1.2 Aims of this thesis

This thesis is mainly concerned with problems in the quantification process caused by the insufficiency of analytic models to accurately predict an absorber's fractional concentration value in a scattering medium (shown in top right of Fig. 1.1). The main purpose of this thesis is to investigate the feasibility of using different experimental and analytical means to recover f_a or SO_2 value. This thesis has the following objectives:

1. to further investigate the performances of differential polarisation technique, which is known by its ability to reject heavily scattering components, that was theoretically examined in previous works (Lu²⁴ and Stockford *et al.*²⁵) using experiment method
2. to find and develop fast, robust and effective analytic techniques to find the value of parameter of interest, with no restriction in their application (in terms of the true SO₂ range where they can be used). This thesis also aims to identify the optimal technique for quantification work under different practical consideration.

With these aims in mind, this study focuses on investigating (experimental and analytical) methods that can be suitably applied and used for accurate quantification of f_a value (or SO₂ in oximetry) via absorption spectroscopy instead of the detection and analysis of photoplethysmographic signals that are used in pulse oximetry. This is owing to the simplicity of absorption spectroscopic system operation and flexibility in its application.

1.3 Contributions of this thesis

The four primary contributions of this thesis are listed as follows.

The first contribution of this thesis is the development of a means to recover f_a value without either using a library of data or the direct use of an attenuation model, which are normally required to determine optical properties values. This value is found via the analysis of attenuation response of different wavelength pairs.

Second, this work found different generic strategies of wavelengths selection to recover f_a value using MLBL. These strategies allow optimal wavelengths to be selected without the use of brute force method which is accepted as a standard method in many related

studies.^{4,25,26}

The third contribution is the development of a suitable fitting model directly from cumulant based model and using knowledge inferred from previously developed Exponential model.²⁷ The process of finding this model does not involve the commonly used heuristic search method.

The fourth is the experimental evaluation of efficiency and practicality of using polarisation subtraction technique using the experiment system designed in this work.

1.4 Structure of this thesis

The rest of chapters is organised as follows.

Chapter 2, “Background and literature review”, provides a discussion of optical properties of a scattering-absorbing medium, an overview of spectroscopic imaging techniques and current state of art of experimental and analytical methods (and their tradeoffs) in their application in scattering media characterisation. This chapter also discusses the effects of scattering on measurables obtained from different imaging techniques and problems in the accurate estimation of a sample’s absorptive components.

Chapter 3, “Experimental investigation of polarisation subtraction technique”, investigates the performance of linear polarisation technique through experimental spectroscopic measurements. The main purpose of this investigation is to examine the practicality of using this technique and its performances at minimising the scattering effects on measurement parameters when this technique is incorporated into the employed optical system.

Chapter 4, “Optical examination of scattering media using linear equation model”, presents

the use of linear equation model to accurately estimate the fractional concentration value of an absorber in a scattering medium using nonpolarised signals. This chapter discusses the basis on which the wavelengths may be selected to yield zero error in the estimated value. This work also considers necessary modifications to the MLBL to account for the effects of wavelength dependent scattering on the signals. The optimal wavelengths and criteria considered in selecting this wavelength combination for a given measurement medium and experiment system are also presented.

Chapter 5, “Absorber’s fractional concentration estimation via the analysis of attenuation of wavelength pairs”, investigates an analytic technique suitably used to find an absorber’s fractional concentration value when there is no restriction on the selection of wavelengths. This method is developed based on the cumulant-based model, and it works without the direct use of an attenuation model. The validity and versatility of this technique are also tested using a medium with more than two absorbers whose extinction coefficient spectral signatures are very similar.

Chapter 6, “Nonlinear fitting of attenuation spectrum and its comparison with other techniques”, uses cumulant-based model to elucidate the physical meaning of the terms in exponential model, which is developed previously on heuristic search basis. Despite the good performance that has been claimed by Rodmell,²⁷ the exponential model requires nine fitting coefficients, so fitting using this model is undoubtedly time consuming. A more efficient model is developed from cumulant based model to improve accuracy of estimated value and decrease the computation time. The performance of this model and the exponential model is also compared via simulations with that of other techniques described in this work.

Chapter 7, “Conclusions and Future work”, sums up the findings, implications and final conclusion of this work. Also included in this chapter are suggestions for future work and further improvements.

Chapter 2

Background and literature review

The purpose of this chapter is to provide context for the research presented in this thesis. The first part of this chapter is focused on a discussion of optical properties of a scattering-absorbing medium. An overview of photon transport models, and instruments and imaging techniques used for the analysis and in imaging of a medium are reviewed in section 2.3 and section 2.4, respectively. Section 2.5 gives a general discussion of state of art of existing analytic models and methods used to find f_a . This provides backgrounds for contributions of this thesis in Chapter 4 to 6. Finally, this chapter includes a brief description of scattering reduction techniques in section 2.6.

2.1 Optical properties of scattering and absorbing media

Spectroscopic measurements of a scattering medium can be used to determine its optical properties via the analysis of its measured properties. These measurement parameters can be in various forms depending on the types of the measurements performed. A range of

these parameters will be discussed later in section 2.4. The decrease in light intensity as it traverses a medium is the most basic parameter used in characterising a medium. It is related to the medium's optical properties and described by the light transmittance, T , as:²⁸

$$T = \frac{I}{I_0} \quad (2.1.1)$$

where I_0 and I are the intensity of illuminating and detected light, respectively. The light attenuation, A , is given by,²⁸

$$A = -\log(T) \quad (2.1.2)$$

$$= -\log\left(\frac{I}{I_0}\right). \quad (2.1.3)$$

Unless stated otherwise, the logarithm term used to produce A in Eq. (2.1.3) is \log_{10} and this is used throughout this work.

2.1.1 Absorption properties

The absorption process in a medium involves a transfer of the photons' energy to the absorbing substances, which causes dissipation of the photon energy. The inverse of the mean distance a photon will travel before being absorbed is given by the absorption coefficient, μ_a , of the sample that is expressed in mm^{-1} . This μ_a is determined by the concentration of absorber(s) in the medium and their corresponding molar absorptivity values:²⁹

$$\mu_a(\lambda) = \sum_{n=1}^{\infty} C_n \varepsilon_n(\lambda) \quad (2.1.4)$$

Here, C_n and $\varepsilon_n(\lambda)$ denote the concentration and wavelength dependent extinction coefficient of n^{th} absorber in the medium with units of mol L^{-1} and $\text{L mol}^{-1} \text{mm}^{-1}$, respectively.

If only an absorber is present in the medium, this work assumes that changes in the measured μ_a value ($\Delta\mu_a$) can only occur under two circumstances, which are when (1) the absorber's concentration value varies as shown in Eq. (2.1.5), or (2) when a different wavelength is used as shown in Eq. (2.1.6).²³ Both of these changes can be quantified by the μ_a value obtained from two successive measurements.

$$\Delta\mu_a = \varepsilon\Delta C \quad (2.1.5)$$

$$\Delta\mu_a = \mu_a(\lambda_1) - \mu_a(\lambda_2) = (\varepsilon(\lambda_1) - \varepsilon(\lambda_2))C \quad (2.1.6)$$

Here, $\mu_a(\lambda_1)$ is the μ_a value measured at λ_1 , ΔC and C are the concentration change and absolute value for absorber concentration, respectively, whilst ε and $\varepsilon(\lambda_1)$ are the extinction coefficient of this absorber at any fixed wavelength and at λ_1 , respectively.

2.1.1.1 Lambert-Beer law

In 1768, Lambert demonstrated the linear relationship between attenuation A and the medium thickness, d , while Beer completed the law by relating A to the medium's μ_a to produce:³⁰

$$A = \mu_a d \quad (2.1.7)$$

Alternatively Eq. (2.1.7) can also be written using Eq. (2.1.3) as:³¹

$$I = I_0 10^{-\mu_a d} \quad (2.1.8)$$

Eq. (2.1.7) and Eq. (2.1.8) are known as the Lambert-Beer law. In a non-scattering medium, light pathlength, d_{ph} , is given by the physical separation between the source and the detector, d . Measurement of A can therefore be used to obtain μ_a . The Lambert-Beer law is still the basis of the vast majority of analytic models used to quantify the absorptive components of a medium.

2.1.2 Scattering properties

The scattering process in a medium does not directly attenuate the intensity of the incoming light but results in a random change in the direction of a propagating photon upon arriving at a boundary with a different refractive index. This causes a diversion of light away from the finite-sized detector and so reduces the intensity of light that reached the detector. The scattering coefficient, μ_s , is used to describe the probability of photon scattering in a medium. The scattering direction of a propagating photon depends on the anisotropy factor, g , which is the mean cosine of the scattering angles, $\langle \cos(\theta) \rangle$, where θ is the scattering angle. A g value approaching -1 , 0 and 1 represents the scattering patterns of strongly backward, isotropic and forward scattering, respectively.²⁸ In many media, including tissue, this scattering direction can be estimated by the Henyey-Greenstein phase

function, which is given by:³²⁻³⁵

$$\cos(\theta) = \begin{cases} \frac{1}{2g} \left\{ 1 + g^2 - \left(\frac{1-g^2}{1-g+2g\xi} \right)^2 \right\} & \text{if } g \neq 0 \\ 2\xi - 1 & \text{if } g = 0 \end{cases} \quad (2.1.9)$$

where ξ is a random number between 0 and 1 drawn from a uniform distribution. The μ_s and g values are two independent parameters,³⁶ and can be used to give the reduced scattering coefficient, μ'_s , which is the reciprocal of the photon effective mean pathlength before a scattering event in units of mm^{-1} ;

$$\mu'_s = (1 - g)\mu_s \quad (2.1.10)$$

2.1.2.1 Photon pathlength and mean free path

In a scattering-absorbing medium, scattering and absorption processes will determine the average distance a photon does travel (light pathlength) before escaping from the medium. This parameter, however, should not be confused with the photon's mean free path. Both the photon pathlength and mean free path values depend on the medium's μ_s and μ_a , and are expressed in units of mm, but they do not have the same meaning. Their differences are outlined as follows.

The scattering process modifies the direction of propagating photons, affecting the propagation time of these photons before exiting a medium, those photons with large traversing times are more likely to be absorbed in the presence of an absorber. The photon pathlength, d_{ph} , is given by this propagation time, t , as

$$d_{\text{ph}} = c_m t \quad (2.1.11)$$

Here, $c_m = c/n_m$ is the velocity of light in the medium with refractive index n_m and $c = 3 \times 10^{11} \text{ mm s}^{-1}$ is the speed of light in a vacuum. The uncertainty in the photon propagating time, and hence the photon pathlength d_{ph} , is the factor which contributes to the inaccurate medium characterisation using the Lambert-Beer law.³⁷

The photon mean free path (*mfp*) describes the mean travel distance of a photon before being scattered or absorbed and it is defined as:³⁸

$$mfp = \frac{1}{\mu_t} \quad (2.1.12)$$

where $\mu_t = \mu_s + \mu_a$ is the total attenuation coefficient. According to Eq. (2.1.12), if a sample's μ_s and(or) μ_a is increased, the *mfp* is decreased, increasing the probability of photons being scattered and(or) absorbed before hitting the detector. This reduces the detected light intensity and results in a higher attenuation value.

2.2 Temporal Point Spread Function and the derivation of attenuation value

The Temporal Point Spread Function (TPSF) is the temporal response of a medium to a delta function of light. In a pure scattering medium, the temporal distribution of photons is broadened by the different paths taken by the photons due to scattering, and this TPSF 'width' increases with the sample's μ'_s , which is apparent in the transmission mode measurement. Therefore the statistical properties of a TPSF are important to quantify the

photon propagation time and the mean pathlength the photons have travelled.

Even though a medium's TPSF can be measured using time domain measurements (described in section 2.4.2), an approximation of the TPSFs of scattering media used in this thesis is derived using the Monte Carlo method which will be described in section 2.3.3. This is due to the complexity and cost of the instruments required for such experiments. An example of a simulated TPSF given from a medium with optical properties shown in Fig. 2.1 is plotted in Fig. 2.2(a). This TPSF is obtained after 20 million photons were launched normally into a rectangular medium which has dimensions of 50 mm \times 45 mm \times 10 mm (L \times H \times W). Photons reaching a finite size detector with detector radius of 3 mm in different time bins are counted and plotted in Fig. 2.2(a). This detector is placed at a distance 10 mm from the source. Also shown in Fig. 2.2(a) are the detected TPSFs when light transmitted through a medium containing only water (i.e. $\mu_s = 0 \text{ mm}^{-1}$), and when the medium has $\mu_s = 8 \text{ mm}^{-1}$ and $g = 0.93$. The mean and variance of photon time-of-flight distribution are shown in Fig. 2.2(a) to increase with the medium's μ_s . Let $S(t)$ represents the distribution of scattered light that reached the detector when $\mu_a = 0 \text{ mm}^{-1}$, the amount of the energy of the detected light, $E(\mu_s)$, after light with energy E_0 illuminated a pure scattering medium can be written as

$$E(\mu_s) = \int_{t=0}^{\infty} S(t) dt \quad (2.2.1)$$

This energy value is lower than E_0 due to the scattering of light away from the detector as shown in Fig. 2.1.

It is possible to determine the TPSF of a medium with uniformly distributed absorbers of different absorption levels using the Monte Carlo method, but running a Monte Carlo

model for a large number of μ_a values is time consuming. Therefore, the incorporation of the absorption effects into the TPSF is performed post-simulation by applying the Microscopic Lambert-Beer law^{39,40} (i.e. $10^{-\mu_a c_m t}$) to every time point of $S(t)$ to produce the energy of light detected from a scattering-absorbing medium given by:

$$E(\mu_s, \mu_a) = \int_{t=0}^{\infty} S(t) 10^{-\mu_a c_m t} dt \quad (2.2.2)$$

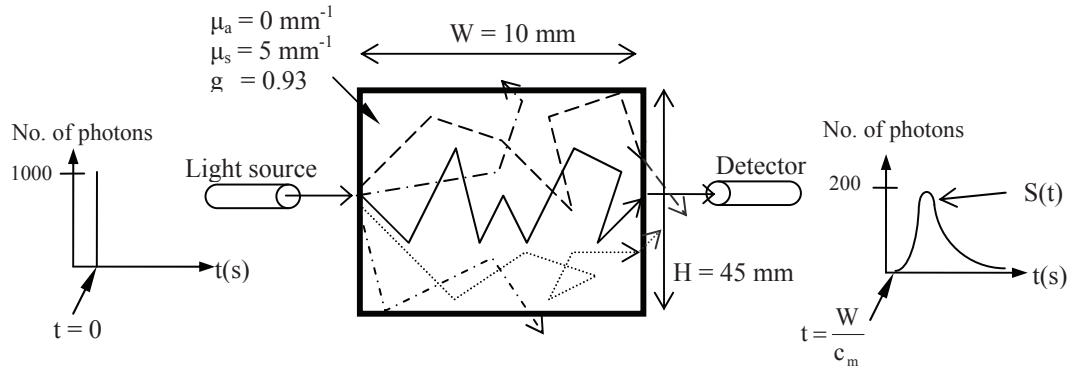
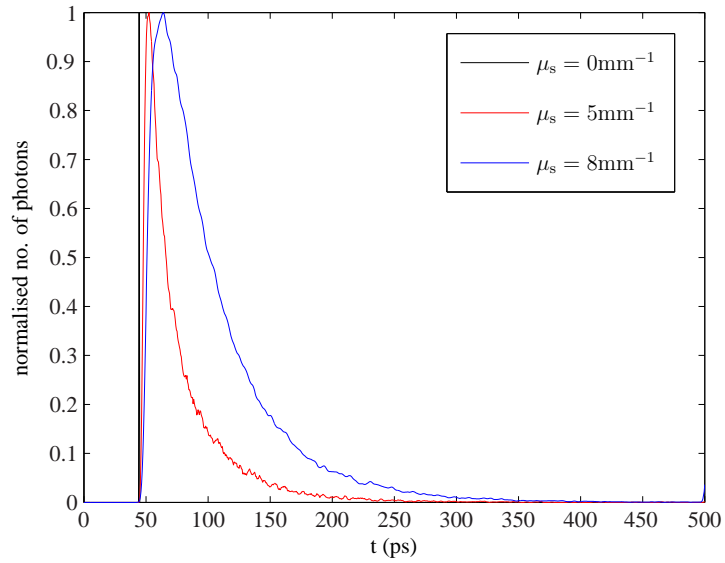
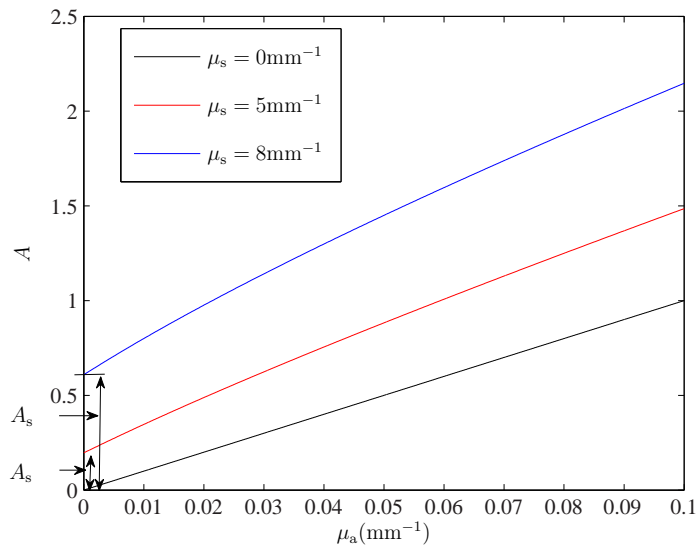


Figure 2.1: The medium used in the Monte Carlo model to produce the TPSF (for $\mu_s = 5 \text{ mm}^{-1}$ and $g = 0.93$) shown in Fig. 2.2(a) (diagram not drawn according to the actual scale for clarity).

Using the relationships in Eq. (2.1.1) - Eq. (2.1.3) and Eq. (2.2.1) - Eq. (2.2.2), the total light attenuation is given by:⁴¹



(a)



(b)

Figure 2.2: (a) The normalised TPSF of a non-scattering and scattering samples ($\mu_s = 5 \text{ mm}^{-1}$ and 8 mm^{-1} , $g = 0.93$ for both), and when $\mu_a = 0 \text{ mm}^{-1}$ in these samples. (b) Attenuation, A , versus absorption coefficient μ_a for these media.

$$A = -\log\left(\frac{E(\mu_s)}{E_0}\right) - \log\left(\frac{E(\mu_s, \mu_a)}{E(\mu_s)}\right) \quad (2.2.3)$$

$$= A_s + \log\left(\int_{t=0}^{\infty} s(t)10^{-\mu_a c_m t} dt\right) \quad (2.2.4)$$

where $E(\mu_s)$ and $E(\mu_s, \mu_a)$ represent the energy of light detected from a scattering medium in the absence and presence of absorption, respectively. A_s is the scattering dependent attenuation offset shown in Fig. 2.2(b), while $s(t)$ describes the probability of detecting photons at a given photon time-of-flight, and is produced by normalising Eq. (2.2.2) using its zeroth moment, i.e. $E(\mu_s)$ in Eq. (2.2.1).⁴² The attenuation values are calculated by applying Eq. (2.2.4) to the TPSF in Fig. 2.2(a) and are shown in Fig. 2.2(b). In the absence of scattering, the linear relationship between A and μ_a is represented by the Lambert-Beer law. Meanwhile, the effects of scattering on the light attenuation can be seen on the A versus μ_a plot when μ_s are 5 mm^{-1} and 8 mm^{-1} in Fig. 2.2(b), in which the nonlinearity in these relationships are produced by the scattering and absorption dependent variation in the photon mean pathlength (expressed in Eq. (2.1.11)). Fig. 2.2(b) also shows that both A_s and the nonlinearity in the A versus μ_a relationship vary with the medium's μ_s . Besides this, the A versus μ_a relationship becomes more linear as μ_a increases, which is when the photon mean pathlength approaches the source-detector distance, as the effect of adding more absorption is to reduce the contribution from photons with longer pathlengths. This will be described later in section 2.6.1.

2.3 Photon transport model

Numerous models have been developed over the past few decades to study the theoretical behaviour of photon propagation in a medium. Many of these studies aim to find a suitable and time-efficient photon transport model to provide a better understanding of a system, to evaluate the performance of optical techniques^{43,44} and even to predict the value of different measurables.^{13,19} It has also become increasingly common to use a photon transport model to solve the inverse problem through numerical modelling of the system³⁸ and by mapping the system's measurables to the sample's optical properties.^{17,45} The basis to all the photon propagation models is the Radiative Transfer Theory (RTT),⁴⁶ which is discussed in the following section.

Radiative Transfer Theory (RTT)

RTT is an equation which has been used rigorously to examine the theoretical behaviour of photon migration in a medium.⁴⁷ It describes the changes in light intensity at time t , at position \mathbf{r} and into the direction, \hat{s} , $I(\mathbf{r}, \hat{s}, t)$. This equation of transfer is expressed as:^{47,48}

$$\frac{1}{c_m} \frac{\partial I(\mathbf{r}, \hat{s}, t)}{\partial t} + \hat{s} \nabla I(\mathbf{r}, \hat{s}, t) = -\mu_t I(\mathbf{r}, \hat{s}, t) + \frac{\mu_s}{4\pi} \int_{4\pi} p(\hat{s}, \hat{s}') I(\mathbf{r}, \hat{s}', t) d\omega' + \epsilon(\mathbf{r}, \hat{s}, t) \quad (2.3.1)$$

where $p(\hat{s}', \hat{s})$ is the scattering phase function which characterises the intensity of light incident in direction \hat{s}' and scattered into direction \hat{s} .⁴⁸ The first term on the right hand side of Eq. (2.3.1) describes the decrease in the light intensity due to scattering and absorption, while the second term refers to the increase in intensity as light is scattered from direction \hat{s}' into \hat{s} . The total increase in the intensity is given by the integration of light

intensity over a solid angle, ω' . The parameter $\epsilon(\mathbf{r}, \hat{s}, t)$ defines the temporal and spatial emittance characteristics of the source. This equation shows that light distribution can be calculated if μ_a , μ_s and the phase function are available.⁴⁶ However, to solve these parameters requires a solution to the RTT, which is difficult for all kinds of media except for those with the simplest geometries. In the following subsections, a review of different models derived from RTT,^{46,47} which are numerical (i.e. Monte Carlo) and analytical (i.e. diffusion equation, Kubelka Munk theory) models, are presented.

2.3.1 Diffusion approximation

The derivation of diffusion equation from RTT shown in Eq. (2.3.1) is based on the assumption that each photon in the medium does not have a preferential propagating direction but rather follows a random walk.⁴⁹ To arrive at the diffusion equation, a narrow collimated beam is often used to illuminate a semi-infinite or an infinite homogeneous scattering medium, and the temporal distribution of photons, $\phi(\mathbf{r}, t)$, can be estimated directly using the diffusion equation which is given by:⁴⁵

$$\frac{1}{c_m} \frac{\partial}{\partial t} \phi(\mathbf{r}, t) - D \nabla^2 \phi(\mathbf{r}, t) + \mu_a \phi(\mathbf{r}, t) = \mathbf{P}(\mathbf{r}, t) \quad (2.3.2)$$

where $\mathbf{P}(\mathbf{r}, t)$ is the source term and D is the diffusion coefficient, which is expressed as^{15,18,45}

$$D = \frac{1}{3(\mu_a + \mu_s(1 - g))} \quad (2.3.3)$$

Patterson *et al.*⁴⁵ has previously derived the transmittance and reflectance spectra for the semi-infinite and infinite slabs from Eq. (2.3.2). It was demonstrated that, using the

derived reflectance response, the parameters μ'_s and μ_a can be obtained by fitting the simulated data to the reported results from human calf muscle measurements.¹⁹ However, the requirements for these results to be valid are that scattering is predominant over absorption, $\mu_a \ll \mu_s(1 - g)$, and the region of interest is located far from the source, boundaries and detector.^{19,45,46,49} Therefore this approximation fails to produce an adequate description of photons at their early interactions with the particles in a highly scattering medium.

2.3.2 Kubelka Munk theory

Kubelka Munk theory is another analytic model derived from RTT. Like the Diffusion approximation, it is an approximation to RTT and it is used to overcome the complexity and difficulty of solving the photon transport problem using RTT.⁴⁶ Kubelka Munk theory describes the propagation of uniformly diffused light in a slab and it is popular for its simplicity as it allows the estimation of a sample's optical properties directly from the deduced reflectance expression which is given by:^{14,46}

$$y_R(\lambda) = \cosh^{-1} \left(\frac{2a(\lambda) + s(\lambda)}{s(\lambda)} \right) \quad (2.3.4)$$

Here, the variable $y_R(\lambda)$ is the negative natural logarithm of the measured reflectance spectrum, while the symbols $a(\lambda)$ and $s(\lambda)$ denote the Kubelka Munk absorption coefficient and scattering coefficient of the sample, respectively.¹⁴

Even though this theory is analytically simple, it is based on the assumptions that there are no boundary mismatches and photons in the medium have undergone isotropic scattering. Both of these assumptions do not hold in the situation when light propagation in the medium is dominated by anisotropic scattering, for example in biological tissues.^{14,46}

2.3.3 Monte Carlo simulation

The earliest use of the Monte Carlo method dates back to 1949, when it was used in studies of stochastic physical processes.⁵⁰ This method is a numerical solution to problems that are difficult to solve by analytic approaches. In its application to spectroscopy, this method is able to produce accurate predictions of photon migration in a scattering medium within the limits of its stochastic nature.⁵¹ This is because this method allows direct handling of arbitrarily complex medium geometries for a range of parameters.⁴⁷

An excellent agreement between experiment results and data predicted using the Monte Carlo model have been presented in several works.^{13,16,19,52} Notably accurate results are predicted using the Monte Carlo method because each individual photon in the simulation is traced along a random walk until the propagation process is halted either when the photon has escaped from the medium or after it has travelled for a considerably long distance. In this case, if $\mu_a \neq 0 \text{ mm}^{-1}$, the contribution of this photon's energy to the detected intensity would be negligible. Unlike the deterministic approaches discussed in section 2.3.1 and section 2.3.2, where the photon direction has been neglected, the propagation direction of each photon in this model is determined and described by longitudinal angle, θ , and azimuthal angle, ϕ , which is given by:^{32,53}

$$\phi = 2\pi\xi \quad (2.3.5)$$

Here, the value of ξ is a random number uniformly distributed between 0 to 1, so that ϕ is uniformly distributed between 0 and 2π . The probability distribution for cosine θ is expressed in Eq. (2.1.9) and θ has a value between 0 to π . For the Monte Carlo model employed in this work, each of these photons propagates in the medium with an incremental

stepsize, Δs , given by³²

$$\Delta s = \frac{-\ln(\xi)}{\mu_s} \quad (2.3.6)$$

This model requires several millions of photons to be traced to produce statistically valid simulation results, particularly if the medium has a thickness of up to several centimetres.⁴⁷ Therefore, the drawback of using this model is that it is computationally intensive and is a time consuming process. It is also less time efficient to use this model for the statistical analysis of a thick, heavily scattering medium, e.g. breast and cerebral tissue,^{28,54} when the transmittance measurements through these tissues are performed.

2.4 Instrumentation for the measurement of optical properties

It was mentioned in section 2.1 and section 2.2 that the absorption and scattering in a medium modify the system's measurables given from different measurement techniques. In the following, continuous intensity spectroscopy which can be used to measure A is briefly reviewed in section 2.4.1. For completeness, time-domain and frequency-domain techniques which can be used to provide temporal information of the propagating light are also discussed. All these measurements can be performed either in transmission or reflectance mode and they are briefly compared here in terms of their performance and cost.

2.4.1 Continuous intensity measurement

The majority of absorption spectroscopy measurements use a continuous intensity technique to characterise a scattering medium. Continuous intensity measurements usually employ a constant intensity light source with the detection of light intensity via a suitable detector such as a photodiode or a Charge-Coupled Detector (CCD).¹² This technique is popular because the equipment is cheaper than for the time-domain and frequency-domain techniques which will be described in the following subsections, and it is also simpler to use.⁵⁵ Moreover, the recent development of hyperspectral cameras which capture images across a series of wavelengths, e.g. 430 nm to 920 nm at an interval of typically 4 nm,⁵⁶ with fast scanning rates⁵⁷ allows a large volume of intensity data to be collected within a relatively short amount of time, making this a favourable choice for spectroscopy. One of the measurement techniques that adopts continuous intensity measurement is polarisation measurement, which is an increasingly popular method to use in spectroscopy to reduce the effects of scattering in the detected light. The polarisation measurement will be introduced later in section 2.6.3 as one of the scattering reduction techniques to be considered in this thesis.

2.4.2 Time-domain measurement

In time-domain measurements, an ultrafast light source and a streak camera can be used to measure the temporal spreading of a short, e.g. picosecond, input pulse after its propagation through a sample. This produces the TPSF of the medium as described in section 2.2. However, to generate an ultrashort pulse, only a single wavelength source such as a solid state laser⁵⁸ or cavity-dumped mode locked dye laser²⁸ can be used. Thus, to perform

measurements at different wavelengths, a tunable laser source or multiple sources are required. The repetition frequency of the light pulse would be coupled and synchronised with the scanning rate of a streak camera, which is expensive and bulky.⁵⁹ Time Correlated Single Photon Counting (TCSPC) is a more affordable alternative to measure the temporal response of the medium. It uses a Photon Multiplier Tube (PMT)⁶⁰ or Avalanche Photodiode (APD)⁶¹ to detect photons at different time bins, but photon detection using these devices is slow and limited to the resolution of 50 ps as compared to 1 ps when a streak camera is used.²⁸

2.4.3 Frequency-domain measurement

In frequency-domain measurements, the measured parameters are the modulation depth, M , and phase shift in relation to the incoming light, ϕ . M is given by I_{ac}/I_{dc} where I_{ac} and I_{dc} are the amplitude of the oscillating and constant light intensities, respectively,²⁹ and both of the parameters M and ϕ vary with a sample's optical properties. This type of measurement employs a radio frequency (RF) modulated light source and a phase sensitive detector. The light source used in this measurement can be either broadband or narrowband and the detector can either be a Photon Multiplier Tube (PMT) or Avalanche Photodiode (APD).^{29,58} One method of demodulation the detected signals is to modulate the gain of the detector at a frequency offset by several kHz from the frequency of the modulated source.⁶² This serves as a down conversion of the RF signal to an Audio frequency (AF) signal, where it is easier to detect small changes in M and ϕ .⁵⁸ An alternative method is to use an external mixer to mix the signal down to an intermediate frequency.⁶³

If the modulation frequency f is less than 200 MHz, then ϕ is approximately linearly

related to the mean of photon pathlength distribution $\langle d_{\text{ph}} \rangle$ and it is given by:^{62,64}

$$\phi \approx \frac{2\pi f \langle d_{\text{ph}} \rangle}{c_m} \quad (2.4.1)$$

However, this equation does not hold for light modulated at a higher frequency. Tromberg *et al.*⁶⁵ showed that photon density waves modulated at higher frequencies become increasingly damped as they propagate at shallower depths, contributing to a very small, if any, change to the measurements on ϕ .⁶⁴

The advantage of using the frequency-domain technique is that without the use of a streak camera and a mode-locked laser source, the equipment involved is less bulky and cheaper as compared to the time-domain technique. Even though measurement of ϕ allows the estimation of $\langle d_{\text{ph}} \rangle$ using light modulated at low frequency, it does not provide complete information about a TPSF.

2.5 Analytic models for obtaining optical coefficients

So far some measurement techniques which can be used for spectroscopy of a scattering medium have been reviewed and the results from these measurements can be analysed to provide an estimation of the value of sample's optical properties (e.g. μ_a). However, the use of Lambert-Beer law in Eq. (2.1.7) as the analytic model would result in a poor estimation of μ_a value as the attenuation A expressed in Eq. (2.2.4) differs from that given by the Lambert-Beer law in terms of the attenuation offset, A_s and nonlinearity in the A versus μ_a relationship shown in Fig. 2.2(b).

Some of the methods such as the simultaneous solution of a linear model or fitting

process using cumulant-based model, exponential model or results simulated by photon transport model were briefly introduced in Chapter 1 as other suitable means used to find f_a value. The use of these and other models and methods, however, has its own tradeoffs and these are discussed in the following subsections.

2.5.1 Linear equation model

The equation deduced by Twersky⁶⁶ is among the earliest works in the efforts to account for the attenuation offset due to scattering. This offset is included in the Lambert-Beer law to give:^{3,66}

$$A = \mu_a d - \log_{10}(10^{-Bw(1-w)d} + q(1 - 10^{-Bw(1-w)d})) \quad (2.5.1)$$

where d represents the ‘light pathlength’, B is a factor which depends on the wavelength, scatterer size and detector geometry, q describes the light detection efficiency and w is the volume fraction of the sample which contains scatterers. This equation shows that the source of light attenuation can be split into absorptive and scattering components. Although this is not strictly true, as the effects of scattering and absorption on the attenuation are inseparable as shown in Eq. (2.2.4), this model has been simplified in the Modified Lambert-Beer law.

2.5.1.1 Modified Lambert-Beer law

Duling and Pittman³ substituted the scattering term (i.e. logarithm term) in Eq. (2.5.1) with a variable, so giving the Modified Lambert-Beer law (MLBL) written as:³

$$A(\lambda) = G + \mu_a(\lambda)d \quad (2.5.2)$$

Here an offset, G , is considered as an estimate of the attenuation due to scattering. Duling and Pittman³ assumed the medium's scattering properties are invariant with changes in the wavelength of the illuminating light, and that the signals detected at any wavelength have the same properties in terms of the light pathlength and attenuation offset. The use of this model was demonstrated in oximetry when two haemoglobin compounds, i.e. deoxyhaemoglobin (Hb) and oxyhaemoglobin (HbO₂), are present in a blood medium. The absorptivities of these absorbers are well-documented and are shown in Fig. 2.3.

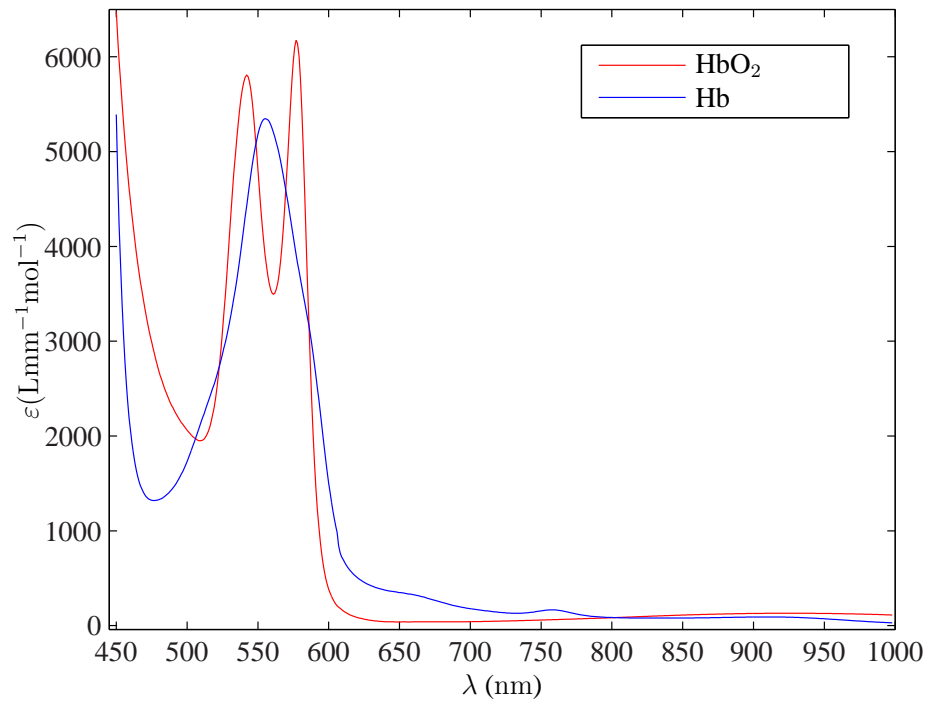


Figure 2.3: The extinction coefficients of HbO₂ and Hb compiled by Zijlstra *et al.*³⁰ (published in Biomedical Optics Research Laboratory-UCL homepage).

In this case, μ_a in the medium is given by:³

$$\mu_a = ((\varepsilon_{\text{HbO}_2} - \varepsilon_{\text{Hb}})\text{SO}_2 + \varepsilon_{\text{Hb}})T_H \quad (2.5.3)$$

where $\varepsilon_{\text{HbO}_2}$ and ε_{Hb} denote the extinction coefficient of HbO₂ and Hb, respectively, SO₂ represents the blood oxygen saturation value or fractional concentration of oxyhaemoglobin with respect to the total haemoglobin concentration. It is given from the concentration of HbO₂ (C_{HbO_2}) and Hb (C_{Hb}) as follows:

$$\text{SO}_2 = \frac{C_{\text{HbO}_2}}{C_{\text{HbO}_2} + C_{\text{Hb}}} \quad (2.5.4)$$

while the total blood concentration, $T_H = C_{\text{HbO}_2} + C_{\text{Hb}}$.

In the demonstration of their work, an isosbestic wavelength pair, which are wavelengths when the extinction coefficient of deoxyhaemoglobin and oxyhaemoglobin are the same (i.e. 420 nm and 450 nm, 520 nm and 546 nm), was used to define a straight line according to Eq. (2.5.2), while a non-isosbestic wavelength was used to estimate the SO₂ given by

$$\text{SO}_2 = \frac{A_{I1}(\varepsilon_{B_m} - \varepsilon_{B_{I2}}) + A_{I2}(\varepsilon_{B_{I1}} - \varepsilon_{B_m}) + A_m(\varepsilon_{B_{I2}} - \varepsilon_{B_{I1}})}{(A_{I2} - A_{I1})\varepsilon_{AB_m}} \quad (2.5.5)$$

where subscripts A and B refer to oxyhaemoglobin and deoxyhaemoglobin compounds. Parameters with subscript $I1$ and $I2$ in Eq. (2.5.5) denote data that are associated with the isosbestic wavelength pair, while those with subscript m correspond to that of the non-isosbestic wavelength. A_{I1} and A_m are the attenuation value measured using one of the isosbestic wavelengths and a non-isosbestic wavelength, respectively. ε_{AB_m} denotes the extinction coefficient difference between oxyhaemoglobin and deoxyhaemoglobin at

the non-isosbestic wavelength.

Instead of limiting the selection of wavelength to isosbestic wavelengths, Smith⁴ generalised the use of MLBL so that SO₂ can be estimated using data at any three wavelengths (i.e. $\lambda_1, \lambda_2, \lambda_3$). Using the assumptions by Duling and Pittman,³ solving the simultaneous equation in Eq. (2.5.2) gives an equation of SO₂, which is expressed as follows:

$$\text{SO}_2 = \frac{A_1(\varepsilon_{B_3} - \varepsilon_{B_2}) + A_2(\varepsilon_{B_1} - \varepsilon_{B_3}) + A_3(\varepsilon_{B_2} - \varepsilon_{B_1})}{A_1(\varepsilon_{AB_2} - \varepsilon_{AB_3}) + A_2(\varepsilon_{AB_3} - \varepsilon_{AB_1}) + A_3(\varepsilon_{AB_1} - \varepsilon_{AB_2})} \quad (2.5.6)$$

Here $\varepsilon_{AB_1} = \varepsilon_{A_1} - \varepsilon_{B_1}$. The G and d in Eq. (2.5.2) are defined as:

$$G = \frac{A_1(\varepsilon_{AB_3}\varepsilon_{B_2} - \varepsilon_{AB_2}\varepsilon_{B_3}) + A_2(\varepsilon_{AB_1}\varepsilon_{B_3} - \varepsilon_{AB_3}\varepsilon_{B_1}) + A_3(\varepsilon_{AB_2}\varepsilon_{B_1} - \varepsilon_{AB_1}\varepsilon_{B_2})}{\varepsilon_{AB_1}(\varepsilon_{B_3} - \varepsilon_{B_2}) + \varepsilon_{AB_2}(\varepsilon_{B_1} - \varepsilon_{B_3}) + \varepsilon_{AB_3}(\varepsilon_{B_2} - \varepsilon_{B_1})} \quad (2.5.7)$$

$$d = \frac{A_1(\varepsilon_{AB_3} - \varepsilon_{AB_2}) + A_2(\varepsilon_{AB_1} - \varepsilon_{AB_3}) + A_3(\varepsilon_{AB_2} - \varepsilon_{AB_1})}{\varepsilon_{AB_1}(\varepsilon_{B_2} - \varepsilon_{B_3}) + \varepsilon_{AB_2}(\varepsilon_{B_3} - \varepsilon_{B_1}) + \varepsilon_{AB_3}(\varepsilon_{B_1} - \varepsilon_{B_2})} \quad (2.5.8)$$

where the wavelength index is shown by the subscript. The details of the derivation of SO₂, G and d shown in Eq. (2.5.5) - Eq. (2.5.8) can be found in Appendix A.

This model is simple to use and it requires only data at three wavelengths to estimate the SO₂ value. However, the accuracy of this estimated value depends on the choice of wavelengths. The optimal wavelengths for oximetry have been proposed by various investigators.^{2,4} Some of these workers employed the types of wavelength suggested by Duling and Pittman (i.e. an isosbestic wavelength pair and a non-isosbestic wavelength),³ while others determined these wavelengths on an empirical basis. In the latter case, the true SO₂ value (which can be measured from the co-oximeter) is required so that the

value estimated by every combination of wavelengths is compared to this value before the optimum wavelengths are decided. Using the selected wavelengths, both Smith⁴ and Alabboud²⁶ reported the estimated SO₂ values with the lowest absolute error, $|\Delta\text{SO}_2|$, of approximately 5%, whereby Delori² observed a mean absolute ΔSO_2 of 14.55% using an isosbestic wavelength pair and a nonisosbestic wavelength.

Several approaches were taken to improve the use of the MLBL and one of these is by using an estimated value of photon pathlength. An example of this approach is presented in a paper by Delpy *et al.*¹⁹ who defined the mean pathlength in Eq. (2.5.2) as $\langle d_{\text{ph}} \rangle = \text{DPF} \times W$, where W is the medium's thickness and DPF is the differential pathlength factor, a value determined from the measured TPSF and from Eq. (2.1.11). The DPF relates changes in the measured attenuation to an incremental step change in the medium's absorption, so giving a more accurate d_{ph} value so that a change in the concentration value can be more accurately estimated by the MLBL. In a similar study, Tsuchiya and Urakami³⁹ demonstrated that the estimation of the absolute change in absorber concentration can be achieved with a single wavelength using the pathlength value directly measured from frequency domain measurements. The concentration change, ΔC , was derived from MLBL as

$$\Delta C = \frac{1}{\varepsilon \langle d_{\text{ph}} \rangle} \Delta A \quad (2.5.9)$$

where ΔA is the changes in the measured attenuation value, and ε is the absorptivity of the present absorber. Meanwhile Mayhew *et al.*⁶⁷ showed that the percentage error in the relative concentration change of less than 10% estimated using the MLBL when photon pathlength is expressed as a nonlinear function of absorption and scattering.

A second approach is to modify the MLBL. Alabboud²⁶ has recently published an

alternative way of using the MLBL to account for the changes in attenuation offset with scattering. This equation is expressed as:²⁶

$$A = Gs + \mu_a d \quad (2.5.10)$$

where G , d and SO_2 (in μ_a expressed in Eq. (2.5.3)) are the free parameters which are varied during the fitting of the model in Eq. (2.5.10) to the attenuation spectrum. The scattering term, s , in the equation is given by the wavelength dependent μ'_s values tabulated by Meinke *et al.*⁶⁸ The error between the actual and calculated SO_2 was shown to have a maximum value of $\pm 10\%$.

It is important to note that some works have also established oximetry using two wavelengths, which is the principle to the operation of the conventional pulse oximetry. Fantini *et al.*²⁹ and Hueber *et al.*⁶⁹ derived an expression of SO_2 obtained by solving the simultaneous equation of the absorption value of a wavelength pair and it is given as follows

$$\text{SO}_2 = \frac{\mu_{a1} \varepsilon_{B2} - \mu_{a2} \varepsilon_{B1}}{\mu_{a2} \varepsilon_{AB1} - \mu_{a1} \varepsilon_{AB2}} \quad (2.5.11)$$

where μ_a values are calculated from Eq. (2.5.2) using the attenuation and d values obtained from the frequency-domain measurements. Maximum errors of 8% and 25% in the estimated SO_2 values were observed by Fantini *et al.*²⁹ and Hueber *et al.*,⁶⁹ respectively, and systematic errors were attributed as the source of these differences.

2.5.2 The solution to an inverse problem using a photon transport model

A popular approach to obtain the optical properties of a medium is to map the simulated results, which are produced by photon transport models discussed in section 2.3, to the measurement parameters. The investigation of a scattering medium begins by performing the measurement using one or a combination of, time domain,^{16,45,70} frequency domain^{18,71,72} or continuous intensity techniques.^{12,56,73,74} Following this, the medium's optical properties are obtained through the fitting procedure using results simulated by models derived from RTT,^{12,45,72,73,75} or based on a library of reflectance (or transmission) spectra given by a Monte Carlo model.^{16,56} Through these mappings, Patterson *et al.*⁴⁵ observed a relative μ_a error of 23%, Qin *et al.*⁷⁵ obtained an average μ'_s error of 7.5% and a minimum μ_a error of 40% and Pifferi *et al.*¹⁶ showed the relative error in the fitted μ_a and μ'_s of $< 10\%$ using data simulated by the Monte Carlo method, while errors of greater than 30% were reported when the diffusion approximation was employed.

The derivatives of RTT such as diffusion theory are more popular as they have shorter computation times and do not require extensive processing. Nevertheless, some research have been done to improve the performance of a Monte Carlo model, such as by the variance reduction technique which allows one to propagate many photons simultaneously, yet still achieve the desired accuracy.⁵³ In other work, by assuming that the anisotropy factor, g , and medium refractive index, n_m , are constant and known parameters, a 'mono Monte Carlo model'^{13,16,17} can be produced and used. The reason this is possible is that it was shown that there is a high similarity in the TPSFs produced by media with different g , therefore by selecting a smaller g value in the Monte Carlo calculation, it shortened

the computation time and gave results with a respectable error in the estimated μ_a and μ_s values of approximately 1% – 2%.¹⁷ However, these errors were shown to increase to 10% when the incorrect n_m was assumed and used.

2.5.3 Cumulant-based method

The propagation time of a photon, t , in a scattering medium is a random variable and the continuous distribution of the detected photons ($S(t)$) is causal. This distribution is previously characterised using the moment generating function, M , by Ostermeyer *et al.*⁷⁶ and Sassaroli *et al.*⁷⁷ In their work, moments of a distribution were used to describe changes in the intensity of a light source due to the optical properties change at each ‘voxel’, i.e. elementary segment, of an absorbing-scattering medium. The n^{th} moment, m_n , of this distribution is written as

$$m_n = \frac{\int_{t=0}^{\infty} S(t)t_i^n dt}{\int_{t=0}^{\infty} S(t)dt} \quad (2.5.12)$$

Here, t_i is the time spent in the medium by the i^{th} detected photon. These moments were used to describe the absorption dependent relative changes in the light intensity, and have a logarithmic relationship with cumulants, κ , of the cumulant generating function, K , which is defined as⁷⁸

$$\ln \left(\sum_{n=0}^{\infty} m_n \frac{(-\mu_a c_m)^n}{n!} \right) = \sum_{n=1}^{\infty} \kappa_n \frac{(-\mu_a c_m)^n}{n!} \quad (2.5.13)$$

$$K = \sum_{n=1}^{\infty} \kappa_n \frac{(-\mu_a c_m)^n}{n!} \quad (2.5.14)$$

Based on Eq. (2.5.13) and the relationship between attenuation and intensity in Eq. (2.1.3), the moment dependent intensity change given by Sassaroli *et al.*⁷⁷ can be converted to the expression of absorption dependent attenuation, A_a , as:^{41,42,79}

$$A_a = \kappa_1 \mu_a c_m - \kappa_2 \frac{(\mu_a c_m)^2}{2!} + \kappa_3 \frac{(\mu_a c_m)^3}{3!} - \kappa_4 \frac{(\mu_a c_m)^4}{4!} + \dots \quad (2.5.15)$$

$$= - \sum_{n=1}^{\infty} \kappa_n \frac{(-\mu_a c_m)^n}{n!} \quad (2.5.16)$$

Both moments and cumulants can be used to describe the μ_a dependent intensity change but the use of cumulants is preferable in this work as they have a non-logarithm relationship with attenuation value, using which a medium will be characterised. From Eq. (2.5.16), the total light attenuation is obtained by adding the attenuation offset, A_s or κ_0 , into the equation to produce

$$A = \kappa_0 - \sum_{n=1}^{\infty} \kappa_n \frac{(-\mu_a c_m)^n}{n!} \quad (2.5.17)$$

This equation is an exact solution to the attenuation value, so it will be used in Chapter 5 and 6 as the expression for the real attenuation and so to theoretically verify the validity

of the proposed models. An equation which is similar to that shown in Eq. (2.5.16) has been reported by Tsuchiya²³ who termed the n^{th} cumulant, κ_n , as the n^{th} derivative of A with μ_a . The parabolic form of A versus μ_a relationship proposed by Lübbers and Wodick⁸⁰ is the truncated form (up to $n = 2$) of cumulant generating function shown in Eq. (2.5.17).

It can be seen from Eq. (2.5.16) that the sample's μ_a can be determined if A_a and all the TPSF cumulants are known. There are different means of calculating the cumulants, among them is by the differentiation of Eq. (2.5.16) with respect to μ_a given by:^{23,41,42}

$$\kappa_n = -\frac{1}{(-c_m)^n} \left. \frac{d^n A_a}{d\mu_a^n} \right|_{\mu_a=0} \quad (2.5.18)$$

Alternatively, cumulants can also be derived from the cumulant generating function of an analytic model, whose expression is not in an infinite summation form,⁴¹ or from a measured TPSF described as follows.

If a sample's TPSF is measured in the time-domain experiment, the moments of this TPSF can be calculated from Eq. (2.5.12) and the n^{th} cumulant is calculated using a recursive formula^{81,82} as follows:

$$\kappa_n = m_n - \sum_{k=1}^{n-1} \frac{(n-1)! \kappa_k m_{n-k}}{(k-1)! (n-k)!} \quad (2.5.19)$$

where κ_1 and κ_2 are the mean and variance of a distribution (of photon time-of-flight), respectively.⁷⁸ If the frequency-domain measurement⁷⁸ is used, the even and odd cumulants are given by the measured attenuation and phase, respectively.^{41,79} Using these cumulants, the change in the μ_a value, $\Delta\mu_a$, can be estimated using the signals measured from the constant intensity measurements. In practice, however, it is impossible to measure all

the cumulants (i.e. up to infinite terms). Therefore the A versus μ_a curve fails to converge to the real curve even with a large number of cumulants, and the accuracy of the μ_a value estimated using this model is limited to a small range of $\Delta\mu_a$.⁴¹ In the work demonstrated by Morris⁴¹, $\Delta\mu_a$ was assumed to have been produced by a variation in HbO₂ and Hb (ΔHbO_2 and ΔHb), and wavelengths 550 nm and 600 nm were chosen to estimate ΔHbO_2 and ΔHb using Eq. (2.1.5). It was shown that using the first four cumulants and the value of ΔA , the mean error in the estimated ΔHbO_2 and ΔHb (from $\Delta\mu_a$) were shown to be less than $\pm 10\%$. These results were consistent for both the transmittance and reflectance data simulated by a Monte Carlo model.

2.5.4 Power law model

The Power law model is designed to determine a medium's optical properties based on the measured parameters and a fitting routine. The nonlinear form of A versus μ_a relationship derived from RTT for the reflectance measurements on a semi-infinite medium with matched boundary was shown to be well approximated by a power law model:¹²

$$A = 1.06 - 1.45\mu^{0.35} \quad (2.5.20)$$

where $\mu = \mu_a/\mu'_s$ is unitless. The power law model shown in Eq. (2.5.20) allows an estimation of a sample's optical properties by fitting this model to the spectrum measured from a continuous source system, but the validity of this model is reported to have restricted to the μ value in the range between 5×10^{-4} and 0.1.

2.5.5 Other fitting models

An exponential model,²⁷ which does not show the limitations shown by Monte Carlo model and diffusion equation, was previously developed on an heuristic basis in the Applied Optics Group in University of Nottingham. This model relates A to μ_a and is expressed as²⁷

$$A = a_1 \exp(-\mu_a b_1) - a_2 \exp(-\mu_a b_2) + e\mu_a + f\mu_a \lambda + g\lambda + h \quad (2.5.21)$$

where $a_1, b_1, a_2, b_2, e, f, g$ and h are the fitting parameters. If this model is fitted to the attenuation spectrum measured from a non-scattering medium ($\mu_a \neq 0 \text{ mm}^{-1}$), all the parameters in the equation, other than the parameter e , would become zero and Eq. (2.5.21) is reduced to the Lambert-Beer law. In a demonstration of the performance of this model using Monte Carlo forward modelled data, the μ'_s of an infinite slab geometry was varied linearly with wavelength while μ_a is as given in Eq. (2.5.3), it was shown that this model can recover SO_2 values with an absolute error of less than 0.3%.²⁷

Other workers such as Kobayashi *et al.*⁸³ proposed a cubic function to represent light attenuation measured from a blood medium expressed as

$$A = a\mu_{aB}^3 + b\mu_{aB}^2 C_{\text{mel}} + c\mu_{aB} C_{\text{mel}}^2 + dC_{\text{mel}}^3 + e\mu_{aB}^2 + f\mu_{aB} C_{\text{mel}} + gC_{\text{mel}}^2 + h\mu_{aB} + iC_{\text{mel}} + j \quad (2.5.22)$$

where μ_{aB} and C_{mel} are the blood absorption coefficient and the concentration of melanin, respectively. Both of these parameters and the coefficients a to j in Eq. (2.5.22) can be determined through the fitting process.

2.6 Scattering minimisation techniques

The previous section has described analytic models which have an increase in complexity beyond the Lambert Beer law as the media are scattering. However, if scattering can be minimised then a simple model such as the linear MLBL model may be applicable. Scattering minimisation techniques are expected to improve the linearity of the A versus μ_a relationship at the cost of higher light attenuation values. The performance of three techniques, namely added absorber, spatial filtering and differential polarisation method, have been compared using the Monte Carlo method within the Applied Optics Group in University of Nottingham.^{24,44} The theory of these and some other techniques that can be used to minimise scattering components in the signals, and the recent development of these methods, are briefly addressed in the following subsections.

2.6.1 Added absorber

A method which linearises the A versus μ_a relationship is by adding absorber into the medium to increase the absorption value of this medium. It was shown in Fig. 2.2(b) that the A versus μ_a relationship becomes increasingly linear in high μ_a region. This is because as μ_a increases, photons with long pathlength are attenuated more heavily than the weakly scattered photons which have travelled at routes closer to the optical axis.⁸⁴ Since the mean and variance of a TPSF have been reduced (i.e. via the absorption), it decreases the uncertainty in the photon pathlength and results in a $\langle d_{\text{ph}} \rangle$ value which is approximately the physical distance between the source and the detector. If the G value is known, using this calculated $\langle d_{\text{ph}} \rangle$ in Eq. (2.5.2) would produce a more accurate estimation of the μ_a value. However, an obvious side effect of using this technique is that it contaminates the

medium and so is not always applicable (e.g. to in vivo application).

2.6.2 Spatial filtering

It is mentioned in section 2.1.2 that photons in a scattering medium propagate in random directions, so heavily scattered photons are expected to exit the sample at positions further away from the optical axis than the weakly scattered photons. Therefore, a spatial filter positioned in front of the detector can be used to reject heavily scattered photons. However, because of the stochastic properties of these heavily scattered photons, not all these photons are rejected via this technique as some of them could escape the medium at position close to the optical axis and be detected.

In practice, scattering in a medium contributes to intensity loss when a detector or camera with a small detection area is employed. Therefore, in spectroscopic measurements of scattering media, an optical lens is commonly used to collect and focus light onto the detector or camera, increasing the amplitude of the light intensity. Provided that all the incoming light is collected by the lens for example in the case of an integrating sphere, the use of optical lens, iris diaphragm or detector with a limited aperture are categorised as spatial filtering.

2.6.3 Differential polarisation technique

The polarisation technique is based on the fact that photons propagate in a scattering medium will have both their directions and polarisation states altered,^{85,86} and only weakly scattered photons will maintain their polarisation states. In this section, linear and circular polarisation measurements are described. The main difference between the two measure-

ments is that, for scattering particles with size greater than the light wavelength (i.e. which is so in many scattering media such as biological tissues, aerosols and the atmosphere) circularly polarised photons propagating through this medium are capable of maintaining their polarisation states to a greater extent and endure more scattering events before their polarisation states are randomised than are linearly polarised photons.⁸⁶ Under these conditions, larger signals are detected from circular polarisation measurements than in the linear polarisation experiment.²⁴ Despite a poorer signal to noise performance, a linear polarisation measurement is better at rejecting highly scattered photons. The properties of photons detected in different polarisation detection channels after polarised light is transmitted through the medium are tabulated in Table 2.1.

The only difference in the categories of photons detected in the reflectance mode from that shown in Table 2.1 is the detection of both surface reflected photons and heavily scattered photons in channel 4.^{24,87} It is clear from Table. 2.1 that the polarisation technique is able to discriminate weakly scattered photons from heavily scattered photons by means of their polarisation states.

Table 2.1: The linear and circular polarisation illumination-detection schemes for transmission mode measurements.

Channel	Illumination	Detection	Types of photons
1	Linear	co Linear	weakly + heavily scattered photons
2	Linear	cross Linear	heavily scattered photons
3	Circular	co Circular	weakly + heavily scattered photons
4	Circular	cross Circular	heavily scattered photons

According to Table 2.1, photons detected in the co-polarisation detection channel, i.e. channel 1 and 3, consist of both weakly scattered photons, which have preserved their

polarisation states, and multiple scattered photons or the depolarised photons. Whereby the cross polarisation detection channel allows only the multiple scattering photons to propagate through the polariser and reach the detector. These multiple scattering photons have random polarisation states, so the probability of these photons distributed across co- and cross-polarisation detection channels is assumed to be equal.⁸⁷ For transmission and reflection measurements, the discrimination of photons with short pathlengths is given by the mathematical subtraction of intensity measured from the co- and cross-polarisation channels given by:^{24,87}

$$I_{\text{sub}} = I_{\parallel} - I_{\perp} \quad (2.6.1)$$

where I_{sub} is the calculated intensity of the weakly scattered photons, whereas I_{\parallel} and I_{\perp} are the intensity of light detected in the co- and cross-polarisation channels, respectively. For the reflectance measurements performed using the circular polarisation scheme, weakly scattered photons are obtained by subtracting the intensity value measured from channel 3 from that measured from channel 2.

The depolarisation rate of the propagating photons can be examined by the degree of polarisation (DOP) which value is in between 0 and 1. It is expressed as the fraction of the detected photons which have maintained their polarisation states,^{24,84,87}

$$DOP = \frac{I_{\parallel} - I_{\perp}}{I_{\parallel} + I_{\perp}} \quad (2.6.2)$$

A high DOP value implies that a high fraction of the propagating photons have their polarisation states maintained, and vice-versa. Previously, experiments using differential polarisation techniques were either to try and improve the resolution of an image⁸⁸⁻⁹⁰ or to linearise the A versus μ_a relationship in the estimation of a medium's absorptive

components.⁹¹

Using a medium with $\mu_s = 5 \text{ mm}^{-1}$, Stockford *et al.*²⁵ concluded that linearly polarised signals given from the subtraction of signals from co- and cross- linear channels yielded the best performance in terms of giving the lowest mean error of 1.2% in the estimated concentration ratio of two absorbers, while Lu *et al.*^{24,44} showed that linear polarisation is the most effective at selecting weakly scattered light from the scattering signals compared to other techniques (i.e. circular differential polarisation, added absorbers and spatial filtering). These techniques were evaluated via simulations and these workers have expressed their concerns over the practicability of using the linear polarisation subtraction technique on a shot-noise limited system when the medium's $\mu_s \geq 7 \text{ mm}^{-1}$.⁴⁴

Experiments have also been used to assess the performance of the differential polarisation technique. An example is the experiment by Siegel *et al.*⁹¹ who used a xenon arc lamp and Charge-Coupled detector (CCD) in the system. This polarisation measurement technique was performed on a tissue phantom to estimate an absorber's concentration value by a shape fitting procedure. They showed an average error in the estimated haemoglobin concentration value of less than 5% when μ_s is a constant. This experiment, however, did not investigate the signal to noise performance of the measured signals when the intensity of these signals could be small and susceptible to noise.

2.6.4 Other techniques

There are other studies which aim to reduce the light scattering in the measurements, with most involving alterations of the optical properties of the measurement subjects, e.g. biological tissue and tissue simulating phantoms. These techniques include administering

chemical agents into a local area of tissue^{92,93} and by compression.⁹⁴ The injection of chemical agents into the target area dehydrates the region of interest⁹² and reduces the cell diameter, lowering the mismatched refractive index between scattering centers and their ‘shrinking’ surrounding. As a consequence the light scattering from the sample is reduced.⁹³

A compression method was previously demonstrated on human skin specimens. It involves asserting pressure on the specimens before the reflected or transmitted signals are measured as it reduces the spacings between intercellular components.⁹⁴ This is because in the process, water is drained out from the specimens. This produces a similar effect to that when chemical agents are used and it was reported to reduce the light scattering and resulted in an increase in the light transmittance.

Time gated measurement is another technique widely used to remove the heavily scattered light by discriminating the early arriving photons and this is mainly used to improve the resolution of an image.⁹⁵ However the implementation of this technique is limited to expensive and bulky experiment setup.

2.7 Conclusion

The problem in accurate quantification of a sample’s absorptive components using the Lambert-Beer law arises when the sample is scattering. The effects of scattering on the measurables, e.g. the measured light intensity and TPSF, were discussed in sections 2.1 and 2.2, and they can be summarised as follows: (1) The photon pathlength, d_{ph} , changes with the medium’s μ_a and μ'_s , (2) A_s is observed when $\mu_a = 0 \text{ mm}^{-1}$, and (3) both A_s and the (nonlinear) A versus μ_a relationship vary with the medium’s μ'_s .

Different techniques and models that are available to extract the optical properties of a scattering medium using data given from absorption spectroscopy measurements were reviewed in section 2.4 and section 2.5. Also discussed in those sections are the tradeoffs in using the corresponding techniques and models.

As the aim of this thesis is to accurately determine the f_a value in a scattering-absorbing medium, continuous intensity imaging technique is chosen to provide the measurement of light attenuation due to simplicity of the system operation, cost and availability of equipments required for such measurements. Chapter 3 is concerned with experimental investigation of polarisation subtraction method to reduce scattering effects on the measured attenuation following the conclusion drawn from theoretical evaluation of different scattering minimisation techniques by Bo,²⁴ and Stockford *et al.*²⁵ Meanwhile analytic models and methods suitably used to find the f_a value (based on nonpolarised attenuation signals) for media considered in this thesis are presented in Chapter 4 to 6.

Chapter 3

Experimental investigation of polarisation subtraction technique

3.1 Introduction

The factors impeding the accurate spectroscopic analysis of a scattering medium have been outlined in Chapter 2. Two strategies that can be used to determine the medium's μ_a without using a library of simulated data have been described. The first aims to find an attenuation model^{4,12,27,83} that approximates the nonlinear relationship between A and medium's μ_a . Using this attenuation model a value for μ_a can be estimated by either fitting this model to the measured attenuation spectrum^{27,83} or through the simultaneous solution of the model,^{3,4} which requires only the attenuation value measured at several wavelengths.

The second aims to suppress the heavily scattered photons, producing a more linear A versus μ_a relationship that can be approximated by the MLBL. Some of these ideas have

been discussed in section 2.6. A number of related studies have also claimed that the spectroscopic analysis of weakly scattered photons are adequate to determine the optical properties of a medium.^{91,96,97} This relies on there being a sufficient number of weakly scattered photons, hence it is not appropriate for thick and heavily scattering tissues such as brain.⁵⁴

This chapter follows on from the theoretical studies conducted by Lu *et al.*⁴⁴ and Stockford *et al.*²⁵ and their assertions on the performance and limitations of the polarisation subtraction technique when it is used in the spectroscopic study of a highly scattering medium. This study aims to experimentally investigate the effectiveness of the linear polarisation subtraction technique in minimising the effects of scattering on the signals, the Signal to Noise performance (S/N) of the polarisation subtracted signals and the practicality of using this technique in experiment.

The prepared scattering phantoms and experimental system used in this work are described in section 3.2, while the modelling of this measurement system and photon transport in scattering phantom media are discussed in section 3.3. The simulation data are useful as a reference to compare with the measured data. These results are presented in section 3.4.1. Also included in this section is a re-examination of the performance of the added absorber and spatial filtering techniques using simulation. The measured and simulated A versus μ_a relationships from linear polarisation measurements are compared in section 3.4.2. This section also presents the results on the depolarisation rate of polarised photons in media of different μ'_s values and the S/N of the linear polarisation system.

3.2 Measurement method and experiment setup

In this section, the preparation of scattering phantoms, the experimental system for transmission mode measurement, and measurement calibration method used for the demonstration of the linear polarisation technique are described.

3.2.1 Scattering phantoms preparation

In the preparation of a scattering phantom, a suspension of polystyrene microspheres and green ink were used as the medium's scatterer and absorber, respectively. They were mixed in water to provide a medium that both absorbed and scattered light. The amount of ink and microspheres used for the experiments are discussed below.

Scattering media with μ_s of 5 mm^{-1} and 7 mm^{-1} were chosen for the demonstration because it was experimentally found that the A versus μ_a relationship is relatively linear when $\mu_s < 5 \text{ mm}^{-1}$ (using the employed measurement system discussed in the following). Furthermore, based on the simulation results of Lu *et al.*,^{24,44} it was concluded that signals measured from a medium with $\mu_s \geq 7 \text{ mm}^{-1}$ and $g = 0.9$ are likely to have a poor S/N value.

Since μ_s and g vary with the measurement wavelength, to obtain a single-valued A versus μ_a relationship a single wavelength light source was used. A laser source was chosen since it has higher output power and light is emitted at a narrower wavelength range compared to that of a Light Emitting Diode (LED) or halogen light source.⁹⁸ The measurement wavelength chosen was $\lambda_m = 671 \text{ nm}$, so the preparation of scattering media with $\mu_s = 5 \text{ mm}^{-1}$ and 7 mm^{-1} requires a microsphere concentration of 1.36 g L^{-1} and 1.904 g L^{-1} , respectively. This wavelength was chosen because it was the emitting

wavelength of an available high power laser (CNI/ MRL-W671). The properties of these microspheres and the calculation of the necessary microsphere concentration values are given in Appendix B. The g value is calculated from Eq. (B.0.11) in Appendix B as 0.91. This value implies that photons in the medium have a high probability of forward scattering,²⁸ which is similar to many kinds of scattering media such as biological tissues and atmospheric aerosols.⁹⁹ These suspensions were mixed using an ultrasonic bath to produce a uniform distribution of scatterers throughout the sample that was then placed into a cuvette with dimensions of 50 mm \times 45 mm \times 10 mm (L \times H \times W).

Water absorbs light with μ_a^w used here to denote the absorption of light by water. Pope *et al.*¹⁰⁰ reported that $\mu_a^w \approx 0.0004 \text{ mm}^{-1}$ when the measurement wavelength is 671 nm. In the experiments, increasing amounts of ink μ_a^{ink} were added to the media producing a μ_a value ranging from 0.0004 mm^{-1} to 0.2254 mm^{-1} in steps of 0.018 mm^{-1} . The mixture of ink and microsphere suspensions was constantly stirred and agitated throughout the measurement processes to prevent the settling of the particles.

3.2.2 Description of the experimental system

In the effort to improve the S/N performance of the spectroscopic system, a lock-in amplifier (LIA) (Stanford Research Systems, SR830) was used. The LIA suppresses the effects of noise on the signals by detecting only the signals which oscillate at the set frequency. The system employing this lock-in signal detection in this study is organised as follows. The modulation of light in the experiment was produced using an optical chopper, which would rotate at the selected frequency (the rotation rate was chosen as 2.74 kHz). Light traversing the sample was collected by a plano-convex lens (with diameter, $\varnothing = 50 \text{ mm}$,

and focal length, $f_L = 125$ mm), which focused the light onto a detector. This detector was connected to the LIA that displayed the amplitude of the detected signals in volts rms, V_{rms} , with data acquisition automated by a computer connected to the LIA via a serial port interface. A diagram on the experiment setup and instruments involved is shown in Fig. 3.1 with an image of the actual measurement system shown in Fig. 3.2.

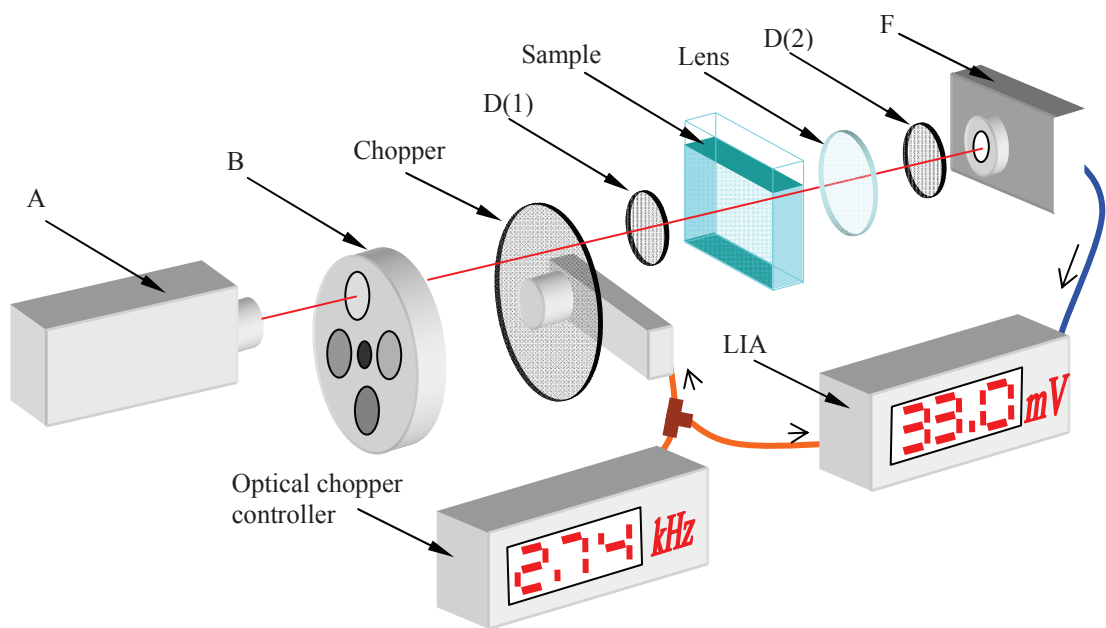


Figure 3.1: Schematic view of polarisation measurement system

In the experiments, a high power solid state laser (CNI/ MRL-W671), which emitted partially polarised light at wavelength 671 nm with an output power and beam diameter of 450 mW and 1 mm, respectively, was used as the point light source (labelled as (A) in Fig. 3.1). The dichroic sheet polarisers (indicated by D(1) and D(2) in Fig. 3.1 and Fig. 3.2) used in these experiments have a laser damage threshold limit of 100 mW mm^{-1} , thus to attenuate the intensity of the illuminating light to a level which is safe to be used

with the polarisers, an optical density(OD) filter of 0.6 (labelled as (B) in Fig. 3.1) was placed in front of the laser source.

The detection of light was by a switchable gain silicon photodiode (PDA36A, Thorlabs[®] Inc) shown as (F) in Fig. 3.1 with a detection area of $3.6 \text{ mm} \times 3.6 \text{ mm}$ and responsivity, $R = 0.44 \text{ AW}^{-1}$ (at 671 nm). This detector has a bandwidth of 785 kHz and gain $G_d = 2.38 \times 10^4 \text{ VA}^{-1}$.



Figure 3.2: The actual polarisation measurement setup. In the diagram- **A**: laser source, **B**: optical density filter, **C**: optical chopper, **D(1)**: polariser(1), **E**: sample, **D(2)**: polariser(2), **F**: photodetector, **G**: lock in amplifier. The convex lens used to focus the transmitted light on to the detector is not shown here.

3.2.2.1 Performing the co-linear and cross-linear polarisation measurements

Following the discussion of Table 2.1, it was decided that based on the results of Lu *et al.*⁴⁴ and Stockford *et al.*²⁵ linear polarisation spectroscopy would be performed. The

extraction of weakly scattered photons relies on the differences in the polarisation states of the detected photons. In the polarisation measurements, the prepared scattering sample was placed between two linear polarisers labelled as D(1) and D(2) in Fig. 3.1 and Fig. 3.2. The linearly polarised light was produced by passing the laser beam through D(1), while co- and cross-linear polarisation detections were achieved by orientating the second polariser (D(2)) at angles of 0° (or 180°) and 90° (or 270°), respectively, with respect to D(1).

The polarisers used in these measurements have an extinction ratio of 1 : 500. This value indicates the ability of polarisers to block the orthogonally polarised light and it is given by the ratio of cross- to co-polarised signals measured after the polarised light passes through D(2) in the absence of a measurement medium.

Measurement calibration is important to remove the contribution of stray light produced by surface reflection and background light on the signals measured from the experiments. Besides, it is also important to provide a reference signal to calculate the attenuation value. The calibration process was achieved by performing the spectroscopic measurement on a pure scattering suspension, which is the medium background, prior to the measurements when the absorber is added. The detected light intensities, when different μ_a^{ink} values (in 0.018 mm^{-1} increments) were introduced into these samples with constant μ_s , are used to give the μ_a dependent attenuation values from Eq. (2.2.4). The attenuation offset, A_s , in the A versus μ_a plot is determined by the logarithm of the ratio of light intensity detected from a pure scattering suspension (i.e. when $\mu_a^{\text{ink}} = 0 \text{ mm}^{-1}$) to the detected intensity when light is transmitted through the cuvette containing only water.

3.3 Modelling of the measurement system and Monte Carlo simulations

The simulation results given by a Monte Carlo model, which is developed within the Applied Optics Group in University of Nottingham,⁹⁰ were compared with the results obtained from the experiments. Unlike the measurement results, these simulation results are not subject to external factors such as error during the preparation of the phantoms and are unaffected by different kinds of noise such as shot noise and readout noise in the system. They can, therefore, be used to examine the resilience of the experimental linear polarisation system to noise. To obtain the simulation data, the measurement system was modelled according to the experimental conditions described in section 3.2. The medium used in the simulation has dimensions $50 \text{ mm} \times 45 \text{ mm} \times 10 \text{ mm}$, and the propagation of photons through this scattering medium was modelled using the Monte Carlo method.

The temporal distribution of photons (i.e. TPSF) traversing the media with μ_s of 5 mm^{-1} and 7 mm^{-1} was derived after 20 million photons were launched into the media at a normal direction to the surface of the samples. In the simulations, if photons arrived at the medium boundary at an angle greater than the critical angle, $\theta_c = 49^\circ$, they would be reflected back into the medium and continue to propagate in the medium. These photons would be refracted and entered the air if they hit the side of the medium at an angle of $\theta < \theta_c$. These photons are not allowed to re-enter the medium. The refracted and reflected angles of the photons are governed by Snell's law, and only the photons escaping at refractance angles within the lens collection angle were scored. The full acceptance angle of the lens, $\theta_a = 23^\circ$, is given by the inverse sine of ratio between the lens radius ($\varnothing/2 = 25 \text{ mm}$) and its focal length ($f_L = 125 \text{ mm}$).¹⁰¹ In addition, photons with a path-

length greater than 1000 mm were discarded because the energy of these photons would be highly attenuated when the medium's $\mu_a \neq 0 \text{ mm}^{-1}$.

The main difference between this work and that performed by Lu *et al.*^{24,44} is the experimental examination of the performance of polarisation subtraction technique in this study. Furthermore different experimental parameters, which include a more heavily scattering medium with a larger dimension, were used in this study to increase the effect of scattering on the attenuation. Besides, a larger sample volume used in this work eases experimental conditions such as the stirring processes and also brings the medium geometry closer to that of realistic scattering media of interest such as human fingers.

3.4 Results and analysis

This study is concerned with investigating the performance of polarisation subtraction technique for practical use, but it is also informative to show and compare the A versus μ_a relationship given from unpolarised (total intensity), polarisation subtraction measurements and other scattering minimisation techniques discussed in section 2.6. Therefore, the work in this study spans from evaluating the performance of different scattering minimisation techniques using simulation to the experimental examination of polarisation measurements used to reject heavily scattered light. These results are presented in two subsequent subsections: simulation results in section 3.4.1 and experimental results in section 3.4.2. The simulation results section presents the TPSFs simulated based on the modelled experimental system and measurement samples. These TPSFs are used to produce the A versus μ_a relationship when polarisation subtraction, added absorber and spatial filtering techniques are used in the system.

Section 3.4.2 contains the experimental results from the polarisation subtraction and unpolarised measurements. The polarisation maintaining signals are given from the measurements described in section 3.2.2, while the unpolarised signals are obtained by summing the signals from the co- and cross-linear polarisation channels. The experimentally measured A versus μ_a relationships for different μ_s are compared and supported using the simulation results. Also discussed in the section are the depolarised rate of photons in different scattering media and the S/N performance of unpolarised and linear polarisation systems.

3.4.1 Simulation results

The simulated TPSF of photons traversing scattering phantoms with μ_s of 5 mm^{-1} and 7 mm^{-1} in the case of the unpolarised and polarisation subtraction measurements are derived using the Monte Carlo method and presented in the following. The ability of added absorber and spatial filtering techniques at rejecting the heavily scattering signals are also re-examined. Both of these techniques are chosen because they are commonly used as means of reducing the heavily scattering photons from the signals.^{24,44}

3.4.1.1 The simulated TPSF of scattering media

Based on the Monte Carlo simulation of photons detected from the modelled measurement system described in section 3.3, the normalised TPSF for samples with μ_s of 5 mm^{-1} and 7 mm^{-1} given from the unpolarised measurements are shown in Fig. 3.3. It can be seen that the mean of photon arrival times increases with the higher μ_s value, and are given by 206 ps and 240 ps when the medium's μ_s is 5 mm^{-1} and 7 mm^{-1} , respectively.

Fig. 3.3 also shows that the variance and hence uncertainty in the photon time-of-flight increases with the sample's μ_s . These TPSFs are used in the next section to show the differences in the A versus μ_a relationship given from the system employing different scattering minimisation methods.

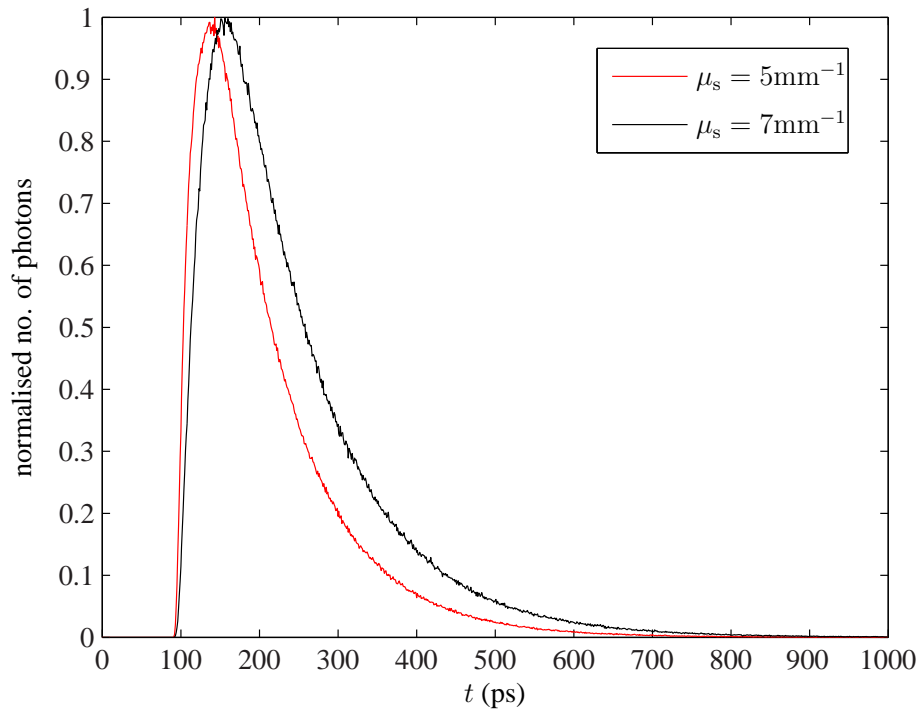


Figure 3.3: The normalised TPSF given from scattering media with μ_s of 5 mm^{-1} and 7 mm^{-1} , and when $\mu_a = 0 \text{ mm}^{-1}$. These Monte Carlo simulated TPSFs are derived from the unpolarised measurements.

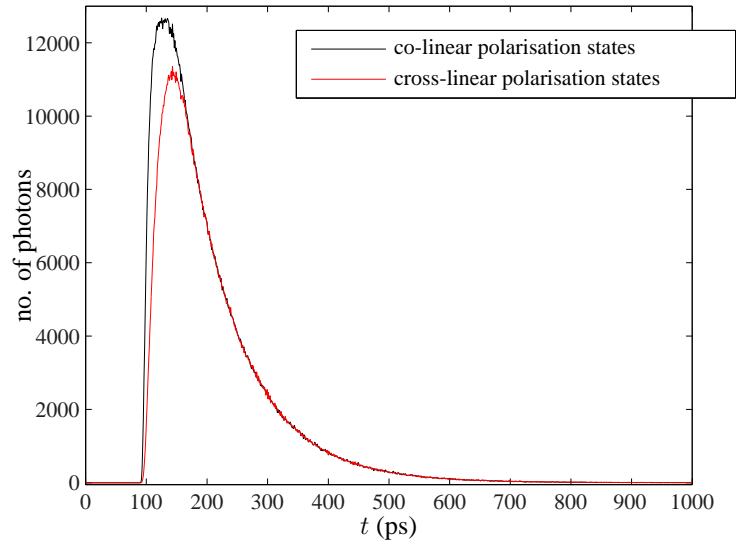
3.4.1.2 Comparing the performance of scattering minimisation techniques

The A versus μ_a relationship given from a scattering medium of any constant μ_s differs by only the nonlinearity of the plot and the A_s value, so TPSF for $\mu_s = 5 \text{ mm}^{-1}$ shown in Fig. 3.3 is used in the following as an example of TPSF measured from the unpolarised

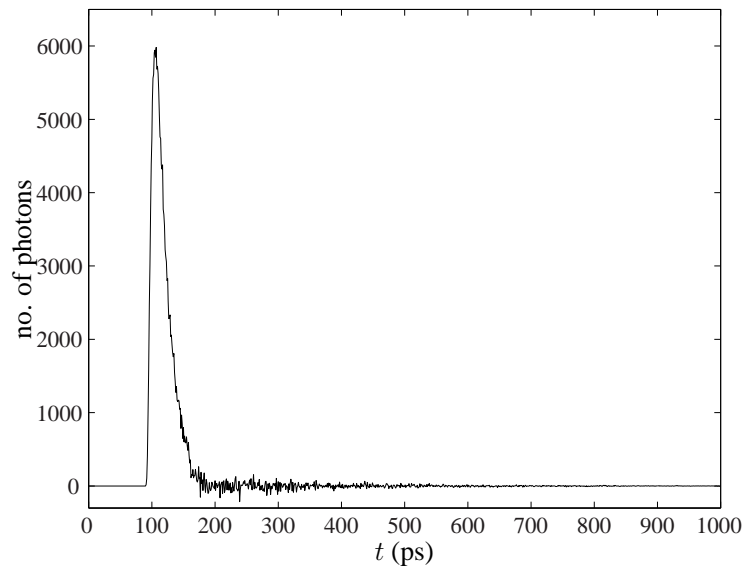
measurements. The μ_a value used in the measurement, which varied from 0.0004 mm^{-1} to 0.2254 mm^{-1} , was applied to each time-point of this TPSF via the Microscopic Lambert Beer law to give the attenuation values from Eq. (2.2.4). The calculated A versus μ_a for the unpolarised measurement is shown in Fig. 3.5.

It was mentioned in section 2.6.3 that the discrimination of weakly scattered light from heavily diffused light using the polarisation measurement is based on the differences in their polarisation states. The polarisation state of each photon is determined by θ and ϕ expressed in Eq. (2.1.9) and Eq. (2.3.5), respectively, and it is described by the Stokes parameters in the Monte Carlo simulation. Further information on the calculation of Stokes parameter values can be found in Appendix C. Shown in Fig. 3.4(a) is the time-of-flight distribution of photons with co- and cross-linear polarisation states produced using the Monte Carlo method. The summation of these TPSFs produced the TPSF shown in Fig. 3.3 (for $\mu_s = 5 \text{ mm}^{-1}$), while their subtraction is the distribution of polarisation maintaining photons shown in Fig. 3.4(b).

Fig. 3.4(b) shows that weakly scattered photons generally arrive at the detector at earlier times than the heavily scattered photons, i.e. cross-linear polarised photons shown in Fig. 3.4(a), and that, due to the noise in the Monte Carlo modelling, the calculated number of weakly scattered photons sometimes exhibit negative values as shown in Fig. 3.4(b). This implies that the assumption that heavily scattering photons are equally distributed across channels 1 and 2 is not necessary true, and can only serve as an approximation in the implementation of this technique. This is because of the statistical uncertainty in the detected scattered signals before the subtraction process shown in Eq. (2.6.1).⁴⁴ Using the TPSF shown in Fig. 3.4(b), the A versus μ_a relationship for the polarisation subtracted signals is shown in Fig. 3.5.



(a)



(b)

Figure 3.4: (a) Monte Carlo simulated time-of-flight distribution of photons with co-linear (dark line) and cross-linear (red line) polarisation states. (b) Time-of-flight distribution of the weakly scattered (i.e. polarisation maintaining) photons given by the differences between TPSF for co- and cross-polarised signals in (a).

While the polarisation state of every photon in the medium is simulated intrinsically within the Monte Carlo method, the detected signals when the added absorber and spatial filtering techniques are implemented in the system are derived post simulation because the exit position and pathlength of each photon were stored during the simulations. To demonstrate the added absorber technique, an additional absorption, $\mu_{a(\text{add})}$, is added to the medium's μ_a and incorporated into the resultant TPSF. Meanwhile, spatial filtering is achieved by modifying the size of the detector aperture, so that only photons with a certain exit angle are scored. Even though both of these techniques are not used in the experiments, their corresponding A versus μ_a curve are plotted in Fig. 3.5.

Fig. 3.5 shows that light attenuation is the highest if an aperture with diameter $\varnothing = 0.04$ mm is used to produce an approximately linear A versus μ_a relationship. This is followed by the added absorber technique when $\mu_{a(\text{add})} = 0.2 \text{ mm}^{-1}$. These \varnothing and $\mu_{a(\text{add})}$ values were chosen because the produced A versus μ_a curve has about the similar linearity as compared to that given by the linear polarisation technique. No test has been performed to compare the linearity of these plots because the results shown in Fig. 3.5 are only to provide a guide about the performance of different techniques at removing the heavily scattering signals. A higher $\mu_{a(\text{add})}$ and a smaller \varnothing would be required to achieve the similar linearity in A versus μ_a relationships shown in Fig. 3.5 if signals are measured from a scattering medium with a higher μ_s .

Based on the results shown in Fig. 3.5, it is reasonable to conclude that as presented previously^{24,44} linear polarisation technique is the best technique as it linearises the A versus μ_a curve while retaining most of the useful signals (lower attenuation values). The main reason the spatial filtering method shows poor scattering rejection performance is due to the detection of heavily scattered photons even when a small detection aperture is

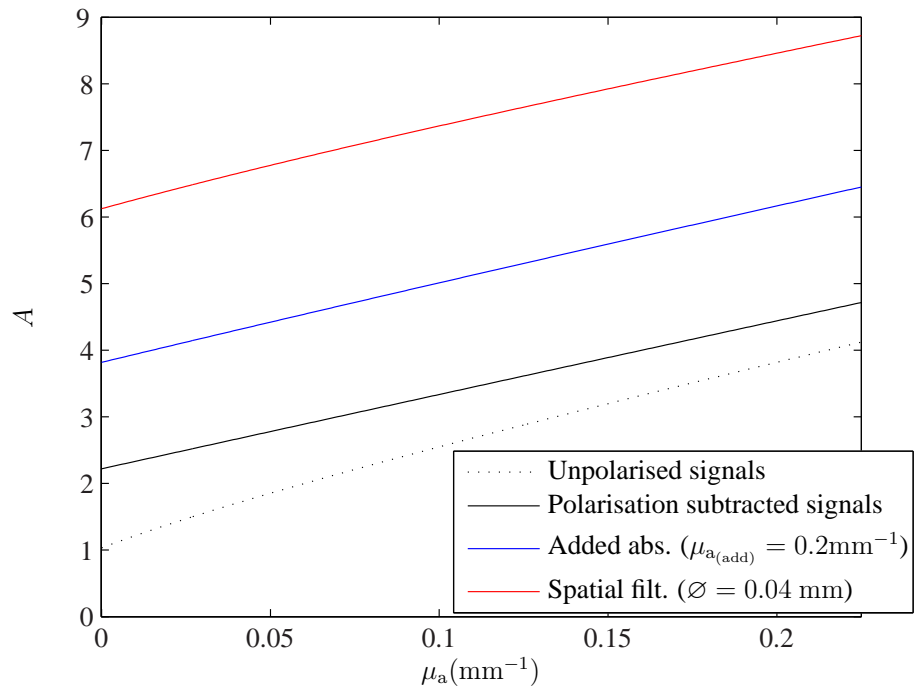


Figure 3.5: The simulated A versus μ_a relationship given from unpolarised measurements (dark dotted line) and when linear polarisation (dark solid line), added absorber (blue line) and spatial filtering technique (red line) are used in the spectroscopy system.

employed. These photons escape from the medium and travelled at directions close to the optical axis of the detector. Thus, any further reduction in the detection aperture might not be able to remove all the heavily scattered photons, yet it would give rise to further attenuation.

3.4.2 Measurement results

The A versus μ_a relationships measured from the unpolarised and linear polarisation measurements are presented here along with the comparison of these results using the simulation results shown in section 3.4.1. This section investigates the degree of polarisation

of the signals measured from media with different μ_s values and the signal to noise performance (S/N) of the unpolarised and polarisation experimental systems. Examination of the depolarisation rate of the photons is important in order to understand the polarisation retention of photons within media with different μ_a and μ_s values, while the S/N investigation determines the practicality of using this technique.

3.4.2.1 Comparison of measured and simulated A versus μ_a relationships

The simulated A versus μ_a relationships were previously shown in Fig. 3.5 (results only shown for the case when the medium's $\mu_s = 5 \text{ mm}^{-1}$). These simulated plots (for unpolarised and polarisation subtracted signals) are shown again in Fig. 3.6. It was found that the simulated and measured A_s (i.e. at $\mu_a = 0 \text{ mm}^{-1}$) values differ by a constant value of 1.5 in both of the μ_s cases (i.e. 5 mm^{-1} and 7 mm^{-1}) when the unpolarised measurements are performed on those samples. The result shown in Fig. 3.6(a) only for the medium with $\mu_s = 5 \text{ mm}^{-1}$ for better illustration. All the measured data will be shown later in Fig. 3.7. Whereby in the case of polarisation subtraction signals, the offset between the simulated and experimentally measured A_s for media with μ_s of 5 mm^{-1} and 7 mm^{-1} are given by 1.1 and 1.0, respectively. Fig. 3.6(b) shows only the measured and simulated polarisation maintained signals given from the medium with $\mu_s = 5 \text{ mm}^{-1}$. All the simulated attenuation values are lower than those that are experimentally measured.

The fairly consistent A_s differences between the simulated data and the results given from measurements performed on different kinds of media imply a systematic error could occur either during the measurements or in the simulations. A possible source of this error is the surface reflection from the lens and cuvette during the measurements.

To allow a comparison between the experiment and simulation results, the differences

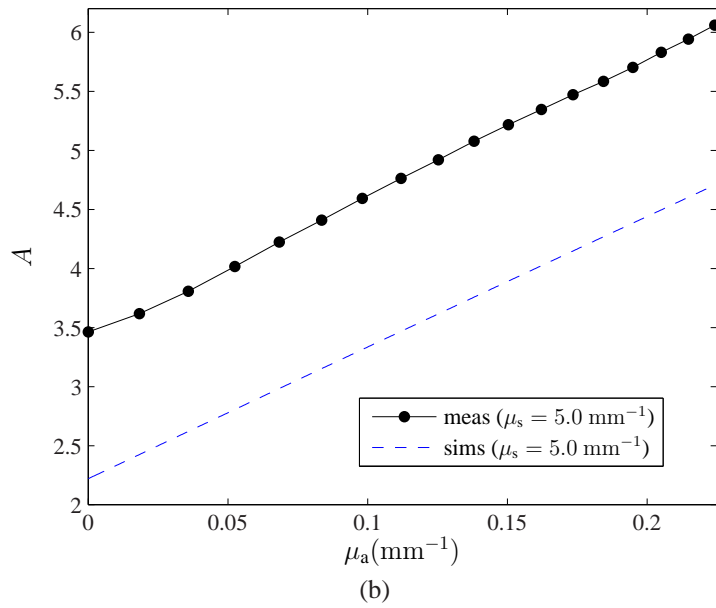
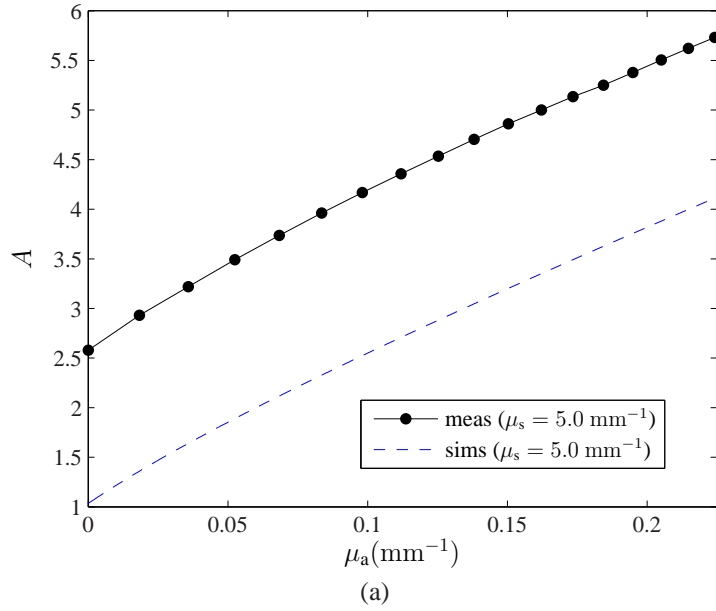
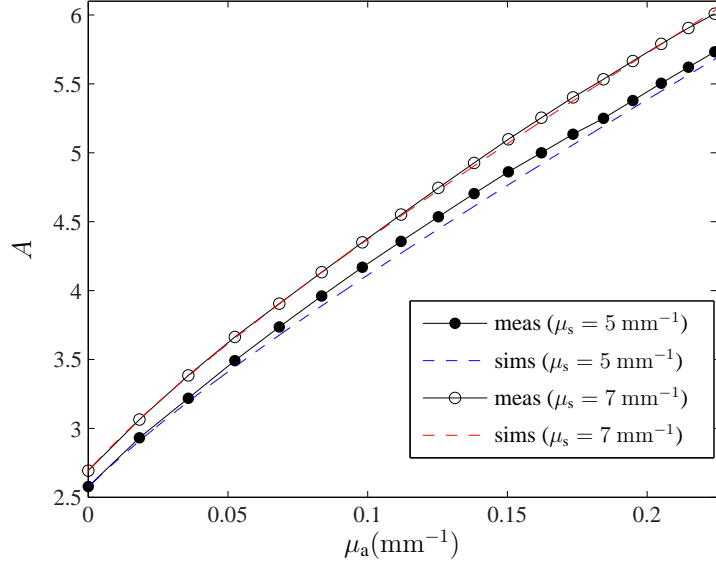


Figure 3.6: The measured (closed circle line) and simulated (blue dashed line) (a) un-polarised signals and (b) polarisation maintaining signals detected from the scattering medium with μ_s of 5 mm^{-1} .

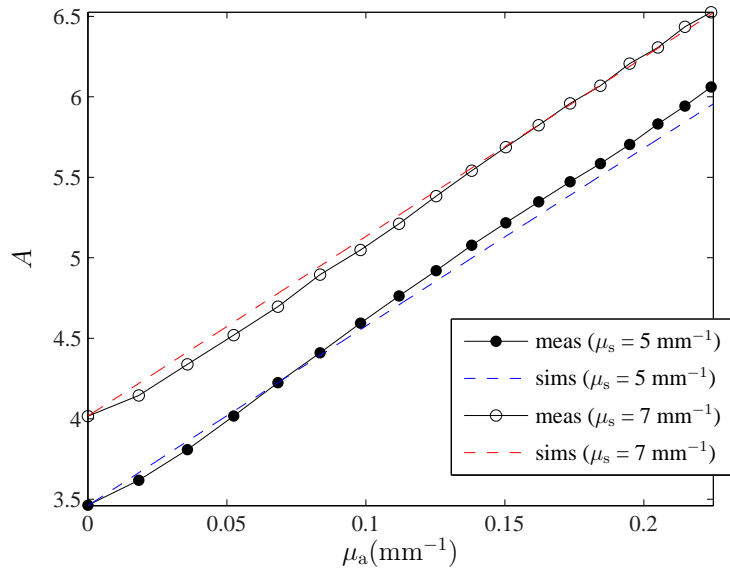
between the plots (shown in Fig. 3.6 for the medium with $\mu_s = 5 \text{ mm}^{-1}$) were minimised by adding the offset values mentioned above to the corresponding simulation results. These offset-corrected plots are shown in Fig. 3.7. Fig. 3.7(a) and Fig. 3.7(b) show the μ_a dependent attenuation values calculated based on the unpolarised and polarisation maintaining signals, respectively, detected from the employed samples. Referring to these plots, as expected, higher attenuation values are measured from the sample with $\mu_s = 7 \text{ mm}^{-1}$ because photons propagating in a higher μ_s medium would have a shorter *mfp* as given in Eq. (2.1.12), increasing the chances of these photons being absorbed (when $\mu_a \neq 0 \text{ mm}^{-1}$), scattered or escaping from the medium at points other than the location of the finite sized detector. The increase in A_s and the nonlinearity of the A versus μ_a plot with μ_s shown in Fig. 3.7(a) were previously observed in Fig. 2.2(b).

Discussion of comparison results

Fig. 3.7(a) shows that even with the corrected plots, an error between the measured and simulated data for the medium with $\mu_s = 5 \text{ mm}^{-1}$ can still be seen. The possibility that this error is due to poor modelling of the system is fairly small as the simulated and experimental data for $\mu_s = 7 \text{ mm}^{-1}$ matched reasonably well. This error is more likely to be a result of mishandling during the preparation of the purely scattering sample when a medium with different μ_s might have been prepared. It is, therefore, informative to find the actual μ_s value for the plots that correspond to the (intended) $\mu_s = 5 \text{ mm}^{-1}$. The search for this value involved running Monte Carlo simulation for photons propagating in medium with different μ_s that ranged between 4.2 mm^{-1} and 5.8 mm^{-1} in 0.1 mm^{-1} increments. This μ_s range was chosen because these values are around $\mu_s = 5 \text{ mm}^{-1}$ which is intended for the performed experiments. A reduction in the differences in the



(a)



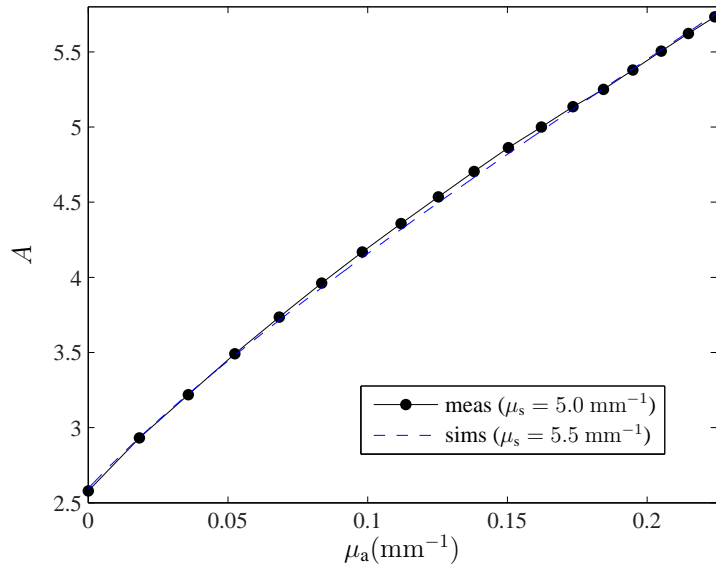
(b)

Figure 3.7: Comparing the measured (open circle and closed circle lines) and offset-corrected simulated (red and blue dashed lines) (a) unpolarised signals and (b) polarisation maintaining signals detected from scattering media with μ_s of 5 mm^{-1} and 7 mm^{-1} .

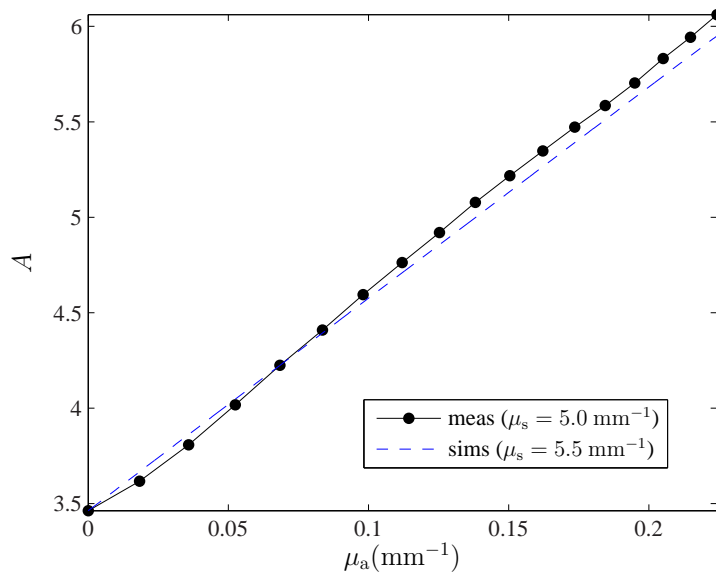
shape between the measured and offset-corrected simulated plots can be observed when the medium's $\mu_s = 5.5 \text{ mm}^{-1}$ is selected in the simulation. The simulated A_s from the unpolarised and polarisation systems are less than those that are experimentally measured by 1.5 and 1.0, respectively. These offsets were added to the simulation data giving the results shown in Fig. 3.8.

If mishandling during the scattering sample preparation is the reason for the error shown in Fig. 3.7 and the actual medium's μ_s is 5.5 mm^{-1} , this suggested that an extra 60 mg of microspheres was added during the preparation of the phantom when no error in the amount of water added into the suspension is assumed. Other potential source of discrepancy is the error in the amount of ink added into the medium, so a range of different μ_a offsets were attempted and added to the μ_a values used in the simulations. It was found that the simulated nonpolarised results fitted reasonably well to the measured nonpolarised data when μ_a values used in the simulations were offset (increased) by 0.003 mm^{-1} . No effort was made to repeat these measurements and to identify the source of the discrepancy mentioned above as the objective of this work was to investigate the performance of polarisation subtraction technique by linearising the A versus μ_a curve, which does not require the attenuation value to be measured with a high degree of accuracy.

It must be mentioned that the accuracy of the estimated value improved by at least 30% when the polarisation subtracted signals are used to give an absorber's concentration value using the Modified Lambert Beer law as compared to that obtained when nonpolarised signals are used (results not shown but see Huong *et al.*).¹⁰² Even though the linear polarisation measurements produce a more linear A versus μ_a relationship as shown in Fig. 3.7(b), smaller signals are detected than in unpolarised measurements. Therefore, the



(a)



(b)

Figure 3.8: The simulated unpolarised and polarisation subtracted signals when the medium's μ_s is 5.5 mm^{-1} (blue dashed line). These signals are compared to the experimentally measured unpolarised and polarisation subtracted signals (closed circle line).

inconsistency between the simulated and measured polarisation subtracted signals shown in Fig. 3.7(b) and Fig. 3.8(b) could possibly be due to the uncertainties in the detected polarised signals as they are more susceptible to system noise.

3.4.2.2 Calculating degree of polarisation

Photons propagating in a medium with a high μ_s have a higher probability of depolarising and being rejected in the polarisation subtraction process. In this work two media of different μ_s are considered. So for the completeness of this study, the ability of photons propagating in each medium to maintain their polarisation states is compared. Using the signals measured from the co- and cross-linear polarisation detection channels, the degree of polarisation of light emerging from samples with μ_s of 5 mm^{-1} and 7 mm^{-1} , are calculated from Eq. (2.6.2) and shown in Fig. 3.9.

The result shows an increase in the degree of polarisation (*DOP*) value with the medium's μ_a . The trend of these *DOP* curves can be explained by noting that heavily scattered photons, whose original polarisation states are destroyed after a few scattering events have, on average, stayed in the medium for a greater amount of time. The energy of these photons is more likely to be absorbed when $\mu_a \neq 0 \text{ mm}^{-1}$ as compared to the weakly scattered photons, hence the amount of heavily scattered photons detected in both of the co-linear and cross-linear detection channels reduces with the increase in medium's μ_a . Consequently, the fraction of weakly scattered photons detected in channel 1 increases with the medium's μ_a .^{103,104}

In addition, these plots show the decrease in *DOP* value with an increase in the sample's μ_s . This is because photons in the medium with $\mu_s = 5 \text{ mm}^{-1}$ are more likely to preserve their polarisation states, hence larger polarisation maintaining signals are de-

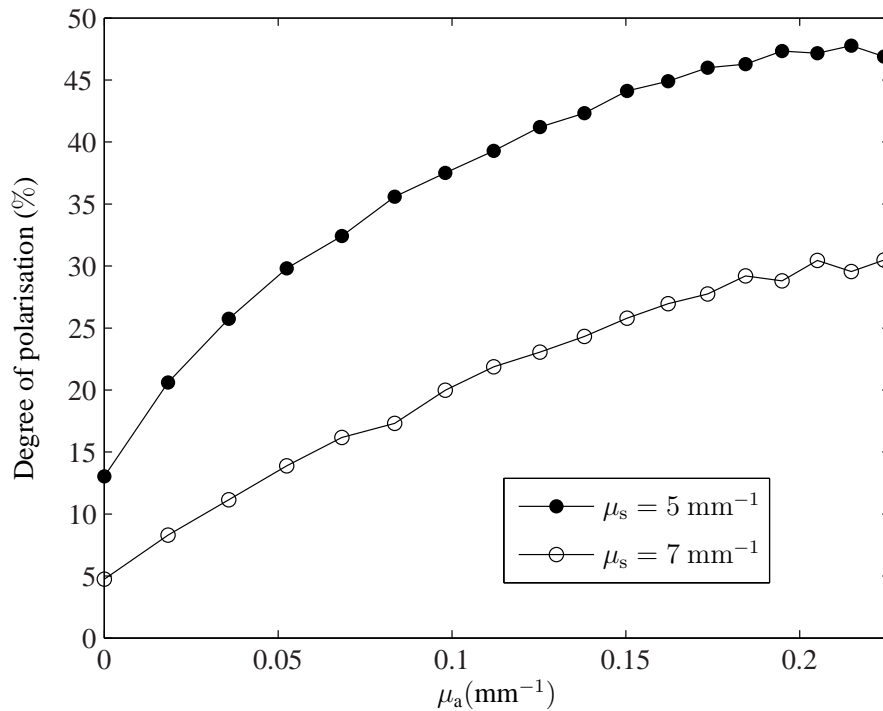


Figure 3.9: The calculated DOP for experimentally measured signals from scattering media with μ_s of 5 mm^{-1} (closed circle line) and 7 mm^{-1} (open circle line).

tected.^{84,104}

3.4.2.3 Evaluating signal to noise performance of the measured signals

A clear indication in the reduction of signals in the case of polarisation subtraction measurements is the increase in the attenuation values shown in Fig. 3.7(b) as compared to the unpolarised signals shown in Fig. 3.7(a). Unlike the unpolarised signals, heavily scattered photons are removed in the linear polarisation measurements. This results in a decrease in the signal levels which could be susceptible to noise. In view of this, it is important to evaluate the S/N performance of the polarisation measurement system. The calculation of the S/N value is described as follows. The optical power of the signal detected in the

experiment, P_{sig} , is given by:¹⁰⁵

$$P_{\text{sig}} = \frac{V_m}{RG_d} \quad (3.4.1)$$

where V_m is the value obtained from the lock-in amplifier while the value of the detector responsivity, $R = 0.44 \text{ AW}^{-1}$, and detector gain, $G_d = 2.38 \times 10^4 \text{ VA}^{-1}$, as previously mentioned in section 3.2.2. The optical power of the detected unpolarised signals, P_{tot} , in Eq. (3.4.1) is given by the sum of the optical power of co- (P_{\parallel}) and cross-polarised light (P_{\perp}):

$$P_{\text{tot}} = P_{\parallel} + P_{\perp} \quad (3.4.2)$$

while the optical power of light incident on the detector, P_{inc} , is given by all the collected light, so $P_{\text{inc}} = P_{\text{tot}}$. Both of the P_{\parallel} and P_{\perp} values are given from Eq. (3.4.1).

For the case of polarisation subtraction measurement, useful signals are the weakly scattered photons with optical power P_{dif} given in Eq. (3.4.3), while the optical power of the incident light is given by the mean of the light optical power measured at both channels P_{inc} in Eq. (3.4.4):²⁵

$$P_{\text{dif}} = P_{\parallel} - P_{\perp} \quad (3.4.3)$$

$$P_{\text{inc}} = \frac{P_{\parallel} + P_{\perp}}{2} \quad (3.4.4)$$

In the experiments, it is assumed that the source of noise on the measured signals is shot noise, so S/N of the signals can reasonably be expressed as

$$S/N = 10 \log_{10} \frac{|I_{\text{sig}}|^2}{I_{\text{sh}}^2} \quad (3.4.5)$$

where the S/N value is in dB. I_{sig} is the photocurrent in the detector and is related to the detector responsivity, R , and detected optical power P_{sig} by:

$$I_{\text{sig}} = RP_{\text{sig}} \quad (3.4.6)$$

P_{sig} is given in Eq. (3.4.2) and Eq. (3.4.3) for the case of signals measured from the unpolarised and polarised experiments, respectively, while I_{sh} denotes the amplitude of shot noise current given by

$$I_{\text{sh}} = \sqrt{2qBP_{\text{inc}}} \quad (3.4.7)$$

Here, $B = 2.74$ kHz is the detection bandwidth.

Using the experimental results shown in Fig. 3.7, S/N values calculated from Eq. (3.4.5) are shown in Fig. 3.10. Since the rejection of heavily scattering photons lowered the signal levels, polarisation subtracted signals show a poorer S/N performance as compared to that measured from the unpolarised experiments.

Photons propagating in the medium with $\mu_s = 7 \text{ mm}^{-1}$ are more likely to undergo scattering processes as governed by Eq. (2.1.12), and have a higher probability of heavy scattering as compared to the case when μ_s is 5 mm^{-1} . Therefore, in the polarisation subtraction experiments, a considerably large amount of signal is being rejected during the subtraction processes, producing a poorer S/N performance shown in Fig. 3.10 when the medium's $\mu_s = 7 \text{ mm}^{-1}$. The differences in the S/N performance between the unpo-

larised and polarised signals associated with this μ_s are also shown to be larger because the rejection of heavily scattered light increased exponentially with the medium's μ_s . This is evident from the results of Morgan and Ridgway⁸⁴ which showed an exponential relationship between the degree of polarisation of polarised light and scatterer concentration.

The small rise in the S/N values of the polarisation subtracted signals in the low μ_a region shown in Fig. 3.10 suggests that when the medium's μ_a is small, depolarised photons with a long pathlength stand a very small chance of being absorbed. These photons can therefore contribute to the shot noise level. However, as μ_a is increased, the energy of these photons is attenuated more quickly than the photons with short pathlength. Based on these plots and the *DOP* plots shown in Fig. 3.9, it is shown that the likelihood for photons with a long pathlength being absorbed is small until when $\mu_a \approx 0.03 \text{ mm}^{-1}$. This explains the observation that there is a sharp rise in the *DOP* values at low μ_a , while a small increase in the S/N plot occurred before the values gradually decrease with increasing μ_a values.

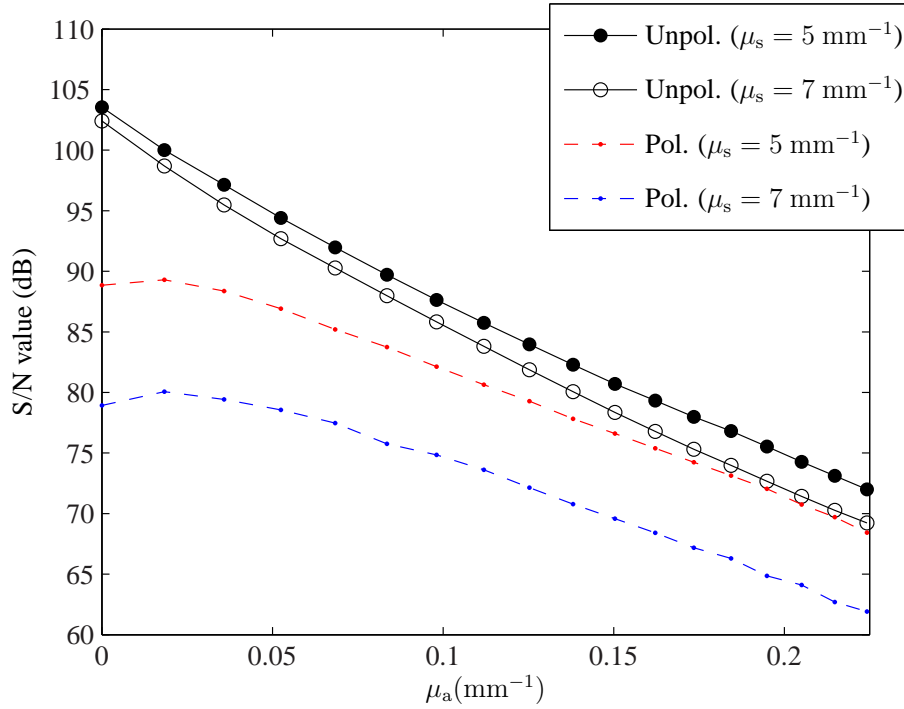


Figure 3.10: The calculated S/N values for the measured unpolarised (Unpol.) and the polarisation subtracted signals (Pol.) versus the sample's μ_a for media with μ_s of 5 mm^{-1} and 7 mm^{-1} .

3.5 Conclusion

The use of linear polarisation technique to reject heavily scattered photons whilst retaining most of their useful information is investigated experimentally. The advantage of employing this technique in the experimental system is that there is no restriction in the selection of wavelengths to quantify an absorber's concentration value using the MLBL, as the resultant A versus μ_a relationship is approximately linear. The results in Fig. 3.7 and Fig. 3.10 show that the use of the polarisation subtraction technique in the experiments produces a more linear A versus μ_a at the price of reduced S/N performance of the

detected signals, so increasing the susceptibility of the signals to noise as compared to unpolarised signals. Besides, the performance of polarisation subtraction technique may also be subject to the rejection ratio of the employed polarisers. Therefore, to perform polarisation subtraction measurements, more robust and sensitive equipment may be needed. These could include a cooled Charge-Couple detector (CCD) and a pair of birefringent polarisers (e.g. Glan-Taylor prisms with a rejection ratio of 1 : 10,000) with high laser damage threshold.

On the contrary, by working on the unpolarised signals, whose amplitude is larger than the polarisation subtracted signals, the signals are less sensitive to noise. This gives a greater leniency and flexibility in the optical devices required for the measurements.

Most importantly, from the discussion of Jacques *et al.*,¹⁰⁶ weakly scattered light, which can be obtained from polarisation subtraction measurements, probed at superficial layer in reflectance mode measurements. Therefore polarisation maintaining light is not suitable for oximetry, which is used as an example of application in this work, when blood SO_2 is the required parameter. This is because blood vessels, from which light that is reflected can be collected and analysed to give an estimation of SO_2 , are found in a deeper region (i.e. at and beyond papillary layer).¹⁰⁷

For the above mentioned reasons, this chapter concludes that polarisation subtraction method is expensive, has limited application and is not suitably used to estimate blood SO_2 value in in-vivo application. The remaining chapters focus on identifying different techniques for the optical characterisation of a scattering medium using the signals given from unpolarised continuous intensity measurements.

Chapter 4

Optical examination of scattering media using linear equation model

4.1 Introduction

In Chapter 3, it was demonstrated that scattering reduction techniques such as polarisation subtraction, added absorber and spatial filtering can reduce the effects of scattering on signals at the price of lower SNR. These methods were also discussed to have limited applications. For this reason, it was decided that different techniques to quantify the fractional concentration value of an absorber in a scattering-absorbing medium using unpolarised measurement would be investigated. Techniques that are available for these quantification works were reviewed in section 2.5. Among them, the simultaneous solution of the MLBL that is used to represent the measured A versus μ_a relationship is mathematically the simplest.¹⁰⁸ Only the absorbers' extinction coefficients and light attenuation from several point measurements are needed in the estimation of this fractional concen-

tration value. Many of the reviewed works²⁻⁴ used MLBL to characterise blood where oxyhaemoglobin (HbO₂) and deoxyhaemoglobin (Hb) are considered the main absorbers, and the fractional concentration of oxyhaemoglobin (SO₂) solving from Eq. (2.5.6) is the required measurement. This analytic model, however, linearly approximates the nonlinear relationship between A and μ_a measured from a scattering medium. This results in poor estimation of SO₂ unless a certain wavelength combination is chosen.^{4,109}

Previously, different wavelength combinations to be used with MLBL were selected by different investigators based on either the lowest mean error in the estimated values or the highest signal to noise ratio of the signals measured using those wavelengths. Among them, Delori suggested the use of two isosbestic wavelengths (i.e. 569 nm and 586 nm shown in Fig. 2.3) and a non-isosbestic wavelength (558 nm) for retinal vessel oximetry.² These wavelengths were chosen because they are closely spaced in the A versus μ_a plot, conforming to a straight line that can be more accurately represented by a MLBL. Smith described how the use of three non-isosbestic wavelengths, whose absorptivity difference (between HbO₂ and Hb), $\Delta\varepsilon$, is positive for one wavelength while negative for the other, are more sensitive to the changes in SO₂.⁴ Both of these works used the measurements from a blood gas analyser in determining the wavelength combination that gives the best estimate of the correct SO₂. Meanwhile Alabboud²⁶ and Stockford *et al.*²⁵ determined their optimal wavelength combinations using simulation. Their approach involved modelling of the employed optical system so that data given from the experiment can be approximated, the value given by different wavelength combinations are compared with the actual value used in the simulations. The optimal combinations of wavelengths were identified based on the error in their estimated value.

Despite the different approaches that have been used to determine the optimal wave-

lengths, a generic means of wavelength selection remained unspecified as the selected wavelengths are based on the observed errors from either a calibrated measurement or simulation. Besides, these workers did not clarify the robustness of their selection, either to noise or as one of the measurement parameters changed.

A different but equally important aspect concerning the selection of wavelengths for oximetry using the MLBL is the signal to noise ratio (SNR) of the signals measured from the selected wavelengths. A study aimed at improving the SNR of the measured signals via the careful selection of wavelengths was previously demonstrated by Sato *et al.*¹¹⁰ In their work, different combinations of dual-wavelengths from the NIR range were arbitrarily selected to monitor the relative concentration change in HbO₂ and Hb, and the SNR of the measured signals were compared. Sato *et al.*¹¹⁰ concluded that the 692 nm, 830 nm pair is optimal due to the highest SNR of the detected signals, but the accuracy of the estimated value has not been tested.

Even though different wavelength combinations have been proposed, it is rather unfortunate from the spectroscopic point of view that the wavelengths selected by all these investigators work desirably well only in their system. This is because the selection of an optimal wavelength combination will change with any measurement parameter that modifies the attenuation spectrum. This precludes any further development in the design of a spectroscopic instrument that does not require a lookup table (such as in pulse oximetry) because no wavelength combination is suitable for generic measurements (of any scattering medium). This is a setback as the selection of a fixed wavelength combination rather than multi or hyperspectral data can reduce the number of wavelengths required for the spectroscopic analysis of a medium using the MLBL, so allowing the use of discrete wavelength lasers and photodiodes, which are cheaper and have faster readout time than,

for example, a CCD.¹¹¹ The aim of the works presented here is to identify the principle which governs the selection of wavelengths to yield zero error in the value estimated using a linear equation model. The linear equation model defined in this chapter can either be a MLBL or its three dimensional equivalent, which is a line in attenuation versus μ_a versus μ'_s space. Two types of scattering media are considered, namely a medium with constant (wavelength invariant) μ'_s and a wavelength dependent scattering medium.

This study begins in section 4.2.1 with a demonstration of error in the f_a value estimated using the MLBL in the case of a wavelength invariant scattering medium. This work uses simulation to help identify factors that determine error in the estimated value because the medium's f_a is known and the simulated data are unaffected by the system noise. The findings deduced from the simulation results are verified mathematically in section 4.2.3.

In practice, the μ'_s value of a scattering medium changes with the light wavelength,^{68,112–114} so strictly the MLBL cannot be used but must be modified to account for this change. This requires knowledge of how a wavelength dependent μ'_s affects the measurables. The wavelength dependent μ'_s values used in this study, and a discussion of how these values modify the measurable space (i.e. TPSF, A) are given in section 4.3. Based on the understanding of the scattering effects, a modified version of the MLBL is proposed in section 4.4, and its performance is examined in section 4.4.1. The derivation of error in the estimated value when this version of MLBL is used and a generic means of selecting wavelengths to theoretically obtain zero error in the estimated f_a value are outlined in section 4.4.2.

The signals measured from a spectroscopy experiment would also be subject to noise that will affect the performance (accuracy of the estimated value). It is therefore interesting to investigate the relationship between the data (i.e. measured attenuation and

absorbers' extinction coefficients) of the selected wavelength combination and the sensitivity of its estimated value to noise as detailed in section 4.5.1. The proof of the discussed theory is based on the noisy signals modelled in section 4.5.2, and the simulated results presented in section 4.5.3 allows the optimal wavelength combination for the considered medium and light illumination-detection system to be identified. The investigation of the performance of different wavelength combinations is via the conventional method which considers the value given by all the wavelength combinations. These values are compared with the actual optical properties values of the medium used in the simulations. All the works demonstrated in this chapter use the optical properties values of human skin with its application to oximetry in mind.

4.2 The Modified Lambert Beer law

Section 2.5.1.1 mentioned that the MLBL expressed in Eq. (2.5.2), as shown again in Eq. (4.2.1), can be solved simultaneously to give the value of G , d , and most importantly, the value of f_a using the attenuation and absorbers' extinction coefficient data at three selected wavelengths as shown in Eq. (2.5.6) - Eq. (2.5.8).

$$A(\lambda) = G + \mu_a(\lambda)d \quad (4.2.1)$$

This model approximates the nonlinear A versus μ_a measured from a scattering medium as linear so error in the estimated f_a value would be expected. The accuracy of the f_a value estimated using the MLBL and attenuation data calculated in section 4.2.1 is presented in section 4.2.2, while the wavelength selection strategy to recover a medium's f_a is outlined

in section 4.2.3.

4.2.1 The simulation of attenuation data for demonstration

To demonstrate the accuracy of the f_a value estimated using the MLBL, the simulated TPSF for medium with $\mu_s = 7 \text{ mm}^{-1}$ shown in Fig. 3.3 is chosen for the following demonstration. The medium's absorption is produced by the absorbers shown in Fig. 2.3. Even though many investigators studying oximetry have not limited their selection of wavelengths and have chosen their wavelengths from the range shown in Fig. 2.3, the focus of this work is on wavelengths in the range 450 nm - 600 nm mainly because the signals measured using wavelengths below 450 nm are small due to the high light absorption, and hence would be more susceptible to noise. The extinction coefficient of the absorbers for wavelengths below 450 nm are not shown in Fig. 2.3, but can be found in Zijlstra *et al.*³⁰ for the wavelength range 400 nm – 1000 nm. The measurement of signals using wavelengths beyond 650 nm (i.e. Red to Near-Infrared range, R-NIR) requires a detector with a large dynamic range due to the small variation in the signals with SO_2 . While the small SO_2 induced changes in attenuation in the R-NIR range is because of the small differences between ϵ_{Hb} and ϵ_{HbO_2} shown in Fig. 2.3, the distinctive differences in the shape of ϵ_{Hb} and ϵ_{HbO_2} can be seen for wavelength range 450 nm – 600 nm, producing a significant variation in the shape of the attenuation spectrum as the SO_2 varies. This SO_2 induced variation in the A spectrum is important because the techniques described later in Chapter 5 and 6 rely on the changes in this shape to recover the medium's absorber fractional concentration value.

The total concentration of absorbers, $T_H = 7 \text{ } \mu\text{mol L}^{-1}$, and $\text{SO}_2 = 80\%$ are chosen

for this demonstration so that they produce a medium with $\mu_a \ll \mu'_s$ similar to that found in most of the scattering media such as biological tissues.^{107,113,115,116} These μ_a values are incorporated into the TPSF via the Microscopic Lambert-Beer law to give the wavelength dependent light attenuation shown Fig. 4.1. The μ_a spectrum is shown in Fig. 4.2 (top).

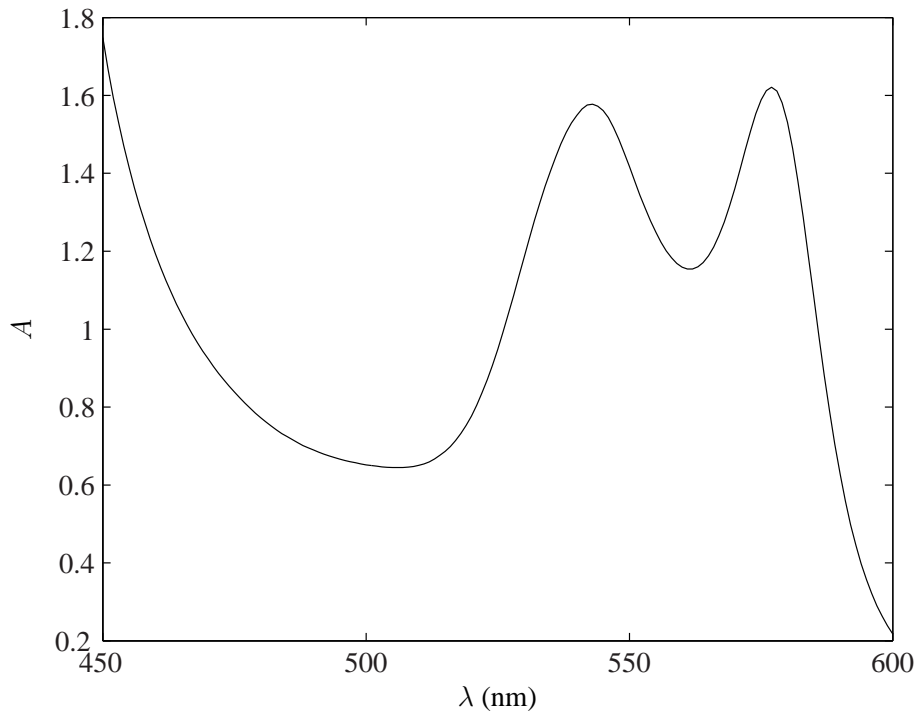


Figure 4.1: The attenuation spectrum of the medium with $\mu_s = 7 \text{ mm}^{-1}$, $g = 0.91$ and $\text{SO}_2 = 80\%$.

4.2.2 Results and discussion

Any wavelengths can be used as λ_1 , λ_2 and λ_3 , and a three dimensional error plot given by the error in the value calculated from every combination of three wavelengths can be used to show changes in the accuracy of the estimated value with different wavelength combinations. However, in the following, λ_1 and λ_2 are chosen as 500 nm and 550 nm,

respectively. These are arbitrary selections as it is easier to demonstrate how the accuracy of the value estimated by the MLBL dependent on the selection of wavelengths by fixing two wavelengths while allowing the error in the estimated value to vary with the third wavelength. The μ_a value of these selected λ_1 and λ_2 is indicated by the cross symbol in Fig. 4.2 (top).

Using Eq. (2.5.6), a calculated SO_2 within the range of -2% and 102% is considered acceptable since there were reports on the analytical arterial blood SO_2 value of about 102% ,¹¹⁷ which was attributed to the error in the analytical procedures and the poor assumptions that were made in the calculations of blood arterial oxygen saturation.¹¹⁷ The error in the calculated value is shown in Fig. 4.2 (bottom).

The error in the estimated value shown in Fig. 4.2 (bottom) is due to the insufficiency of the MLBL at describing the relationship between the measured A and μ_a of a scattering medium. Fig. 4.2 shows that zero error is produced when $\mu_{a3} = \mu_{a1}$ or $\mu_{a3} = \mu_{a2}$ (indicated by the dashed lines), and the error in the estimated value increases as the μ_{a3} value is progressively dissimilar to the μ_{a1} and μ_{a2} . A further demonstration of the MLBL given by different wavelength combinations will be shown next.

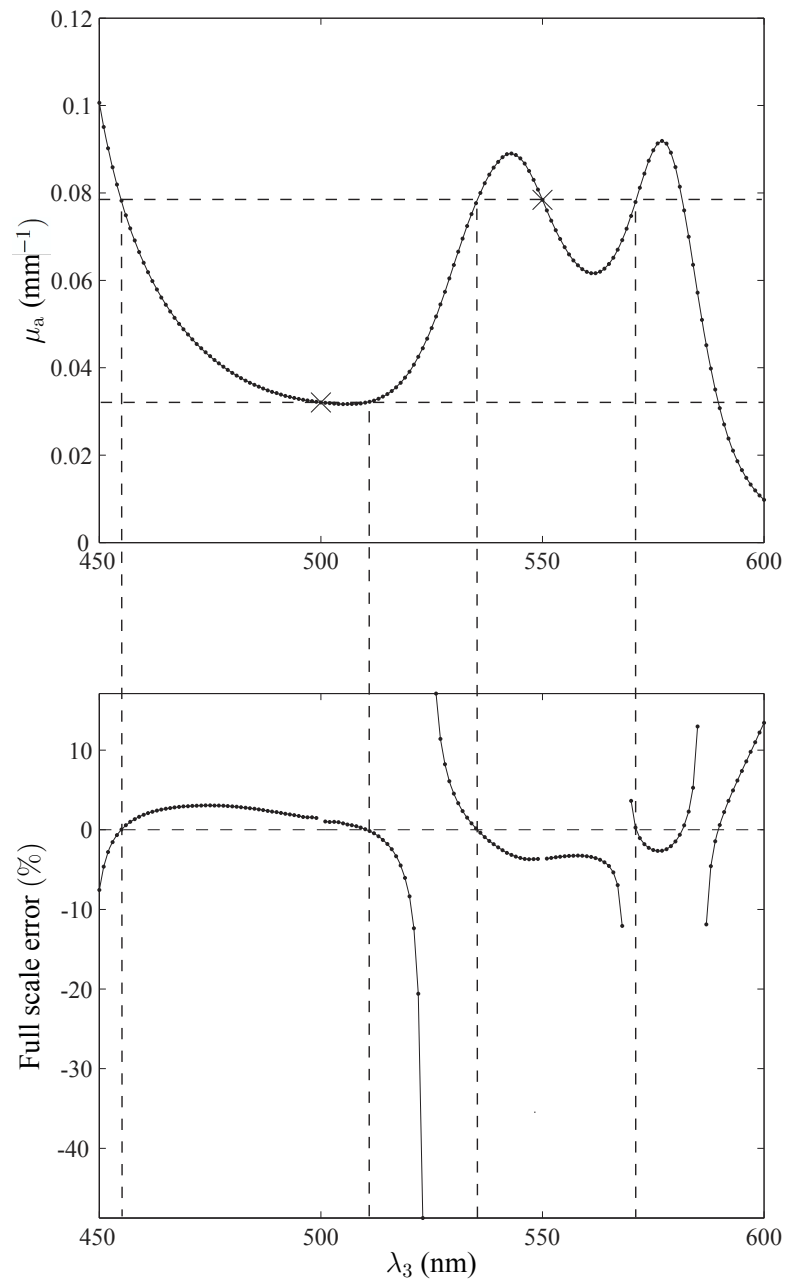


Figure 4.2: (top) The variation in μ_a with λ_3 (shown on the x-axis) when $\text{SO}_2 = 80\%$ and the location of the μ_a of $\lambda_1 = 500$ nm and $\lambda_2 = 550$ nm on the plot (indicated by the cross symbols). (bottom) The error in the calculated SO_2 in relation to the μ_a of λ_3 . The attenuation data used for the demonstration are described in section 4.2.1. The error in the estimated SO_2 outside the range -2% to 102% is not shown in the diagram.

4.2.2.1 Analysis of results

It must be mentioned that the medium's μ_a cannot be calculated from Eq. (2.5.3) without knowing the medium's absorbers total concentration value (T_a), where, from Eq. (2.5.3) the μ_a of a medium with two absorbers can also be written as

$$\mu_a = \alpha T_a \quad (4.2.2)$$

where α is the relative specific absorption coefficient of the medium with absorbers A and B at λ_x given by

$$\alpha(\lambda_x) = (\varepsilon_A(\lambda_x) - \varepsilon_B(\lambda_x))f_a + \varepsilon_B(\lambda_x) \quad (4.2.3)$$

The T_a value does not vary with the measurement wavelength, so wavelength pairs that give the same α produce the same μ_a value. Since the T_a is, in practice, unknown and cannot be estimated by the MLBL as discussed in Appendix A, the results from MLBL presented in the following are in α space.

Based on the error plot shown in Fig. 4.2, an example of wavelength combinations that produced a reasonably accurate value is $\lambda_1 = 500$ nm, $\lambda_2 = 550$ nm and $\lambda_3 = 455$ nm (with error of about 0.02%). The location of these points on A and α versus wavelength spaces, and A versus α is shown in Fig. 4.3. The data of λ_1 and λ_2 (indicated by plus symbol), and that of λ_3 (open circle) are shown in these plots. The α value of the selected points given from Eq. (4.2.3) using the estimated f_a are marked by red crosses in Fig. 4.3 (top right and bottom right). Also shown in Fig. 4.3 (top right) is the MLBL given by the calculated G , d and f_a in Eq. (2.5.6) - Eq. (2.5.8) (red line). Referring to Fig. 4.2 (bottom) the medium's f_a can be recovered using data at these selected points, so the calculated α

intersect the true values shown in Fig. 4.3 (bottom right).

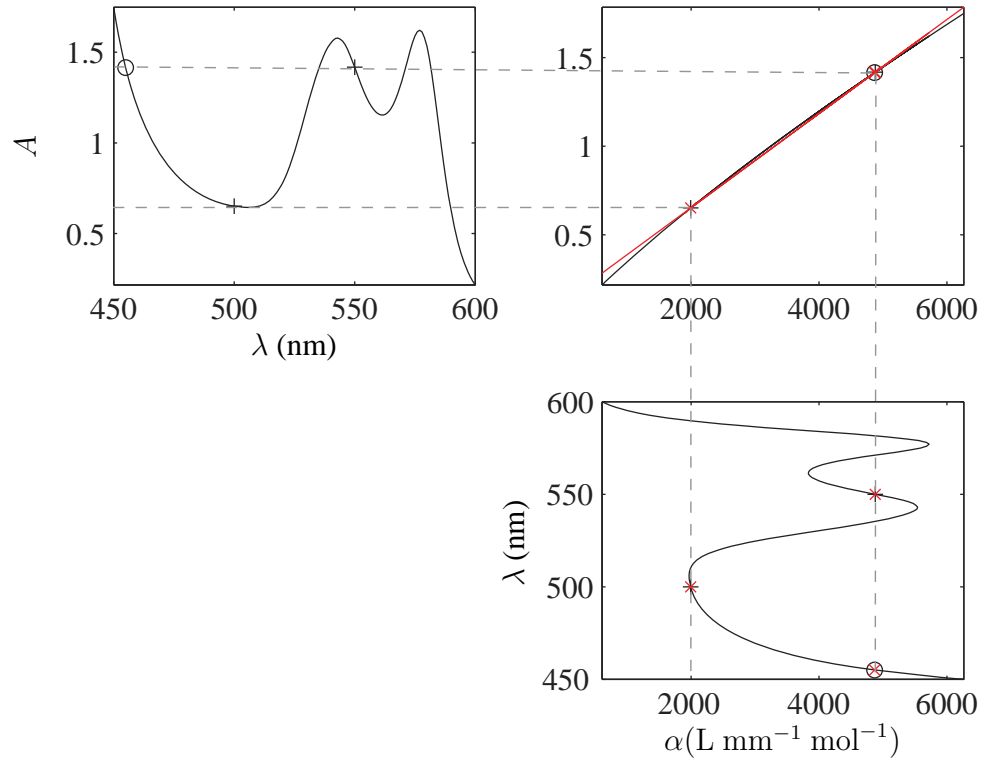


Figure 4.3: (top left) The variation in A with λ (shown on the x-axis) when $\text{SO}_2 = 80\%$. (top right) The relationship between A and the medium's α . (bottom right) The actual α versus λ . The location of $\lambda_1 = 500$ nm, $\lambda_2 = 550$ nm (both indicated by the plus symbol) and $\lambda_3 = 455$ nm (circle symbol) are shown on the plots. The α values given by the f_a calculated using data at the selected points are marked by red crosses (the calculated $f_a = 80.02\%$). The MLBL defined using the data of these wavelengths is also shown on the top right of the diagram (red line).

It was shown in Fig. 2.2 and Fig. 3.7, and again in Fig. 4.3, that attenuation has a single-valued relationship with μ_a (i.e. α) when the medium's μ'_s is a constant value, so from the results in Fig. 4.2 and Fig. 4.3 wavelengths that can reproduce the true SO_2 value can be identified as those with any two of the three wavelengths that give the same attenuation value. These wavelengths can be determined directly from their attenuation value, which

can be obtained using a spectrometer or hyperspectral camera. The above observation remains valid when other wavelengths are selected as λ_1 and λ_2 . The validity of this will be mathematically evaluated in section 4.2.3.

The largest error can be seen in Fig. 4.2 (bottom) when $\lambda_3 = 523$ nm, so it is informative to show the MLBL defined by the data at these wavelengths and the location of α values on the plots given by the calculated f_a value. Using the data at $\lambda_1 = 500$ nm, $\lambda_2 = 550$ nm and $\lambda_3 = 523$ nm, the collinearity of these points in A versus α is obtained when $f_a = 32\%$, which disagrees with the true f_a of 80 %, and the line (i.e. the MLBL) given by the calculated G , d and f_a connecting these points is shown in Fig. 4.4 (top right). Unlike the results shown in Fig. 4.3, differences between the actual and the calculated α values (indicated by red crosses) resulted from the error in the estimated f_a value can be seen in Fig. 4.4 (top right and bottom right). From the discussion of Fig. 4.2, the difference between α of λ_3 and that of λ_1 (and λ_2) could potentially be the source of the observed error, as will be mathematically examined in the next section.

It must also be mentioned that noticeable improvements in the accuracy of the estimated value given by this method can be observed if the A versus μ_a relationship is more linear as it can be more accurately approximated by the MLBL. Based on the attenuation and α spectra shown in Fig. 4.3 and Fig. 4.4, this can be achieved by working on a smaller wavelength range where changes in photon mean pathlength with wavelength is small. In the case when a similar photons' pathlength is measured across a wavelength range, the selection of any three wavelengths from this range give an f_a value using Eq. (2.5.6) with low error. Besides oximeters usually measure arterial SO_2 in the range of 80% to 100%, so a desirable accuracy can be achieved by selecting a combination of three wavelengths which works at this SO_2 range by sacrificing accuracy of the estimated value at lower SO_2

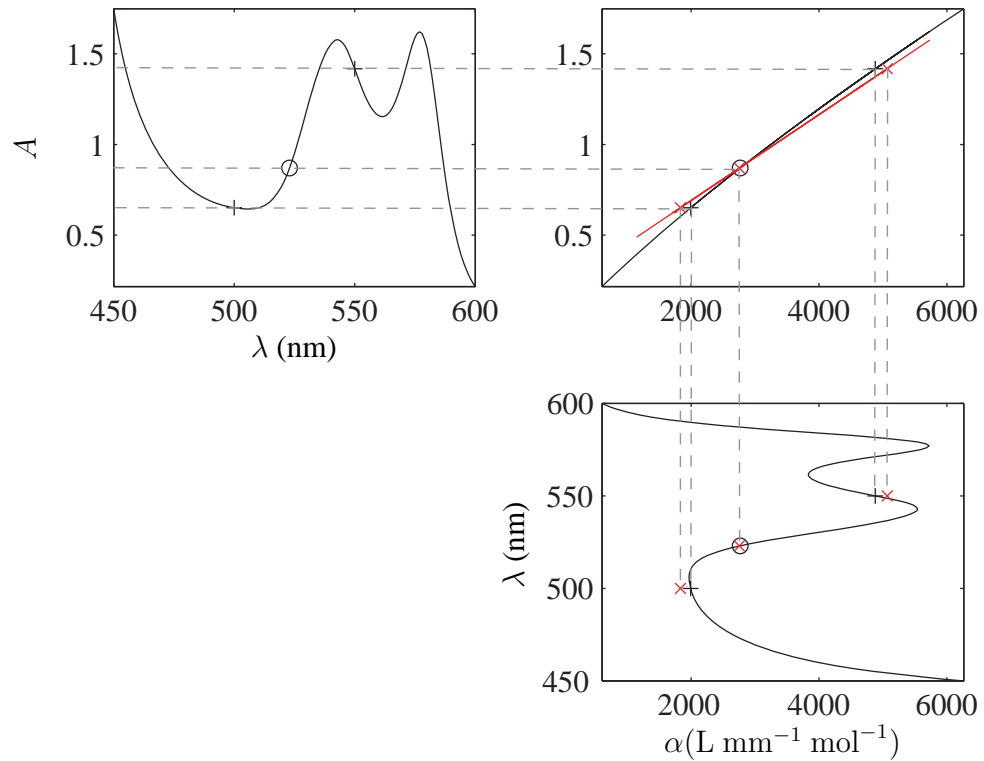


Figure 4.4: (top left) The variation in A with λ (shown on the x-axis) when $\text{SO}_2 = 80\%$. (top right) The A versus the medium's α relationship. (bottom right) The actual α versus λ . The location of $\lambda_1 = 500$ nm, $\lambda_2 = 550$ nm (both indicated by the plus symbol) and $\lambda_3 = 523$ nm (circle symbol) on the plots. The α values given by the calculated f_a value of 32 % are marked by red crosses. The MLBL defined using the data of the selected wavelengths is drawn on the top right of the diagram (red line).

values.

4.2.3 Derivation of error in the estimated value

The accuracy of the value estimated using the MLBL depends critically on the data (i.e. optical properties and measured attenuation values) of the selected three wavelengths as shown in Fig. 4.3 and Fig. 4.4. To examine this error, let the error in the estimated f_a

value, E , be written as

$$E = f'_a - f_a \quad (4.2.4)$$

Here, f'_a is the value estimated by the MLBL shown in Eq. (2.5.6) for the case of a medium with absorber A and B, whilst f_a is the actual f_a value. Substituting Eq. (2.5.6) into Eq. (4.2.4) gives

$$E = \frac{A_1(\varepsilon_{B_3} - \varepsilon_{B_2}) + A_2(\varepsilon_{B_1} - \varepsilon_{B_3}) + A_3(\varepsilon_{B_2} - \varepsilon_{B_1})}{A_1(\varepsilon_{AB_2} - \varepsilon_{AB_3}) + A_2(\varepsilon_{AB_3} - \varepsilon_{AB_1}) + A_3(\varepsilon_{AB_1} - \varepsilon_{AB_2})} - f_a \quad (4.2.5)$$

Rearranging Eq. (4.2.5) provides

$$E = \frac{A_1\varepsilon_{B_{32}} + A_2\varepsilon_{B_{13}} + A_3\varepsilon_{B_{21}} - f_a [A_1(\varepsilon_{AB_2} - \varepsilon_{AB_3}) + A_2(\varepsilon_{AB_3} - \varepsilon_{AB_1}) + A_3(\varepsilon_{AB_1} - \varepsilon_{AB_2})]}{A_1(\varepsilon_{AB_2} - \varepsilon_{AB_3}) + A_2(\varepsilon_{AB_3} - \varepsilon_{AB_1}) + A_3(\varepsilon_{AB_1} - \varepsilon_{AB_2})} \quad (4.2.6)$$

where $\varepsilon_{B_{32}} = \varepsilon_{B_3} - \varepsilon_{B_2}$. Eq. (4.2.6) can also be written as

$$E = \frac{A_1 [f_a(\varepsilon_{AB_3} - \varepsilon_{AB_2}) + \varepsilon_{B_{32}}] + A_2 [f_a(\varepsilon_{AB_1} - \varepsilon_{AB_3}) + \varepsilon_{B_{13}}] + A_3 [f_a(\varepsilon_{AB_2} - \varepsilon_{AB_1}) + \varepsilon_{B_{21}}]}{A_1(\varepsilon_{AB_2} - \varepsilon_{AB_3}) + A_2(\varepsilon_{AB_3} - \varepsilon_{AB_1}) + A_3(\varepsilon_{AB_1} - \varepsilon_{AB_2})} \quad (4.2.7)$$

Rearranging Eq. (4.2.7) and using α shown in Eq. (4.2.3) to give

$$E = \frac{A_1(\alpha_3 - \alpha_2) + A_2(\alpha_1 - \alpha_3) + A_3(\alpha_2 - \alpha_1)}{A_1(\varepsilon_{AB_2} - \varepsilon_{AB_3}) + A_2(\varepsilon_{AB_3} - \varepsilon_{AB_1}) + A_3(\varepsilon_{AB_1} - \varepsilon_{AB_2})} \quad (4.2.8)$$

The μ_a value is related to α via Eq. (4.2.2), so from the discussion of the results in section 4.2.1 the error E becomes zero when one of the following conditions are satisfied:

$$\alpha_3 = \alpha_1 \quad (4.2.9)$$

or

$$\alpha_3 = \alpha_2 \quad (4.2.10)$$

To proof this, let $\alpha_3 = \alpha_1$ so that Eq. (4.2.7) becomes

$$\begin{aligned} E &= \frac{A_1(\alpha_1 - \alpha_2) + A_2(\alpha_1 - \alpha_1) + A_3(\alpha_2 - \alpha_1)}{A_1(\varepsilon_{AB_2} - \varepsilon_{AB_3}) + A_2(\varepsilon_{AB_3} - \varepsilon_{AB_1}) + A_3(\varepsilon_{AB_1} - \varepsilon_{AB_2})} \\ &= \frac{A_1(\alpha_1 - \alpha_2) + A_3(\alpha_2 - \alpha_1)}{A_1(\varepsilon_{AB_2} - \varepsilon_{AB_3}) + A_2(\varepsilon_{AB_3} - \varepsilon_{AB_1}) + A_3(\varepsilon_{AB_1} - \varepsilon_{AB_2})} \end{aligned} \quad (4.2.11)$$

In the case of a medium with wavelength invariant μ'_s , the medium's α (and hence the μ_a) exhibits a single-valued relationship with the measured attenuation, so let $A(\lambda) = f(\alpha(\lambda))$, which denotes the attenuation value as a single-valued function of α at the measurement wavelength gives

$$E = \frac{f(\alpha_1)(\alpha_1 - \alpha_2) + f(\alpha_3)(\alpha_2 - \alpha_1)}{f(\alpha_1)(\varepsilon_{AB_2} - \varepsilon_{AB_3}) + f(\alpha_2)(\varepsilon_{AB_3} - \varepsilon_{AB_1}) + f(\alpha_3)(\varepsilon_{AB_1} - \varepsilon_{AB_2})} \quad (4.2.12)$$

The $\alpha_1 = \alpha_3$, so $f(\alpha_1) = f(\alpha_3)$, and Eq. (4.2.11) is reduced to

$$E = \frac{(f(\alpha_1) - f(\alpha_1))(\alpha_1 - \alpha_2)}{f(\alpha_1)(\varepsilon_{AB_1} - \varepsilon_{AB_3}) + f(\alpha_2)(\varepsilon_{AB_3} - \varepsilon_{AB_1})} = 0 \quad (4.2.13)$$

The above derivations confirm the findings from Fig. 4.2 that zero error can be obtained when $\alpha_3 = \alpha_1$ or $\alpha_3 = \alpha_2$. The reason this gives zero error is that when any two of the three measurement points overlap one another in A versus α space, while the third point is at a location other than that of the first two points, then the straight line formed by these points intersects the true A versus α at these selected points as shown in Fig. 4.3. This straight line can then be accurately represented by the MLBL.

4.3 Investigation of the effects of varying μ'_s on TPSF and attenuation

In previous sections, a strategy to recover the fractional concentration value of an absorber in a medium with constant μ'_s using the MLBL as also assumed by investigators such as Duling and Pittman,³ Delori,² Zhang *et al.*⁴⁰ and Smith⁴ is described. However, the assumption of a medium with constant μ'_s is not true as changes in wavelength modify the μ'_s of a scattering medium. This is because the scattering cross section, size parameter and g vary with the measurement wavelength (refer to Appendix B). This complicates the quantification of f_a using the MLBL as the latter does not account for the variation in A with the varying μ'_s .^{3,4} Thus, this work considers a similar approach to that taken by Alabboud,²⁶ in which the necessary modification on the MLBL to include the effects of scattering on attenuation value is determined. To do so, it is essential to understand the effects that wavelength dependent scattering have on the TPSF and hence light attenuation, and this is discussed in the next section. The demonstration of the scattering effects on attenuation and TPSF begins in section 4.3.1 with a discussion of the absorption and scattering properties of the medium used in this work, its geometry and the light source-detector configuration. The version of MLBL modified based on the medium optical properties used in this work is described in section 4.4.

4.3.1 Description of the medium and experimental system

The μ'_s values of intralipid-10% across the wavelength range of 400 nm to 1000 nm (Staveren *et al.*¹¹⁸) are chosen as the wavelength dependent μ'_s values. These μ'_s vary

monotonically with wavelength and are shown in Fig. 4.5. This monotonic variation in μ'_s with wavelength is common for many kinds of scattering medium such as biological tissues,^{68,112,113} plant species,¹¹⁹ and atmospheric aerosols.¹¹⁴

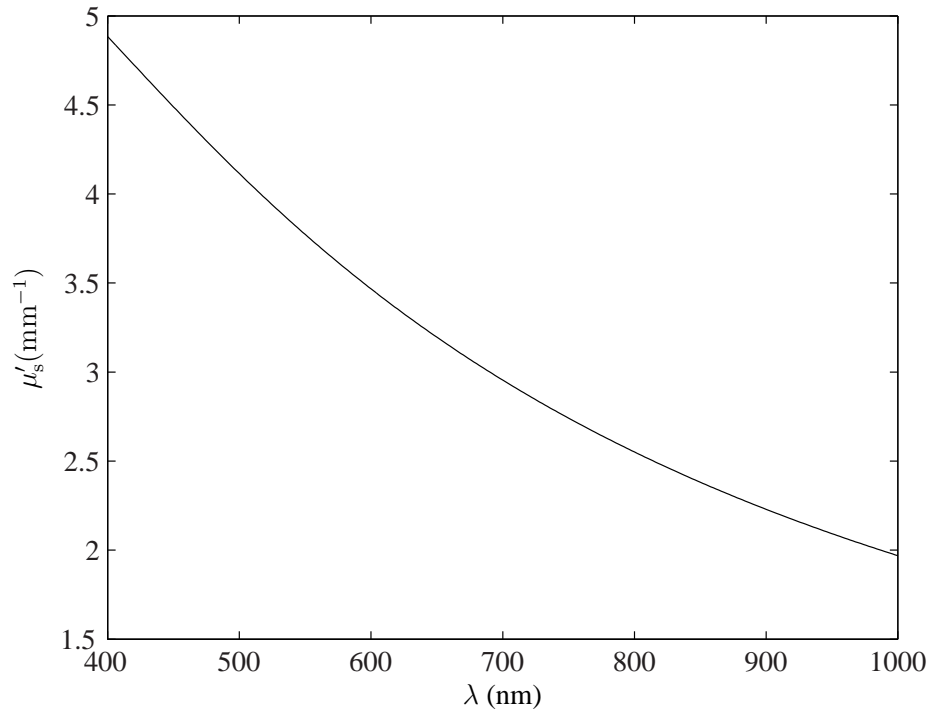


Figure 4.5: The variation in μ'_s with wavelength in the range 400 nm – 1000 nm (taken from Staveren *et al.*).¹¹⁸

The modelling of the spectroscopic measurements of a wavelength dependent scattering medium uses a wavelength range of 450 nm to 600 nm to illuminate an infinite slab as shown in Fig. 4.6. This infinite slab has $\mu_a = 0 \text{ mm}^{-1}$ and wavelength dependent μ'_s values shown in Fig. 4.5. The photon propagation using 20 million photons launched normally into the medium was simulated by a Monte Carlo model. In the simulations, photons with a pathlength greater than 1000 mm were discarded due to their negligible contribution to the overall intensity when the medium's $\mu_a \neq 0 \text{ mm}^{-1}$ as discussed in

section 3.3. The reflection angle of these photons as they reached the medium's boundary is governed by Snell's law. An annular detector with inner and outer radius of 2.5 mm and 3.5 mm, respectively, as shown in Fig. 4.6 was used to detect the reflected photons. This detector is placed directly at the medium boundary. This type of detector geometry is chosen to minimise the detection of surface reflected light, which carries little or no information about the medium absorbers' properties. Besides, this configuration is similar to that of the ocean optics miniature fiber optics spectrometer (USB 2000) and is used in the Monte Carlo simulations as an example of experimental system to obtain the attenuation spectra for the following demonstration works.

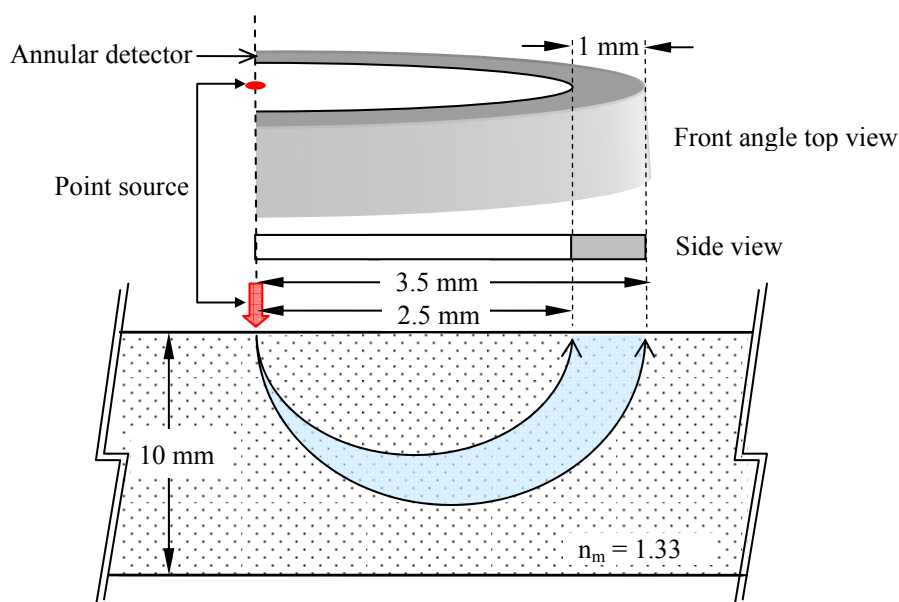


Figure 4.6: The infinite slab and the light illumination-detection system used in the Monte Carlo simulations.

4.3.2 Simulation results

The temporal distribution of photons arriving at the detector, when light of different wavelengths was used to illuminate the medium, are plotted in Fig. 4.7.

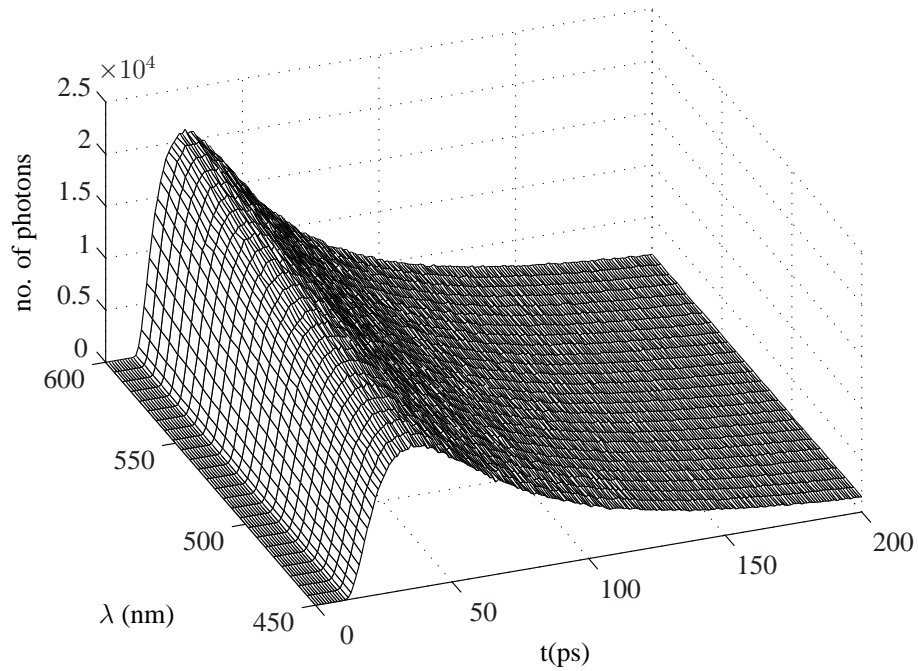


Figure 4.7: The variation in TPSF with wavelength when $\mu_a = 0 \text{ mm}^{-1}$.

It is shown in Fig. 4.3 and Fig. 4.4 that A has a single-valued relationship with μ_a when the μ'_s of the medium is wavelength invariant. This is not the case when μ'_s varies with wavelength as it modifies A . So, it is informative to demonstrate the variation in A with the varying μ'_s when the medium's μ_a is a constant by arbitrarily choosing μ_a as a constant value of 0.1 mm^{-1} , 0.2 mm^{-1} and 0.4 mm^{-1} . Each of these μ_a values is substituted into the Microscopic Lambert-Beer law in Eq. (2.2.4) and incorporated into the TPSFs shown in Fig. 4.7, giving the A versus wavelength curves shown in Fig. 4.8. It can be seen from

these plots that the relationship between A and wavelength at any μ_a is approximately linear. There is a nonlinear change in A with μ_a at any wavelength, and this nonlinearity changes with the wavelength. Each wavelength indicates a different μ'_s value shown in Fig. 4.5, so the observed nonlinear A versus μ_a relationship for a specific wavelength is as shown in Fig. 4.3 and Fig. 4.4.

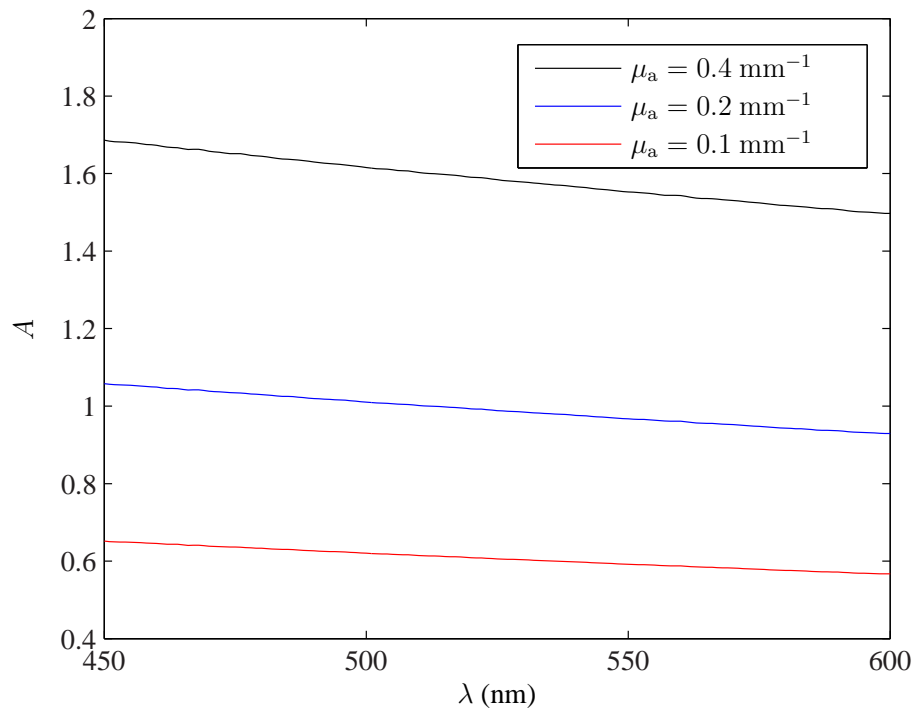


Figure 4.8: The variation in A with wavelength when μ_a is a constant.

A demonstration of the variation in A with wavelength dependent μ_a and μ'_s values is shown by using the TPSFs in Fig. 4.7 and the extinction coefficients of the absorbers shown in Fig. 2.3. The total concentration of these absorbers in the medium is chosen as a constant value of $T_H = 58 \mu\text{mol L}^{-1}$ so that the variation in μ_a at a wavelength can be observed only when the SO_2 varied. The choice of medium absorbers, μ'_s and μ_a ranges used in this demonstration resemble those of the human tissue.^{112,118,120}

The effects of these wavelength dependent μ_a values are introduced into its associated TPSF (which also varies with the wavelength) via the Microscopic Lambert-Beer law to produce an example of A versus μ_a relationship when $SO_2 = 80\%$ as shown in Fig. 4.9. This SO_2 value is chosen as it is the mean SO_2 value (of capillaries) commonly reported from spectroscopic measurements performed at the surface of the skin.¹²⁰⁻¹²²

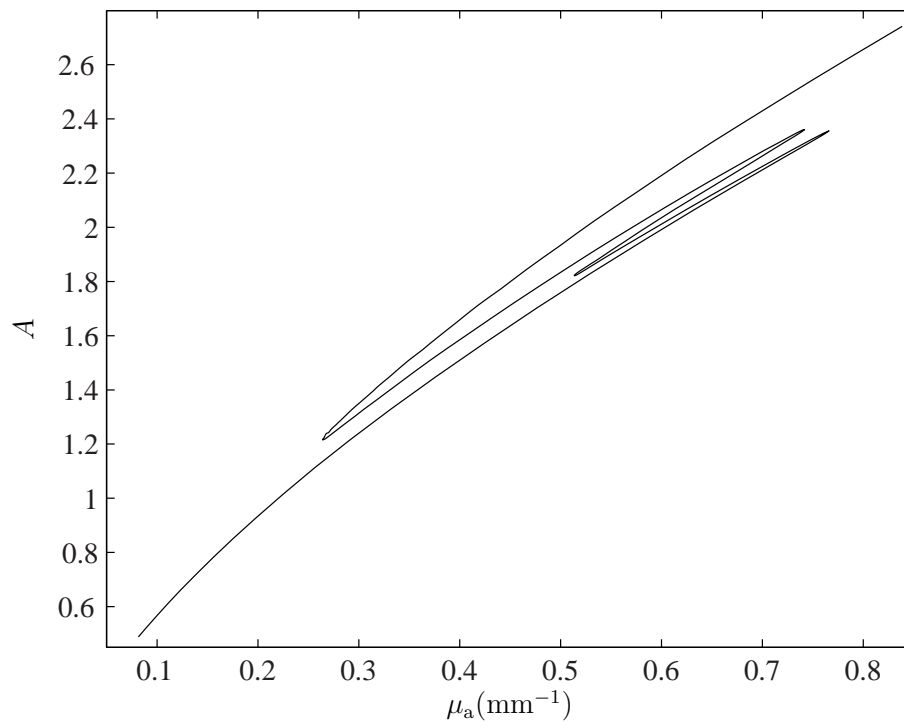


Figure 4.9: The A versus μ_a relationship from a wavelength dependent scattering-absorbing medium and when the medium's $SO_2 = 80\%$.

4.3.2.1 Discussion of results

Several points can be noted from the above results:

1. For a pure scattering medium with wavelength dependent μ'_s , the TPSF changes with wavelength

2. In the case of a constant μ_a (but wavelength dependent μ'_s) medium, attenuation has an approximately linear negative relationship with wavelength
3. In the case of a constant μ'_s (but wavelength dependent μ_a) medium, attenuation changes nonlinearly and has a single-valued relationship with the varying μ_a
4. For a wavelength dependent absorbing-scattering medium, the A versus μ_a relationship is a multi-valued function as more than an attenuation value can be observed at each μ_a value depending on the employed wavelength

Hence, the MLBL is not wholly suitable as the analytic model because it assumes a single-valued linear relationship between A and μ_a . Ideally to approximate the true A versus μ_a versus μ'_s relationship (i.e. $A(\mu_a(\lambda), \mu'_s(\lambda))$), a version of MLBL that takes into account the above points is needed. The process involved in developing such a model is described in the following section.

4.4 The wavelength dependent Modified Lambert-Beer law

The MLBL (via its parameters G , d and f_a) in Eq. (4.2.1) is a linear approximation of the A versus μ_a relationship given from a sample with constant μ'_s . These parameters need to be redefined each time μ'_s changes since this alters the A versus μ_a relationship. This is in order to allow a more accurate estimation of the f_a value. The fact that both the μ_a and μ'_s of any scattering sample are, in practice, varying with wavelength presents challenges to the use of the MLBL model. A more suitable analytic model to use for characterising

this medium is a version of MLBL described by Alabboud²⁶ and shown in Eq. (2.5.10). In his demonstration of using this model, the wavelength dependent μ'_s values observed by Meinke *et al.*⁶⁸ are required, and the parameters in Eq. (2.5.10) were solved via the nonlinear fitting of this model to the measured A .

In the following, the MLBL shown in Eq. (4.2.1) is modified to account for the changes in light attenuation value as the medium's μ'_s is varied with wavelength. Based on the A versus λ relationships shown in Fig. 4.8, light attenuation (which depends on both μ_a and μ'_s) is assumed to vary linearly with μ'_s when μ_a is a constant. This linear variation in A with μ'_s is represented by a wavelength, λ , term, which is used to replace the constant attenuation offset, G , in the MLBL to give

$$A = \mu_a d + K\lambda \quad (4.4.1)$$

Here, A is the attenuation measured using λ , d is a parameter often taken to be photon mean pathlength, and K represents the 'gradient' of the A versus λ relationship shown in Fig. 4.8. Both of the parameters d and K are variable. This equation is termed as the *wavelength dependent MLBL*. As the name suggests, a wavelength term, $K\lambda$, is included into MLBL to account for the effects of varying scattering. Eq. (4.4.1) reduces to the MLBL shown in Eq. (4.2.1) if the medium's μ'_s (i.e. λ term) is a fixed value. Eq. (4.4.1) also shows that the non-zero and varying A value is given by the value of $K\lambda$ when either $\mu_a = 0 \text{ mm}^{-1}$ or μ_a is a constant.

This version of MLBL does not require the exact μ'_s values to be known as the effects of the varying μ'_s on A is given by the wavelength value. Besides, instead of solving the parameters in Eq. (4.4.1) using the fitting routine as practised by Alabboud,²⁶ the assump-

tion made by Duling *et al.*³ and Smith⁴ is used. With the light attenuation measured using two wavelengths are given by

$$A(\lambda_1) = \mu_a(\lambda_1)d + K\lambda_1 \quad (4.4.2)$$

$$A(\lambda_2) = \mu_a(\lambda_2)d + K\lambda_2 \quad (4.4.3)$$

The d and K values in Eq. (4.4.1), although not strictly true in the case of wavelength dependent scattering-absorbing media, are assumed to be wavelength invariant, so that they can be solved using the set of simultaneous equations in Eq. (4.4.2)- (4.4.3) to give:

$$d = \frac{A_2\lambda_1 - A_1\lambda_2}{\lambda_1\mu_{a2} - \lambda_2\mu_{a1}} \quad (4.4.4)$$

$$K = \frac{A_2\mu_{a1} - A_1\mu_{a2}}{\lambda_2\mu_{a1} - \lambda_1\mu_{a2}} \quad (4.4.5)$$

The intensity measurement performed using λ_3 allows $\mu_a(\lambda_3)$ to be determined, where it can be derived from Eq. (4.4.1) as

$$\mu_{a3} = \frac{A_3 - K\lambda_3}{d} \quad (4.4.6)$$

In the case of a medium with absorber A and B, the f_a value is related to this μ_a as follows

$$\mu_{a3} = (\varepsilon_{AB3}f_a + \varepsilon_{B3})T_a \quad (4.4.7)$$

where ε_{AB3} denotes $\varepsilon_A(\lambda_3) - \varepsilon_B(\lambda_3)$ and T_a is the absorbers' total concentration. Substi-

tuting Eq. (4.4.4), Eq. (4.4.5) and Eq. (4.4.7) into Eq. (4.4.6) gives

$$f_a = \frac{A_1(\lambda_2 \varepsilon_{B_3} - \lambda_3 \varepsilon_{B_2}) + A_2(\lambda_3 \varepsilon_{B_1} - \lambda_1 \varepsilon_{B_3}) + A_3(\lambda_1 \varepsilon_{B_2} - \lambda_2 \varepsilon_{B_1})}{A_1(\lambda_3 \varepsilon_{AB_2} - \lambda_2 \varepsilon_{AB_3}) + A_2(\lambda_1 \varepsilon_{AB_3} - \lambda_3 \varepsilon_{AB_1}) + A_3(\lambda_2 \varepsilon_{AB_1} - \lambda_1 \varepsilon_{AB_2})} \quad (4.4.8)$$

which shows that f_a value can be solved by using data at three wavelengths as compared to a minimum of 16 wavelengths that was required in the fitting process of Alabboud.²⁶ As discussed in section 4.2.1, the absorbers' total concentration is incorporated into parameter d so cannot be estimated. Using Eq. (4.4.7) and Eq. (4.4.8), d and K shown in Eq. (4.4.4) and Eq. (4.4.5) can also be expressed as

$$d = \frac{A_1(\varepsilon_{AB_3} \lambda_2 - \varepsilon_{AB_2} \lambda_3) + A_2(\varepsilon_{AB_1} \lambda_3 - \varepsilon_{AB_3} \lambda_1) + A_3(\varepsilon_{AB_2} \lambda_1 - \varepsilon_{AB_1} \lambda_2)}{\lambda_1(\varepsilon_{AB_2} \varepsilon_{B_3} - \varepsilon_{AB_3} \varepsilon_{B_2}) + \lambda_2(\varepsilon_{AB_3} \varepsilon_{B_1} - \varepsilon_{AB_1} \varepsilon_{B_3}) + \lambda_3(\varepsilon_{AB_1} \varepsilon_{B_2} - \varepsilon_{AB_2} \varepsilon_{B_1})} \quad (4.4.9)$$

$$K = \frac{A_1(\varepsilon_{AB_3} \varepsilon_{B_2} - \varepsilon_{AB_2} \varepsilon_{B_3}) + A_2(\varepsilon_{AB_1} \varepsilon_{B_3} - \varepsilon_{AB_3} \varepsilon_{B_1}) + A_3(\varepsilon_{AB_2} \varepsilon_{B_1} - \varepsilon_{AB_1} \varepsilon_{B_2})}{\lambda_1(\varepsilon_{AB_3} \varepsilon_{B_2} - \varepsilon_{AB_2} \varepsilon_{B_3}) + \lambda_2(\varepsilon_{AB_1} \varepsilon_{B_3} - \varepsilon_{AB_3} \varepsilon_{B_1}) + \lambda_3(\varepsilon_{AB_2} \varepsilon_{B_1} - \varepsilon_{AB_1} \varepsilon_{B_2})} \quad (4.4.10)$$

Taking the plot shown in Fig. 4.9 as a model of a real A versus μ_a relationship, the wavelength dependent MLBL defined by three data points (indicated by plus symbol) and the real attenuation response in A versus μ_a versus wavelength space are shown in Fig. 4.10 while Fig. 4.11 shows the values approximated by the wavelength dependent MLBL and the real attenuation values on A versus μ_a plot. Similar to the discussion of section 4.2.1, the parameter f_a in the wavelength dependent MLBL is given by the f_a value during which the selected three points become collinear in the A versus μ_a space. This f_a can take any value. In this case, however, d and K cannot be determined directly as the gradient and offset of the straight line which connects the collinear points on A

versus μ_a plot (dark dashed line in Fig. 4.11) because the wavelength dependent MLBL does not describe the A versus μ_a relationship as a single-valued straight line. Besides, both of the parameters d and K are intimately linked in Eq. (4.4.1), where solving for d requires a known value of K and vice-versa. A comparison between these plots in Fig. 4.11 reveals a lack in the inflexions of the wavelength dependent MLBL compared to the true response.

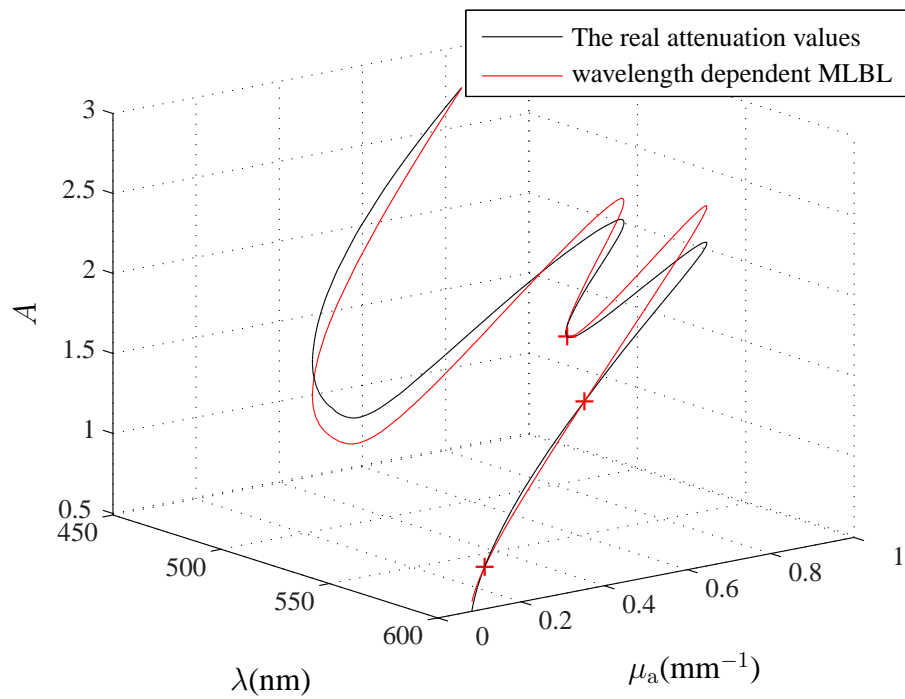


Figure 4.10: The real attenuation values in A versus μ_a versus λ space (when the medium's μ'_s varies with wavelength, $\text{SO}_2 = 80\%$ and $T_H = 58 \mu\text{mol L}^{-1}$) and its approximation using the wavelength dependent MLBL. The data points on which the parameters in the wavelength dependent MLBL are found are indicated by the plus symbol.

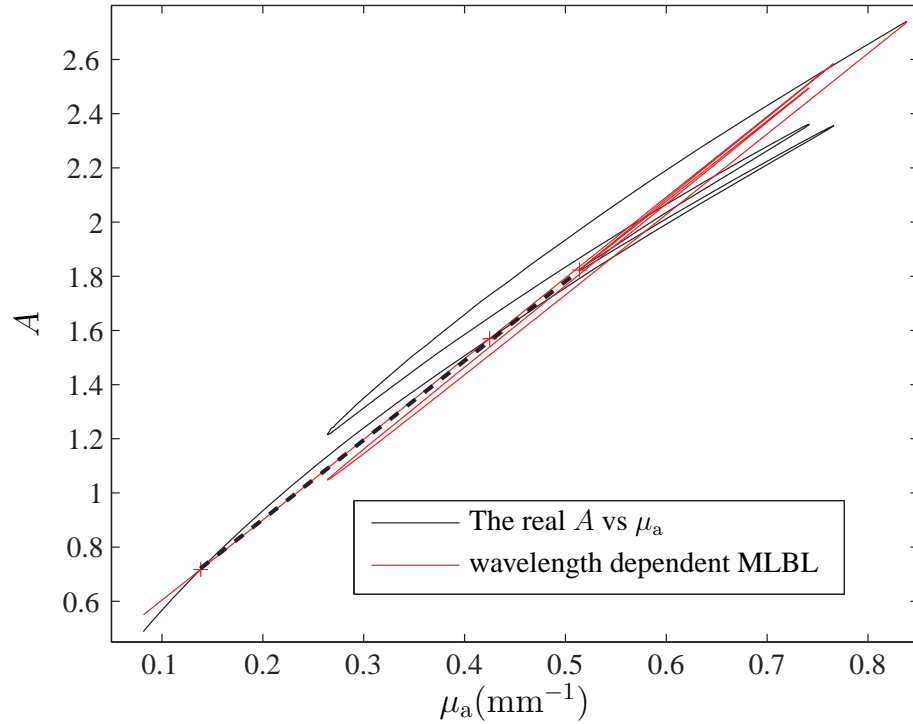


Figure 4.11: The wavelength dependent MLBL and the real attenuation values (shown in Fig. 4.10) in A versus μ_a space. The dark dashed line is to show the collinearity of the points. The data points using which the parameters in the wavelength dependent MLBL are found are indicated by the plus symbol.

4.4.1 Results and discussion

Similar to the result shown in section 4.2.1, the accuracy of the value estimated by the wavelength dependent MLBL depends on the selection of wavelength combinations, so it is important to understand how the accuracy of the estimated value varies with the data of the selected wavelengths and the conditions these wavelengths should fulfil to yield zero error in the calculated f_a value. This can be done by calculating the f_a value given by all the combinations of three wavelengths based on a given attenuation spectrum.

In this work, the attenuation spectrum shown in Fig. 4.12(a) is used as an example of

attenuations measured from a scattering-absorbing medium. This attenuation spectrum was derived from a medium with wavelength dependent μ'_s shown in Fig. 4.5 (for the wavelength range of 450 nm – 600 nm). The medium's absorbers, SO₂ and geometry, and the light illumination-detection system are the same as that used to produce the A versus μ_a in Fig. 4.9. The medium's μ_a is shown in Fig. 4.12(b). For a better visual understanding, instead of examining the relationship between the accuracy of the estimated SO₂ value and data (i.e. μ_a , A) of every combination of three wavelengths, λ_1 is selected as an isosbestic wavelength (i.e. 586 nm shown in Fig. 2.3) because the measured attenuation is insensitive to the variation in SO₂, allowing the error in the estimated value to depend only on the data of λ_2 and λ_3 which are varied across the wavelength range 450 nm – 600 nm.

In processing this A spectrum, the SO₂ value given by different combination of $\lambda_1 = 586$ nm, λ_2 and λ_3 is calculated from Eq. (4.4.8) and the calculated full scale error, ΔSO_2 , is shown in Fig. 4.13. Only the combinations of wavelengths that produced an estimated SO₂ value that is within the range of –2% to 102% are shown in Fig. 4.13, and the calculated error of greater than 10% or less than –10% is plotted as 10% and –10%, respectively. Eq. (4.4.8) is derived from the simultaneous wavelength dependent MLBL equations, therefore the different permutations of λ_2 and λ_3 , when used with $\lambda_1 = 586$ nm produce the same results. This is the reason for the diagonally symmetrical error plot shown in Fig. 4.13 and the same error plot is produced when either λ_2 or λ_3 is selected as 586 nm while λ_1 is varied across 450 nm – 600 nm.

Referring to Fig. 4.13, it can be seen that most of the combinations of λ_2 and λ_3 (with $\lambda_1 = 586$ nm) that produced considerably lower error (but non-zero) are from within the wavelength range of 540 nm – 600 nm which is close to the selected λ_1 . In addition,

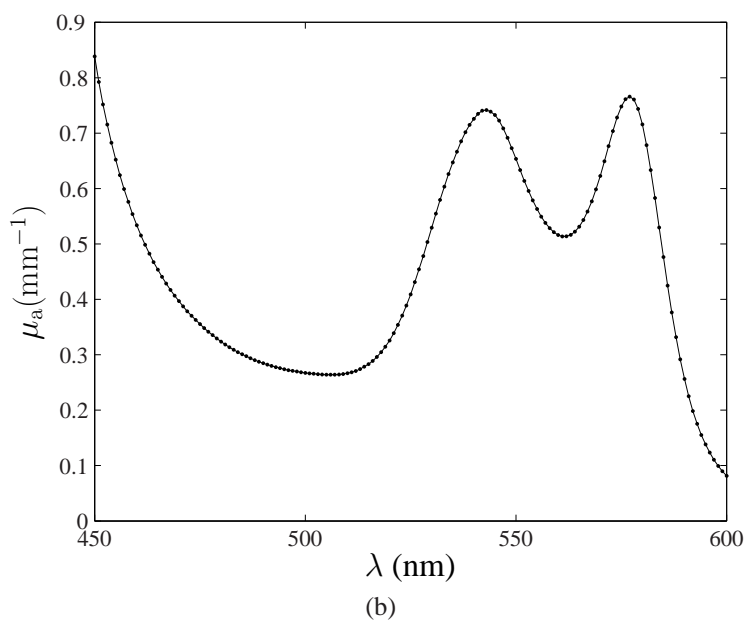
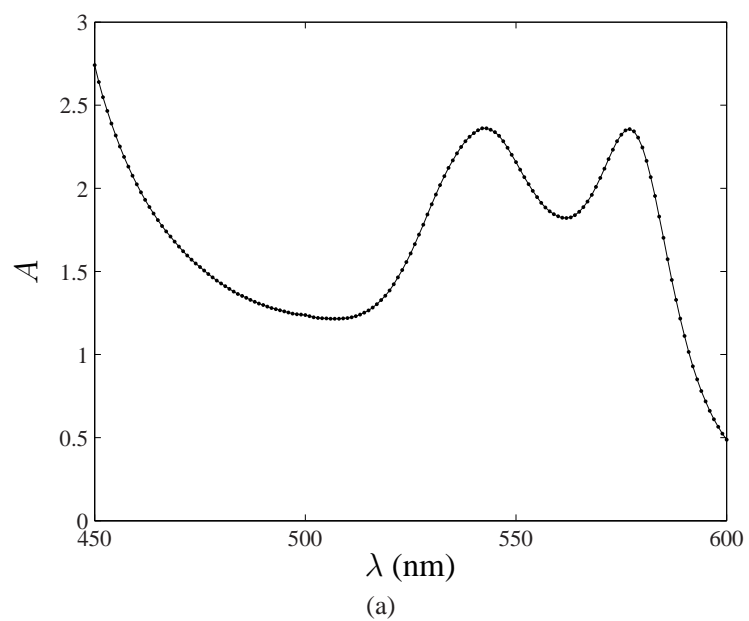


Figure 4.12: The (a) attenuation and (b) μ_a spectra for a wavelength dependent scattering-absorbing medium with μ'_s shown in Fig. 4.5. The medium's $\text{SO}_2 = 80\%$ and the absorbers' total concentration $T_H = 58 \mu\text{mol L}^{-1}$.

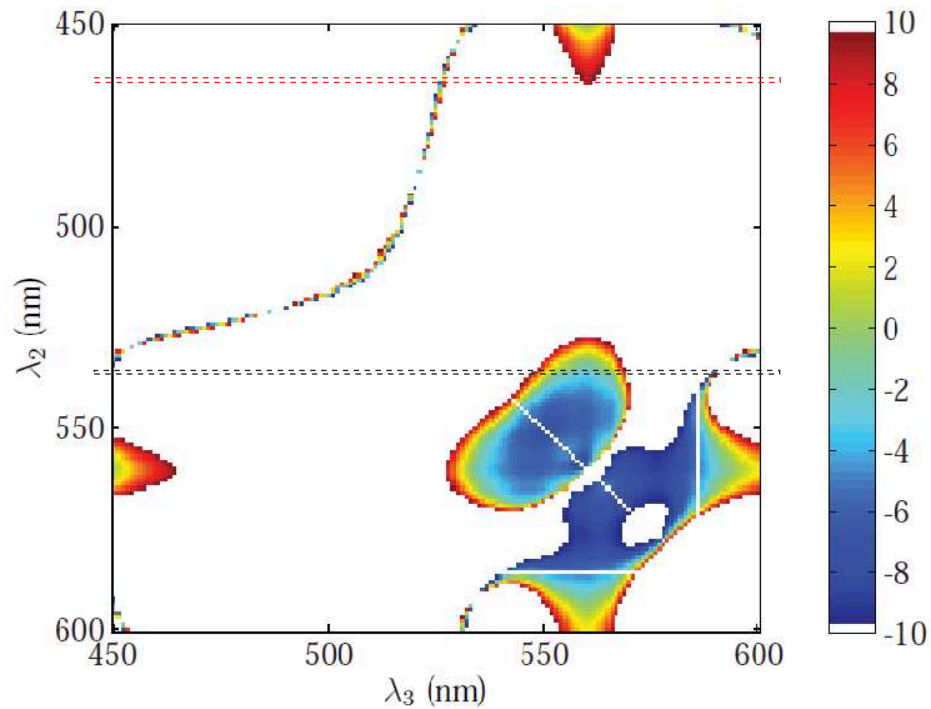


Figure 4.13: The calculated full scale error ΔSO_2 (in %) given by different combinations of $\lambda_1 = 586$ nm, λ_2 and λ_3 when the set SO_2 is 80%. The error given by the wavelength combination that yielded SO_2 not within the range of -2% to 102% is not shown here and the error greater than 10% or less than -10% are plotted as 10% and -10% , respectively.

an invalid SO_2 value is calculated if the same wavelength is selected twice in solving the three simultaneous equations in Eq. (4.4.1) (i.e. shown as white when λ_2 (or λ_3) is 586 nm and when $\lambda_2 = \lambda_3$), which is when these equations become ill-conditioned.

4.4.1.1 Analysis of results

To investigate the reason low error is produced by a certain combinations of λ_2 and λ_3 with 586 nm, the μ_a and A spectra shown in Fig. 4.12 are replotted in Fig. 4.14 (top and middle) and this study focuses on examining the error in the value given by fixing λ_2 while

varying λ_3 , and its relation to the μ_a and A data of the wavelengths. Following the findings discussed in section 4.2.3, 467 nm (region enclosed by red dashed line in Fig. 4.13) whose μ_a is closest to that of λ_1 (see Fig. 4.14 (top) when $\text{SO}_2 = 80\%$) is chosen as λ_2 to examine error in the value when varying λ_3 . Also used for demonstration is 540 nm (enclosed by dark dashed line in Fig. 4.13) that has a different μ_a value to that of λ_1 (refer to Fig. 4.14 (top)). The error in the value given from the combination of wavelengths $\lambda_1 = 586$ nm, $\lambda_2 = 467$ nm (and 540 nm) and then varying λ_3 is shown in Fig. 4.14 (bottom). Also shown in this diagram are the location of the selected λ_1 and λ_2 (indicated by plus and cross symbols) on these plots.

A larger error in the value given by most of the λ_3 observed in Fig. 4.14 (bottom) compared to that in Fig. 4.2 (bottom) suggesting a more stringent condition to zero error in the value estimated using the wavelength dependent MLBL in the case of wavelength dependent scattering-absorbing media. A possible reason is that not only is the wavelength dependent MLBL subject to the error in the A versus μ_a relationship approximation (as also observed in the case when the MLBL is used), this error heightens when this model is used to approximate the A value moving in the A versus $\mu_a(\lambda)$ versus $\mu_s(\lambda)$ space, which is evidence from the differences in the plots shown in Fig. 4.11.

It becomes clear from the results shown in Fig. 4.14 that the low errors are produced by the wavelength (λ_3) whose A lies along the straight line (gray and red dashed lines) that connects the selected λ_1 and λ_2 , and with the condition that the μ_a of this wavelength is also collinear with that of λ_1 and λ_2 in the μ_a versus wavelength space. However, no wavelength combination shown in Fig. 4.13 is able to produce zero error as it is a result of poor resolution of the used spectra. The errors are shown to increase as A and μ_a of λ_3 move away from the value that intersects this line.

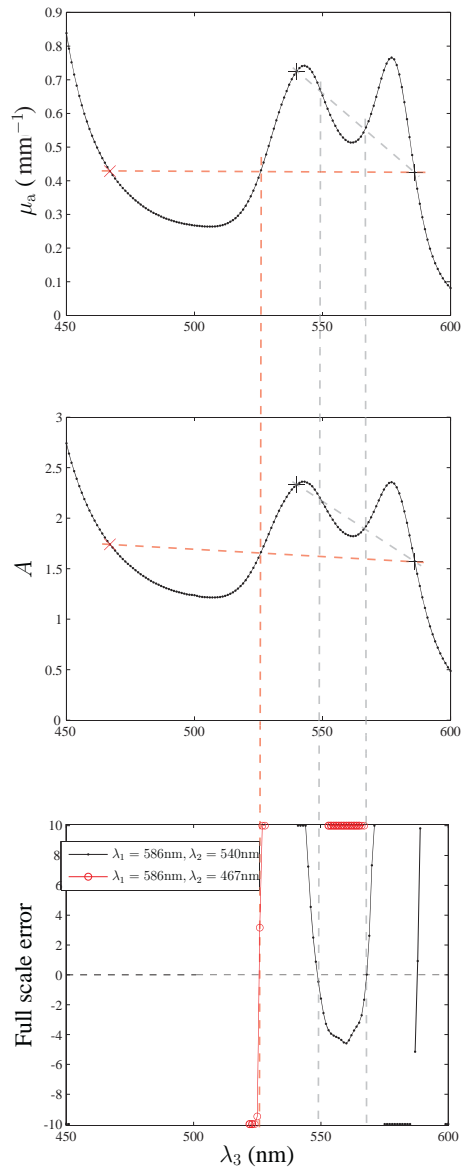


Figure 4.14: (top and middle) The μ_a and A spectra when the medium's $\text{SO}_2 = 80\%$. (bottom) The calculated error when $\lambda_1 = 586 \text{ nm}$, $\lambda_2 = 467 \text{ nm}$ (and 540 nm), and λ_3 is from the wavelength range $450 \text{ nm} - 600 \text{ nm}$ (shown on the x-axis). The location of 467 nm and 540 nm on the μ_a and A spectra are marked by red cross and dark plus symbols, respectively. The error in the calculated SO_2 outside the range of -2% to 102% is not shown in the diagram. The calculated error of less than -10% and greater than 10% are plotted as -10% and 10% , respectively. A dashed line is drawn (in the bottom plot) across zero error as a guide.

In the following, the μ_a and attenuation spectra shown in Fig. 4.14 (top and middle) are used to help understand how the points which are collinear in A and μ_a versus wavelength spaces are able to reproduce the true f_a value using the wavelength dependent MLBL. The selection of wavelengths that are collinear on μ_a and A spectra shown in Fig. 4.14 (top and middle) is restricted by the sampling resolution of the spectra, so the combination of $\lambda_1 = 586$ nm, $\lambda_2 = 540$ nm and $\lambda_3 = 549$ nm, which are almost collinear in the plots, is chosen for the demonstration. The A and μ_a spectra are plotted on the top left and bottom right of Fig. 4.15, respectively, and the selected points on these spectra are indicated by the cross symbol. Also shown in top right of Fig. 4.15 is the true A versus μ_a relationship. It can be seen by plotting these points on the A versus μ_a plot in Fig. 4.15 (top right) that they lie along a straight line in A versus μ_a (dashed line). These results can also be plotted in α space as shown in Fig. 4.3 and Fig. 4.4, but they are not used in Fig. 4.15 because the aim is to understand the reason for the zero error in Fig. 4.14 (bottom) without intending to show the α values given by the estimated f_a .

The linear relationship between the points in the A versus wavelength and A versus μ_a spaces shown in Fig. 4.15 agree with the assumption made in section 4.4, where it is assumed that both parameters d (i.e. gradient in A versus μ_a plot) and K (i.e. gradient in A versus λ plot) in wavelength dependent MLBL are constant. Therefore, if these points are used to find the value of parameters in wavelength dependent MLBL, the true f_a value can be recovered and the defined wavelength dependent MLBL line would intersect the true A versus μ_a plot at these corresponding points.

In addition to the discussion of Fig. 4.15, it can also be noticed from Fig. 4.14 that wavelengths with the same μ_a reproduce the medium's SO_2 . It was shown in Fig. 4.8 that these wavelengths produce the same gradient in A versus λ space, which agrees with the

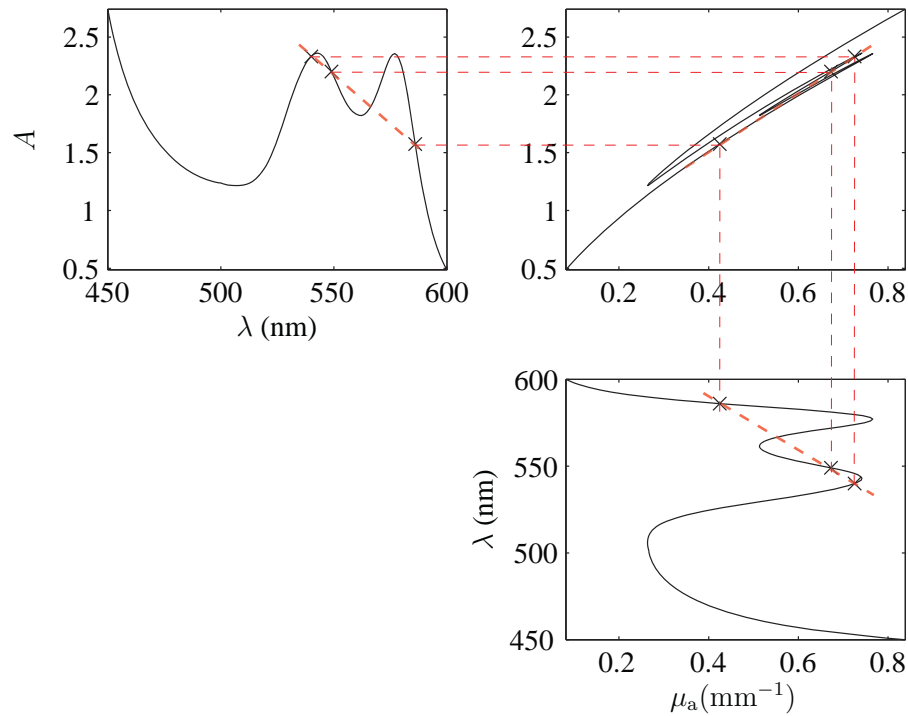


Figure 4.15: (top left) The variation in A with the wavelength when the medium's $\text{SO}_2 = 80\%$. (top right) The A versus μ_a relationship. (bottom right) The variation in μ_a with the wavelength. The location of the selected wavelengths is indicated by crosses. The dashed lines are drawn to show the collinearity of the points.

assumption of the wavelength dependent MLBL (i.e. a constant K value). To demonstrate this, take the absorption and attenuation spectra for $\text{SO}_2 = 80\%$ shown in Fig. 4.14 (top and middle) as an example, they are replotted in Fig. 4.16. The collinearity of wavelengths with the same μ_a (e.g. around 462 nm, 529 nm and 585 nm marked by red crosses) on A versus wavelength space in Fig. 4.16 means that the same gradient would be calculated.

The error of about 4% when $\lambda_3 = 525$ nm (with $\lambda_1 = 586$ nm and $\lambda_2 = 467$ nm) shown in Fig. 4.14 is due to the poor spectral resolution when μ_a of these wavelengths is not exactly identical. The validity of these is examined mathematically in the next section.

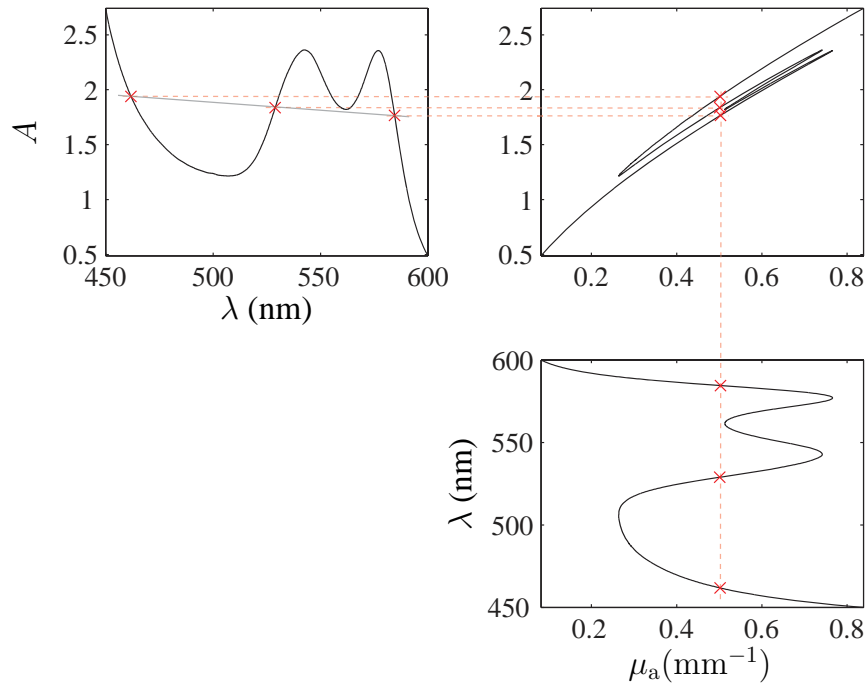


Figure 4.16: (top left) The variation in A with the wavelength when the medium's $\text{SO}_2 = 80\%$. (top right) The A versus μ_a relationship. (bottom right) The variation in μ_a with the wavelength. The location of the selected wavelengths is indicated by crosses. The collinearity of the points given by wavelengths with the same μ_a can be seen in A versus wavelength.

4.4.2 Strategies for optimal selection of wavelengths

An explanation of the differences between the wavelength dependent MLBL and the true A versus μ_a relationship shown in Fig. 4.11, and the error shown in Fig. 4.14 (bottom) is that the assumption made about the constant d and K values are not true. This is because both of these parameters change with the varying μ_a and μ'_s . This can be understood by referring to Fig. 4.9, where the nonlinear A versus μ_a relationship shows that d is a varying parameter, while Fig. 4.8 shows that the gradient of the A versus λ plot, K , changes with μ_a . Thus, without a careful selection of wavelengths (as shown in the example in

Fig. 4.14), this would result in an error in f_a value estimated using Eq. (4.4.8). For this reason, it is useful to derive an expression of error in the value given by the wavelength dependent MLBL and to theoretically identify the factors that determined this error. Similar to that mentioned in section 4.2.3, this error, E , can be written as

$$E = f'_a - f_a \quad (4.4.11)$$

where f'_a and f_a denote the value estimated using the wavelength dependent MLBL shown in Eq. (4.4.8) and the true f_a value, respectively. Substituting Eq. (4.4.8) into Eq. (4.4.11) gives

$$E = \frac{A_1(\lambda_2\varepsilon_{B_3} - \lambda_3\varepsilon_{B_2}) + A_2(\lambda_3\varepsilon_{B_1} - \lambda_1\varepsilon_{B_3}) + A_3(\lambda_1\varepsilon_{B_2} - \lambda_2\varepsilon_{B_1})}{A_1(\lambda_3\varepsilon_{AB_2} - \lambda_2\varepsilon_{AB_3}) + A_2(\lambda_1\varepsilon_{AB_3} - \lambda_3\varepsilon_{AB_1}) + A_3(\lambda_2\varepsilon_{AB_1} - \lambda_1\varepsilon_{AB_2})} - f_a \quad (4.4.12)$$

Rearranging Eq. (4.4.12) and using α expressed in Eq. (4.2.3) to provide

$$E = \frac{A_1(\lambda_2\alpha_3 - \lambda_3\alpha_2) + A_2(\lambda_3\alpha_1 - \lambda_1\alpha_3) + A_3(\lambda_1\alpha_2 - \lambda_2\alpha_1)}{A_1(\lambda_3\varepsilon_{AB_2} - \lambda_2\varepsilon_{AB_3}) + A_2(\lambda_1\varepsilon_{AB_3} - \lambda_3\varepsilon_{AB_1}) + A_3(\lambda_2\varepsilon_{AB_1} - \lambda_1\varepsilon_{AB_2})} \quad (4.4.13)$$

It is shown in Fig. 4.9 that for the case of a wavelength dependent scattering-absorbing medium, attenuation has a multi-valued relationship with μ_a , thus finding a wavelength combination which would produce $E = 0$ in Eq. (4.4.13) is not straightforward. The condition to zero error via an appropriate selection of wavelengths, however, can be inferred from the results shown in Fig. 4.14 - Fig. 4.16, and an understanding of the wavelength dependent MLBL. This work assumes that wavelengths whose measured data satisfied the assumptions made by the wavelength dependent MLBL reproduce the true f_a value. The

following subsections mathematically verify the viability of different strategies for wavelength selection (strategy I and strategy II) to recover a medium's f_a determined from the results shown in Fig. 4.14.

4.4.2.1 Wavelengths selection strategy I:

Fig. 4.8, Fig. 4.14 and Fig. 4.16 show that if three wavelengths with identical μ_a are chosen as the measurement wavelengths, their attenuation value form a linear relationship with wavelength as assumed by the wavelength dependent MLBL, so allowing the medium's f_a to be recovered using this model. To prove this, let the α of these wavelengths related by

$$\alpha_1 = \alpha_2 = \alpha_3 \quad (4.4.14)$$

So that substituting Eq. (4.4.14) into Eq. (4.4.13) gives

$$E = \frac{[A_1(\lambda_2 - \lambda_3) + A_2(\lambda_3 - \lambda_1) + A_3(\lambda_1 - \lambda_2)]\alpha_3}{A_1(\lambda_3\varepsilon_{AB_2} - \lambda_2\varepsilon_{AB_3}) + A_2(\lambda_1\varepsilon_{AB_3} - \lambda_3\varepsilon_{AB_1}) + A_3(\lambda_2\varepsilon_{AB_1} - \lambda_1\varepsilon_{AB_2})} \quad (4.4.15)$$

Rewriting Eq. (4.4.15) as

$$E = \frac{[A_1(\lambda_2 - \lambda_3 + \lambda_1 - \lambda_1) + A_2(\lambda_3 - \lambda_1) + A_3(\lambda_1 - \lambda_2)]\alpha_3}{A_1(\lambda_3\varepsilon_{AB_2} - \lambda_2\varepsilon_{AB_3}) + A_2(\lambda_1\varepsilon_{AB_3} - \lambda_3\varepsilon_{AB_1}) + A_3(\lambda_2\varepsilon_{AB_1} - \lambda_1\varepsilon_{AB_2})} \quad (4.4.16)$$

which is reduced to

$$E = \frac{[(A_1 - A_2)(\lambda_1 - \lambda_3) - (A_1 - A_3)(\lambda_1 - \lambda_2)]\alpha_3}{A_1(\lambda_3\varepsilon_{AB_2} - \lambda_2\varepsilon_{AB_3}) + A_2(\lambda_1\varepsilon_{AB_3} - \lambda_3\varepsilon_{AB_1}) + A_3(\lambda_2\varepsilon_{AB_1} - \lambda_1\varepsilon_{AB_2})} \quad (4.4.17)$$

Next, from the results in Fig. 4.14 and Fig. 4.16, collinearity of the selected wavelengths in A versus wavelength space can be observed when their α are identical. The collinearity in A versus wavelength space means that the same gradient can be measured, so setting the relationship between A of these wavelengths in A versus wavelength space as

$$\frac{A_1 - A_2}{\lambda_1 - \lambda_2} = \frac{A_1 - A_3}{\lambda_1 - \lambda_3} \quad (4.4.18)$$

which can also be written as

$$(A_1 - A_2)(\lambda_1 - \lambda_3) = (A_1 - A_3)(\lambda_1 - \lambda_2) \quad (4.4.19)$$

Substitute Eq. (4.4.19) into Eq. (4.4.17) leads to zero error as follows:

$$E = \frac{[(A_1 - A_3)(\lambda_1 - \lambda_2) - (A_1 - A_3)(\lambda_1 - \lambda_2)]\alpha_3}{A_1(\lambda_3\varepsilon_{AB_2} - \lambda_2\varepsilon_{AB_3}) + A_2(\lambda_1\varepsilon_{AB_3} - \lambda_3\varepsilon_{AB_1}) + A_3(\lambda_2\varepsilon_{AB_1} - \lambda_1\varepsilon_{AB_2})} = 0 \quad (4.4.20)$$

which is in good agreement with the error plot shown in Fig. 4.16.

4.4.2.2 Wavelengths selection strategy II:

The second approach to potentially obtaining zero error is by selecting the wavelengths whose α are related by Eq. (4.4.21) (as shown in the top diagram of Fig. 4.14 (indicated by dark plus symbol)), wherein Eq. (4.4.14) is the subset of Eq. (4.4.21) when the differences between α of three wavelengths are zero.

$$\frac{\alpha_1 - \alpha_2}{\lambda_1 - \lambda_2} = \frac{\alpha_1 - \alpha_3}{\lambda_1 - \lambda_3} \quad (4.4.21)$$

Rearranging Eq. (4.4.21) to give α_3 as

$$\alpha_3 = \frac{\alpha_1(\lambda_3 - \lambda_2) - \alpha_2(\lambda_3 - \lambda_1)}{\lambda_1 - \lambda_2} \quad (4.4.22)$$

From Eq. (4.4.13), the error can also be written as

$$E = \frac{\alpha_1(A_2\lambda_3 - A_3\lambda_2) + \alpha_2(A_3\lambda_1 - A_1\lambda_3) + \alpha_3(A_1\lambda_2 - A_2\lambda_1)}{A_1(\lambda_3\varepsilon_{AB_2} - \lambda_2\varepsilon_{AB_3}) + A_2(\lambda_1\varepsilon_{AB_3} - \lambda_3\varepsilon_{AB_1}) + A_3(\lambda_2\varepsilon_{AB_1} - \lambda_1\varepsilon_{AB_2})} \quad (4.4.23)$$

Substituting Eq. (4.4.22) into Eq. (4.4.23) gives

$$E = \frac{\alpha_1(A_2\lambda_3 - A_3\lambda_2) + \alpha_2(A_3\lambda_1 - A_1\lambda_3) + \frac{\alpha_1(\lambda_3 - \lambda_2) - \alpha_2(\lambda_3 - \lambda_1)}{\lambda_1 - \lambda_2}(A_1\lambda_2 - A_2\lambda_1)}{A_1(\lambda_3\varepsilon_{AB_2} - \lambda_2\varepsilon_{AB_3}) + A_2(\lambda_1\varepsilon_{AB_3} - \lambda_3\varepsilon_{AB_1}) + A_3(\lambda_2\varepsilon_{AB_1} - \lambda_1\varepsilon_{AB_2})} \quad (4.4.24)$$

And rearranging Eq. (4.4.24) provides

$$E = \frac{\alpha_1\lambda_2(A_1\Delta\lambda_{32} + A_2\Delta\lambda_{13} + A_3\Delta\lambda_{21}) - \alpha_2\lambda_1(A_1\Delta\lambda_{32} + A_2\Delta\lambda_{13} + A_3\Delta\lambda_{21})}{(\lambda_1 - \lambda_2)(A_1(\lambda_3\varepsilon_{AB_2} - \lambda_2\varepsilon_{AB_3}) + A_2(\lambda_1\varepsilon_{AB_3} - \lambda_3\varepsilon_{AB_1}) + A_3(\lambda_2\varepsilon_{AB_1} - \lambda_1\varepsilon_{AB_2}))} \quad (4.4.25)$$

where $\Delta\lambda_{12}$ refers to $\lambda_1 - \lambda_2$. Rearranging Eq. (4.4.25) yields

$$E = \frac{(A_1(\lambda_3 - \lambda_2) + A_2(\lambda_1 - \lambda_3) + A_3(\lambda_2 - \lambda_1))(\alpha_1\lambda_2 - \alpha_2\lambda_1)}{(\lambda_1 - \lambda_2)(A_1(\lambda_3\varepsilon_{AB_2} - \lambda_2\varepsilon_{AB_3}) + A_2(\lambda_1\varepsilon_{AB_3} - \lambda_3\varepsilon_{AB_1}) + A_3(\lambda_2\varepsilon_{AB_1} - \lambda_1\varepsilon_{AB_2}))} \quad (4.4.26)$$

which can also be written as

$$E = \frac{(A_1(\lambda_3 - \lambda_2 + \lambda_1 - \lambda_1) + A_2(\lambda_1 - \lambda_3) + A_3(\lambda_2 - \lambda_1))(\alpha_1\lambda_2 - \alpha_2\lambda_1)}{(\lambda_1 - \lambda_2)(A_1(\lambda_3\varepsilon_{AB_2} - \lambda_2\varepsilon_{AB_3}) + A_2(\lambda_1\varepsilon_{AB_3} - \lambda_3\varepsilon_{AB_1}) + A_3(\lambda_2\varepsilon_{AB_1} - \lambda_1\varepsilon_{AB_2}))} \quad (4.4.27)$$

$$= \frac{[(A_1 - A_3)(\lambda_1 - \lambda_2) - (A_1 - A_2)(\lambda_1 - \lambda_3)](\alpha_1\lambda_2 - \alpha_2\lambda_1)}{(\lambda_1 - \lambda_2)(A_1(\lambda_3\varepsilon_{AB_2} - \lambda_2\varepsilon_{AB_3}) + A_2(\lambda_1\varepsilon_{AB_3} - \lambda_3\varepsilon_{AB_1}) + A_3(\lambda_2\varepsilon_{AB_1} - \lambda_1\varepsilon_{AB_2}))} \quad (4.4.28)$$

It can be inferred from the results shown in Fig. 4.14 and Fig. 4.15 that wavelengths whose α are as given in Eq. (4.4.21) produce the same gradient in A versus wavelength space as follows:

$$\frac{A_1 - A_2}{\lambda_1 - \lambda_2} = \frac{A_1 - A_3}{\lambda_1 - \lambda_3} \quad (4.4.29)$$

which can also be written in the form shown in Eq. (4.4.19). Substituting Eq. (4.4.19) into Eq. (4.4.28) gives zero error as follows:

$$E = \frac{[(A_1 - A_3)(\lambda_1 - \lambda_2) - (A_1 - A_3)(\lambda_1 - \lambda_2)](\alpha_1\lambda_2 - \alpha_2\lambda_1)}{(\lambda_1 - \lambda_2)(A_1(\lambda_3\varepsilon_{AB_2} - \lambda_2\varepsilon_{AB_3}) + A_2(\lambda_1\varepsilon_{AB_3} - \lambda_3\varepsilon_{AB_1}) + A_3(\lambda_2\varepsilon_{AB_1} - \lambda_1\varepsilon_{AB_2}))} = 0 \quad (4.4.30)$$

This confirms the validity of the discussion of Fig. 4.15, where selecting collinear points in both μ_a versus wavelength and A versus wavelength spaces reproduces the f_a value.

4.5 Noise sensitivity investigation

As mentioned in section 4.3, the μ_s and g of any scattering medium vary with wavelength, so the following work considers the practicality of using the wavelength dependent MLBL to find f_a of wavelength dependent scattering-absorbing media based on the attenuation

signals measured under a noisy condition. Although it is demonstrated in section 4.4.1 and section 4.4.2 that the error in this value can be minimised with a proper selection of wavelengths, this error is also, in practice, dependent upon the noise in the system. Therefore consistency in the value estimated based on the noise affected data of different combination of wavelengths is investigated herein. Factors that determine the consistency in the estimated value are explored mathematically in section 4.5.1. The validity of these is verified using the noisy data generated in section 4.5.2, and the error in the value estimated by different wavelength combinations is presented in section 4.5.3. Section 4.5.3 also discusses the criteria considered when selecting the optimal wavelength combination for the spectroscopy analysis of a medium.

4.5.1 Derivation of noise sensitivity of the estimated value

The f_a value estimated using the wavelength dependent MLBL is given from Eq. (4.4.8) where the attenuation values (i.e. A_1 , A_2 and A_3) are the only variable in the equation that are directly affected by the noise. The uncertainty in this f_a value, which depends upon measurement parameters (i.e. A_1 , A_2 and A_3) that have random and independent uncertainties, can be expressed using the error of propagation approach¹²³ as follows:

$$\delta f_a^2 = \left(\frac{\partial f_a}{\partial A_1} \right)^2 \Delta A_1^2 + \left(\frac{\partial f_a}{\partial A_2} \right)^2 \Delta A_2^2 + \left(\frac{\partial f_a}{\partial A_3} \right)^2 \Delta A_3^2 \quad (4.5.1)$$

where ΔA_1 is the variation in $A(\lambda_1)$ dependent on noise. Differentiating f_a in Eq. (4.4.8) with respect to the measured attenuation (A_1 , A_2 and A_3) leads to

$$\delta f_a^2 = \frac{\beta (\lambda_1(\varepsilon_{A_3} \wedge \varepsilon_{B_2}) + \lambda_2(\varepsilon_{A_1} \wedge \varepsilon_{B_3}) + \lambda_3(\varepsilon_{A_2} \wedge \varepsilon_{B_1}))^2}{(A_1(\varepsilon_{AB_3}\lambda_2 - \varepsilon_{AB_2}\lambda_3) + A_2(\varepsilon_{AB_1}\lambda_3 - \varepsilon_{AB_3}\lambda_1) + A_3(\varepsilon_{AB_2}\lambda_1 - \varepsilon_{AB_1}\lambda_2))^4} \quad (4.5.2)$$

where $\varepsilon_{A_3} \wedge \varepsilon_{B_2}$ denotes $\varepsilon_{A_3}\varepsilon_{B_2} - \varepsilon_{A_2}\varepsilon_{B_3}$, and

$$\beta = \Delta A_1^2(A_3^2\lambda_2^2 + A_2^2\lambda_3^2 - 2A_2A_3\lambda_2\lambda_3) + \Delta A_2^2(A_3^2\lambda_1^2 + A_1^2\lambda_3^2 - 2A_1A_3\lambda_1\lambda_3) + \Delta A_3^2(A_2\lambda_1 - A_1\lambda_2)^2$$

while δf_a is a measure of the uncertainties in the estimated f_a value, determining the sensitivity of this value to the noise in A_1 , A_2 and A_3 . The $\frac{\partial f_a}{\partial A}$ terms quantify changes in the f_a value when light attenuation measured using the selected wavelengths (i.e. A_1 , A_2 , A_3) is varied. The measured attenuations are subject to changes due to the noise, so the combination of wavelengths whose estimated values are relatively insensitive to noise should be determined only by their corresponding absorbers' extinction coefficients.

Based on Eq. (4.5.2), $\delta f_a = 0$ can theoretically be achieved by reducing the summation of terms in the numerator of Eq. (4.5.2) to zero. However, there would be an expensive trade-off between the robustness of the performance of a selected wavelength combination to noise and the sensitivity of the estimated value to the medium's SO_2 induced variation in A . This is because, in addition to noise, changes in SO_2 also modify A , so selecting a combination of wavelengths that produce $\delta f_a = 0$ may also result in an estimated value that is insensitive to the changes in the medium's SO_2 .

4.5.2 The simulation of noisy data for demonstration

The results shown in Fig. 4.13 - Fig. 4.16 are based on attenuations produced by Monte Carlo simulations when noise in the measurement system (i.e. shot noise, quantisation noise, and readout noise) was not considered. Even though the simulated signals are subject to the statistical noise in the Monte Carlo simulation,¹²⁴ the effect of this noise on the signals is arguably small as can be seen in Fig. 4.17. The attenuation spectrum shown in Fig. 4.10, Fig. 4.15 and Fig. 4.16 appeared almost flat (noiseless) and is practically unrealistic, therefore wavelengths selected based on these simulated data may not give a satisfactory result when they are used on a noisy signal. In this section, noisy data are simulated and wavelength combinations which produce a lower overall Δf_a as compared to that given by other wavelength combinations are determined to verify the validity of the conclusions drawn in section 4.4 and section 4.5.1. This investigation begins by adding shot and quantisation noises onto the light intensity in simulations. The resultant intensity signals give the ‘noisy’ attenuation which will be used in the following section in determining the wavelength combinations that are appropriate for characterising a medium with a range of possible SO₂ value. The noisy signal generation process is described next.

Assuming the employed system is both shot noise and quantisation noise limited and the CCD camera used in the spectroscopic system has the specifications shown in Table 4.1 that are the specifications of a CCD camera (Sensicam QE pco. imaging from the Cooke corporation).

The number of photo-generated electrons, n_e , in the CCD wells is related to the detected light intensity (i.e. I_0 and I) by:¹²⁵

Table 4.1: The camera specifications.

Specification	Value
quantum efficiency	0.65
detector area	$6 \times 10^{-5} \text{ m}^2$
full well capacity	18,000 electrons
dynamic range	12 bit

$$n_e = \frac{I \times t \times A_{\text{det}} \times \xi \times \lambda}{h \times c} \quad (4.5.3)$$

where t is the detector integration time (in s) and is chosen as $t = 0.03$ s in this study, while A_{det} and ξ are detector area and quantum efficiency, respectively. The parameter h , c , and λ are the planck constant ($h = 6.62 \times 10^{-34} \text{ m}^2 \text{ kg s}^{-1}$), the speed of light in the vacuum ($c = 3 \times 10^8 \text{ m s}^{-1}$), and the light wavelength.

The uncertainty in the detected electrons (shot noise) follows a Poisson distribution,¹²⁶ hence the `poissrnd` function in Matlab[®] is used to generate a random number from the Poisson distribution. The mean parameter used in the `poissrnd` function is given by the value of n_e shown in Eq. (4.5.3), and the resultant randomly generated number of electrons denoted by $n_{e(\text{noise})}$.

In addition to the Poisson noise, another source of noise on the signals is the quantisation error. The quantisation procedure in the imaging system, which converts the number of electrons in the CCD wells to the discrete signal levels, changes the real value of the signals¹²⁷ due to the number of possible signal levels in a camera. To include the effects of this quantisation error by the analog to digital converter (ADC) of the camera, the signal level corresponding to $n_{e(\text{noise})}$ is rounded to the nearest discrete signal level before

converting it back to the number of electrons, $n_{e(\text{noise})}$ ¹²⁸ as follows:

$$n_{e(\text{noise})} = \text{round} \left(\frac{n_{e(\text{noise})}}{\text{ADU}} \right) \times \text{ADU} \quad (4.5.4)$$

Here, ADU denotes analog-to-digital conversion units of the camera and it describes the conversion efficiency of the camera from the number of electrons in the CCD well to the discrete signals levels,¹²⁸ which is given by

$$\text{ADU} = \frac{18,000}{2^{12}} = 4.4 \quad (4.5.5)$$

The $n_{e(\text{noise})}$ in Eq. (4.5.4) is used to give the ‘noise-affected’ I from Eq. (4.5.3). The noisy A value, A_N , is calculated as

$$A_N = \log \left(\frac{I_{0(\text{noise})}}{I_{(\text{noise})}} \right) \quad (4.5.6)$$

where $I_{0(\text{noise})}$ and $I_{(\text{noise})}$ denote the simulated noisy I_0 and I values, respectively.

An example of the modelled noisy attenuation spectrum A_N can be seen in Fig. 4.17. This spectrum is derived from the intensity data which give the ‘noiseless’ attenuation spectrum A_{MC} previously shown in Fig. 4.15 (top left). This A_{MC} is also plotted in Fig. 4.17 for reference. The noise-affected signals are used in next section to demonstrate the sensitivity of the value given by the wavelength dependent MLBL to system noise.

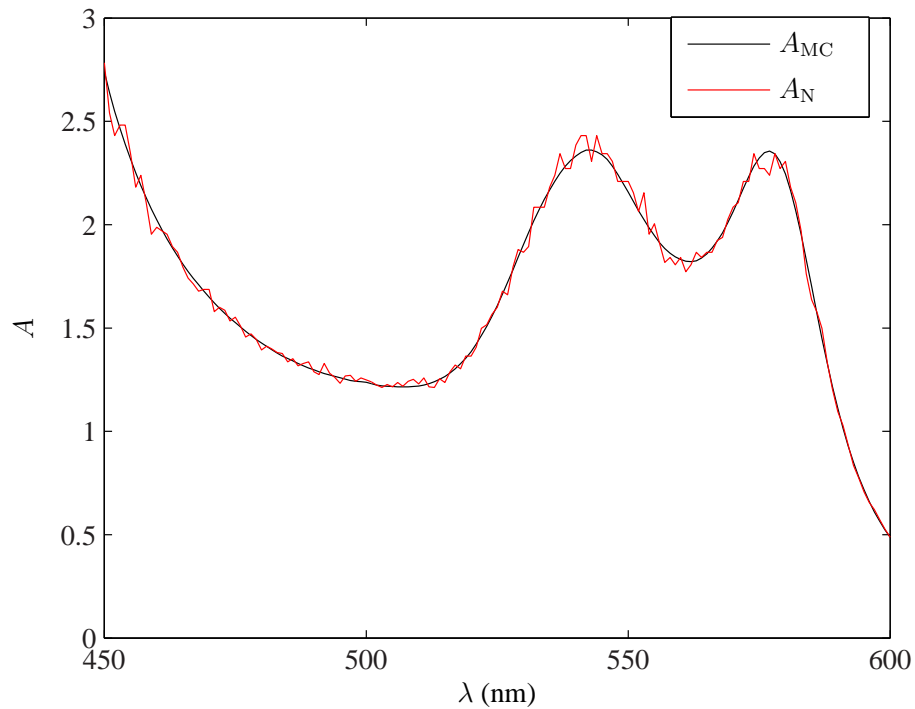


Figure 4.17: The ‘noiseless’ attenuation spectrum given from the Monte Carlo simulations when the set $SO_2 = 80\%$ (A_{MC}) and an example of a modelled noisy attenuation spectrum (A_N).

4.5.3 The selection of optimal wavelengths for practical spectroscopy

Even though it is useful to determine the optimum wavelength combination to be used in analysing a specific medium, the priority here is to demonstrate the validity of the theories discussed in section 4.4.1 and section 4.5.1, and to establish the link between error and standard deviation of the estimated value and the data of the selected wavelengths. This is because the selection of an optimum wavelength combination is subject to changes when any of the following parameters, which would modify the A value, vary;

1. Different (or additional) absorbers are in the medium
2. The medium’s SO_2 value

3. Medium geometry, structure and layer
4. The scattering parameters (i.e. g, μ_s) of the medium
5. Light illumination and detection system
6. Noise in the experimental system

Since the main concern here is to assess the theories discussed above, the sampling resolution of attenuation and absorbers' extinction coefficient spectra of 1 nm would be sufficient for this purpose and they are used in the following.

The TPSFs and medium absorbers' extinction coefficient spectra are shown in Fig. 4.7 and Fig. 2.3, respectively, and let the non-varying total hematocrit concentration T_H is set at $58 \mu\text{mol L}^{-1}$; using these information, the attenuation spectra for different SO_2 (varied from 0% to 100% at the step size of 1%) are derived from Eq. (2.2.4) and represented by A_{MC} . These attenuation spectra give the 'noisy' signals by following the steps described in section 4.5.2. For the A_{MC} of each SO_2 , this process is iterated 300 times, generating 300 different sets of 'noisy' attenuation spectra. The processing of these noisy attenuation spectra produced 300 different values of ΔSO_2 (given from each three-wavelength combination) from which the mean (μ_{err}) and standard deviation (σ_{err}) of ΔSO_2 are calculated. Fig. 4.18 shows the flow diagram of the noisy attenuation spectrum generation process and the evaluation of error performance of each wavelength combination. The whole process is repeated for A_{MC} for different SO_2 (denoted by $\text{SO}_{2(t)}$ in Fig. 4.18). The wavelengths selected from this process consisted of a combination of three wavelengths that produced the lowest overall mean and standard deviation of ΔSO_2 , $\mu_{\text{err}} \pm \sigma_{\text{err}}$ value (i.e. $\overline{\Delta\text{SO}_{2(s)}}$ in Fig. 4.18).

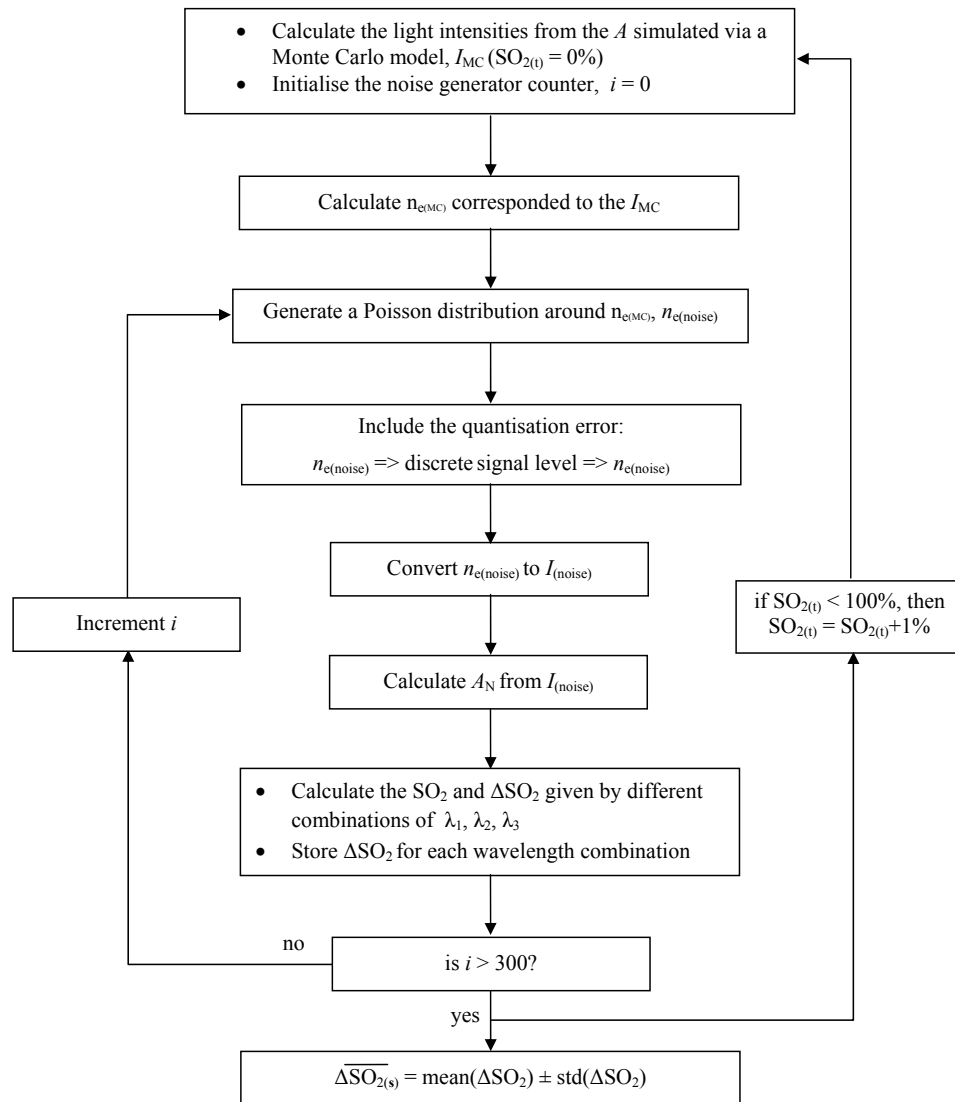


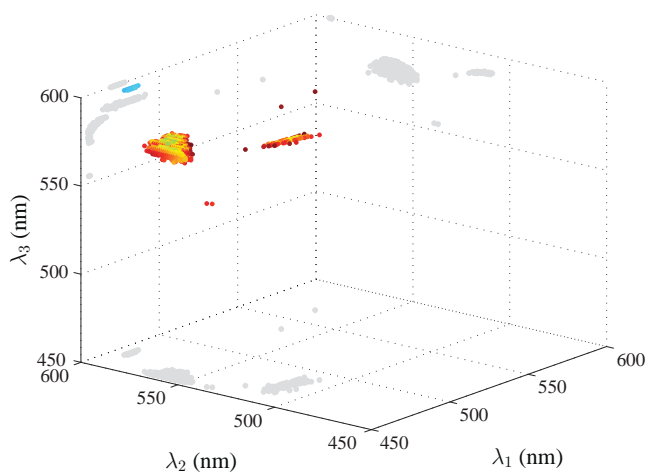
Figure 4.18: The processes involved in generating noisy attenuation spectra and the evaluation of the accuracy and noise-sensitivity of the SO_2 value given by different wavelength combinations.

4.5.3.1 Results and discussion

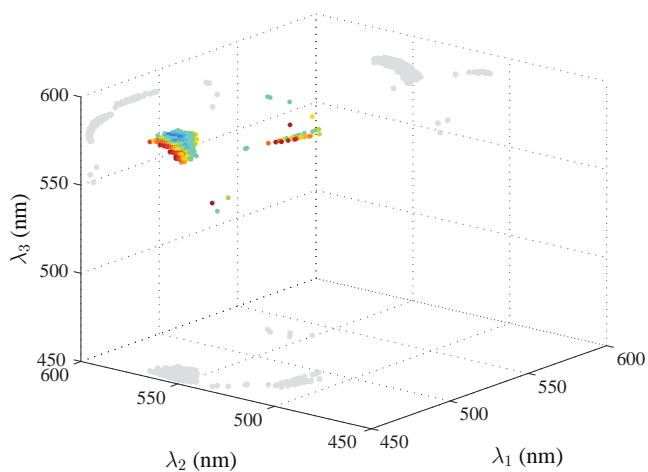
Besides the full SO₂ range of 0% – 100% as shown in Fig. 4.18, the optimum wavelength combination for a smaller SO₂ range of 50% – 90%, which is the realistic range for the mean blood oxygen saturation across arteries, veins and capillaries,¹²⁹ is also identified. The objective of this is to investigate the repeatability of the performance of different wavelength combinations when a different SO₂ range is considered. The mean of the μ_{err} and σ_{err} values given by each wavelength combination when the set SO₂ is varied across the two considered ranges are plotted in Fig. 4.19 and Fig. 4.20, respectively. The combinations of three wavelengths that yield an estimated SO₂ value that is not within the analytical range of –2% to 102% during one of the iteration processes (denoted by i in Fig. 4.18) are not shown in these diagrams.

Some of these wavelength combinations may produce small variation in the estimated value but a large mean error, and vice versa. So to identify a combination of three wavelengths with the best performance in terms of the lowest mean error and high repeatability in the estimated value, the threshold limit for the mean σ_{err} is selected as 2.5%. This work assumes that if the mean σ_{err} is greater than the set threshold value, the value would be sensitive to the noise, so only the values given by the wavelength combinations that produced mean σ_{err} within these limits are plotted in Fig. 4.19 and Fig. 4.20. The optimum wavelength combination is then selected based on the lowest mean error shown in Fig. 4.19 and this selection is valid only for the set threshold value. The colour bars shown at the bottom of the diagrams in Fig. 4.19 and Fig. 4.20 indicate the value of the mean μ_{err} and σ_{err} , respectively. The shadow of these data (shown as gray) projected on the Y-Z plane (i.e. when $\lambda_1 = 600$ nm), X-Z plane (i.e. when $\lambda_2 = 600$ nm), and X-Y plane (i.e.

when $\lambda_3 = 450$ nm) are also included in the diagrams to provide a better illustration of the combinations of wavelengths that give the corresponding performance.



(a) $\text{SO}_2 = 0\% - 100\%$



(b) $\text{SO}_2 = 50\% - 90\%$

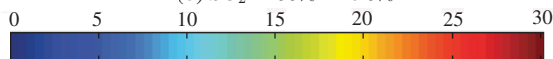
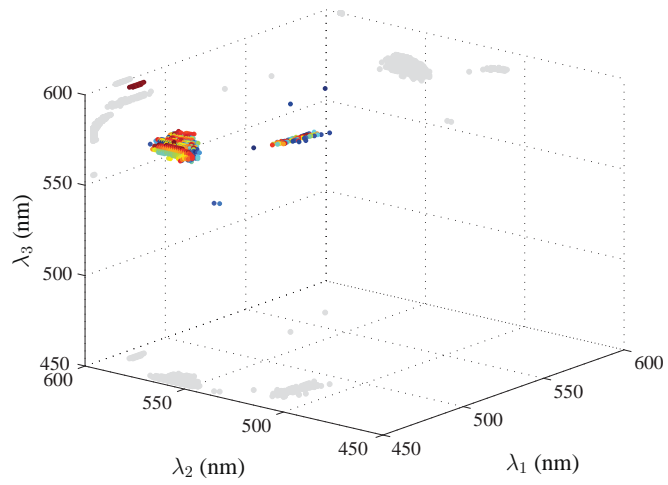
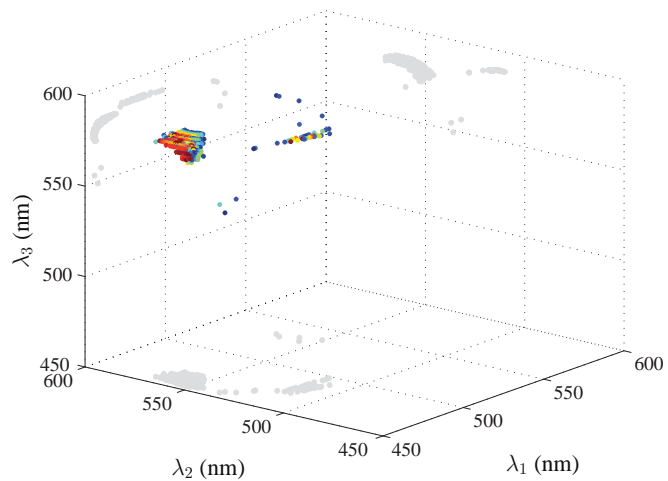


Figure 4.19: Mean of absolute μ_{err} values when the set SO_2 varied from (a) 0% to 100% and (b) 50% to 90%. The combinations of wavelengths that failed to produce a value within the range -2% to 102% during one of the iteration processes or produced a mean of $\sigma_{\text{err}} > 2.5\%$ are not shown in the diagram. The colour bar indicates the magnitude of the mean μ_{err} .



(a) $\text{SO}_2 = 0\% - 100\%$



(b) $\text{SO}_2 = 50\% - 90\%$



Figure 4.20: Mean of absolute σ_{err} values when the set SO_2 varied from (a) 0% to 100% and (b) 50% to 90%. The combinations of wavelengths that failed to produce a value within the range -2% to 102% during one of the iteration processes or produced a mean of $\sigma_{\text{err}} > 2.5\%$ are not shown in the diagram. The colour bar indicates the magnitude of mean σ_{err} .

Unlike the result shown in Fig. 4.13, the combination of closely spaced wavelengths are not seen in Fig. 4.19 and Fig. 4.20. A possible reason for this is that in the absence of noise, the A and μ_a values of the closely spaced wavelengths may be considerably similar, satisfying the conditions outlined in section 4.4.2. However, in the presence of noise, the differences in their A values increase with noise, upsetting those conditions hence producing a large ΔSO_2 .

The increase in the number of wavelength combinations that produced a mean $\sigma_{\text{err}} \leq 2.5\%$ with reduction in the considered SO_2 range can be seen in Fig. 4.19 that increased from 383 combinations (when the considered SO_2 range is $0\% - 100\%$) to 681 wavelength combinations for a smaller SO_2 range (i.e. $50\% - 90\%$ range). This is due to the fact that some of these wavelengths can produce valid SO_2 estimates only within a certain SO_2 range depending on the A and μ_a values of these wavelengths as discussed in section 4.4.2, and the susceptibility of the signals to noise. Besides, the selected threshold (σ_{err}) value also affects the number of wavelength combinations shown in those diagrams.

According to Fig. 4.19(a) and Fig. 4.20(a), wavelength combinations 469 nm, 593 nm, 600 nm produce the lowest mean μ_{err} for the SO_2 range of $0\% - 100\%$, with a mean of μ_{err} and σ_{err} are given by 8.9% and 2.49%, respectively. Fig. 4.19(b) shows that 458 nm, 560 nm, 584 nm is the best wavelength combination for the case of SO_2 range of $50\% - 90\%$ as it produced the lowest mean μ_{err} with mean $\mu_{\text{err}} \pm \sigma_{\text{err}} = 6.95\% \pm 2.48\%$. Meanwhile, there is a high consistency in the value estimated using the combination of 456 nm, 551 nm, 577 nm. Fig. 4.20 shows that this wavelength combination gave $\sigma_{\text{err}} = 0.0028\%$ for both of the considered SO_2 ranges, with the mean μ_{err} is given by 25% and 15% when the SO_2 range is $0\% - 100\%$ and $50\% - 90\%$, respectively. The mean and standard deviation of ΔSO_2 given by the above mentioned wavelength combinations

at different set SO_2 value are plotted in Fig. 4.21. The larger error in the value estimated using these wavelengths compared to the results in Fig. 4.14, which is the case when the measured attenuation is not subject to the shot and quantisation noises discussed in section 4.5.2, suggesting the high sensitivity of this analytical approach to the noise.

Therefore, in addition to the fact that the accuracy of the estimated value depends upon the ability of the wavelength dependent MLBL to accurately approximate the true attenuation value, the effects of noise on the attenuation also influence the performance of the wavelength dependent MLBL model.

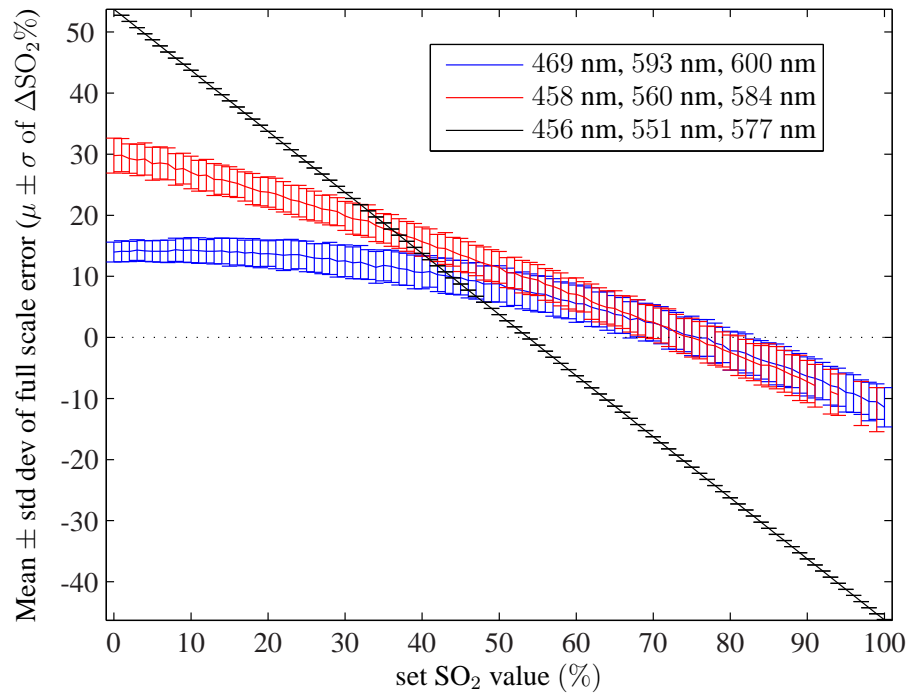


Figure 4.21: Mean and standard deviation (shown as error bar) of the full scale error in the value estimated using different wavelength combinations. Zero mean error is drawn as dotted line as a guide.

It can be seen from Fig. 4.21 that, even though 469 nm, 593 nm, 600 nm produced a lower mean SO_2 across SO_2 range of 50% – 90% as compared to that given by 458 nm,

560 nm, 584 nm, it was not chosen as the optimal wavelength combination for this SO₂ range because the standard deviation of the calculated error in this SO₂ range is, on average, greater than the set threshold value (mean $\sigma_{\text{err}} = 2.65$). The combination of 456 nm, 551 nm, 577 nm produced $\delta f_a \approx 0$ in Eq. (4.5.2), which is due to the collapse of the bracket term in the expression to approximately zero, hence the estimated values are insensitive to noise as can be seen from the small variance in the estimated values shown in Fig. 4.21. However, the value estimated using this wavelength combination is also insensitive to the changes in A with the medium's SO₂ because SO₂ = 54% is calculated regardless of the set SO₂. Based on these results, it is reasonable to select the combination of 469 nm, 593 nm and 600 nm as the best wavelengths for the considered wavelength range and sampling resolution because of the robustness and accuracy of its estimated values across the full SO₂ range. In the case when three absorbers are in the medium, a new generic wavelength combinations for the considered medium and measurement system can be selected following the steps described earlier, this wavelength combination can be determined by including the effects the additional absorbers have on the measurable during the modelling.

Again, it is important to note here that the performance of the wavelength combinations shown in Fig. 4.19 and Fig. 4.20 are valid only for the signals measured from a medium whose geometry and optical properties, detector geometry and the measurement mode described in section 4.3.1. In addition, these error plots may differ for different camera specifications. The changes in the error performance of the selected wavelengths when a different detection system and measurement mode are used will be shown later in Chapter 6. Even so, the criteria considered in selecting the optimal wavelengths discussed above are useful as a guide in finding the best wavelengths for spectroscopy analysis of a

medium, and the same approach would be applied when the properties of a medium and experiment system are known.

4.6 Conclusion

In this chapter, wavelength combinations able to reproduce the true f_a value using linear equation models are theoretically identified as those with either the same μ_a value or μ_a values that are collinear in absorption spectrum. This is a generic means of optimal wavelengths selection to deduce f_a value based on the measured data without using brute force method. However, the fulfilment of wavelengths with these conditions is restricted to the sampling resolution of the employed spectra, and the selection of an optimal wavelength combination varies with the parameters described in section 4.5.3. It was found that wavelengths which are closely spaced are considerably more sensitive to noise. The combination of wavelengths whose performance is robust towards the noise may also be insensitive to the medium's SO_2 induced variation in attenuation in its application in oximetry. Therefore the selection of wavelengths that reproduce f_a (or SO_2) value involves identifying wavelengths that are distantly spaced, sensitive to changes in f_a and that have satisfied the strategies discussed in section 4.4.2. In case when the medium's f_a is subject to changes and fast processing speed is required for quantification work, the optimal wavelength combination to be used with linear equation model can be identified through numerical modelling of the measurement system and medium. This wavelength combination can be determined in pre-measurement stage using brute force method, which is a more computational intensive method, demonstrated in section 4.5.3. The wavelength combination selected using this method, however, allow fast estimation of f_a value during

the measurement. The use of three wavelengths to find the f_a value of a medium and the generic strategies of optimal wavelengths selection presented in this chapter revealed several methods potentially used in oximetry. The application of these methods is not restricted to a specific optical system or measurement sites. One possible method is to manually identify different combination of three wavelengths that satisfied either one of the strategies discussed in section 4.4.2 under different f_a value in pre-measurement stage. The collinearity of attenuation value of these wavelength combinations is then evaluated to determine the wavelength combination that is able to recover the f_a value. Another method similar to this is discussed in the next chapter.

Chapter 5

Absorber's fractional concentration estimation via the analysis of attenuation of wavelength pairs

5.1 Introduction

The main objective of the work in Chapter 4 was to explore strategies to identify a combination of three wavelengths, which can be used with the linear equation model for spectroscopic analysis of a scattering medium. It was discussed in Chapter 4 that the search of an optimal wavelength combination for a certain SO_2 range required the optical system, medium's optical properties (i.e. μ_a and μ'_s) and geometries (of the medium and detector) used in the measurements to be modelled, but that this selection of wavelengths is subject to change when one of these measurement parameters is varied. The search of this optimal wavelength combination is useful when there is a limitation on the number

of wavelengths that can be used for spectroscopic examination of a specific medium such as an oximeter where three fixed wavelengths must be selected.

The availability of spectroscopy using a broadband source and hyperspectral cameras or spectrometers, which are able to measure signals across a wide range of wavelength, means there is much less restriction in the wavelengths to be used. Hence in this chapter, an analytical approach able to determine an optimal choice of a restricted set of wavelengths as the medium's f_a value is varied is investigated.

In section 5.2.1, the requirement needed to recover the f_a value in a medium is specified, unlike Chapter 4, no attenuation model is required in the estimation of this value. The limitation of using this approach and the potential sources of error in the estimated value are discussed in section 5.2.2. Two types of scattering-absorbing media are again considered in this work: wavelength-invariant scattering and wavelength dependent scattering media. Even though changes in the measurement wavelengths means the medium's μ'_s will be different, these variations can be insignificant if a sufficiently narrow wavelength range where changes in μ'_s are very slight^{3,4} is used. This type of scattering medium is considered in this study as the constant scattering medium.

The strategy used to identify the appropriate wavelengths based on the attenuation measured from a wavelength invariant scattering medium is described in section 5.3. This section also includes a demonstration of the estimation of f_a value using the data at these wavelengths. A similar method is employed for the case when a medium's μ'_s changes with wavelength and this is discussed in section 5.4. Since no attenuation model is needed in the estimation of the f_a value, an approach is required to process the measured attenuation spectrum and to determine a certain combination of wavelengths, using the data of which the medium's f_a value can be recovered. This would require knowing how

the attenuation, which is the only measurable from continuous intensity measurements, of different combination of wavelengths vary with the medium's f_a . So the attenuation response depending on the optical properties (i.e. μ_a, μ'_s) of a medium is derived mathematically in this chapter to identify a suitable approach used for analysing the measured data.

This approach is also used in section 5.5 to find the fractional concentration value of an absorber in a wavelength dependent scattering-absorbing medium that contains three absorbing species. Lastly, the selection of optimal wavelength range for quantification work using this approach is determined in section 5.6.

5.2 Estimation of fractional concentration value using a wavelength pair

It was discussed in section 2.2 that scattering in a medium causes an attenuation offset and a nonlinear relationship between A and μ_a , and it can be seen from the work reviewed in section 2.5 that medium characterisation using data at two different wavelengths is the minimum requirement for the estimation of the f_a value.

In this work, an attenuation spectrum measured using a continuous intensity technique is needed for analysis but the estimation of f_a value involves using data at two wavelengths. More importantly, an approach that is different from that reviewed in Chapter 2 is practised and this will be demonstrated in section 5.2.3.1. The description of this quantification method is preceded with the derivation of the f_a value in section 5.2.1 and a discussion of the range of acceptable error defined in this study. This is followed by a

description of the steps and equations involved in exploring the approach that can be used to determine a medium's f_a value in section 5.3.2 and section 5.4.2.

5.2.1 Deriving the fractional concentration value of an absorber

The error plot shown in Fig. 4.2 obtained when the MLBL is used in the case of a scattering medium with wavelength-invariant μ'_s points out an interesting fact, which is that a zero error is obtained if the μ_a of any two wavelengths (e.g. λ_1 and λ_2) are identical regardless of the selection of the third wavelength as follows:

$$\mu_{a1} = \mu_{a2} \quad (5.2.1)$$

From Eq. (4.2.2), Eq. (5.2.1) can also be written as

$$\alpha_1 T_a = \alpha_2 T_a \quad (5.2.2)$$

The absorbers' total concentration, T_a , can be cancelled out in Eq. (5.2.2) to give

$$\alpha_1 = \alpha_2 \quad (5.2.3)$$

In the case of a medium with two absorbers, namely absorber A and B, the medium's α is given from Eq. (4.2.3), so that Eq. (5.2.3) can also be written as

$$[(\varepsilon_{A_1} - \varepsilon_{B_1})f_a + \varepsilon_{B_1}] = [(\varepsilon_{A_2} - \varepsilon_{B_2})f_a + \varepsilon_{B_2}] \quad (5.2.4)$$

From the discussion of Fig. 4.2, it is reasonable to deduce the fractional concentration value of an absorber directly from Eq. (5.2.4) using the extinction coefficients of the present absorbers, where solving for the value of f_a in Eq. (5.2.4) gives

$$f_a = \frac{\varepsilon_{B_1} - \varepsilon_{B_2}}{\varepsilon_{A_2} - \varepsilon_{B_2} - \varepsilon_{A_1} + \varepsilon_{B_1}} \quad (5.2.5)$$

While Eq. (5.2.5) is the simplest form of f_a previously shown in Eq. (2.5.5), Eq. (2.5.6) and Eq. (2.5.11), the true f_a value can be recovered using Eq. (5.2.5) only if the selected wavelength pair abides by the condition shown in Eq. (5.2.3). Eq. (5.2.5) does not include the value of measured attenuations, instead, these are used to identify the wavelength pairs that satisfy Eq. (5.2.3) before f_a is calculated from Eq. (5.2.5). Take, for example, the case when the medium's μ'_s is invariant with wavelength, $A(\alpha)$ is a single-valued function as shown in Fig. 3.7 and Fig. 4.3, so wavelength pairs with the same α give the same attenuation. This is further elaborated in section 5.3.

5.2.2 Derivation of error arising from quantisation

In practice, a wide range of spectral resolutions are available for different spectrometers and hyperspectral cameras, with the typical spectral resolution of these cameras ranging from 0.25 nm to 4 nm⁵⁶ (with efforts to acquire higher spectral resolutions still ongoing).^{130,131}

However, even under noiseless conditions and with the finest currently available detector sampling interval, it is still unlikely that a wavelength pair with the same A can be found. The importance of finding this wavelength pair will be discussed in section 5.3.2. This is with an exception when the continuous attenuation spectrum is sampled at a suffi-

cient rate to satisfy the Nyquist criterion and reconstructed via a convolution with the sinc function,¹³² whose operation involves summing the reconstructed sample at an infinite time point. While the use of this sinc function is impractical, the use of an approximation to the sinc function that is finite in length would result in interpolation error.¹³² Therefore, without an ideal reconstruction of signals, the closest agreement to the same A given by a wavelength pair, i.e. λ_1 and λ_2 , can be written as

$$A(\lambda_1) + \Delta A = A(\lambda_2) \quad (5.2.6)$$

where ΔA is the error between attenuation of λ_1 and λ_2 . In view of this, the α spectra used in this work are sampled at a discrete sampling interval matching that of the measured attenuation spectra (i.e. 1 nm is used in this work), so that the closest agreement in the α of a wavelength pair to Eq. (5.2.3) (under a f_a value) is given by

$$\alpha_1 + \Delta\alpha = \alpha_2 \quad (5.2.7)$$

where $\Delta\alpha$ is the difference between the relative specific absorption coefficient at λ_1 (i.e. α_1) and λ_2 (i.e. α_2) due to the sampling resolution of the employed spectra. Substituting Eq. (4.2.3) into Eq. (5.2.7) gives

$$(\varepsilon_{A_1} - \varepsilon_{B_1})f_a + \varepsilon_{B_1} + \Delta\alpha = (\varepsilon_{A_2} - \varepsilon_{B_2})f_a + \varepsilon_{B_2} \quad (5.2.8)$$

And solving for f_a in Eq. (5.2.8) gives

$$f_a = \frac{\varepsilon_{B_1} - \varepsilon_{B_2} + \Delta\alpha}{\varepsilon_{A_2} - \varepsilon_{B_2} - \varepsilon_{A_1} + \varepsilon_{B_1}} \quad (5.2.9)$$

The error in the f_a value given from Eq. (5.2.9), Δf_a , can be expressed as

$$\Delta f_a = f_a - f'_a \quad (5.2.10)$$

$$= -\frac{\Delta\alpha}{\varepsilon_{A_2} - \varepsilon_{B_2} - \varepsilon_{A_1} + \varepsilon_{B_1}} \quad (5.2.11)$$

Here, f_a is the medium's true f_a value given from Eq. (5.2.5) while f'_a is the value given by a wavelength pair whose α do not match exactly due to quantisation error (shown in Eq. (5.2.7)). Eq. (5.2.11) shows that error in the estimated value depends on the value of $\Delta\alpha$ and differences in the extinction coefficients of the medium absorbers, $\Delta\varepsilon$, at the selected wavelength pair. It is unlikely to find a wavelength pair whose α are identical using the sampling resolution of the measuring instruments, so an absolute error in f_a (in %) of $|\Delta f_a| \leq 0.5\%$ is considered as acceptable. Any wavelength pair that is able to give an error of within this limit as compared to the medium's true f_a is desirable and is referred to here as the *right wavelength pair*.

This technique is demonstrated using attenuation data and medium's absorbers described in section 5.2.3. The result on the accuracy of the f_a value estimated based on these simulated data and with α of the selected wavelength pair comply with Eq. (5.2.3) is presented in section 5.2.3.1.

5.2.3 Demonstration of the technique

For the sake of demonstration, the simulated TPSF given when an infinite slab has a wavelength invariant μ'_s of 3.5 mm^{-1} shown in Fig. 4.7 (i.e. when $\lambda = 550 \text{ nm}$) is used as an example of the distribution of photons. The description of the medium and source-detector system used in the simulations can be found in section 4.3. In the absence

of absorption, the same TPSF is measured regardless of the emitting wavelength of the employed light source and it is plotted in Fig. 5.1.

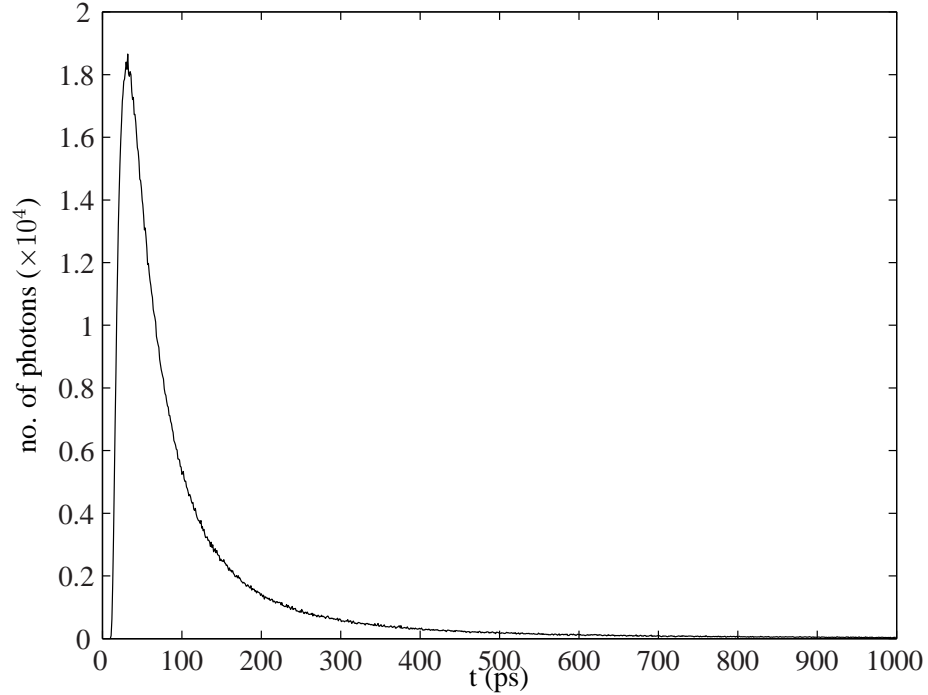


Figure 5.1: The simulated TPSF of a scattering medium with $\mu'_s = 3.5 \text{ mm}^{-1}$ after 20 million photons were launched into an infinite slab described in section 4.3 and light propagation of these photons is simulated by the Monte Carlo method. The μ_a of this medium is 0 mm^{-1} .

However, if oxy- and deoxy-haemoglobin whose extinction coefficients in the range of 450 nm – 600 nm shown in Fig. 2.3 were the medium's absorbers, then the simulated TPSF would change with the wavelength dependent μ_a value. The reason this wavelength range is chosen is that it is likely to find a wavelength pair that gives small $\Delta\alpha$ using the spectral resolution of 1 nm (hence producing $|\Delta f_a| \leq 0.5\%$) under a given f_a while other reason will be discussed in section 5.6. In the following, T_H and SO_2 are set as $58 \mu\text{mol L}^{-1}$ and 80%, respectively, to give a variation in the medium's μ_a with wave-

length shown in Fig. 5.2 (top). Based on these μ_a and the TPSF shown in Fig. 5.1, the light attenuation value is calculated using:

$$A = A_s + \log \left(\int_{t=0}^{\infty} s(t) 10^{-\mu_a c_m t} dt \right) \quad (5.2.12)$$

which is rewritten from Eq. (2.2.4). The calculated attenuation spectrum is plotted in Fig. 5.2 (middle). This spectrum will be used for the demonstration of the technique in the following.

5.2.3.1 Results on the estimation of value using a wavelength pair

It is mentioned in section 5.2.1 that wavelengths whose α (hence μ_a) are equal can be used to recover the medium's f_a using Eq. (5.2.5). For demonstration purposes, let wavelength 533 nm selected as λ_1 , so by coupling 533 nm (indicated by open-circle symbol in Fig. 5.2) with another wavelength which displays the same μ_a (marked by dotted line in Fig. 5.2), e.g. around 460 nm, 550 nm or 570 nm, the true SO₂ value can, in theory, be obtained.

The full scale error in the SO₂ calculated using Eq. (5.2.5) when λ_2 is a wavelength chosen from the range 450 nm – 600 nm is shown in Fig. 5.2 (bottom). Also shown in the diagram is a dotted line drawn across $\Delta\text{SO}_2 = 0\%$ as a guide. The pairing of λ_2 (shown on the x-axis of Fig. 5.2) with 533 nm that produces an estimate of SO₂ value of less than -2% or greater than 102% is not shown in Fig. 5.2.

Similar to the conclusions drawn in section 4.2.1, where it was mentioned that in this case a wavelength pair measuring an equal attenuation value means that their μ_a values are identical. Fig. 5.2 shows that wavelength pairs with the same μ_a can be identified from

their attenuation value (as they produce the same attenuation). This is verified mathematically in section 5.3.1.

It can be seen from Fig. 5.2 that the error in the estimated SO_2 value increases as the μ_a (hence attenuation) at different λ_2 is progressively dissimilar to that at λ_1 , which is when Eq. (5.2.3) no longer holds. Low SO_2 errors are observed in Fig. 5.2 (bottom) when λ_2 is selected as 460 nm or 550 nm or 570 nm, but these wavelengths failed to produce $\Delta\text{SO}_2 = 0\%$ due to the non-zero $\Delta\alpha$ as discussed in section 5.2.2. This result shows that the data of two wavelengths are sufficient to give an estimate of fractional concentration value of an absorber with a reasonable accuracy, but that depends on the sampling resolution of the employed spectra because of the need to match attenuation values.

The variation in SO_2 changes the μ_a , and hence the attenuation value measured at certain wavelengths, so wavelengths that measured the same attenuation (e.g. when $\text{SO}_2 = 80\%$) will not in general have the same value when the SO_2 changes. The attenuation spectra for different SO_2 values are shown in Fig. 5.3. Even if a wavelength pair that can measure the same attenuation value throughout all SO_2 values existed, the estimated SO_2 value is constant (as the value estimated using Eq. (5.2.5) depends only upon the absorbers' extinction coefficients of the wavelength pair), so cannot be used for oximeter. Thus, a different wavelength pair needs to be identified as the SO_2 varied. The processing of a discretely sampled attenuation spectrum to identify these wavelengths will now be discussed.

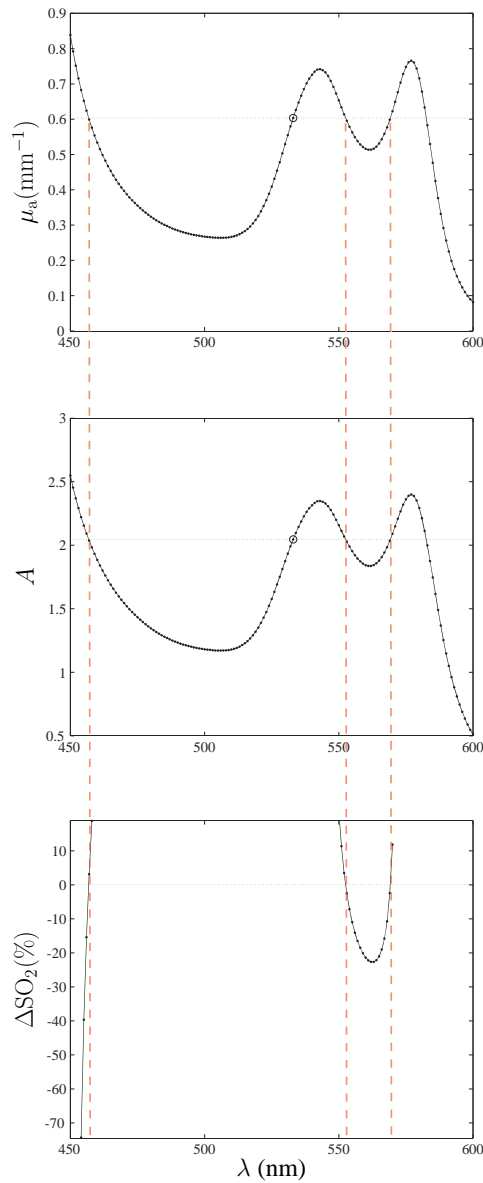


Figure 5.2: (top and middle) The μ_a and attenuation spectra of a modelled wavelength invariant scattering medium when $\text{SO}_2 = 80\%$. Also drawn in these diagram is the location of the selected wavelength $\lambda_1 = 533 \text{ nm}$ (indicated by open-circle symbol). A dotted line is drawn to show the value of μ_a and attenuation measured using $\lambda_1 = 533 \text{ nm}$. (bottom) The calculated full scale error, ΔSO_2 , when $\lambda_1 = 533 \text{ nm}$. A dotted line is drawn as a reference to the location of $\Delta\text{SO}_2 = 0\%$. The ΔSO_2 for the calculated SO_2 outside the range of -2% to 102% is not shown in the diagram.

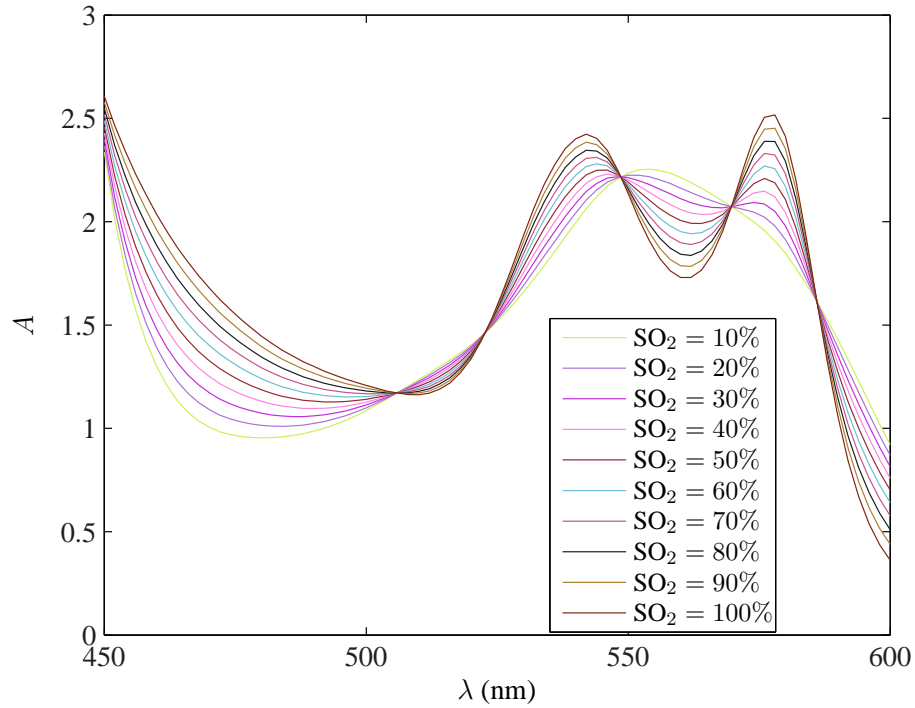


Figure 5.3: The variation in the attenuation spectrum measured from a scattering medium with constant μ'_s as SO_2 changed from 10% – 100%.

5.3 Considering a medium with wavelength-invariant μ'_s

In this section, a simplified case where the medium's μ'_s is assumed to be a wavelength independent constant is considered. The medium's α is, in practice, unknown and light attenuation is the only parameter that can be measured via the continuous intensity measurement. Therefore the right wavelength pairs can only be found based on the measured attenuation. The attenuation response of different wavelength pairs is mathematically derived in section 5.3.1. The derivations from this section provide the basis used in developing the analytical method discussed in section 5.3.2. This method involves analysing

the attenuation of certain wavelength pairs collected in the pre-measurement stage in section 5.3.3. The accuracy of the value estimated using this method is presented in section 5.3.4.

5.3.1 The selection of wavelength pairs and their attenuation responses

In the case when a medium's μ'_s is a constant value, the produced TPSF (when $\mu_a = 0 \text{ mm}^{-1}$) is non-varying with wavelength, section 2.5.3 mentioned that the measured A can be represented by an infinite summation of TPSF cumulants, which is restated as follows:

$$A(\lambda) = \kappa_0 - \sum_{n=1}^{\infty} \kappa_n \frac{(-\mu_a(\lambda)c_m)^n}{n!} \quad (5.3.1)$$

where all the cumulant values are non-zero. The A versus μ_a relationship is a single-valued function as demonstrated in section 4.2.1, which means that wavelength pair with the same μ_a measure the same A . This can be proved using Eq. (5.3.1) to express the difference between A of a wavelength pair as

$$A(\lambda_1) - A(\lambda_2) = - \sum_{n=1}^{\infty} \kappa_n \frac{(-\mu_a(\lambda_1)c_m)^n}{n!} + \sum_{n=1}^{\infty} \kappa_n \frac{(-\mu_a(\lambda_2)c_m)^n}{n!} \quad (5.3.2)$$

If μ_a of this wavelength pair are identical (i.e. $\mu_{a_1} = \mu_{a_2}$), then Eq. (5.3.2) is reduced to

$$A(\lambda_1) - A(\lambda_2) = - \sum_{n=1}^{\infty} \kappa_n \frac{(-\mu_a(\lambda_2)c_m)^n}{n!} + \sum_{n=1}^{\infty} \kappa_n \frac{(-\mu_a(\lambda_2)c_m)^n}{n!} = 0 \quad (5.3.3)$$

which shows that the same attenuation is measured. However, if α of a wavelength pair is as shown in Eq. (5.2.7), using the relationship between α and μ_a in Eq. (4.2.2) to give

$$\mu_a(\lambda_1) = \mu_a(\lambda_2) + \Delta\mu_a \quad (5.3.4)$$

Eq. (4.2.2) mentioned that μ_a is related to α by a constant T_a (i.e. at a specific time point), so $\Delta\mu_a$ shown in Eq. (5.3.4) denotes the error in the μ_a value given by the non-zero $\Delta\alpha$ between a wavelength pair. Using Eq. (5.3.4), the non-zero difference between attenuation at λ_1 and λ_2 is given by

$$\begin{aligned} A(\lambda_1) - A(\lambda_2) &= -\sum_{n=1}^{\infty} \kappa_n \frac{(-(\mu_a(\lambda_2) + \Delta\mu_a)c_m)^n}{n!} + \sum_{n=1}^{\infty} \kappa_n \frac{(-\mu_a(\lambda_2)c_m)^n}{n!} \\ &= -\sum_{n=1}^{\infty} \kappa_n \frac{-(\Delta\mu_a c_m)^n}{n!} \end{aligned} \quad (5.3.5)$$

which shows that wavelength pair with dissimilar μ_a produces a non-zero attenuation difference, ΔA .

5.3.2 The search of the optimal wavelength pairs

Fig. 5.2 shows that a medium's f_a can be determined from Eq. (5.2.5) via a manual selection of a suitable wavelength pair based on their attenuation value, but this approach is impractical when the experiments involved processing a large number of attenuation spectra. For this reason, a possible approach towards an automatic selection of the optimal wavelength pairs is described here.

Wavelength pairs with the same α can be identified for different f_a values in the pre-experimental stage so that the optimal choice of wavelength pair can be automatically

determined via the analysis of the attenuation values of these wavelength pairs. However, wavelength pairs that follow the condition shown in Eq. (5.2.3) are limited by the sampling resolution of the employed spectra, which may lead to an error in the estimated value as expressed in Eq. (5.2.11) and shown in Fig. 5.2.

An interpretation from the derivations in section 5.2.2 and section 5.3.1 is that the α of the right wavelength pairs for a certain f_a value would in practice be related by Eq. (5.2.7), where the small but non-zero $\Delta\alpha$ is due to the limitation in the resolution of the employed spectra, so these wavelength pairs are able to produce a narrow distribution of ΔA values around zero compared to those produced by wavelength pairs with large and random $\Delta\alpha$ as given in Eq. (5.3.5). Since more than a right wavelength pair can be found for each f_a (for absorbers' extinction coefficients in the wavelength range 450 nm – 600 nm shown in Fig. 2.3) and all these right wavelength pairs can be collected during the pre-measurement stage and used for the analysis, a straightforward approach to find the optimal choice of the wavelength pairs (grouped under a set) is by evaluating the sum of ΔA values given by different sets of wavelength pairs. The data of the selected set of wavelength pairs (that produced the lowest sum of absolute ΔA) can in theory be used to give an estimate of the medium's f_a with an absolute error of less than 0.5%.

The feasibility to search and group the wavelength pairs in pre-measurement stage for the analysis is described in section 5.3.3, and the result on the accuracy of value estimated using the described approach is presented in section 5.3.4.

5.3.3 Grouping the wavelength pairs

It was discussed in section 5.3.2 that more than a single wavelength pair would be collected for each f_a for the analysis of their attenuation response in finding a medium's f_a . A sufficient number of data points would also guarantee a more reliable data (derived from the attenuation response of these wavelength pairs) used for the analysis and minimise the possibility of obtaining a false positive result as will be further elaborated in section 5.4.3. The α changes with the f_a value, so a different set of wavelength pairs that produced low error in Eq. (5.2.11) when the medium's f_a varies need to be found.

Section 5.2.2 mentioned that wavelength pairs which produce $\Delta f_a = \pm 0.5\%$ as compared to the set f_a value are considered as acceptable. It is straightforward to identify the right wavelength pairs for each set f_a as the f_a value given by different combination of wavelength pair can be calculated from their corresponding absorbers' extinction coefficients shown in Eq. (5.2.5) and it is independent of the measured attenuation value. Thus, all the wavelength pairs that give Δf_a within this limit are stored as the right wavelength pairs for this f_a . The (set) f_a value during which these wavelengths are identified and stored is represented by f_a^* (or SO_2^* if the extinction coefficients of absorbers shown in Fig. 2.3 were used) and these collected wavelength pairs are valid only for the corresponding f_a^* . This is because as the set f_a changes, a larger difference between α values of each wavelength pair in this group can be observed, producing $|\Delta f_a|$ greater than 0.5% as given in Eq. (5.2.9). The search of these right wavelengths is then repeated for different f_a^* that varied from -2% to 102% in 1% increments. This analytical range is considered valid in this study due to the reason described in section 4.2.1.

Once the medium's absorbers and their extinction coefficients are identified, the right

wavelength pairs for each f_a^* can be determined and stored during the pre-measurement stage.

5.3.4 Results and analysis

Since the right wavelength pairs whose Δf_a is non-zero are collected, the calculated ΔA would theoretically fluctuate around zero as given in Eq. (5.3.5). Fig. 5.4 is a demonstration of the ΔA value given by certain right wavelength pairs (collected when $\text{SO}_2^* = 80\%$) using α and attenuation spectra shown in Fig. 5.2. These spectra (sampled at 1 nm) are derived from a medium with wavelength invariant μ'_s and when the medium's $\text{SO}_2 = 80\%$.

For simplicity only the data of $\lambda_1 = 530$ nm and $\lambda_2 = 558$ nm (indicated by red circle), which is one of the right wavelength pairs, is examined here. This wavelength pair gives an error of $\Delta \text{SO}_2 = 0.2\%$ and $\Delta A = 0.0015$. The reason a non-zero ΔSO_2 is obtained is that α of this wavelength pairs is not exactly identical, hence giving a non-zero ΔA as shown in Fig. 5.4 (top right). Therefore the mean of α of this wavelength pair calculated using the corresponding SO_2^* value and from Eq. (4.2.3) is used in Fig. 5.4 to plot against the calculated ΔA . This is repeated for other right wavelength pairs producing the ΔA versus mean α plot shown in Fig. 5.4 (top right). Notice that α values are plotted (instead of μ_a) because the T_H value that is required in the calculation of μ_a in Eq. (4.2.2) is not estimated. This calculation of α is important in finding the f_a of a medium with wavelength dependent μ'_s that will be discussed later in section 5.4.2.

Although the result in Fig. 5.4 confirmed the small variation in ΔA value (given by the right wavelength pairs) around zero, there remains a need to assess the ability of the method discussed in section 5.3.2 to find a medium's SO_2 . This is again by using the

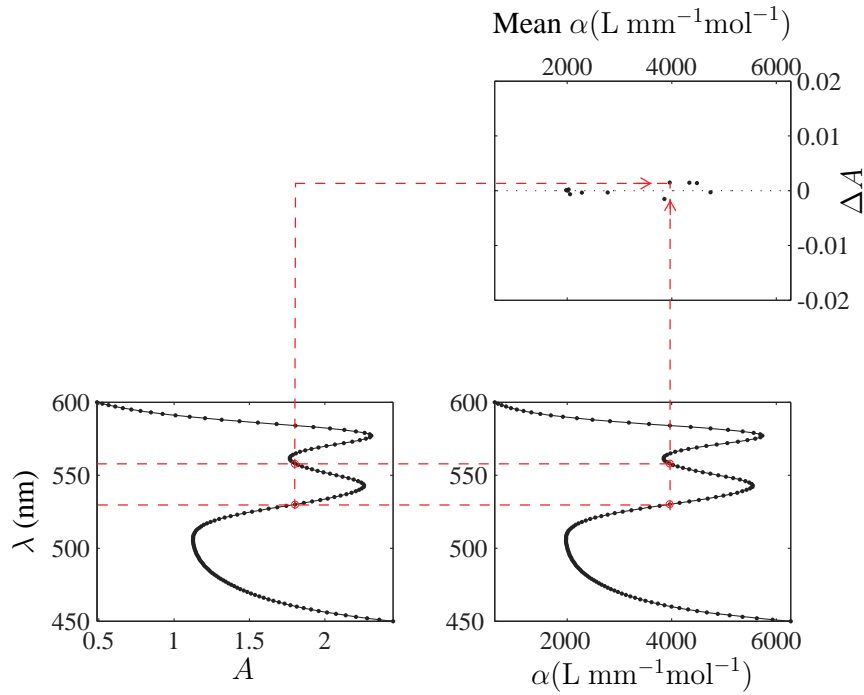


Figure 5.4: (bottom left and bottom right) Attenuation and α spectra of a medium with $\text{SO}_2 = 80\%$. (top right) The ΔA versus mean α relationship produced by certain right wavelength pairs. $\Delta A = 0$ (dark dotted line) is also drawn as a guide. The data of wavelength pair: 530 nm and 558 nm selected for discussion in the text are indicated by red circle and dashed line.

attenuation spectrum shown in Fig. 5.4 (bottom left). The dual-wavelengths grouped following the steps described in section 5.3.3 are used to give the ΔA . The sum of absolute ΔA given by wavelength pairs stored in each group (associated with different SO_2^*) is calculated and plotted in Fig. 5.5(a) against the corresponding SO_2^* .

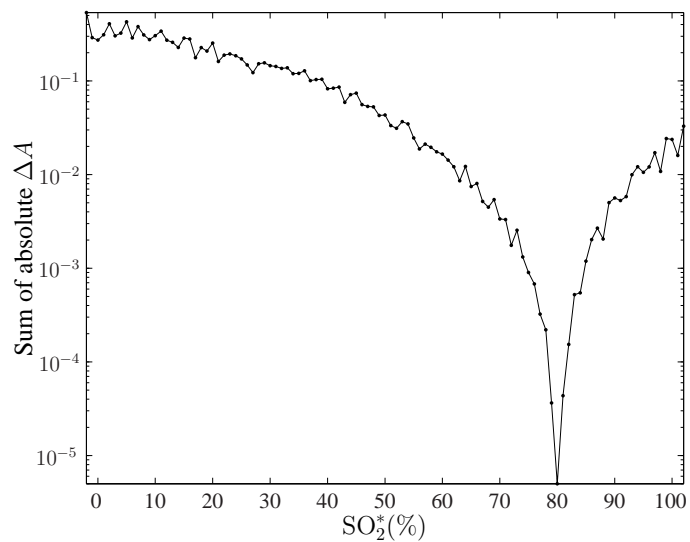
Referring to Fig. 5.5(a), the minimum sum of absolute ΔA is produced by the wavelength pairs stored when $\text{SO}_2^* = 80\%$. This SO_2^* matched with that used to produce the attenuation spectrum shown in Fig. 5.4 (bottom left). The ΔA versus mean α plot given by all the right wavelength pairs collected when $\text{SO}_2^* = 80\%$ is shown in Fig. 5.5(b).

Also shown in this diagram is the relationship produced by the wavelength pairs identified when $\text{SO}_2^* = 60\%$, which in theory produce large and random $\Delta\alpha$ when the true SO_2 is 80% , to serve as a comparison of the distribution of the ΔA values.

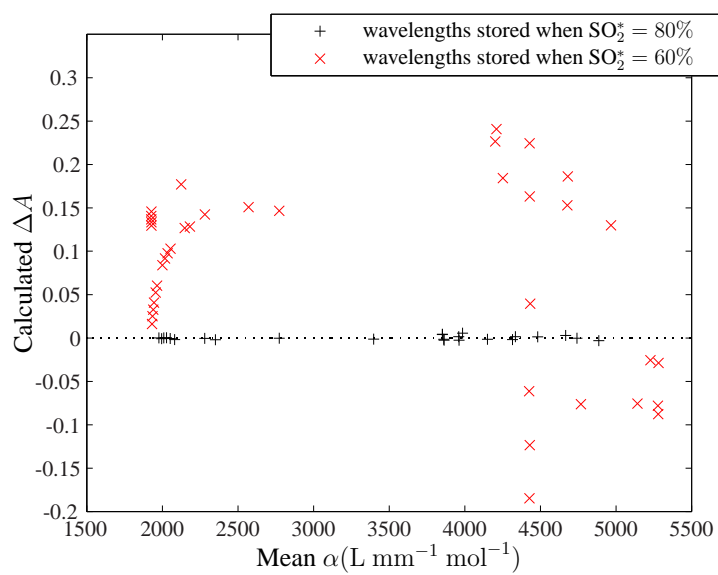
5.4 Considering a wavelength dependent scattering medium

When a medium's μ'_s varies with wavelength, the search of a wavelength pair agreeing to the condition shown in Eq. (5.2.3) is not straightforward and cannot be identified directly from their measured attenuation value. This is because the relationship between the measured A and μ_a is a multi-valued function as previously shown in section 4.3. Therefore, the first step towards identifying a right wavelength pair from an attenuation spectrum measured from this kind of medium is to understand how the measured attenuation varies with a medium's μ_a and μ'_s . This knowledge is inferred in the following from what is observed from simulated results and through mathematical derivations. The viability to express the measured attenuation mathematically is because, as mentioned in section 2.5.3 and section 5.3.1, this value can be represented by Eq. (5.3.1). But Eq. (5.3.1) is not valid for the medium considered in this section, and a modification to this expression is required to account for the variation in cumulants with wavelength. This is discussed in the following.

To begin with, changes in TPSF cumulants with the wavelength-varying μ'_s are examined. Using the plot shown in Fig. 4.5 as an example of the wavelength dependent μ'_s , a range of different TPSFs given from an infinite slab with these μ'_s values (in the wavelength range of 450 nm – 600 nm) and when $\mu_a = 0 \text{ mm}^{-1}$ were shown in Fig. 4.7. This surface plot of TPSF shows that the statistical properties of a TPSF changes with



(a)



(b)

Figure 5.5: (a) The sum of absolute ΔA versus SO_2^* . (b) The calculated ΔA versus mean α for the group with the right wavelength pairs (stored when $SO_2^* = 80\%$) and wavelength pairs collected when $SO_2^* = 60\%$. $\Delta A = 0$ (indicated by the dotted line) is also drawn in the diagram as a guide.

the wavelength of the illuminating light. Each TPSF in Fig. 4.7 is associated with wavelength of a single wavelength light source, and the variation in the statistical properties of each TPSF can be quantified using the TPSF cumulants values derived from Eq. (2.5.19). Based on the deduced cumulant values, the relationship between wavelength and different TPSF cumulants is plotted in Fig. 5.6, where for simplicity only cumulants of up to the third order, $n = 3$, are shown.

Fig. 5.6 shows that instability in the gradient of a cumulant versus wavelength plot increases with the order of cumulant, n . This can be understood by referring to Eq. (2.5.19) from which the cumulant values are calculated, where it can be seen that the n^{th} cumulant is dependent on the n^{th} and lower moments. The numerical instability in the calculations of higher moments is due to the increase in the order of polynomial term (t^n) shown in Eq. (2.5.12).¹³³ This instability propagated to the subsequent iterations via the recursive formula used in giving the cumulant value shown in Eq. (2.5.19). The significant finding shown in Fig. 5.6 is that the cumulants approximately decrease linearly with wavelength when the monotonic variation in the medium's μ'_s with wavelength is as shown in Fig. 4.5. This trend also observed at higher order cumulants ($n \geq 4$). This is useful information and is used in the following section to deduce an expression of the attenuation given from a scattering medium whose μ'_s values are as shown in Fig. 4.5.

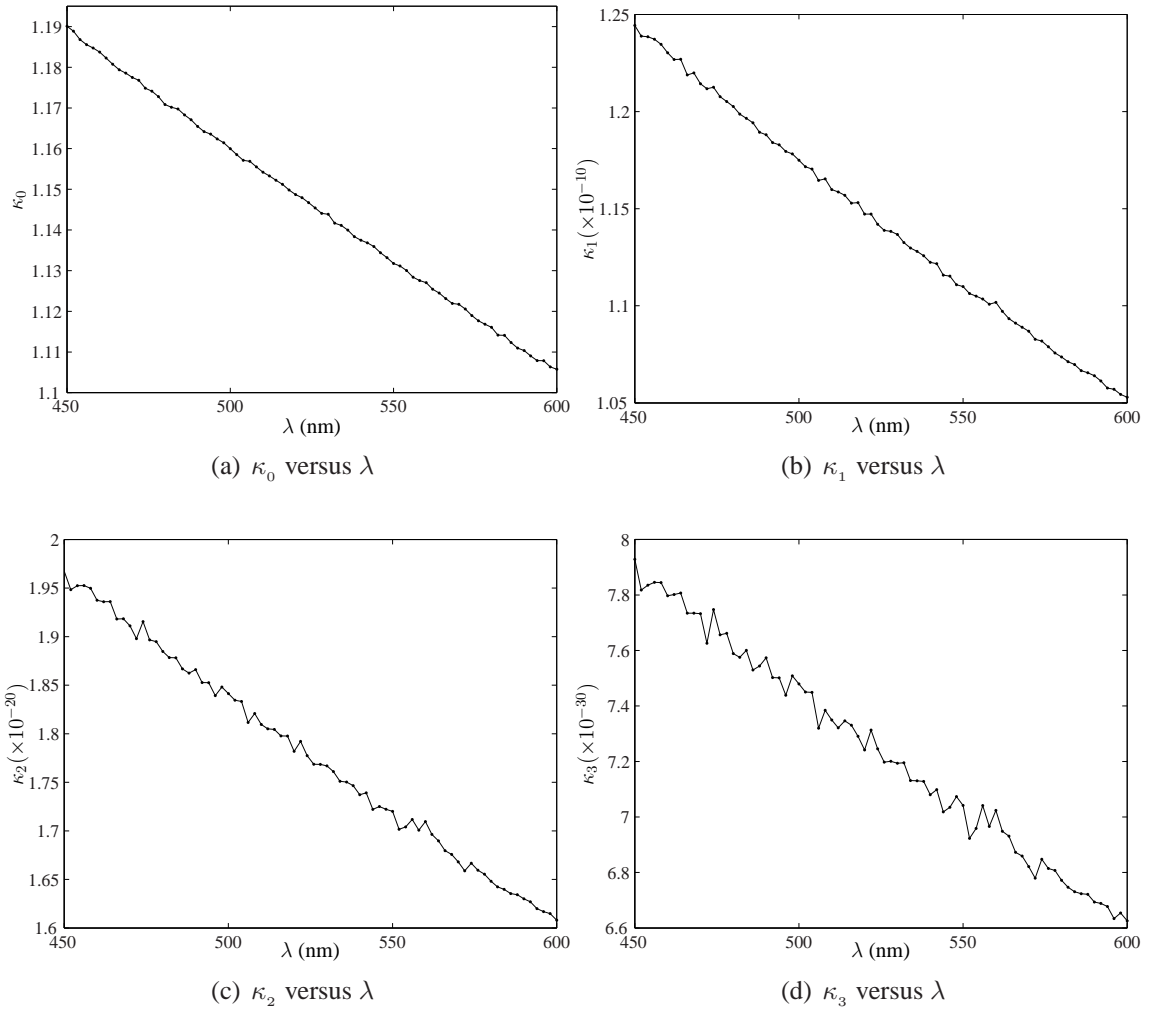


Figure 5.6: The variation in cumulants (up to the third order cumulant) with wavelength in the range 450 nm – 600 nm. These values are calculated from the TPSFs (when $\mu_a = 0 \text{ mm}^{-1}$) shown in Fig. 4.7.

5.4.1 The selection of wavelength pairs and their attenuation responses

Referring to the relationship between TPSF cumulant and wavelength shown in Fig. 5.6, the n^{th} cumulant of a TPSF measured using wavelength λ , $\kappa_n(\lambda)$, can be estimated as

$$\kappa_n(\lambda) = a_n + b_n\lambda \quad (5.4.1)$$

where a_n and b_n are constant values and represent the intercept (at $\lambda = 450$ nm) and gradient values of the n^{th} order cumulant versus wavelength plot shown in Fig. 5.6. Substituting the constant cumulant terms in Eq. (5.3.1) with that expressed in Eq. (5.4.1) gives an expression of attenuation value as a function of wavelength dependent μ_a and μ'_s , which can be written as

$$A(\lambda) = \kappa_0(\lambda) - \sum_{n=1}^{\infty} \kappa_n(\lambda) \frac{(-\mu_a(\lambda)c_m)^n}{n!} \quad (5.4.2)$$

$$= a_0 + b_0\lambda - \sum_{n=1}^{\infty} (a_n + b_n\lambda) \frac{(-\mu_a(\lambda)c_m)^n}{n!} \quad (5.4.3)$$

In this case wavelength pair with the same μ_a cannot be identified directly from the measured attenuation value because the difference between their measured attenuation is non-zero, which can be proved by expressing these differences using Eq. (5.4.3). Assuming that a wavelength pair, i.e. λ_1 and λ_2 , are selected as measurement wavelengths, the difference in their attenuation value is given by

$$A_1 - A_2 = b_0(\lambda_1 - \lambda_2) - \sum_{n=1}^{\infty} (a_n + b_n\lambda_1) \frac{(-\mu_{a1}c_m)^n}{n!} + \sum_{n=1}^{\infty} (a_n + b_n\lambda_2) \frac{(-\mu_{a2}c_m)^n}{n!} \quad (5.4.4)$$

where A_1 and μ_{a_1} represent $A(\lambda_1)$ and $\mu_a(\lambda_1)$, respectively. If the μ_a of this wavelength pair have the same value ($\mu_{a_1} = \mu_{a_2}$), Eq. (5.4.4) can be simplified to Eq. (5.4.5) which shows that its value is a non-zero.

$$A_1 - A_2 = b_0(\lambda_1 - \lambda_2) - \sum_{n=1}^{\infty} b_n(\lambda_1 - \lambda_2) \frac{(-\mu_{a_1} c_m)^n}{n!} \quad (5.4.5)$$

In Eq. (5.4.5) the value of both the wavelengths used (i.e. λ_1 and λ_2) and attenuation terms (i.e. A_1 and A_2) measured from experiments are known, so by normalising Eq. (5.4.5) with the difference between the wavelengths used, it removes the wavelength terms (on right hand side of Eq. (5.4.5)) leaving the unknowns (i.e. μ_a and b_n) on the right hand side as follows:

$$\frac{A_1 - A_2}{\lambda_1 - \lambda_2} = b_0 - \sum_{n=1}^{\infty} b_n \frac{(-\mu_{a_1} c_m)^n}{n!} \quad (5.4.6)$$

Expanding the summation terms in Eq. (5.4.6) gives

$$\frac{A_1 - A_2}{\lambda_1 - \lambda_2} = b_0 + b_1 \mu_{a_1} c_m - b_2 \frac{(\mu_{a_1} c_m)^2}{2!} + b_3 \frac{(\mu_{a_1} c_m)^3}{3!} + \dots \quad (5.4.7)$$

This ratio between the attenuation difference and wavelength separation can be obtained from the gradient value between the selected points on a measured attenuation spectrum, and is represented in the following by m_a . It can also be seen from Eq. (5.4.7) that wavelength pairs with the same μ_a will produce the same m_a value. This is in good agreement with what was shown in Fig. 4.8, where it can be seen that wavelengths whose μ_a are identical have the same gradient (i.e. m_a) in A versus wavelength space.

As mentioned in section 5.3.3 a pre-measurement process is required to identify the

wavelength pairs whose α are identical for each SO_2 . The calculated m_A value given by these wavelength pairs is then processed to determine the wavelength pair that could reproduce the medium's SO_2 using the absorbers' extinction coefficients of the corresponding wavelength pair. This process will be described in the next section.

Similar to the consideration of quantisation in section 5.2.2, if α of a wavelength pair are related by Eq. (5.2.7), substituting μ_{a_1} shown in Eq. (5.3.4) into Eq. (5.4.4) gives

$$A_1 - A_2 = b_0(\lambda_1 - \lambda_2) - \sum_{n=1}^{\infty} (a_n + b_n \lambda_1) \frac{(-\mu_{a_2} c_m - \Delta\mu_a c_m)^n}{n!} + \sum_{n=1}^{\infty} (a_n + b_n \lambda_2) \frac{(-\mu_{a_2} c_m)^n}{n!} \quad (5.4.8)$$

The gradient of this wavelength pair in A versus wavelength space is given by

$$\frac{A_1 - A_2}{\lambda_1 - \lambda_2} = b_0 + b_1 \mu_{a_2} c_m - b_2 \frac{(\mu_{a_2} c_m)^2}{2!} + b_3 \frac{(\mu_{a_2} c_m)^3}{3!} + \dots - \frac{\Delta\mu_a \Delta_{\text{dev}} c_m}{\lambda_1 - \lambda_2} \quad (5.4.9)$$

Here, Δ_{dev} is the $\Delta\mu_a$ dependent size of deviation in the gradient value (of two points on an attenuation spectrum) from the value given by Eq. (5.4.7). For simplicity, only Δ_{dev} given from cumulants up to order $n = 3$ is shown here and is given by:

$$\Delta_{\text{dev}} = \left[\kappa_1(\lambda_1) - \kappa_2(\lambda_1) c_m \left(\frac{\Delta\mu_a}{2} + \mu_{a_2} \right) + \kappa_3(\lambda_1) c_m^2 \left(\frac{(\Delta\mu_a + \mu_{a_2})(\Delta\mu_a + 3\mu_{a_2}) - \Delta\mu_a \mu_{a_2}}{6} \right) \right] \quad (5.4.10)$$

where $\kappa_1(\lambda)$ represents $a_1 + b_1 \lambda$.

5.4.2 Processing an attenuation spectrum

Eq. (5.4.7) and Eq. (5.4.9) show that each wavelength pair yields a m_A value, which can be calculated from the measured attenuation spectrum, while section 5.3.3 mentioned that more than a wavelength pair is collected for each set f_a in the pre-measurement stage. The m_A value given by different combination of wavelength pairs will be analysed to identify the set with the right wavelength pairs. This analytical method is discussed as follows.

5.4.2.1 Approximating the attenuation change of different wavelength pairs

It can be seen from Eq. (5.4.7) that the infinite sum of terms used in expressing the gradient value (in A versus wavelength space) is taking the form of Taylor series expansion of an exponential function with the n^{th} coefficient is given by the gradient of the n^{th} cumulant versus wavelength plot (b_n). On the contrary, Eq. (5.4.9) shows that a set of different wavelength pairs with random and large Δ_{dev} deters the produced m_A versus μ_a (in this work α is used instead as T_a is an unknown) relationship from following an exponential curve. Therefore, a possible solution to determine the right wavelength pairs is by analysing the shape of the calculated m_A versus α given by different group of wavelength pairs.

The conformity of the calculated m_A versus α relationship to an exponential curve can be determined via a nonlinear fitting of a reference curve to the calculated m_A versus α plot. This reference curve is represented by m'_A and is expressed as follows:

$$m'_A = \exp(a + b\alpha) \quad (5.4.11)$$

where a and b are the fitting parameters used to approximate the coefficient of the terms

in Eq. (5.4.7). While the use of $\exp(b\alpha)$ may be sufficient to approximate the m_A versus α relationship shown in Eq. (5.4.7), the parameter a is included in this model to provide an extra degree of freedom in the fitting process. Expanding the exponential term in Eq. (5.4.11) gives

$$m'_A = \left(1 + a + \frac{a^2}{2} + \frac{a^3}{3!} + \dots\right) + \left(b + ab + \frac{a^2b}{2} \dots\right)\alpha + \left(b^2 + ab^2 + \dots\right)\frac{\alpha^2}{2!} + \dots \quad (5.4.12)$$

Eq. (5.4.11) can sufficiently be used as the reference model because, unlike the polynomial equation, it includes the sum of infinite series. However, Eq. (5.4.11) is not an exact representation of Eq. (5.4.7) as Fig. 5.6 shows that different gradients, which are approximated by coefficients in Eq. (5.4.12), should be measured.

Demonstration of the evaluation model's performance

The adequacy of using this model is investigated using the attenuation spectrum of a medium with wavelength dependent μ'_s and when this medium's SO_2 is 80% shown in Fig. 4.14 (middle plot). This attenuation spectrum and the corresponding wavelength dependent α values are plotted in the lower left and lower right panels of Fig. 5.7. Shown in the upper right panel of this diagram is the m_A versus mean α relationship given by the wavelength pairs collected when $\text{SO}_2^* = 80\%$ and the evaluation curve produced by fitting of the calculated m_A versus mean α relationship using the model in Eq. (5.4.11). The variable α in Eq. (5.4.11) is given by those used in producing the m_A versus mean α relationship. The reason mean α is used has been explained in section 5.3.4. The non-zero m_A means that a different A is measured using each wavelength pair. Taking the data of 465 nm and 527 nm (indicated by gray circle and dashed lines in Fig. 5.7),

which is one of the right wavelength pairs as an example, Fig. 5.7 (lower left panel) shows that even though these wavelengths have a similar α value, a large and non-zero ΔA is measured. This attenuation difference is due to the effect of wavelength dependent μ'_s on the measured attenuation, giving a m_A value (indicated by gray solid line), which varied with the mean α of the wavelength pair, as shown in Eq. (5.4.7). Notice that the calculated

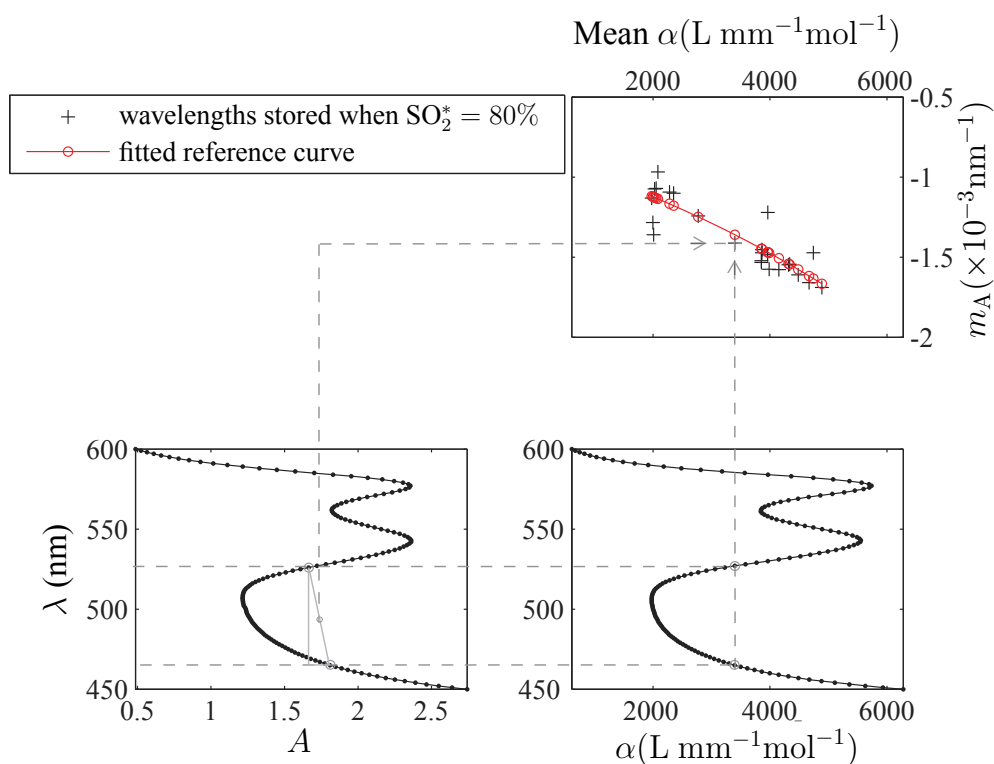


Figure 5.7: (bottom left and right) The attenuation and α spectra when the medium's $\text{SO}_2 = 80\%$. (top right) The m_A versus mean α given by all the right wavelength pairs (plus symbol) and the fitted reference curve (open circle red line) is drawn as a guide. The data of one of the right wavelength pairs: 465 nm and 527 nm selected for discussion in the text are marked by gray circle and dashed line.

m_A versus the mean α of each collected wavelength pair shown in Fig. 5.7 (top right) is, as expected from the derivations in section 5.4.1, following an exponential curve, which

can be reasonably approximated by the fitted reference curve (shown as the open circle red line), but a noticeable number of outliers in the data can be seen from this plot. The presence of these outliers can be understood from the fact that these wavelength pairs are collected on the basis that the produced absolute ΔSO_2 is less than 0.5% (under a certain SO_2^*), the non-zero $|\Delta\text{SO}_2|$ is given from a wavelength pair with $\Delta\alpha \neq 0$, producing m_A value that deviates from following an exponential curve as evident from Eq. (5.4.9).

5.4.2.2 The optimal wavelength pairs and their attenuation response

From the discussion of section 5.2.2 and section 5.4.1, small difference in the α (i.e. $\Delta\alpha$) of the right wavelength pairs identified for an f_a^* will be calculated when this f_a^* matches the medium's f_a . The $\Delta\alpha$ values produced by this set of wavelength pairs will be considerably smaller than that given by the wavelength pairs collected during other f_a^* . The non-zero $\Delta\alpha$ is discussed in section 5.2.2 as the result of the discrete sampling interval of α spectra that are used in this work. These wavelength pairs would produce a m_A versus mean α plot that can be fitted with the model shown in Eq. (5.4.11) with the least error. Conversely, the group with wavelength pairs stored during other f_a^* have large and different $\Delta\alpha$ values and are expected to produce a m_A versus α relationship that deviates significantly from that of an exponential. It must also be mentioned that even though the use of other T_H value in the simulation of attenuation data modifies the range of μ_a and A values, it does not affect the performance of the described method. This is because the overall trend of m_A versus mean α remains unaltered.

Therefore, by evaluating the differences between the calculated m_A versus α plot and the fitted reference curve in Eq. (5.4.11), the group containing all the right wavelength pairs can be identified as a group which produced the least difference between the two

curves. This will be demonstrated graphically in the next section.

The technique described above involves analysing the gradients of different wavelength pairs in A versus wavelength space to identify the right wavelength pairs and to reproduce the true f_a , so it is termed here as the *gradient processing* technique. A summary of the steps and processes involved in determining the wavelength pairs which are able to recover the true f_a value in different kinds of medium considered in this study is shown in Fig. 5.8.

5.4.3 Results and discussion

In the following demonstration, the attenuation spectrum shown in Fig. 5.7 (bottom left) given from a wavelength dependent scattering-absorbing medium is used as an example of measured data to investigate the performance of the method described in section 5.4.2.1. The extinction coefficients of the medium's absorbers used in producing this attenuation spectrum are shown in Fig. 2.3, and this medium has $T_H = 58 \mu\text{mol L}^{-1}$ and $\text{SO}_2 = 80\%$. The groups of wavelength pairs stored during different SO_2^* (i.e. f_a^* term in section 5.3.3) are used to produce m_A versus mean α plots. Each of these plots is then fitted using the reference model shown in Eq. (5.4.11) as previously demonstrated in Fig. 5.7, the sum of the absolute error between the calculated plot and fitted reference curve is calculated and denoted in the following by E_{fit} .

A plot of E_{fit} values given by different groups of wavelength pairs is shown in Fig. 5.9(a), these E_{fit} values are plotted on a log scale for clarity. The SO_2 value during which the wavelength pairs are stored, SO_2^* , are shown on the x-axis. Fig. 5.9(a) shows that E_{fit} has a minimum value when $\text{SO}_2^* = 80\%$, this suggests that wavelength pairs stored during

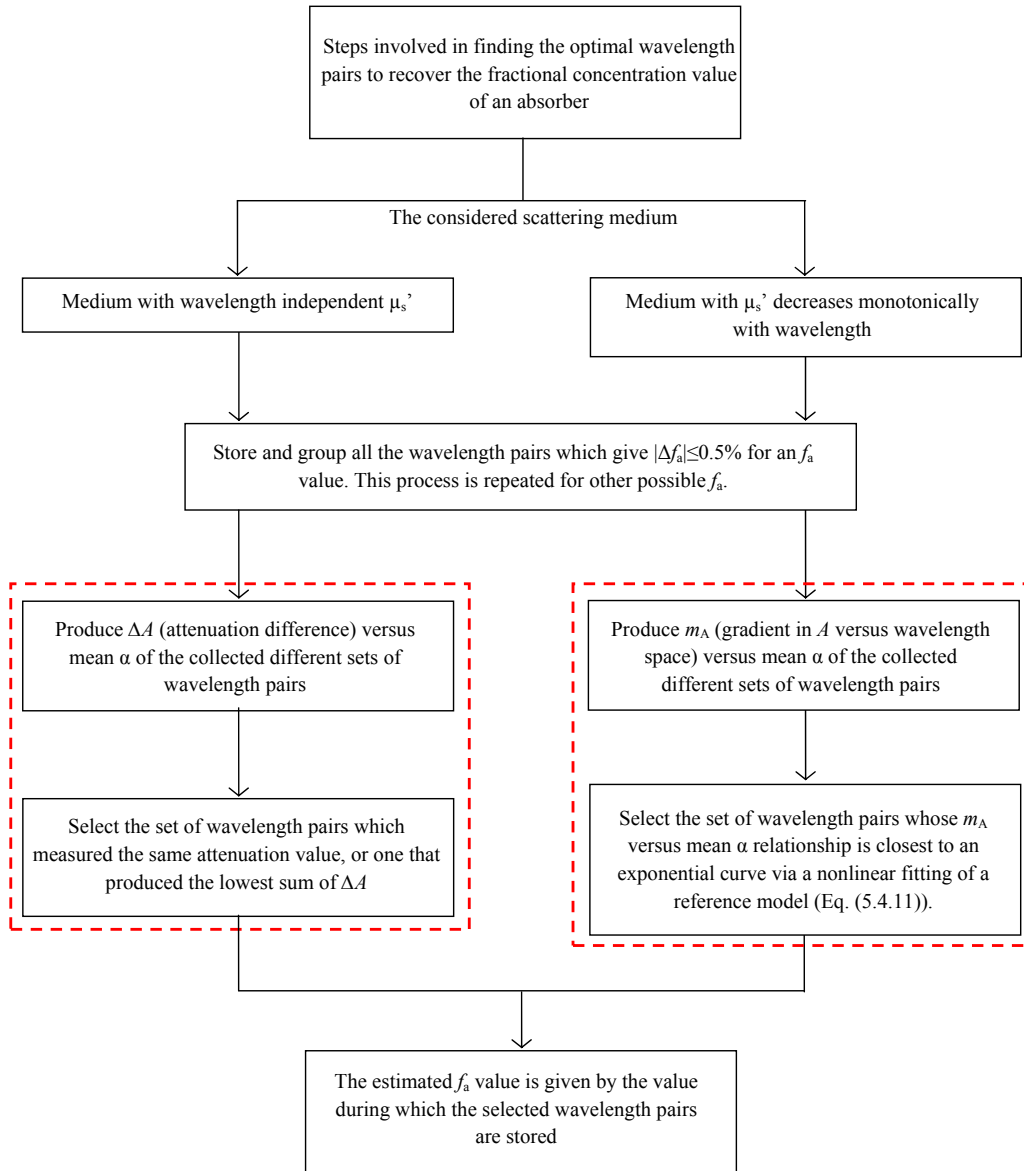


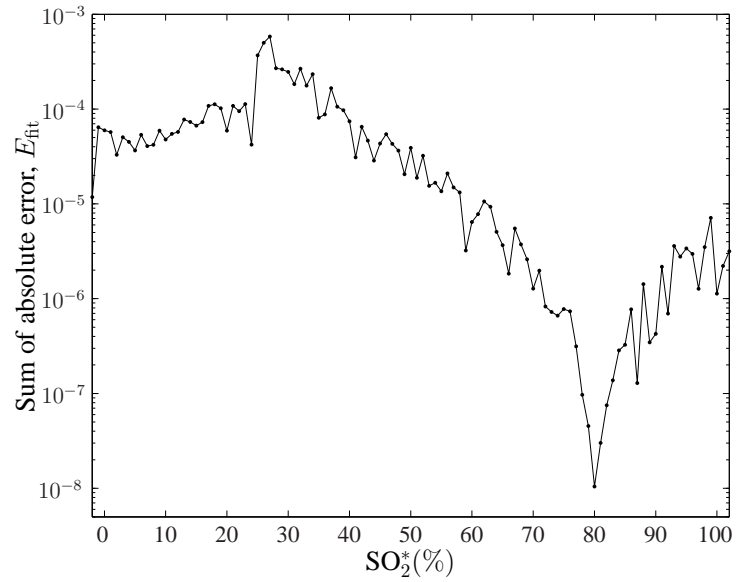
Figure 5.8: Steps involved in finding the right wavelength pairs (enclosed by red-dashed box) to recover the true fractional concentration value of an absorber in different kinds of scattering medium considered in this study.

$SO_2^* = 80\%$, which produced $SO_2 = 80\% \pm 0.5\%$, are the group containing all the right wavelength pairs. As the SO_2 value used in producing the attenuation spectrum shown in Fig. 5.7 (bottom left) is given by 80% , this confirmed the validity of using this approach to recover the true f_a value for the case considered herein.

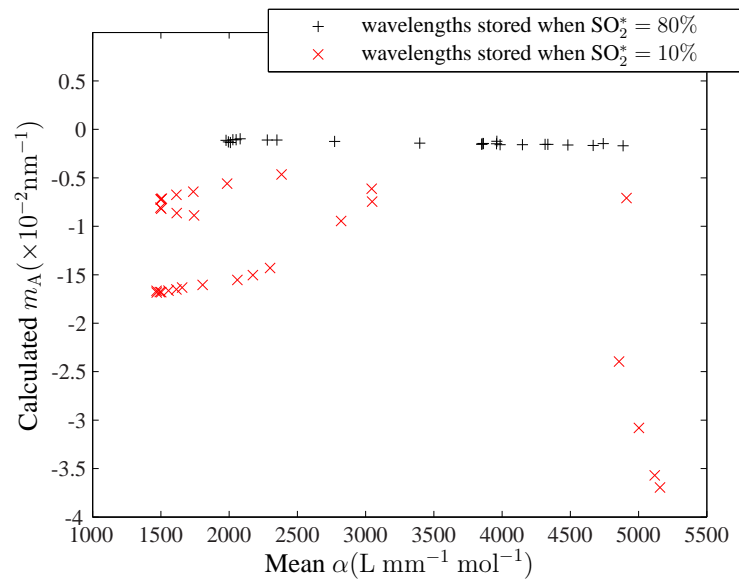
The ability of this technique to identify the group with all the right wavelength pairs can be understood from Fig. 5.9(b). It is shown that the calculated plot (dark plus symbol) followed an exponential shape, which can be fitted reasonably well using the reference model in Eq. (5.4.11). The fitted evaluation curve on the produced relationship is previously shown in Fig. 5.7 (top right). The overall Δ_{dev} of wavelength pairs stored during $SO_2^* = 80\%$, although it is non-zero due to the sampling resolution of the employed spectra, is considerably smaller than the value produced by those collected during other SO_2^* .

The conformity of the m_A versus α relationship produced by the right wavelength pairs to an exponential curve compared to that given by other set of wavelength pairs is demonstrated by taking the calculated plot produced by the wavelength pairs collected when $SO_2^* = 10\%$ as an example of those whose α values are related by large and random $\Delta\alpha$ values when the medium's $SO_2 = 80\%$. These wavelength pairs produce randomly scattered points on m_A versus mean α plot shown in Fig. 5.9(b) (indicated by red cross symbol), which apparently did not follow an exponential trend.

The result in Fig. 5.9 shows that the described technique works reasonably well in recovering the true SO_2 value, so it is interesting to extend this investigation and apply this method on the attenuation spectrum measured when a medium has a different SO_2 value. To do so, the TPSFs shown in Fig. 4.7 are used. The medium's absorbers' extinction coefficients and the total concentration value are the same as that used for demonstration



(a)



(b)

Figure 5.9: (a) The calculated E_{fit} versus SO_2^* . (b) The calculated m_A versus mean α plots of the group with the right wavelength pairs (stored when $\text{SO}_2^* = 80\%$) and wavelength pairs collected when $\text{SO}_2^* = 10\%$.

in Fig. 5.9, and the attenuation spectrum for each SO_2 used in this study is given from Eq. (5.2.12). These attenuation spectra are used to find the medium's SO_2 , the error

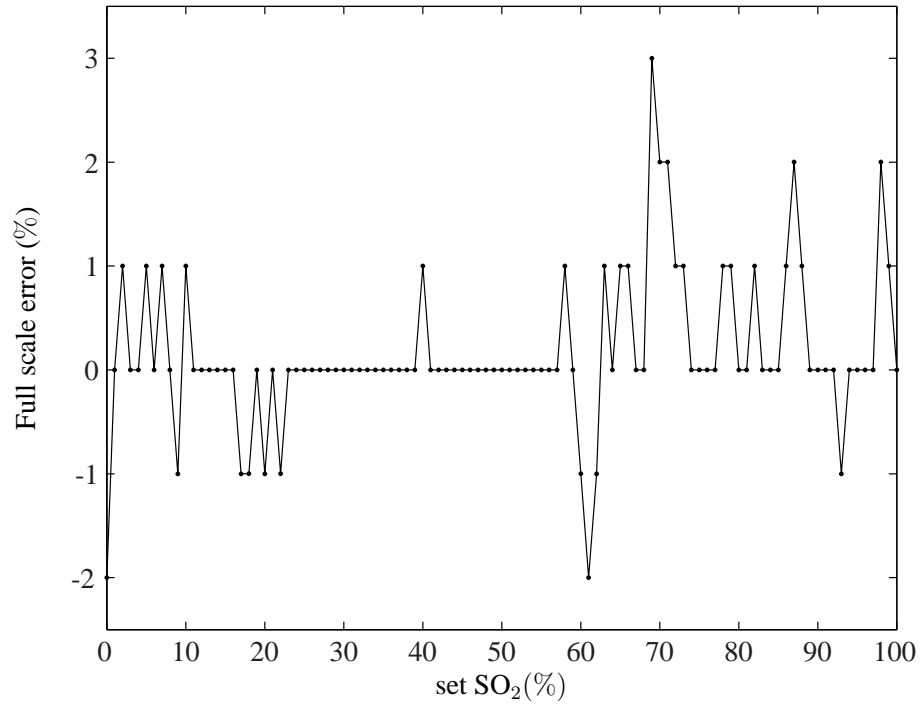


Figure 5.10: Full scale error in the estimated value, ΔSO_2 , versus the set SO_2 . The sampling resolution of the employed spectra is 1 nm. The maximum error of 3 % is observed when the set $\text{SO}_2 = 69\%$.

between the estimated and true SO_2 are calculated and plotted in Fig. 5.10. The reason the calculated values appeared discretised is that the estimated value is given by the discrete SO_2^* value during which the selected group of wavelength pairs are stored.

Fig. 5.10 shows that $\Delta\text{SO}_2 = 3\%$ is the maximum error in the value estimated using this method and this error is observed when attenuation spectrum for SO_2 of 69% is processed. This error can be understood by inspecting the plot of the calculated E_{fit} versus SO_2^* produced during the analysis of this attenuation spectrum shown in Fig. 5.11(a). It can be seen that the minimum E_{fit} value is given by the group of wavelength pairs stored

when $\text{SO}_2^* = 72\%$. An investigation of the source of this error begins by plotting the calculated m_A versus α relationship given by the wavelength pairs collected when SO_2^* is 69% and 72% shown in Fig. 5.11(b) (indicated by dark plus and red cross symbol, respectively). A comparison between these relationships reveals that a small number of significant outliers in the plot given by wavelength pairs collected when $\text{SO}_2^* = 69\%$ could possibly be the reason for this error as they impede a proper evaluation of the m_A versus α relationship using the reference model shown in Eq. (5.4.11). The reason these outliers are observed can be found in section 5.4.2. In this case, this error can be minimised by either reducing the $|\Delta\text{SO}_2|$ limit or by increasing the sample size, or both. Even though a decrease in the range of acceptable $|\Delta\text{SO}_2|$, which is produced by wavelength pairs with an overall smaller $\Delta\alpha$, may theoretically improve the accuracy of the value estimated using this approach (via a decrease in the number of significant outliers on the plot), it should be without sacrificing the adequacy of data points available for the analysis. Taking the wavelength pairs collected when $\text{SO}_2^* = 72\%$ as an example, these wavelength pairs would, in theory, produce m_A versus α relationship that do not follow an exponential curve when the medium's SO_2 is not 72%, so the number of significant outliers is expected to increase when more data points are used. The validity of this and the error in the estimated value when spectra with a higher resolution are used are investigated in the following.

To investigate if the sample size is the source of the error in Fig. 5.10, the number of right wavelength pairs, i.e. the data points on the m_A versus mean α plot, can be increased through the linear interpolation of extinction coefficients and attenuation data to produce spectra with a sampling resolution of 0.5 nm and the right wavelength pairs are re-identified through the process described in section 5.3.3. The approach described earlier is then used on the interpolated attenuation spectra to give an estimate of the SO_2 .

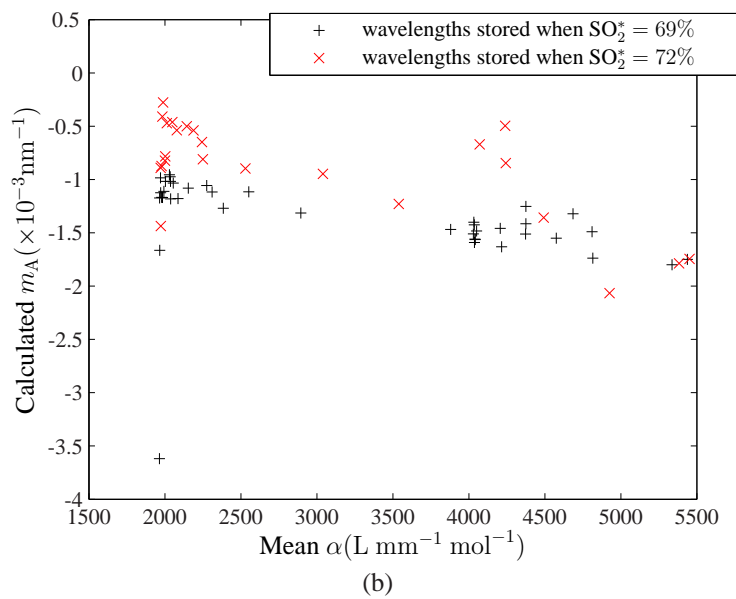
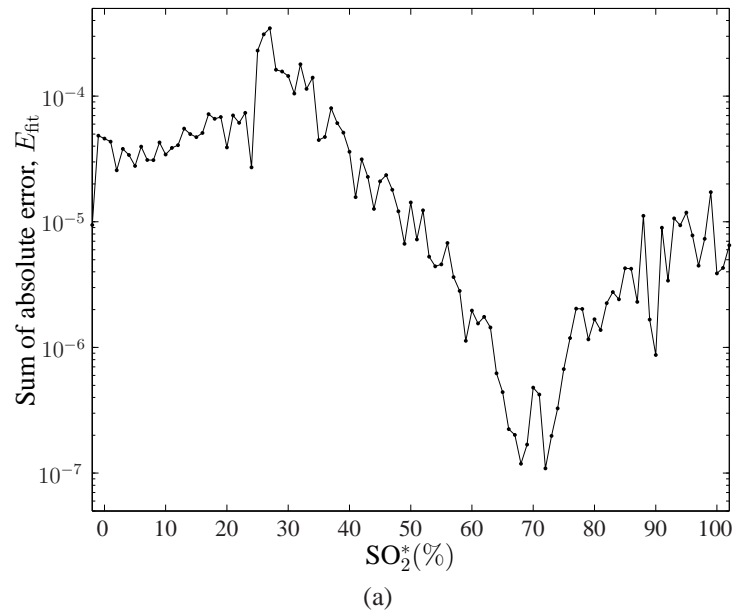


Figure 5.11: (a) The plot of the calculated E_{fit} versus SO_2^* produced when processing the attenuation spectrum for $\text{SO}_2 = 69\%$. (b) The calculated m_A versus mean α relationships of wavelength pairs gathered when SO_2^* is 69% and 72% are indicated by plus and cross symbols, respectively.

The full scale error in the estimated SO_2 value is calculated and shown in Fig. 5.12. This plot showed that there are significant improvements in the accuracy of the estimated SO_2 when a smaller sampling interval is employed. This result is obtained when no changes are made on the tolerance range of $|\Delta\text{SO}_2|$. This is because the decrease in sampling interval led to an increase in the number of collected wavelength pairs (due to their ability to produce $|\Delta f_a| \leq 0.5\%$ under a f_a^*). Consequently, more data points on m_a versus α plots are considered in the fitting process before the E_{fit} values are calculated and compared. This reduces the uncertainties in the estimation of SO_2 , so increasing the accuracy of the estimated value.

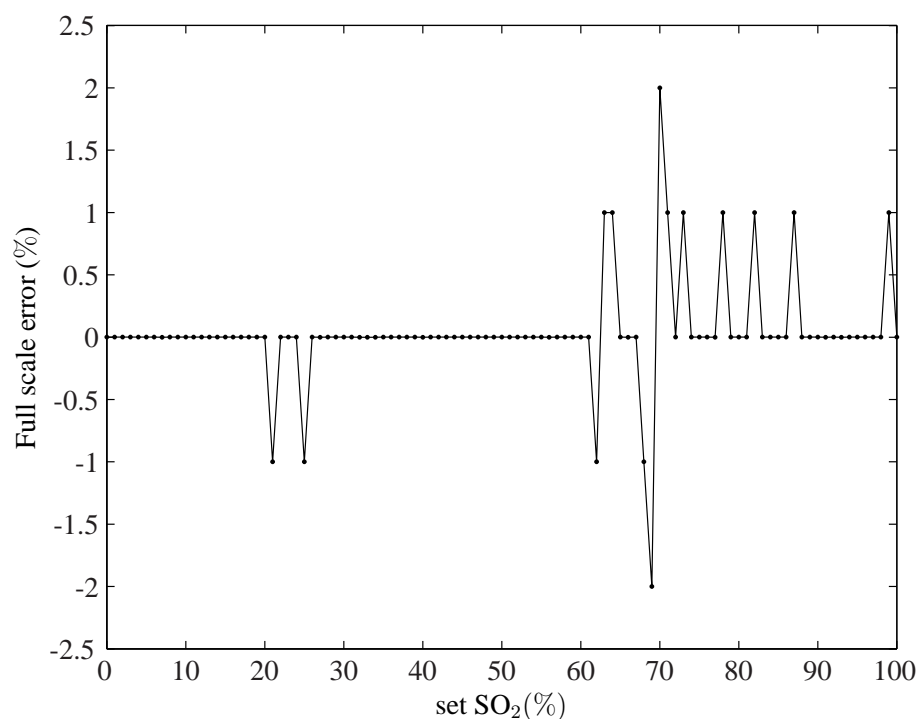


Figure 5.12: Full scale error in the estimated value, ΔSO_2 , versus actual SO_2 when the sampling resolution of the employed spectra is 0.5 nm.

Fig. 5.10 and Fig. 5.12 show that a non-zero error is obtained at certain SO_2 for the case

when the medium's μ'_s varies with wavelength. Since the wavelength pairs are selected based on the closest fit in the calculated m_A versus mean α relationship to an exponential, the inadequacy of the reference model used in representing this relationship could be the reason for the observed error. This is because wavelength pairs collected in the pre-experimental stage were based on the calculated f_a , which error falls in the acceptable tolerance range of $\pm 0.5\%$. These wavelength pairs have a non-zero $\Delta\alpha$, producing m_A values which deviate away from an exponential. Therefore, the reference model should account for these variation when assessing the plot given by different groups of wavelength pairs.

5.5 Considering a scattering medium with three absorbers

In the previous sections, the aim was to determine the fractional concentration value of an absorber in different kinds of (considered) scattering media containing two absorbers, but in practice there can be more than two absorbers in a medium. The method developed above is based on the fact that only two absorbers are present in a medium, so it is informative to investigate changes in the data analysis when more than two absorbers are in a medium with wavelength dependent μ'_s and to examine the performance of this method in recovering the f_a value.

5.5.1 Deriving fractional concentration value of different absorbers

Assuming that a wavelength dependent scattering-absorbing medium has three absorbing species, i.e. absorber A, B and C, the medium's absorption is given by absorptivities and

concentration of these absorbers as follows:

$$\mu_a(\lambda) = \varepsilon_A(\lambda)C_A + \varepsilon_B(\lambda)C_B + \varepsilon_C(\lambda)C_C \quad (5.5.1)$$

Here C and ε denote absorber's concentration and extinction coefficient in mol L^{-1} and $\text{L mol}^{-1} \text{ mm}^{-1}$, respectively, while their subscripts represent the corresponding absorber. Eq. (5.5.1) can also be written as

$$\mu_a(\lambda) = \varepsilon_A(\lambda)C_A + \varepsilon_B(\lambda)C_B + \varepsilon_C(\lambda)(T_a - C_A - C_B) \quad (5.5.2)$$

$$= [\varepsilon_A(\lambda) - \varepsilon_C(\lambda)]C_A + [\varepsilon_B(\lambda) - \varepsilon_C(\lambda)]C_B + \varepsilon_C(\lambda)T_a \quad (5.5.3)$$

where T_a denotes the absorbers' total concentration ($T_a = C_A + C_B + C_C$). If f_a and f_b represent the fractional concentration value of absorber A and B, respectively, and are given by

$$f_a = \frac{C_A}{C_A + C_B + C_C} \quad (5.5.4)$$

$$f_b = \frac{C_B}{C_A + C_B + C_C} \quad (5.5.5)$$

Using the expression of f_a and f_b shown in Eq. (5.5.4) and Eq. (5.5.5), rearranging Eq. (5.5.3) provides

$$\mu_a(\lambda) = (\varepsilon_{AC}(\lambda)f_a + \varepsilon_{BC}(\lambda)f_b + \varepsilon_C(\lambda))T_a \quad (5.5.6)$$

where $\varepsilon_{AC}(\lambda)$ represents $\varepsilon_A(\lambda) - \varepsilon_C(\lambda)$. Eq. (5.5.6) can also be written as

$$\mu_a(\lambda) = \alpha T_a \quad (5.5.7)$$

where

$$\alpha = (\varepsilon_{AC}(\lambda)f_a + \varepsilon_{BC}(\lambda)f_b + \varepsilon_C(\lambda)) \quad (5.5.8)$$

Previously it was shown that the f_a value can be recovered using a wavelength pair whose α have the same value. In the case of a medium with three absorbers, however, solving for f_a in Eq. (5.5.6) by means of the relationship in Eq. (5.2.3) requires f_b to be known, and vice-versa. Both of the f_a and f_b values are unknowns, so solving for these parameters required data of at least another wavelength pair to give the second relationship of α similar to that shown in Eq. (5.2.3). Otherwise Eq. (5.2.3) would become ill-conditioned as there can be an infinite number of solutions for the value of f_a and f_b .¹³⁴ Intuitively, these f_a and f_b values can be given from a combination of three wavelengths whose α are identical (i.e. $\alpha_1 = \alpha_2 = \alpha_3$), in which more than two simultaneous equations (shown in Eq. (5.2.3)) that are required to derive f_a and f_b can be deduced from these α . Among these relationships are:

$$\alpha_1 = \alpha_2 \quad (5.5.9)$$

$$\alpha_1 = \alpha_3 \quad (5.5.10)$$

Substituting Eq. (5.5.8) into Eq. (5.5.9) and Eq. (5.5.10), and rearranging these expres-

sions provides

$$(\varepsilon_{AC_1} - \varepsilon_{AC_2})f_a + (\varepsilon_{BC_1} - \varepsilon_{BC_2})f_b + \varepsilon_{C_1} - \varepsilon_{C_2} = 0 \quad (5.5.11)$$

$$(\varepsilon_{AC_1} - \varepsilon_{AC_3})f_a + (\varepsilon_{BC_1} - \varepsilon_{BC_3})f_b + \varepsilon_{C_1} - \varepsilon_{C_3} = 0 \quad (5.5.12)$$

where ε_{AC_1} denotes $\varepsilon_A(\lambda_1) - \varepsilon_C(\lambda_1)$. Solving Eq. (5.5.11) and Eq. (5.5.12) simultaneously gives f_a and f_b expressed in terms of the extinction coefficients of the present absorbers given by

$$f_a = \frac{\varepsilon_{B_1}(\varepsilon_{C_2} - \varepsilon_{C_3}) + \varepsilon_{B_2}(\varepsilon_{C_3} - \varepsilon_{C_1}) + \varepsilon_{B_3}(\varepsilon_{C_1} - \varepsilon_{C_2})}{(\varepsilon_{B_{12}} - \varepsilon_{C_{12}})(\varepsilon_{C_{13}} - \varepsilon_{A_{13}}) + (\varepsilon_{A_{12}} - \varepsilon_{C_{12}})(\varepsilon_{B_{13}} - \varepsilon_{C_{13}})} \quad (5.5.13)$$

and

$$f_b = \frac{\varepsilon_{A_1}(\varepsilon_{C_2} - \varepsilon_{C_3}) + \varepsilon_{A_2}(\varepsilon_{C_3} - \varepsilon_{C_1}) + \varepsilon_{A_3}(\varepsilon_{C_1} - \varepsilon_{C_2})}{(\varepsilon_{B_{12}} - \varepsilon_{C_{12}})(\varepsilon_{C_{13}} - \varepsilon_{A_{13}}) + (\varepsilon_{A_{12}} - \varepsilon_{C_{12}})(\varepsilon_{B_{13}} - \varepsilon_{C_{13}})}, \quad (5.5.14)$$

where,

$$\varepsilon_{B_{xy}} = \varepsilon_B(\lambda_x) - \varepsilon_B(\lambda_y).$$

In the next section, an approach that can be used to determine a set of combinations of three wavelengths with the same α based on the measured attenuation spectrum is described, and the medium's f_a and f_b values are recovered using Eq. (5.5.13) and Eq. (5.5.14), respectively. The validity of this and the accuracy of the estimated values are also investigated.

5.5.2 Gradient response of different wavelength pairs

It was discussed in section 5.4.1 that each wavelength pair gives a m_a value, which will be analysed to find the medium's f_a value, but if three absorbers were present in a medium, at least data at three wavelengths (i.e. λ_1 , λ_2 and λ_3) are required in the estimation of f_a and f_b values as shown in Eq. (5.5.9) - Eq. (5.5.14). In this work, these wavelengths are arranged to provide a λ_1, λ_2 pair and a λ_1, λ_3 pair, producing two m_a values as shown in section 5.4.1.

Assuming that the cumulants of TPSFs measured from a wavelength dependent scattering medium when $\mu_a = 0 \text{ mm}^{-1}$ are as expressed in Eq. (5.4.1), the linear variation in these cumulants with wavelength gives an expression of attenuation shown in Eq. (5.4.3). Based on this equation, and given that the α of each wavelength pair (i.e. λ_1, λ_2 pair and λ_1, λ_3 pair) are related by Eq. (5.5.9) and Eq. (5.5.10) to give μ_a of the same value via Eq. (5.5.7), the m_a value given by these wavelength pairs can be expressed as:

$$\frac{A_1 - A_2}{\lambda_1 - \lambda_2} = b_0 - \sum_{n=1}^{\infty} b_n \frac{(-\mu_{a1} c_m)^n}{n!} \quad (5.5.15)$$

$$\frac{A_1 - A_3}{\lambda_1 - \lambda_3} = b_0 - \sum_{n=1}^{\infty} b_n \frac{(-\mu_{a1} c_m)^n}{n!} \quad (5.5.16)$$

which is as demonstrated in section 5.4.1 and shown in Eq. (5.4.6). Since these wavelength pairs have the same μ_a value, it is immediately apparent from Eq. (5.5.15) and Eq. (5.5.16) that the same m_a versus α plot will be produced by λ_1, λ_2 pair and λ_1, λ_3 pair. Hence the optimal choice of three-wavelength combination can be identified by

means of comparing the m_A versus α produce by the wavelength pairs (arranged from a combination of three-wavelength), removing the necessity of using an evaluation model as discussed in section 5.4.2. This will be described later in section 5.5.4. But the availability of three wavelengths that followed Eq. (5.5.9) and Eq. (5.5.10) is limited by the resolution of the employed spectra as μ_a of these wavelengths are more realistically to be related by

$$\mu_{a_1} = (\alpha_2 + \Delta\alpha_{12})T_a = \mu_{a_2} + \Delta\mu_{a_{12}} \quad (5.5.17)$$

$$\mu_{a_1} = (\alpha_3 + \Delta\alpha_{13})T_a = \mu_{a_3} + \Delta\mu_{a_{13}} \quad (5.5.18)$$

where $\Delta\mu_{a_{12}}$ is the difference between μ_a of λ_1 and λ_2 , and $\Delta\mu_{a_{13}}$ is that between μ_a of λ_1 and λ_3 , and $\Delta\mu_{a_{12}} \neq \Delta\mu_{a_{13}}$. Similar to that shown in Eq. (5.4.9), using the relationship between μ_a values of these wavelength pairs shown in Eq. (5.5.17) and Eq. (5.5.18), the gradient of these wavelength pairs in A versus wavelength space, m_A , are given by

$$\frac{A_1 - A_2}{\lambda_1 - \lambda_2} = b_0 - \sum_{n=1}^{\infty} b_n \frac{(-\mu_{a_1} c_m)^n}{n!} + \frac{\Delta\mu_{a_{12}} \Delta_{\text{dev}_{12}} c_m}{\lambda_1 - \lambda_2} \quad (5.5.19)$$

$$\frac{A_1 - A_3}{\lambda_1 - \lambda_3} = b_0 - \sum_{n=1}^{\infty} b_n \frac{(-\mu_{a_1} c_m)^n}{n!} + \frac{\Delta\mu_{a_{13}} \Delta_{\text{dev}_{13}} c_m}{\lambda_1 - \lambda_3} \quad (5.5.20)$$

Here, $\Delta_{\text{dev}_{12}}$ and $\Delta_{\text{dev}_{13}}$ are related to $\Delta\mu_{a_{12}}$ and $\Delta\mu_{a_{13}}$, and the values given from cumulants up to the third order are shown in Eq. (5.4.10).

5.5.3 Identifying and storing different wavelength combinations

It is shown in Eq. (5.5.9) - Eq. (5.5.14) and section 5.5.2 that a combination of three wavelengths is required to determine the f_a and f_b values in a medium with three absorbers. Similar to the discussion of section 5.3.3, only the combinations of three wavelengths that produce an absolute error (in the estimated f_a and f_b) of $\leq 0.5\%$ for the considered f_a and f_b values will be collected during the pre-processing stage as wavelengths with the same μ_a (i.e. same α) may not be available. Again, the feasibility of identifying these three-wavelength combinations before the measurements is because only the absorbers' extinction coefficient data are required in the estimation of f_a and f_b values shown in Eq. (5.5.13) and Eq. (5.5.14).

All the right three-wavelength combinations are gathered for each f_a and f_b to produce two sets of m_A versus α relationships from each group of three-wavelength combinations during the analysis. This is to increase the amount of data points, so decreasing the uncertainties in the estimation of absorbers' fractional concentration value as discussed in section 5.4.3.

5.5.3.1 Description of the wavelength combinations storing process

Assuming that oxyhaemoglobin (HbO_2), carboxyhaemoglobin (COHb), and deoxyhaemoglobin (Hb) in blood are the absorbers A, B and C, respectively, in Eq. (5.5.1). The molar absorptivities of these absorbers in the wavelength range 450 nm – 600 nm compiled by Zijlstra *et al.*³⁰ are shown in Fig. 5.13. The saturation of haemoglobin with oxygen (i.e. HbO_2) and carbon monoxide (i.e. COHb) are represented by SO_2 and SCO , and can be calculated from Eq. (5.5.13) and Eq. (5.5.14), respectively.

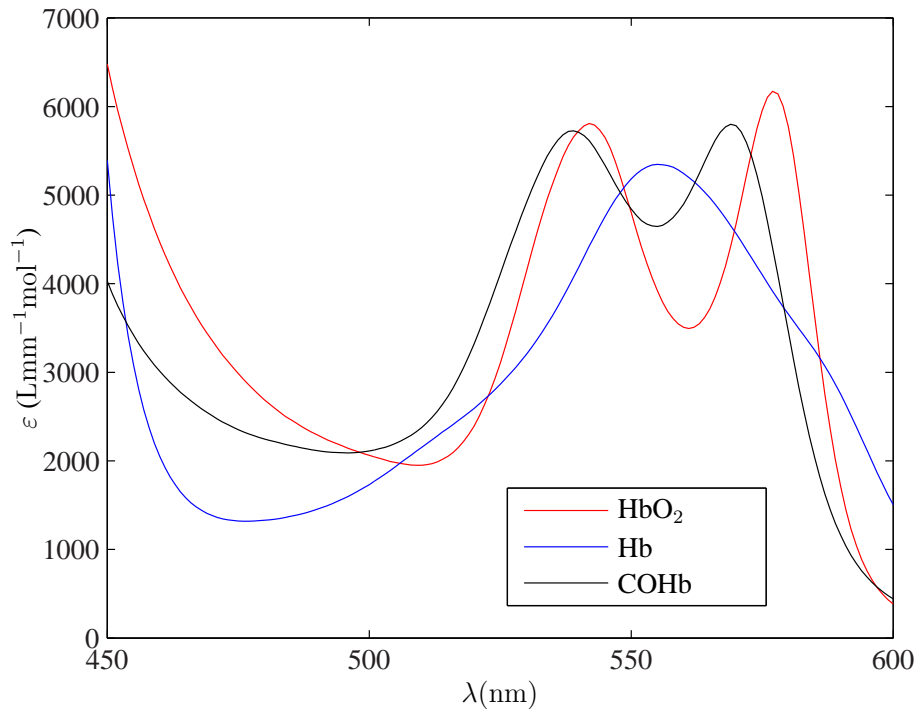


Figure 5.13: The molar absorptivities of oxyhaemoglobin (HbO₂), deoxyhaemoglobin (Hb) and carboxyhaemoglobin (COHb). These data are taken from Zijlstra *et al.*³⁰ (published in Biomedical Optics Research Laboratory-UCL homepage).

An increase in the amount of data points can be achieved by linearly interpolating the extinction coefficient spectra shown in Fig. 5.13, and a sampling resolution of 0.5 nm is used in the following. This is because it was noticed during this work that with the sampling resolution of 1 nm only a combination of three wavelengths is collected for certain f_a and f_b , hindering a proper analysis of the produced m_A versus α relationships.

Using the interpolated extinction coefficient spectra, SO₂ and SCO values given by every combination of three wavelengths are calculated from Eq. (5.5.13) and Eq. (5.5.14), respectively. With SO₂^{*} and SCO^{*} representing the SO₂ and SCO levels during which a combination of three wavelengths is stored, each wavelength combination was grouped by

following the steps described as follows: First, let $|\Delta\text{SO}_2|$ denote the absolute difference between the SO_2^* and the calculated SO_2 (from Eq. (5.5.13)), while $|\Delta\text{SCO}|$ represent the error between SCO^* and the calculated SCO (from Eq. (5.5.14)), the combinations of three wavelengths which produce $|\Delta\text{SO}_2| \leq 0.5\%$ for a particular SO_2 level (i.e. $\text{SO}_2^* = 0\%$ to begin with) are identified.

Next, the SCO calculated from the extinction coefficients of these wavelength combinations with ΔSCO of less than $\pm 0.5\%$ for a particular SCO level (SCO^*) are collected. The calculated SO_2 and SCO values are represented in the following by $\text{SO}_{2(\text{cal})}$ and $\text{SCO}_{(\text{cal})}$, respectively.

This process is repeated for different SCO^* values that are varied from 0% to 102% in 1% increments and the whole process is continued for different SO_2^* (SO_2^* from 0% to 102%), but the summation of SCO^* and SO_2^* can never exceed 102% . For example, if SO_2^* is 30% , the maximum possible analytical value for SCO^* is 72% , therefore only the combinations of three wavelengths which give $|\Delta\text{SCO}| \leq 0.5\%$ for different SCO^* up to $\text{SCO}^* = 72\%$ would be collected.

Finally, the combinations of the three wavelengths collected for each SO_2^* and SCO^* levels (i.e. giving $|\Delta\text{SO}_2| \leq 0.5\%$ and $|\Delta\text{SCO}| \leq 0.5\%$ at this SO_2^* and SCO^*) are stored as a group. The flow diagram of this storing process is summarised in Appendix D.

5.5.4 Determining the optimum group of wavelength combinations

From the discussion of section 5.5.2, the combinations of three wavelengths collected in each group are used to produce two m_A versus mean α relationships. The differences between these curves can be evaluated to identify the group with three-wavelength com-

binations that are able to recover the medium's true SO₂ and SCO values.

Similarly, E_{fit} is used to represent the mean sum of the absolute error between the two m_a versus μ_a plots (given by λ_1, λ_2 pairs and λ_1, λ_3 pairs stored within a group). The selected wavelength combinations will produce $E_{\text{fit}} = 0$ if α of each three-wavelength combination are identical. But if the α of a combination of three wavelengths are related by large and dissimilar $\Delta\mu_{a12}$ and $\Delta\mu_{a13}$ (under a certain f_a and f_b values), there would be a large difference between their calculated m_a . The size of these errors depends on the differences between α (hence μ_a) values of the selected three-wavelength combinations, $\Delta\mu_{a12}$ and $\Delta\mu_{a13}$ shown in Eq. (5.5.19) and Eq. (5.5.20).

In practice, it is unlikely to find any three wavelengths with the same α value for a particular f_a and f_b levels, so a non-zero E_{fit} is expected, and the search for the group with wavelength combinations which produced the lowest E_{fit} value is performed instead. This is because the combinations of three wavelengths that are able to recover SO₂ and SCO with errors of less than 0.5% would have small $\Delta\mu_{a12}$ and $\Delta\mu_{a13}$ values. The right set of three wavelengths can, therefore, be identified as those which produced the smallest difference in their calculated m_a value given from the combination of λ_1, λ_2 pair and λ_1, λ_3 pair.

5.5.5 Demonstration of the technique

A strategy that can be used to recover a medium's true SO₂ and SCO values has been described in section 5.5.4. The validity of this method is demonstrated in the following on an attenuation spectrum of a medium with wavelength dependent μ'_s which gives the TPSFs shown in Fig. 4.7 when medium's $\mu_a = 0 \text{ mm}^{-1}$. For demonstration purposes, the

medium's absorbers shown in Fig. 5.13 with $\text{SCO} = 15\%$, $\text{SO}_2 = 80\%$, and the absorbers total concentration, $T_H = 58 \mu\text{mol L}^{-1}$ are used to give the medium's μ_a (with a spectral resolution of 0.5 nm) from Eq. (5.5.6). Based on the TPSFs and the calculated wavelength dependent μ_a values, this attenuation spectrum is derived from Eq. (5.2.12) and is shown in Fig. 5.14.

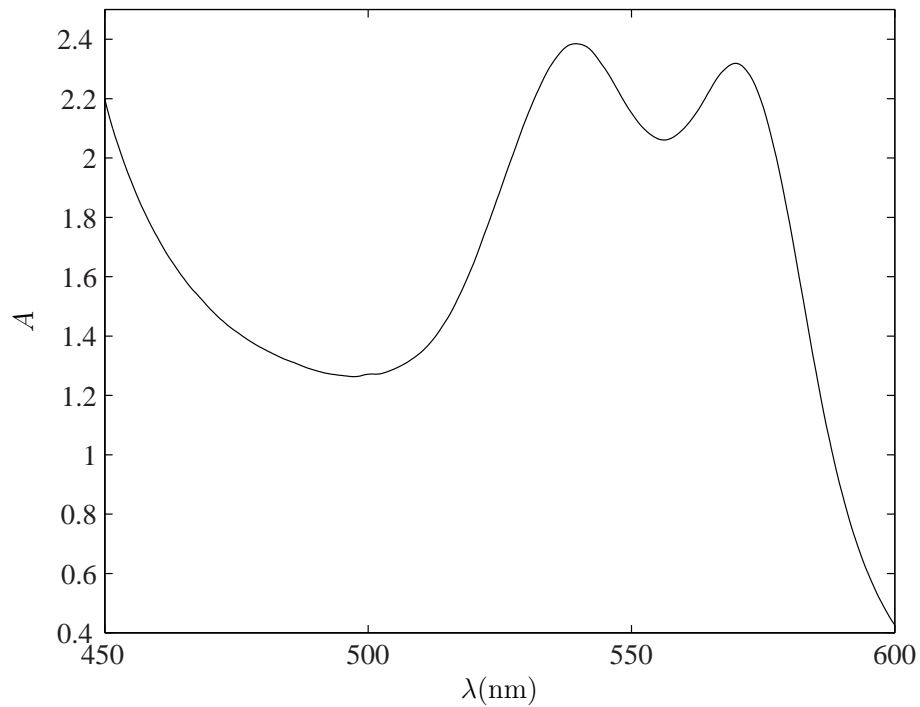


Figure 5.14: The modelled attenuation spectrum given from blood with $\text{SCO} = 15\%$ and $\text{SO}_2 = 80\%$. The variation in the medium's μ'_s with wavelength (in the range of 450 nm – 600 nm) is shown in Fig. 4.5.

The groups of the three-wavelength combinations stored during the pre-processing stage, as described in section 5.5.3, are used in the analysis. The α of each three-wavelength combination used in producing the m_a versus α plots is given by the mean of their α as discussed in section 5.3.2. The SO_2 and SCO used in the calculation of α value from Eq. (5.5.8) are given by the value of SO_2^* and SCO^* during which the corre-

sponding wavelengths are collected.

5.5.5.1 Results and analysis

The calculated E_{fit} given from the groups of wavelength combinations stored at different SO_2^* and SCO^* are shown in Fig. 5.15. For a better illustration, only the E_{fit} calculated from m_A versus mean α curves produced by wavelengths stored for SO_2^* of 0%, 20%, 40%, 60%, 80% and 90% are shown here. The SCO^* value during which these wavelengths are concurrently stored are shown on the x-axis. The maximum summation of SCO^* and SO_2^* is 102%, and no wavelength is collected (during the pre-measurement stage) if their summation has exceeded 102%, which is the reason why some of the plots in Fig. 5.15 appeared to have discontinued after a certain SCO^* .

The E_{fit} given by three-wavelength combinations stored during $\text{SO}_2^* = 80\%$, $\text{SCO}^* = 14\%$ has the lowest value compared to that produced by the wavelength combinations stored during all other SO_2^* and SCO^* levels. This includes those (SO_2^* and SCO^* levels) that are not shown in Fig. 5.15. Thus, wavelength combinations collected during this SO_2^* and SCO^* are expected to reproduce the true SO_2 and SCO . These wavelength combinations produced $\text{SO}_{2(\text{cal})} = 80\% \pm 0.5\%$ and $\text{SCO}_{(\text{cal})} = 14\% \pm 0.5\%$, which agree reasonably well with the $\text{SO}_2 = 80\%$ and $\text{SCO} = 15\%$ that were used in the simulations to produce the spectrum shown in Fig. 5.14.

To demonstrate how this group of wavelength combinations is identified through this process, the m_A versus mean α relationships given by wavelengths stored during $\text{SO}_2^* = 80\%$, $\text{SCO}^* = 14\%$ are shown in Fig. 5.16 (indicated by dark closed and red open circle symbols). The wavelengths stored during $\text{SO}_2^* = 60\%$, $\text{SCO}^* = 15\%$ are arbitrarily selected as an example of the group with wavelength pairs (arranged from the combina-

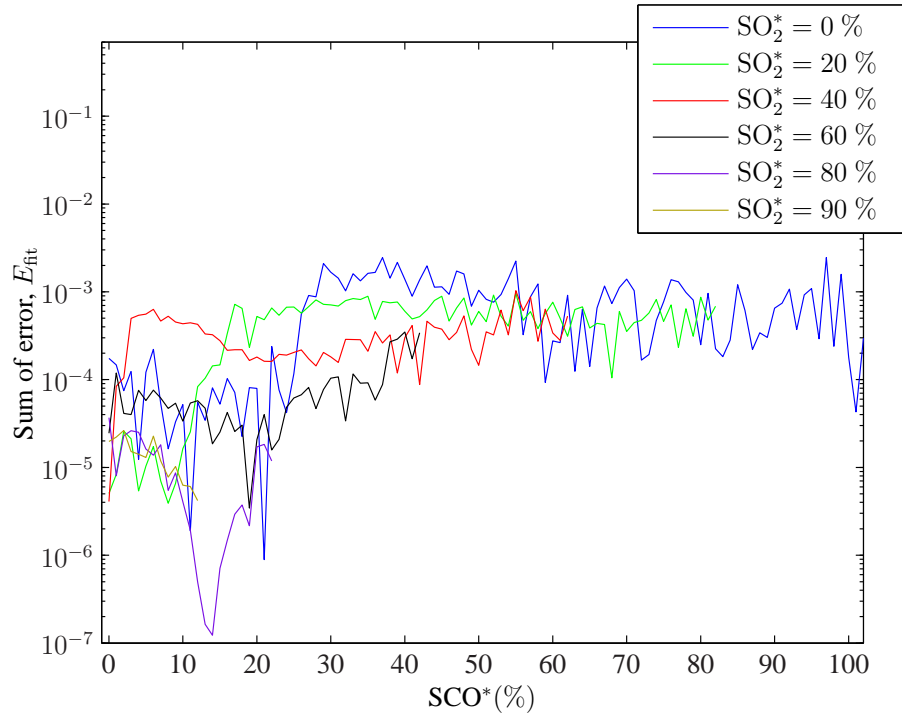


Figure 5.15: The calculated E_{fit} given by the wavelength combinations stored during different SO_2^* and SCO^* levels.

tions of three wavelengths) whose α of each pair are related by a large and random $\Delta\alpha$ value when the true SO_2 and SCO are given by 80% and 15%, respectively. The calculated m_A given by the wavelength pairs from this group are also shown in Fig. 5.16 (blue plus and green cross symbols). These plots show that there are considerably smaller differences between the m_A versus α relationships produced by the group with the right wavelength pairs (dark closed and red open circle symbols). The error E_{fit} is calculated as $1.2 \times 10^{-7} \text{nm}^{-1}$ compared to $E_{\text{fit}} = 2.5 \times 10^{-5} \text{nm}^{-1}$ given by wavelengths collected when $\text{SO}_2^* = 60\%$ and $\text{SCO}^* = 15\%$, where the magnitude of this error has increased to about two folds.

Even though this approach does not consider all the points on the measured attenuation

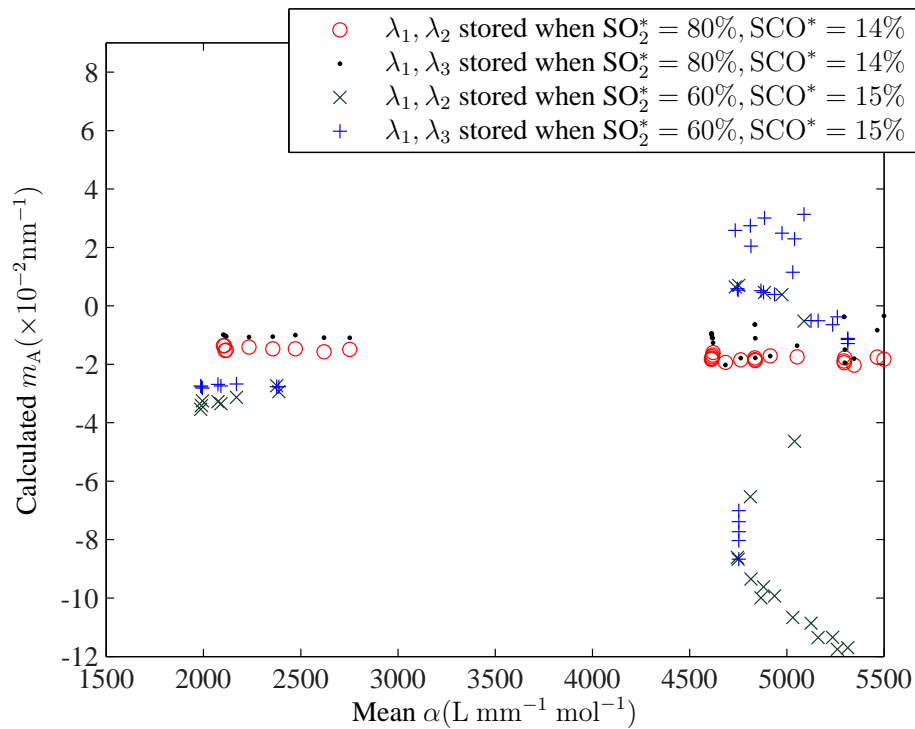


Figure 5.16: The m_A versus mean α relationships of wavelength pairs (arranged from the combinations of three wavelengths) given from the group with the right three-wavelength combinations (stored during $\text{SO}_2^* = 80\%$ and $\text{SCO}^* = 14\%$) and wavelengths stored during $\text{SO}_2^* = 60\%$ and $\text{SCO}^* = 15\%$.

spectrum, attenuations measured at more than one wavelength pair are considered during the process of determining an f_a value. Therefore, this technique is expected to be more resilient to noise than the simultaneous solution of the linear equation models which uses data of only three wavelengths. The robustness of this quantification method to noise will be examined in Chapter 6 when it is compared with another approach that uses data of all the wavelengths in the considered wavelength range.

5.6 The sensitivity analysis and optimum wavelength range

In the previous sections, it was shown that the estimation of an f_a can be achieved by processing the attenuation of different wavelength pairs. The limitation of using this approach in characterising a medium with wavelength dependent μ'_s , however, is that it depends largely on the variation in the calculated m_A with mean α of each wavelength pair. The changes in μ_a range with f_a value differed for different wavelength range as can be seen from the spectra employed for the above demonstrations shown in Fig. 2.3, thus it is interesting to investigate the optimal wavelength range to be used for the analysis of a medium using the described technique and this is discussed in this section.

According to Eq. (5.4.7), if TPSF cumulants change linearly with wavelength, the m_A value given by a wavelength pair with the same μ_a value can be expressed as

$$\frac{A_1 - A_2}{\lambda_1 - \lambda_2} = b_0 + b_1(\mu_{a_1} c_m) - \frac{1}{2!} b_2(\mu_{a_1} c_m)^2 + \frac{1}{3!} b_3(\mu_{a_1} c_m)^3 - \dots \quad (5.6.1)$$

The changes in this m_A value with μ_a can be deduced by differentiating Eq. (5.6.1) with respect to μ_a as follows:

$$\frac{d}{d\mu_{a_1}} \frac{A_1 - A_2}{\lambda_1 - \lambda_2} = b_1 c_m - b_2 \mu_{a_1} c_m^2 + \frac{1}{2} b_3 (\mu_{a_1})^2 c_m^3 - \dots \quad (5.6.2)$$

where it can be seen that the sensitivity of the calculated m_A depends upon the μ_a value of the selected wavelength pair. This μ_a value is related to the absorbers' fractional concentration as shown in Eq. (2.5.3) and Eq. (5.5.6), where changes in f_a value modifies the μ_a value. It is desirable that m_A is sensitive to this variation so that the right wavelength pairs, and hence the true f_a value can be determined.

By referring to the example of absorbers' extinction coefficient spectra shown in Fig. 2.3, the ε of absorbers in the wavelength range 650 nm to 1000 nm (Red to Near Infrared region, R-NIR) are comparatively smaller and constant than those in 450 nm – 600 nm. Therefore, the μ_a given from any wavelength in R-NIR does not show a noticeable change in its value as the f_a varied. This is in contradiction to the presumption on which the approach described above is founded, where it is assumed that wavelength pairs which failed to reproduce the true f_a value would have a large $\Delta\mu_a$. In this case, $\Delta\mu_a$ is small hence small variation in the gradient values as shown in Eq. (5.3.5) are produced even by the groups with the wrong wavelength pairs, which renders the identification of the group with the right wavelengths difficult. For this reason, if the absorptivities of the medium absorbers are as shown in Fig. 2.3, the quantification approach used in this chapter would work best at wavelength range 450 nm – 600 nm where the μ_a dependent variation in attenuation value, which varies with the medium's f_a , is the most pronounced.

5.7 Conclusion

This chapter has presented another analytical technique which can be used to find the fractional concentration value of absorbers in different types of scattering media considered in this study with reasonable accuracy (maximum error of 3% depending upon the resolution of the employed spectra). Unlike the method discussed in Chapter 4, the approach used in this chapter offers the flexibility of choosing different wavelength combinations which produce low error as the medium true f_a changes.

It was shown in section 5.3 that if a medium has constant μ'_s , the true f_a can be recovered by a wavelength pair which measured the same attenuation value. If a medium's μ'_s

changes with wavelength, the right wavelength pairs (collected during the pre-processing stage) can be identified by analysing the gradient value of these wavelength pairs on the measured attenuation spectrum.

The drawback of using this approach is that the accuracy of the estimated value depends largely on the relationship between gradients of the points in A versus wavelength space and the mean α of these chosen wavelengths. Thus, insufficiency either in the number of the collected wavelengths (due to the large sampling interval of the employed spectra) or the employed curve evaluation model may hinder a proper evaluation of the m_A versus α plots. Besides, this technique depends on the difference between μ_a of different wavelength pairs, $\Delta\mu_a$, in differentiating the group with the right wavelength pairs from that containing the wrong ones. This is also the reason why the wavelength range where μ_a variation is small when f_a changes is not the optimum choice of wavelengths for this method.

The advantage of using this approach, however, is that it does not consider all the wavelengths; instead, only the right wavelength pairs collected at different f_a (and f_b) level are used in the analysis. These wavelength pairs can be collected during the pre-processing, reducing the amount of time required during the processing of the measured attenuation. Most importantly, other than the need to have an attenuation model to help understanding how the measured attenuation varies with the medium's μ'_s , this technique does not require any model in deducing the fractional concentration value of absorbers present in the scattering media considered in this work. This is because finding a suitable attenuation model via either heuristic search method or analytical solution of photon transport model, which performance is restricted to certain media or geometries, to accurately determine the f_a value can be challenging. The performance of the method described in this chapter

is, on the contrary, not subject to the inadequacy of the defined model at describing the absorption-scattering processes of photons propagate in a medium, and its application is not limited to any specific medium. The estimation of the absorbers' fractional concentration value is based only on the absorbers' extinction coefficient values of the selected wavelengths. While this method considers only the theoretically deduced relationship of certain wavelength pairs to recover the f_a value, another method that uses data of all wavelengths and a fitting routine to find the true f_a value is described in Chapter 6.

Chapter 6

Nonlinear fitting of attenuation spectrum and its comparison with other techniques

6.1 Introduction

Given that a sample has a range of possible f_a value and a known behaviour of how scattering varies with wavelength, the search of a generic combination of wavelengths for a specific measurement system, which produced the lowest mean error in the values estimated using a linear equation model, was described in Chapter 4. The estimation of an absorber's fractional concentration value in this medium is based only on the measured attenuation and absorbers' extinction coefficients for the selected three wavelengths, so the accuracy of this value depends critically on the selection of wavelength combination. The method described in Chapter 5 considered and analysed only the attenuation value of

different wavelength pairs selected in the pre-measurement stage during the estimation of the f_a value. It was also shown that the accuracy of the estimated value depends on the number of collected wavelength pairs.

A common practice in the spectroscopic study of a scattering medium is to use forward data (for the solution of an inverse problem) derived from photon transport models to fit to the measured spectrum to extract the optical properties of a medium.^{12,16,45,56} Alternatively, different curve fitting models, which described the attenuation of light depending on the medium's optical properties, can be used to recover the f_a value through the fitting of these models to the measured attenuation spectrum. Possible models include Kubelka Munk and the power law model described in section 2.3.2 and section 2.5.4 respectively, and the version of MLBL used by Alabboud²⁶ discussed in section 2.5.1.1.

An exponential model, which is not developed from photon transport model, was briefly introduced in section 2.5.5 as a fitting model that can be used to recover the f_a value when it was used to fit to the data from continuous intensity measurements.²⁷ Unlike the case when the diffusion approximation discussed in section 2.3.1 or Kubelka Munk model is used, the validity of this model is not limited to any type of medium geometry or experimental system. This model fitted relatively well to the measured attenuation spectrum,²⁷ implying that it can adequately describe the absorption and scattering processes of photons in the medium which give the corresponding attenuation spectrum. It may, therefore, be of value to try and understand the physical meaning of parameters and terms in this model by comparison with the cumulant based attenuation model shown in Eq. (2.5.17) whose terms have definite physical significance. The other objective is to find an attenuation model that is more suitably used to reproduce the attenuation spectrum (hence recovering the medium's f_a) measured from the type of medium considered in this

study.

To achieve that, this chapter begins with a more detailed discussion of the exponential model in section 6.2, while the role of cumulants and the connection between these cumulants in describing the measured attenuation are discussed in section 6.3.1. This work is concerned with scattering media with wavelength-invariant and wavelength dependent μ_s values. The use of an exponential model on the attenuation spectrum measured from these media are discussed in section 6.3.2 and section 6.3.3, respectively. The link between the terms in the cumulant based attenuation model and that in the exponential model is also established in these sections. Based on the knowledge of how the attenuation changes with a medium's μ'_s and μ_a , the criteria used in a model to account for these changes are described and a more suitable attenuation model to be used in this work is derived in section 6.4. The search for the optimum value of parameters in an attenuation model is discussed in section 6.5, and the accuracy of the value estimated using both the exponential model and the new version of attenuation model derived from this work is compared using simulations in section 6.6. The performance of these models is also compared with the techniques described in Chapter 4 and 5, with the results presented in section 6.7.

6.2 The exponential model (Heuristic search-based model)

The performance of the exponential model mentioned in Eq. (2.5.21) and shown again in Eq. (6.2.1) was previously investigated using the transmittance data of a 10 mm thick infinite slab.²⁷ This exponential model was used to fit to the measured attenuation spectrum to extract the medium's optical properties values.²⁷

$$A = a_1 \exp(-\mu_a b_1) - a_2 \exp(-\mu_a b_2) + e\mu_a + f\mu_a \lambda + g\lambda + h \quad (6.2.1)$$

The variables a_1 , b_1 , a_2 , b_2 , e , f , g , and h shown in Eq. (6.2.1) are the fitting parameters. In the case of two absorbers (i.e. Hb and HbO₂) in blood, the SO₂ value is related to μ_a via

$$\mu_a = (\varepsilon_{AB} \text{SO}_2 + \varepsilon_B) T_H \quad (6.2.2)$$

where $\varepsilon_{AB} = \varepsilon_A - \varepsilon_B$ is the extinction coefficient difference between absorber A and B, which represent HbO₂ and Hb, respectively. Substituting Eq. (6.2.2) into Eq. (6.2.1) gives

$$A = a_1 \exp(-(\varepsilon_{AB} \text{SO}_2 + \varepsilon_B) T_H b_1) - a_2 \exp(-(\varepsilon_{AB} \text{SO}_2 + \varepsilon_B) T_H b_2) + e(\varepsilon_{AB} \text{SO}_2 + \varepsilon_B) T_H \dots \\ + f\lambda(\varepsilon_{AB} \text{SO}_2 + \varepsilon_B) T_H + g\lambda + h \quad (6.2.3)$$

In that demonstration, the μ'_s value of the slab was varied linearly from 0.8 mm⁻¹ to 1.2 mm⁻¹ with wavelength of the illuminating light, λ and is given by:²⁷

$$\mu'_s = m\lambda - c \quad (6.2.4)$$

where $m = 0.002 \times 10^6 \text{ mm}^{-2}$ and $c = 0.1 \text{ mm}^{-1}$ are the gradient and intercept values of μ'_s versus λ relationship. The μ'_s and λ are in units of mm⁻¹ and mm respectively, with λ varied from $450 \times 10^{-6} \text{ mm}$ to $650 \times 10^{-6} \text{ mm}$. The photon propagation in the medium was simulated by means of Monte Carlo simulations.²⁷ Using the derived TPSFs and absorbers' extinction coefficients in the wavelength range of 450 nm to 650 nm, the

attenuation spectrum on which the exponential model was fitted to was calculated from Eq. (5.2.12).²⁷ This model was shown to produce an f_a value with an absolute error of less than 0.3%.²⁷ The attenuation values given by this fitting model and the accuracy of the estimated SO₂ when each of the terms in Eq. (6.2.3) is introduced into the model can be found in the work by Rodmell.²⁷ A demonstration of the quality of fit using this fitting model will be shown later in section 6.6.

The terms in the exponential model shown in Eq. (6.2.1) were previously found by an heuristic search technique and based mainly on the changes in the measured attenuation spectrum depending on the medium's μ'_s and μ_a .²⁷ Even though this model is termed as the exponential model in the work by Rodmell,²⁷ to prevent confusion between the exponential model shown in Eq. (6.2.1) and the single exponential model shown in Eq. (5.4.11), the exponential model shown in Eq. (6.2.1) is referred to in this study as the Heuristic search-based model (HS model).

It was briefly mentioned in section 2.5.5 that this HS model reduces to the Lambert-Beer law when $\mu'_s = 0 \text{ mm}^{-1}$. Two additional points should also be mentioned with regard to the way this model accounts for the effects of light scattering and absorption on the measured attenuation. First, the variation in attenuation with μ'_s is described by wavelength (i.e. λ) terms, in which a linear relationship between μ'_s and λ term shown in Eq. (6.2.4) is assumed. Second, this model considers the inseparable influences of μ'_s and μ_a components on attenuation by including the $\mu_a \lambda$ term in the expression. A further understanding of the meaning of each term in this HS model can be achieved by associating these terms to the coefficients in cumulant based attenuation model in section 6.3.2 and section 6.3.3.

6.3 Relating Heuristic search-based model to cumulant based attenuation model

The attenuation value given from a spectroscopic experiment can theoretically be expressed using the cumulant generating function⁴¹ while the HS model shown in Eq. (6.2.1) was reported to be able to reproduce the attenuation spectrum,²⁷ so it is of interest to investigate the relationship between these two models. The light attenuation as a function of cumulants, its statistical significance and the relationship between cumulants are discussed in section 6.3.1. This is followed by a discussion of the link between the cumulant based attenuation model and the HS model in section 6.3.2 and section 6.3.3. The A versus μ_a relationship given by cumulant based attenuation model and HS model when the value of parameters in HS model is derived from the cumulant values is shown later in section 6.3.4.

6.3.1 Expressing the TPSF cumulants

It was mentioned in section 2.5.3 that the cumulant generating function described the properties of a photon time-of-flight distribution, with the latter carrying information about the scattering and absorption processes of photons propagating in a medium. This function is comprised of an infinite power series of μ_a whose coefficients contain the cumulant values. For convenience of reference, light attenuation given by the summation of the attenuation offset, κ_0 , and cumulant generating function shown in Eq. (2.5.17) is written again in Eq. (6.3.1), where the summation term in Eq. (6.3.1) can be expanded to give Eq. (6.3.2).

$$A = \kappa_0 - \sum_{n=1}^{\infty} \kappa_n \frac{(-\mu_a c_m)^n}{n!} \quad (6.3.1)$$

$$= \kappa_0 + \kappa_1 \mu_a c_m - \kappa_2 \frac{(\mu_a c_m)^2}{2!} + \kappa_3 \frac{(\mu_a c_m)^3}{3!} - \dots \quad (6.3.2)$$

These cumulants are uniquely related to the moments (i.e. m) of a TPSF⁸¹ and so vary with changes in the TPSF. They can be calculated from the recursive formula shown in Eq. (2.5.19). The first two cumulants, which represent mean and variance of a TPSF¹³⁵ are given by:^{78,135}

$$\kappa_1 = m_1 = \mu \quad (6.3.3)$$

$$\kappa_2 = m_2 - m_1^2 = \sigma^2 \quad (6.3.4)$$

It must be mentioned that all the cumulants are unrelated to each other. Taking κ_2 expressed Eq. (6.3.4) as an example, it can be seen that the measure of the spread of this distribution around the mean (i.e. variance) is calculated by subtracting the mean (i.e. κ_1).¹³⁶

It is shown in Eq. (6.3.2) that the attenuation is expressed as an infinite summation of a power series of μ_a which is unattainable, so there is a need to identify a closed form expression which can approximate this function. This function has a similar form to the Taylor series expansion of an exponential equation, but that the coefficients in the (cumulants based) function have different values than those found in the exponential series. Thus a more suitable attenuation model is investigated in section 6.4.

6.3.2 Considering a medium with wavelength-invariant μ'_s

Referring to the HS model, if a sample's μ'_s is invariant with wavelength, the λ terms (i.e. $f\mu_a\lambda$ and $g\lambda$) in the equation, which represent the effects of wavelength dependent scattering component on the measured attenuation, would become constant. They can then be included into parameter $e\mu_a$ and h , so that this model is reduced to

$$A = a_1 \exp(-\mu_a b_1) - a_2 \exp(-\mu_a b_2) + e\mu_a + h \quad (6.3.5)$$

Since the effects of varying μ'_s on attenuation are excluded from the HS model, it is referred to in the following as the μ'_s invariant HS model. The two exponential terms shown in Eq. (6.3.5) are to provide more degrees of freedom, allowing a greater number of parameters to vary¹³⁷ during the fitting. Expanding the exponential terms in Eq. (6.3.5) as a Taylor series and rearranging the equation gives

$$A = \underbrace{(a_1 - a_2 + h)}_{\kappa_0} - \underbrace{(a_1 b_1 - a_2 b_2 - e)}_{\kappa_1} \mu_a + \underbrace{(a_1 b_1^2 - a_2 b_2^2)}_{\kappa_2} \frac{\mu_a^2}{2!} - \underbrace{(a_1 b_1^3 - a_2 b_2^3)}_{\kappa_3} \frac{\mu_a^3}{3!} + \dots \quad (6.3.6)$$

It can be seen by comparing the μ'_s invariant HS model and cumulant based attenuation model that these two models have a similar form. The coefficient of the terms in the μ'_s invariant HS model can, although not strictly true, be associated with the cumulants shown by the underbraces. An explanation of this is provided later in section 6.3.4. Meanwhile it is mentioned in section 6.3.1 that TPSF cumulants are unrelated, which is the possible reason why the $e\mu_a$ term is included in Eq. (6.3.6) as it is to break the link between the coefficient of first order term (approximated by κ_1) from that of the rest of the terms. Based on the accuracy of the estimated value, it seems acceptable not to break the link

between coefficients corresponding to higher order cumulants and this is elaborated in the next section.

6.3.3 Considering a medium with wavelength dependent μ'_s

If the medium's μ'_s value varied approximately linearly with wavelength, the μ'_s invariant HS model shown in Eq. (6.3.5) is no longer valid as it does not account for the μ'_s dependent variation in attenuation due to the absence of a λ term in the model. The HS model shown in Eq. (6.2.1) is more suitable to approximate the attenuation spectrum measured from this kind of medium.

Similar to section 6.3.2, the coefficients of terms in this model can be associated with the cumulant values. This is achieved by first expanding the exponential terms in Eq. (6.2.1) and then grouping terms to give:

$$A = \underbrace{(a_1 - a_2 + h + g\lambda)}_{\kappa_0(\lambda)} - \underbrace{(a_1b_1 - a_2b_2 - e - f\lambda)}_{\kappa_1(\lambda)} \mu_a + \underbrace{(a_1b_1^2 - a_2b_2^2)}_{\kappa_2} \frac{\mu_a^2}{2!} - \underbrace{(a_1b_1^3 - a_2b_2^3)}_{\kappa_3} \frac{\mu_a^3}{3!} + \dots \quad (6.3.7)$$

This equation shows that the attenuation offset and mean pathlength (i.e. κ_0 and κ_1) vary linearly with the wavelength, which is indicated by the presence of variable λ in the first and second terms in Eq. (6.3.7). If the medium's μ'_s is as shown in Fig. 4.5, the validity of these agrees with the results shown in Fig. 5.6(a) and Fig. 5.6(b) for the relationship between the zeroth and first order cumulants and the wavelength. Taking the parameters associated with the $\kappa_0(\lambda)$ shown in Eq. (6.3.7) as an example, the summation of $a_1 - a_2 + h$ gives the intercept value of $\kappa_0(\lambda)$ in Fig. 5.6(a) while the parameter g is the gradient of the plot.

The HS model assumes terms associated with higher order cumulants (cumulant order, $n > 1$) do not vary with wavelength. This is not true as all cumulants are wavelength dependent as shown in Fig. 5.6. From the accuracy of the estimated value that was reported,²⁷ this seems to suggest that the variation in coefficients (associated with high order cumulants) with wavelength can be ignored. A possible explanation of this is that the ‘skeleton’ of an attenuation spectrum can sufficiently be described by the terms and coefficients related to lower order cumulants, while those associated with higher order cumulants are used to add details to the spectrum, so a precise value for these coefficients (correspond to higher order cumulants) is not strictly required. This could also be the reason why no additional parameter is included in Eq. (6.3.6) and Eq. (6.3.7) to separate the coefficients associated with high order cumulants. The adequacy of using this HS model in expressing the measured attenuation is further investigated in section 6.6. But prior to that, the difference in the attenuation values given by the cumulant based attenuation model and that from the HS model is graphically demonstrated in the next section.

6.3.4 Deriving parameters of Heuristic-search based model from cumulants

Previously, it was shown that coefficients of the terms in the HS model shown in Eq. (6.2.1) and Eq. (6.3.5) can be associated with cumulants. A test for the equality of both of these parameters is performed in the following when the value of parameters in HS model is solved using the cumulants. For a better illustration, the single-valued A versus μ_a relationship measured from a medium with non-varying μ'_s is employed in the following demonstration so that the μ'_s invariant HS model shown in Eq. (6.3.5) can be used. Using

the simulated TPSF shown in Fig. 5.1, an attenuation value is calculated from Eq. (5.2.12) as μ_a varied from 0 mm^{-1} to 0.5 mm^{-1} , these are plotted in Fig. 6.1.

It is not possible to measure all of the cumulants (since they are an infinite number),¹³⁸ so a truncated cumulant series is used. Besides, it is also interesting to show how well a truncated cumulant based function is able to reproduce the true attenuation values. These cumulants are derived from the TPSF which gave the attenuation values shown in Fig. 6.1 and they are calculated from the recursive formula shown in Eq. (2.5.19). Using these cumulant values, the value of parameters in HS model can be obtained. The number of cumulants chosen for this demonstration is based on the quantity that is required to solve the parameters in the HS model. The six unknown parameters shown in Eq. (6.3.6) can be derived using a minimum of six cumulants, so cumulants of up to order 5 (including κ_0) are calculated. An example of the steps involved in deriving these parameter values from a finite number TPSF cumulants is provided in Appendix E. The derived values are then substituted into Eq. (6.3.5) to give the attenuation value as a function of μ_a .

6.3.4.1 Results and discussion

The attenuation values given by the truncated cumulant based attenuation model and μ'_s invariant HS model, whose coefficients are derived from a finite number of cumulants, are shown in Fig. 6.1. The value shown inside the parentheses in Fig. 6.1 indicates the maximum order of cumulants used in deducing the attenuation value.

Fig. 6.1 shows that the attenuation value given by the truncated cumulant based attenuation model agreed well to the true value in small μ_a region (μ_a range of 0 mm^{-1} to 0.05 mm^{-1}), but a large error in attenuation value can be observed in the high μ_a region. This discrepancy is consistent with the results observed in other work,^{41,135} where the

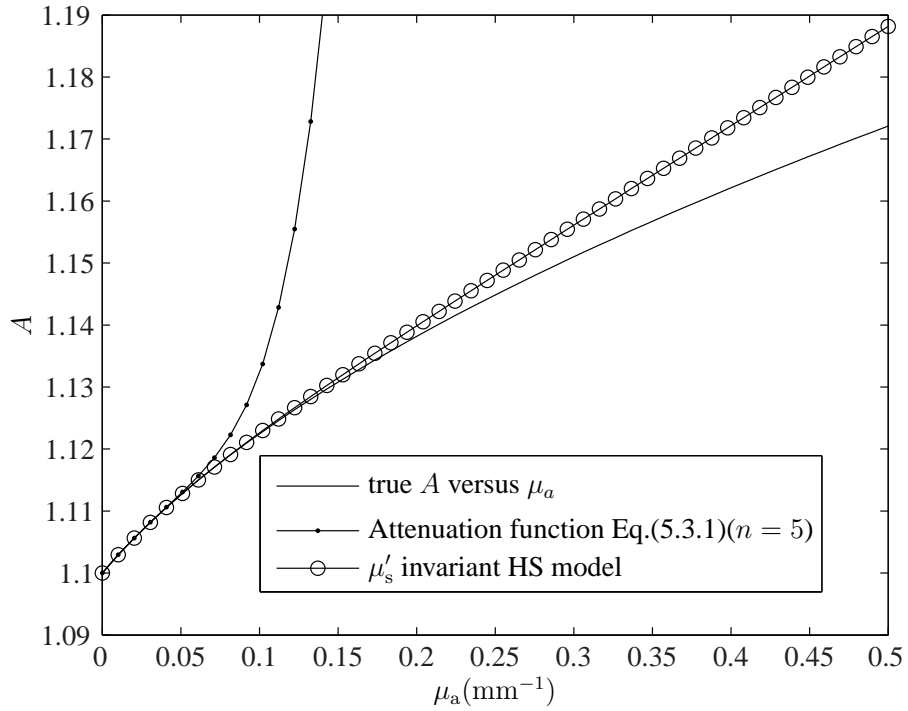


Figure 6.1: The true (solid line) and the calculated A versus μ_a relationship given by a truncated cumulant based attenuation model (closed circle line) and μ'_s invariant HS model when its coefficients are solved using a finite number of cumulants (open circle line).

growing deviation of attenuation from the true value as μ_a increased implies the need for higher order cumulants (i.e. in this case $n > 5$).⁴¹ This is because the high order cumulants cannot be neglected as the summation of all (infinite) TPSF cumulants is required to guarantee the convergence of attenuation given from cumulant based attenuation model to the real A versus μ_a relationship.⁴¹

The coefficients in μ'_s invariant HS model are derived from only a limited number of cumulants with all these coefficients, except those corresponding to κ_0 and κ_1 , are connected; but there are considerably lower errors (i.e. in high μ_a region) between the true A versus μ_a relationship and that given by this model as compared to the truncated cumu-

lant based attenuation model. This is because, unlike the truncated cumulant series, the exponential terms in the μ'_s invariant HS model include non-zero high order coefficients (i.e. up to an infinite number of terms), which suppresses the error in the high μ_a region. Another interpretation from this result is that the coefficients in μ'_s invariant HS model are not equivalent to the cumulants values. This can also be seen from Eq. (6.3.6) which shows that the coefficient of all terms beyond the first order term in the power series are linked. The parameter values derived from a limited number of cumulants are, therefore, not optimal to reproduce the attenuation values. A more appropriate approach that can be used to search for the optimum value of these parameters is described in section 6.5.

6.4 The empirically based model

As discussed in section 6.3.2 and section 6.3.3, the HS model shown in Eq. (6.2.1) takes the form of cumulant based attenuation model, but this model does not include the variation in the higher order cumulants ($n > 1$) with the measurement wavelength, which can be seen from the absence of wavelength term for coefficients associated with higher order cumulants in Eq. (6.3.7).

So in this section, an attenuation model that can be more suitably used to reproduce the attenuation value measured from the medium considered in this work is suggested. Any further improvement in the accuracy of the estimated value when this version of attenuation model is used is examined later in section 6.6. To arrive at this model, it is necessary to understand the effects photon scattering and absorption processes have on the measured attenuation spectrum. Based on an absorbing-scattering medium with the μ'_s described in Fig. 4.5, changes in attenuation value with the medium's μ_a and μ'_s are

summarised below.

1. In the absence of scattering, $\mu'_s = 0 \text{ mm}^{-1}$, the linear relationship between A and μ_a is governed by the Lambert-Beer law and is given by

$$A = \mu_a d \quad (6.4.1)$$

Here, d is the separation between the light source and the detector.

2. In the case of a medium with wavelength dependent μ'_s (shown in Fig. 4.5), light attenuation varies linearly with the wavelength when the medium's μ_a is a constant value
3. If both of the medium's μ_a and μ'_s are wavelength dependent, the measured attenuation can be expressed as an infinite summation of power series of μ_a whose coefficients are given by the cumulant values which vary with wavelength

A fulfilment to the criterion mentioned above in point (3) can be achieved by assuming that in the absence of absorption, cumulants vary linearly with wavelength as shown in Fig. 5.6 to give the attenuation shown in Eq. (5.4.3), which is rewritten in the following for convenience:

$$A(\lambda) = a_0 + b_0 \lambda - \sum_{n=1}^{\infty} (a_n + b_n \lambda) \frac{(-\mu_a(\lambda) c_m)^n}{n!} \quad (6.4.2)$$

Eq. (6.4.2) can also be written as

$$A(\lambda) = a_0 + b_0 \lambda - \sum_{n=1}^{\infty} a_n \frac{(-\mu_a(\lambda) c_m)^n}{n!} - \lambda \sum_{n=1}^{\infty} b_n \frac{(-\mu_a(\lambda) c_m)^n}{n!} \quad (6.4.3)$$

Letting the infinite summation of terms containing a_n (and b_n in Eq. (6.4.3)) be approximated by an exponential term as the latter includes an infinite summation of terms and is able to converge to the true A versus μ_a curve as shown in Fig. 6.1 gives an expression of attenuation as

$$A = a_0 + b_0\lambda - f \exp(-g\mu_a) - h\lambda \exp(-k\mu_a) \quad (6.4.4)$$

where a_0 , b_0 , f , g , h and k are parameters to be varied. In the case when μ_a is a constant, Eq. (6.4.4) can be reduced to a linear equation, complying with the condition described above in point (2). Expanding the exponential terms in Eq. (6.4.4) as a Taylor series and rearranging the equation provides

$$A = \underbrace{(a_0 + b_0\lambda - f - h\lambda)}_{\kappa_0(\lambda)} + \underbrace{(fg + h\lambda k)}_{\kappa_1(\lambda)} \mu_a - \underbrace{(fg^2 + h\lambda k^2)}_{\kappa_2(\lambda)} \frac{\mu_a^2}{2!} + \dots \quad (6.4.5)$$

It can be seen from Eq. (6.4.5) that the exponential terms in Eq. (6.4.4) give non-zero and wavelength dependent coefficient value for infinite terms, but the coefficients for all terms, except from the zeroth order term, are linked. To break the connection between the coefficient of terms in Eq. (6.4.5), which follows from the independence of cumulants from each other as discussed in section 6.3.1, additional terms can be added into Eq. (6.4.5). Similar to the steps taken by Rodmell²⁷ the connection between coefficient of terms associated with cumulant of order greater than one ($> \kappa_1$) is ignored here. The reason the first cumulant (mean) is segregated from the rest has been explained in section 6.3.3. Besides, an increase in the number of additional parameters to break the connection between coefficient of higher order terms in the power series would also increase the overall

complexity of the model, so this can result in an over-fitting of the measured attenuation spectrum.¹³⁹

Thus, by adding an extra term, $m\mu_a$, into Eq. (6.4.4) gives

$$A = a_0 + b_0\lambda - f \exp(-g\mu_a) - h\lambda \exp(-k\mu_a) + m\mu_a \quad (6.4.6)$$

Rearranging Eq. (6.4.6) provides

$$A = \underbrace{(a_0 + b_0\lambda - f - h\lambda)}_{\kappa_0(\lambda)} + \underbrace{(fg + h\lambda k + m)}_{\kappa_1(\lambda)} \mu_a - \underbrace{(fg^2 + h\lambda k^2)}_{\kappa_2(\lambda)} \frac{\mu_a^2}{2!} + \dots \quad (6.4.7)$$

In the absence of scattering, all parameters other than the parameter m in Eq. (6.4.6) are zero, and Eq. (6.4.6) is reduced to the Lambert-Beer law. It is apparent by comparing the model shown in Eq. (6.2.1) and Eq. (6.4.6) that the HS model and this new version of attenuation model are similar, except that the coefficient of each term in the newly derived model is wavelength dependent in order to account for the variation in all the cumulants with wavelength. The attenuation model shown in Eq. (6.4.6) is developed based on observation of the results and knowledge acquired in the study so it is termed here as the *Empirically based model* (E-based model). This model is a closer approximation to the cumulant based attenuation model as it is derived from the latter, so it is expected to be a more suitable model used at reproducing the true f_a value. The accuracy of its estimated values is compared with that given by the HS model in section 6.6.

6.5 The search of optimum value of fitting parameters

In section 6.3.4, it was demonstrated that the parameters in the μ'_s invariant HS model are derived from a finite number of cumulants which can, in practice, be calculated from signals measured using time-domain or frequency-domain techniques. However, the use of either a time-domain or a frequency-domain system is not the objective of this work. Besides, the coefficients in HS model are not equivalent to the cumulants and the values derived from the cumulants are not optimal, which is why the produced attenuation failed to converge to the true values shown in Fig. 6.1. The optimum value for parameters in a model can be found via the least square fitting or non-derivative optimisation method.^{140–142} While both of these methods would produce the same results in most of the cases,¹⁴⁰ the former, which uses derivatives and partial derivatives to find the local minima,¹⁴³ is preferable when the function to be minimised is a quadratic¹⁴⁴ while the latter is particularly useful when the data are noisy¹⁴⁵ or when the function has many local minima as the least square method has high rates of local convergence.^{141,142} Both of the unconstrained least square and non-derivative optimisation methods place no limitations on the value of the estimates and are available in Matlab[®] function: `lsqnonlin` and `fminsearch`, respectively. Constrained nonlinear optimisation methods can also be used to find the optimal value of parameters in a model but boundary value for fitting parameters is required, so it is not considered in this study. For the above mentioned reasons, the unconstrained nonlinear optimisation method is used in the following.

6.5.1 The curve fitting routine

The optimisation method employed in this work uses the Nelder-Mead search¹⁴⁶ to seek for an optimal value for the fitting parameters to minimise the error between the attenuation estimated by a curve fitting model (e.g. Eq. (6.2.1)) and one that is measured.

The fitting parameters in a model can be categorised as linear and nonlinear parameters. The linear parameter is a parameter which changes the output (i.e. attenuation value) in a linear way, whereas a nonlinear parameter modifies the output nonlinearly.¹⁴⁷ Taking the HS model shown in Eq. (6.2.1) as an example of curve fitting model, the linear parameters are a_1 , a_2 , e , f , g and h while the nonlinear parameters consist of b_1 , b_2 and f_a in μ_a . The search of the value of these fitting parameters begins by assigning each of these parameters with a starting value. None of these values are known, so they are all set to one. This value is chosen as other initial values have attempted and similar results are obtained. These values are then substituted into the curve fitting model (i.e. HS model shown in Eq. (6.2.1)) to give the attenuation values, A_c . The resolution of the calculated A_c spectrum depends on the spectral resolution of the medium's absorptivity spectra. The linear parameters change the attenuation linearly, so during each iteration of the fitting procedure, the linear parameters are computed with the backslash operator (\backslash) and they are given from

$$\mathbf{k} = \mathbf{X} \backslash \mathbf{A} \quad (6.5.1)$$

where \mathbf{k} is an array containing the value of a_1 , a_2 , e , f , g and h . \mathbf{A} is the measured attenuation and \mathbf{X} is a function of b_1 , b_2 and f_a values. The value of nonlinear parameters (i.e. b_1 , b_2 and f_a) are searched by the nonlinear optimisation routine. This optimisation method does not apply constraints to the value of these parameters (e.g. f_a should

be within the range of 0% to 100%) but it will seek for a new value for each nonlinear parameter according to the size of error (ΔE) between the calculated attenuation spectrum, A_c , and the true attenuation spectrum, A_m , with an aim to minimise this ΔE value. The reason the value of linear and nonlinear parameters are searched separately is that this optimisation method works better when only a few variables are involved.¹⁴⁸ In this case, only the value for parameter b , b_1 and f_a are searched using this function. Besides, the use of backslash operator in calculating the value of linear parameters compels the convergence of the calculated to the true values.

If $\Delta E \geq 1 \times 10^{-20}$, the search for a new value for these fitting parameters would continue and a new value is automatically assigned to each fitting parameter. With these values, new A_c values are calculated and a smaller ΔE would be expected. This process is iterated until ΔE is less than 1×10^{-20} or when the number of iteration (N) has exceeded 1000. These ΔE and iteration limits are chosen because it was found from this work that both of these values are sufficient for the A_c spectrum to converge to that which has been measured. A decrease in the ΔE limit or an increase in the number of iterations, or both, may improve the accuracy of the estimated value, although this would also result in an increase in the computation time. In addition, the iteration process is halted if changes in the value of all parameters become less than 1×10^{-20} , where the optimal value of each parameter is assumed to have been obtained. By the end of the iteration, the value of these fitting parameters is updated. The returned values are given by the value of parameters used in the final iteration. The search for the value of these fitting parameters is summarised in Fig. 6.2.

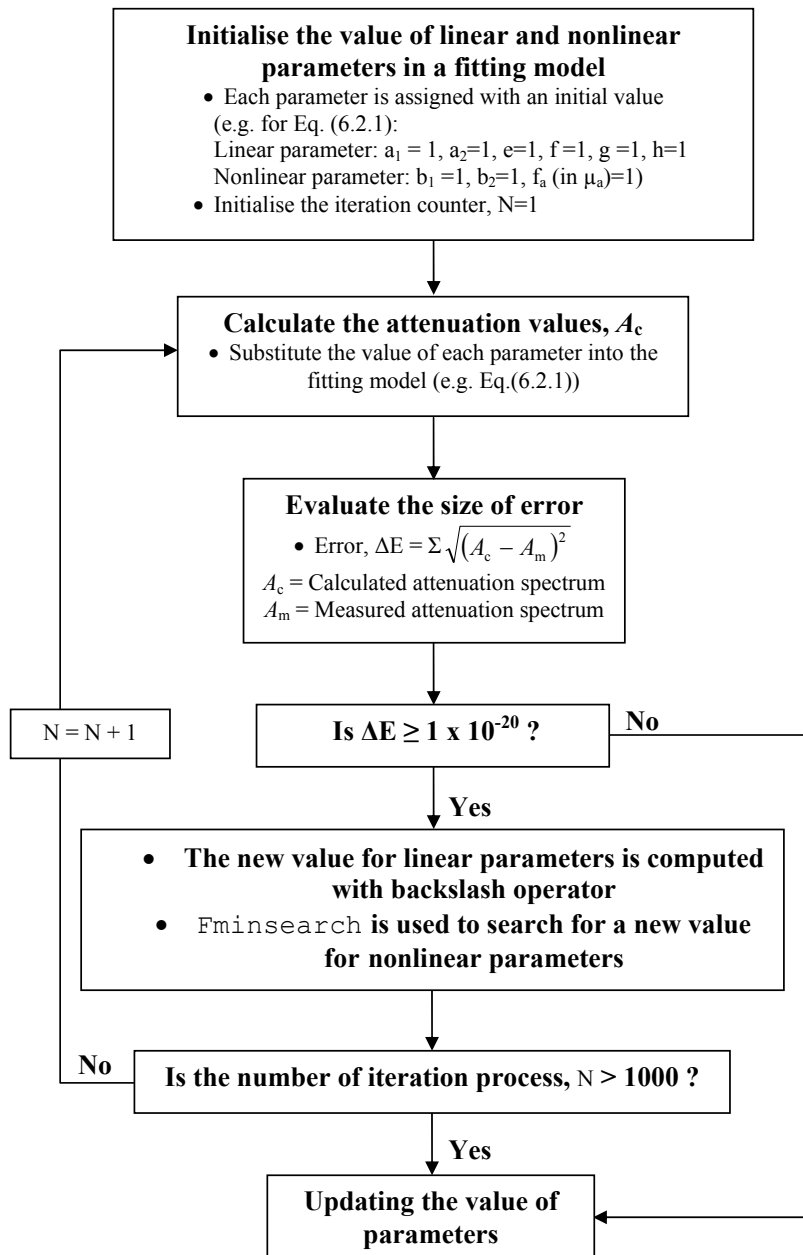


Figure 6.2: Flow diagram of the fitting routine.

6.6 Comparison of the performance of curve fitting models

It was mentioned in section 6.5 that the search for the value of parameters in a model can be obtained via the fitting of the corresponding model to the measured attenuation spectrum and the process is shown in Fig. 6.2. In this section, the accuracy of the f_a value estimated via the fitting of the HS model and the E-based model to the measured signals is examined and compared using the attenuation spectra of a wavelength dependent scattering-absorbing medium. Even though the μ'_s invariant HS model shown in Eq. (6.3.5) does not include the variation in attenuation value with changes in the medium's μ'_s , its performance in terms of error in the estimated value is also shown in the following.

The attenuation spectrum for different SO_2 values (varied from 0% to 100% in 1% increments) is calculated from Eq. (5.2.12) based on the TPSFs and extinction coefficient data shown in Fig. 4.7 and Fig. 2.3, respectively. The oxy- and deoxyhaemoglobin are the medium's absorbers giving the medium's μ_a expressed in Eq. (6.2.2). Substituting this expression of μ_a into the employed fitting models: HS model in Eq. (6.2.1), μ'_s invariant HS model in Eq. (6.3.5) and E-based model in Eq. (6.4.6), so that SO_2 become one of the fitting parameters as shown in Eq. (6.2.3) when HS model is used. Notice that in the case of a medium with three absorbers, the medium's μ_a shown in Eq. (5.5.1) would be substituted into these models.

The estimation of T_H is complicated as it is tied to other fitting parameters. An example of these parameters, in the case of the HS model shown in Eq. (6.2.1), are b_1 , b_2 , e and f . Even though the T_H of haemoglobin components in blood would change with time, parameters that are multiplied to this T_H would be modified during the fitting process to

‘correct’ this value. Therefore the μ_a in the employed fitting models (i.e. HS model and E-based model) can reasonably be replaced by α given in Eq. (4.2.3).

It must be mentioned that during the fitting process, each model is fitted to the attenuation values in A versus wavelength space (instead of that in A versus μ_a space). This is because the medium’s f_a and T_H that are required to give the μ_a are in practice unknown, and attenuation value is the only measurable from continuous intensity measurement that can be used to give an estimate of f_a value. This fitting process relies largely on the SO_2 dependent variation in the attenuation spectrum (which is most apparent in the wavelength range of around 500 nm – 600 nm as shown in Fig. 5.3), therefore, accuracy of the estimated value depends on the precision of the curve fitting models at describing the underlying (scattering and absorption) processes that give the corresponding measured attenuation spectrum. Using the attenuation spectrum corresponded to different SO_2 value, the value of all fitting parameters including the SO_2 value are returned at the end of fitting process. This process is then continued for the attenuation spectrum for other SO_2 values.

6.6.1 Results and analysis

The absolute errors in SO_2 estimated by different curve fitting models are shown on a log plot in Fig. 6.3 for clarity and the mean of these absolute errors is shown in Table 6.1. Error in the estimated SO_2 , whose values are not within the range of -2% to 102% , is not plotted in Fig. 6.3, e.g. when the set $\text{SO}_2 > 87\%$ for the value estimated by μ'_s invariant HS model shown in Eq. (6.3.5). The reason these invalid SO_2 values are produced is that the employed optimisation method does not apply boundary values to its fitting parameters.

A comparatively large error in the value produced by the μ'_s invariant HS model can be

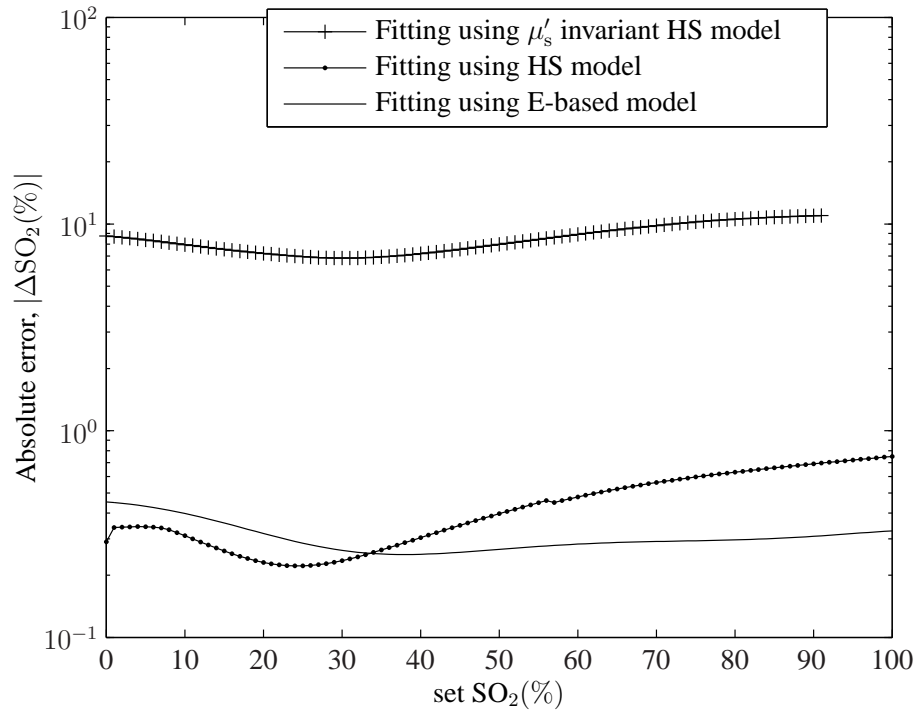


Figure 6.3: Error in the SO_2 value estimated using different curve fitting models when they are used on the attenuation spectrum for different SO_2 (shown on the x-axis). The error in the estimated SO_2 outside the range of -2% to 102% is not shown in the diagram.

seen in Fig. 6.3 and Table 6.1. This can be understood by the fact that this model does not account for the variation in attenuation with wavelength dependent μ'_s component. The mean error in the estimated SO_2 given by the HS model shown in Eq. (6.2.1) is slightly

Table 6.1: Mean of error in the SO_2 value given by different fitting models.

Fitting model	No. of fitting parameters	Mean of absolute error (%)
μ'_s invariant HS model	7	8.45
HS model	9	0.44
E-based model	8	0.307

higher (with an error of 0.14%) than what was claimed.²⁷ A possible reason for this is the larger magnitude of μ'_s values and the nonlinear variation in these μ'_s with wavelength that are used in this demonstration. The error in the value given by this model is also shown to increase in the higher SO₂ region and appeared to have a greater fluctuation compared to that produced by E-based model. Notice that the amplitude of humps and dips in the spectrum increases with the medium's SO₂ (as shown in Fig. 5.3), a possible explanation of the observed error is that the HS model does not describe this underlying process efficiently so producing local minimum of the function that is not globally optimal.¹⁴⁹

It can be concluded by comparing the results given by each fitting model shown in Fig. 6.3 and Table. 6.1 that the E-based model has slightly better performance in terms of the accuracy of the estimated value when SO₂ > 35% for the case considered in this work. The main difference between the HS and E-based models is the exclusion of the variation in higher order cumulants ($n > 1$) with wavelength in the former model. But based on the discussion in section 6.3.3 and accuracy of the computed values, it seems to suggest that the effects of the variation in higher-order cumulants with wavelength on attenuation are considerably small and, therefore, can be ignored for the case of μ'_s considered in this work.

6.7 Comparing the performances of quantification approaches used in this study

So far three different approaches that can be used to estimate an f_a value in a medium with wavelength varying μ_a and μ'_s values have been described, they are (1) fixed wavelengths

technique which uses linear equation model in Chapter 4, (2) the analysis of gradient (m_A) value given from different wavelength pairs in Chapter 5, and (3) curve fitting models that are described in this chapter. The error in the f_a value estimated using these methods has been demonstrated on simulated reflectance data for an infinite slab generated using the Monte Carlo method.

The spectroscopic study of a scattering-absorbing medium can be performed using either the transmittance or reflectance measurements. While both of the diffuse reflectance and transmittance measurements can be used for the application on a bulk and thick medium, i.e. breast,^{115,150} transmittance measurement can suitably be used for the optical spectroscopy of a thin and weakly scattering medium.¹⁵¹

The results shown in Table 6.1 and Fig. 6.3 show that the E-based model is suitable model to recover a medium's f_a value by the fitting of this model to the attenuation spectrum of the corresponding medium whose μ'_s values are shown in Fig. 4.5. Therefore, the performance of this model is compared in the following with the other methods discussed in Chapter 4 and 5. Also used for comparison is the HS model shown in Eq. (6.2.1), as it was previously reported to be a good curve fitting model to recover SO_2 value.²⁷ To demonstrate the performance of the techniques described in Chapter 4 and 5, the combination of wavelengths 469 nm, 593 nm, 600 nm, which is the best combination for overall SO_2 , selected in Chapter 4 is used in the following as the fixed wavelengths to give an estimate of SO_2 using the wavelength dependent MLBL shown in Eq. (4.4.1). Meanwhile, the groups of dual-wavelength combinations collected at different f_a value are used to give m_A values for the analysis described in Chapter 5. The techniques described in Chapter 4 and 5 are referred to in the following demonstrations as the *Solving a linear equation model* and *Gradient processing method*, respectively.

Description of the medium and measurement system

The ability of these methods to recover a medium's f_a value is investigated in the following using reflectance and transmittance data. The infinite slab with wavelength dependent μ'_s and μ_a , and detector used for the measurements in transmittance and reflectance modes in Monte Carlo simulations are shown in Fig. 6.4. The wavelength dependent μ'_s values of this medium (in the wavelength range of 450 nm – 600 nm) are shown in Fig. 4.5. For each simulation, 20 million photons are launched normally into the medium and the propagation of photons in these media are given in Appendix C. The photon pathlength cutoff, reflectance and refraction angles of these photons are described in section 3.3. For the case of reflectance measurements, an annular detector with inner and outer radii of 2.5 mm and 3.5 mm, respectively, is used so that the detection of surface reflected light can be minimised, while a detector with aperture diameter, $\varnothing = 50$ mm, is employed in the transmittance measurement. These detector sizes are chosen so that a sufficient number of photons (i.e. more than 1 million photons) are collected. The medium and experimental system used for the reflectance measurement are the same as those used to produce the results shown in Fig. 4.13, Fig. 5.10 - Fig. 5.12 and Fig. 6.3. These simulations produced TPSFs which are used to give attenuation spectra for a medium with absorbers shown in Fig. 2.3. The attenuation spectrum as SO₂ was varied from 0% to 100% in 1% increments is calculated from Eq. (5.2.12). The T_H is either tied to other parameters as previously mentioned in section 4.4 and section 6.6 or its changes have no effect on the data analysis as discussed in section 5.4.2.1, so all the methods work in α space. Each technique is applied to each attenuation spectrum to give an estimation of the SO₂ value with the acceptable analytical range of -2% to 102%. Similar to the results shown in previous chapters, the estimated value outside this range will not be shown on

the plot.

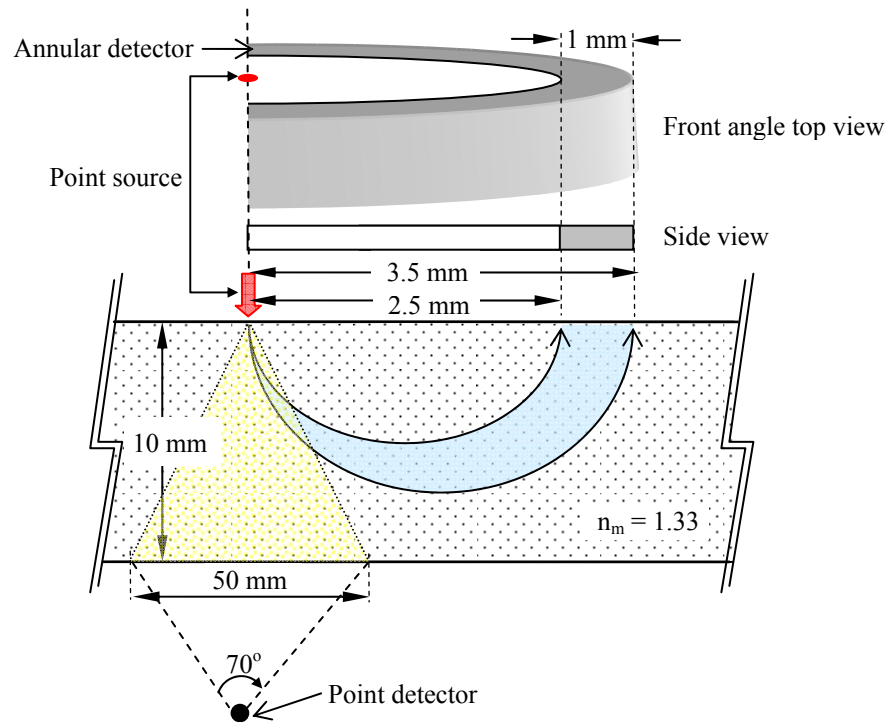


Figure 6.4: The infinite slab and detectors used for reflectance and transmittance measurements in Monte Carlo simulations.

The results are presented in three different subsections as follows: in the first subsection, simulation data are derived from the reflectance mode measurement and the errors ΔSO_2 given by different techniques are shown in section Result (1). This is followed by the results on error in the calculated values when the techniques are used to estimate SO_2 based on the transmittance data in section Result (2). In each of these sections, the error in the value given by each technique when spectra with sampling resolution of 1 nm and 0.5 nm are employed is presented. As mentioned in section 4.5.2, the measured data are, in practice, subject to quantisation error and noise in the system. For this reason,

the robustness of the discussed techniques to noise are compared and presented in section Result (3). A discussion of these results is in section 6.8.

6.7.1 Result (1) : Error in SO₂ estimated based on reflectance data

Fig. 6.5 shows the full scale error in the value estimated using different methods based on the attenuation spectrum for different values of SO₂ measured in the reflectance mode versus the set SO₂ (shown on x-axis). The estimation of SO₂ value is based on the attenuation spectrum with spectral resolution of 1 nm (Fig. 6.5(a)) and 0.5 nm (Fig. 6.5(b)). The techniques used are the simultaneous solution of wavelength dependent MLBL using data at 469 nm, 593 nm, 600 nm (red line), the processing of gradient value of different wavelength pairs in A versus wavelength space (closed circle green line), the fitting of the HS model (blue line), and the E-based model (dark line) to the measured data. The results are discussed in detail in section 6.8.

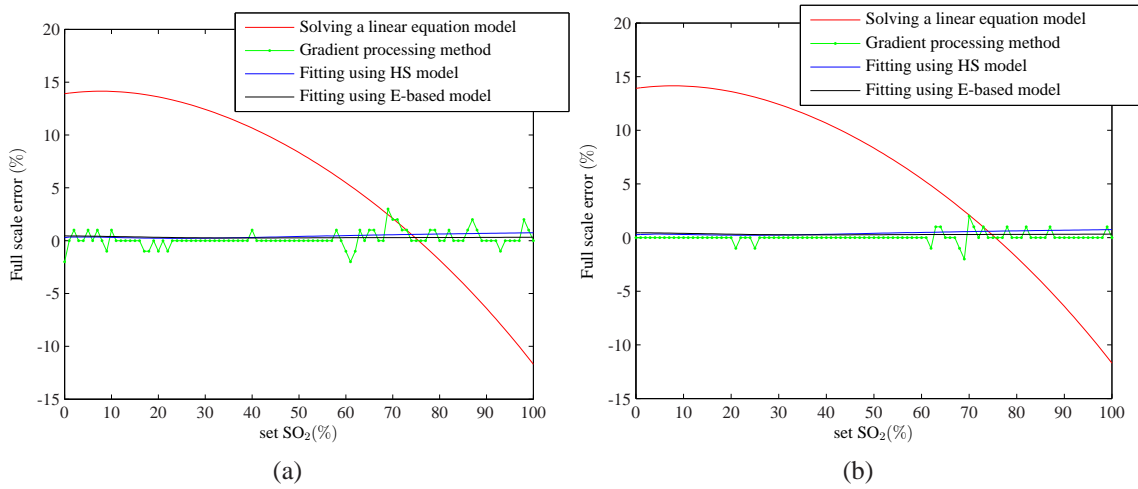


Figure 6.5: Full scale error in the SO_2 estimated using different techniques versus the actual SO_2 (shown on x-axis). The estimation of SO_2 is based on the attenuation spectra measured in reflectance mode with spectral resolution of (a) 1 nm (b) 0.5 nm.

6.7.2 Result (2) : Error in SO_2 estimated based on transmittance data

Fig. 6.6 shows ΔSO_2 estimated using different techniques based on the attenuation spectrum for different values of SO_2 measured in transmittance mode versus the actual SO_2 (shown on x-axis). The error in the value estimated based on spectra with spectral resolution of 1 nm and 0.5 nm is shown in Fig. 6.6(a) and Fig. 6.6(b), respectively. The techniques used are the simultaneous solution of wavelength dependent MLBL using data at 469 nm, 593 nm, 600 nm (red line), the analysis of gradient of different wavelength pairs in A versus wavelength space (closed circle green line), the fitting of data using the HS model (blue line), and the E-based model (dark line). The reason the ΔSO_2 given by the wavelength dependent MLBL appears discontinuous after the set $\text{SO}_2 = 95\%$ is due

to the selection of wavelengths. A more detail discussion of this and the results shown in Fig. 6.6 can be found in section 6.8.

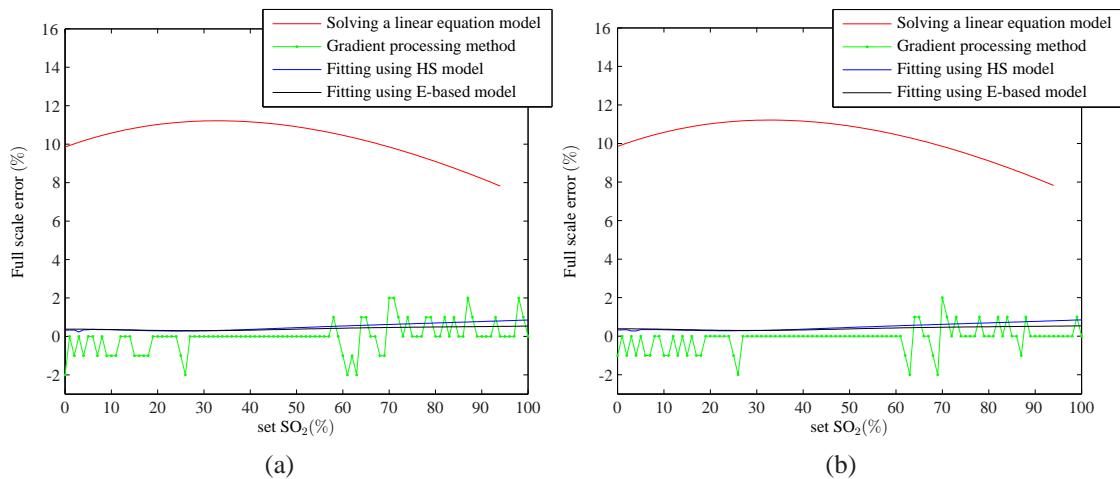


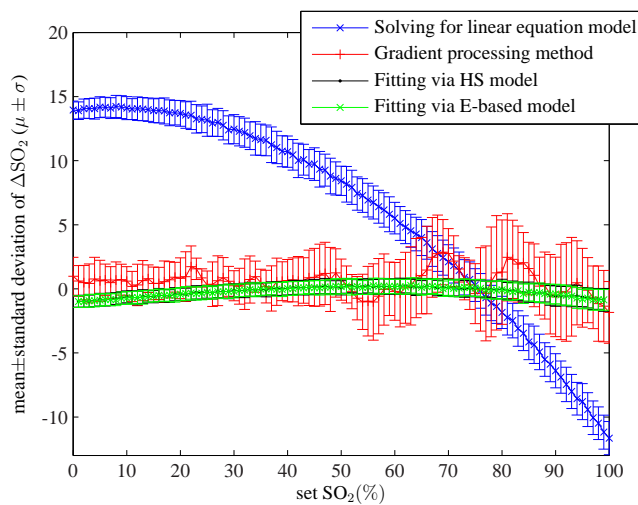
Figure 6.6: Full scale error in the SO_2 estimated using different techniques. The estimation of SO_2 is based on the attenuation spectra measured in transmittance mode with spectral resolution of (a) 1 nm (b) 0.5 nm. Error in the estimated SO_2 outside the range of -2% to 102% is not plotted in the diagram.

6.7.3 Result (3) : Comparing noise robustness of different techniques

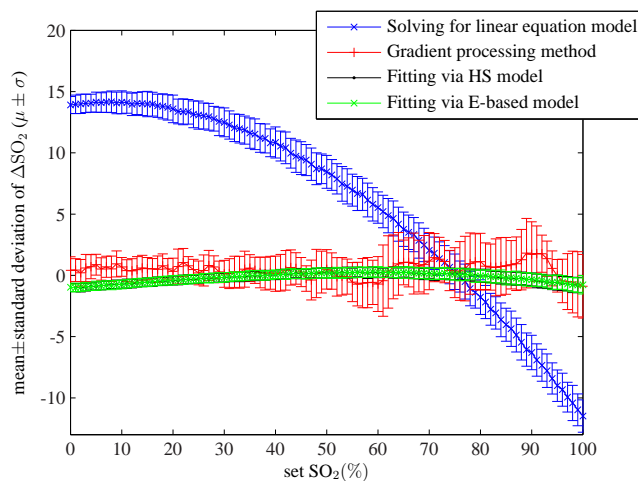
A comparison of the robustness of the techniques discussed in Chapter 4, 5 and in this chapter to noise can be performed by modelling the noisy data following the steps shown in Fig. 4.18. The attenuation data used to produce the noisy signals from reflectance and transmittance measurements are given by those that are used to give the error plots shown in Fig. 6.5 and Fig. 6.6, respectively. Different techniques are then used on the modelled noisy signals to give an estimate of the SO_2 value.

As described in Fig. 4.18, 300 sets of noisy attenuation spectra are generated for each SO_2 , which varied between 0% and 100% in steps of 1%. Based on these attenuation

spectra, the mean and standard deviation of errors given by different techniques are calculated for the case when the noisy attenuation spectra are measured in the reflectance and transmittance modes, and the results are shown in Fig. 6.7 and Fig. 6.8, respectively. The mean (μ) and variance (σ) of these errors are denoted by $\mu \pm \sigma$, these values are shown in Fig. 6.7 and Fig. 6.8 when the reflectance and transmittance data with spectral resolution of 1 nm and 0.5 nm are used and they are summarised in Table 6.2. The noisy reflectance data (with a sampling interval of 1 nm) used in giving the results in Fig. 6.7(a) are the same as that used in section 4.5.3, therefore similar error in the values given by the wavelength dependent MLBL (based on the data of 469 nm, 593 nm, 600 nm) can be seen in Fig. 4.21 and Fig. 6.7(a). Similar to that mentioned in Result (2) section, the reason that SO_2 (hence ΔSO_2) estimated by the wavelength dependent MLBL appeared discontinuous after set $\text{SO}_2 = 80\%$ shown in Fig. 6.8 is due to the selection of wavelength combinations. A further discussion of this and the rest of these results is in section 6.8.

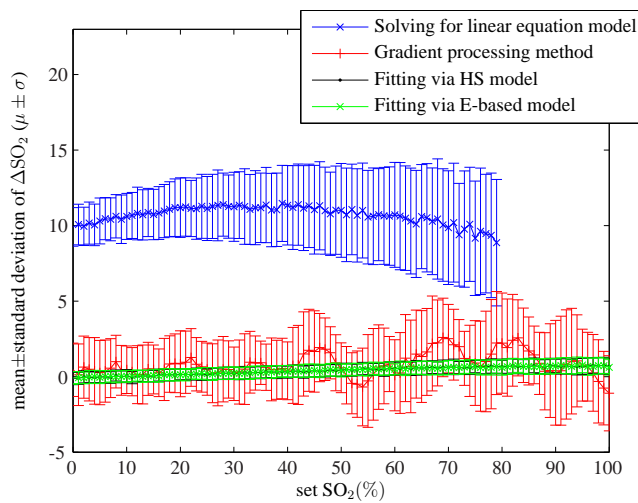


(a)

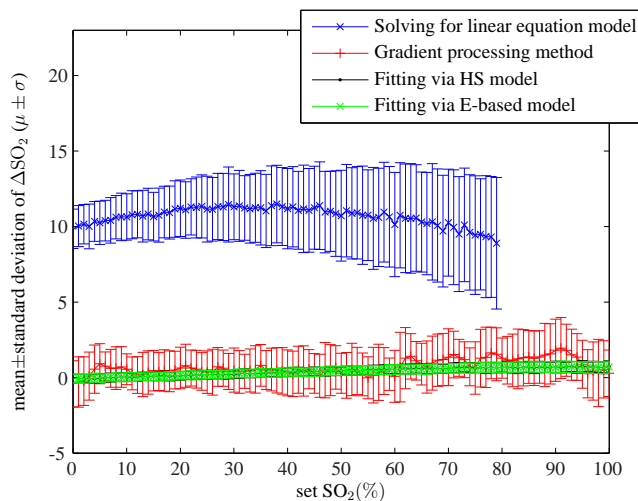


(b)

Figure 6.7: Mean of error in the SO_2 estimated using different methods versus the true SO_2 (shown on x-axis). These values are calculated based on the reflectance signals measured in the presence of noise. The standard deviation of the calculated errors is indicated by the size of the error bar. These mean and standard deviation are given by the error in the SO_2 estimated based on 300 sets of attenuation spectra (for each SO_2). The mean error in the estimated SO_2 outside the range of -2% to 102% during one of the iterations (in Fig. 4.18) is not plotted in the diagram. The sampling resolution of the employed spectra is (a) 1.0 nm and (b) 0.5 nm.



(a)



(b)

Figure 6.8: Mean of error in the SO_2 estimated using different methods versus the set SO_2 (shown on x-axis). These values are calculated based on the transmittance signals measured in the presence of noise. The standard deviation of the calculated errors is indicated by the size of the error bar. These mean and standard deviation are given by the error in the SO_2 estimated using 300 sets of attenuation spectra (for each SO_2). The mean error in the estimated SO_2 outside the range of -2% to 102% during one of the iterations (in Fig. 4.18) is not plotted in the diagram. The sampling resolution of the employed spectra is (a) 1.0 nm and (b) 0.5 nm.

Table 6.2: The average of mean and standard deviation of the calculated absolute error in the values given by different techniques based on the noisy reflectance and transmittance data.

Technique	mean $\mu \pm \sigma$ (in %)			
	^a R _{1nm}	^b R _{0.5nm}	^c T _{1nm}	^d T _{0.5nm}
Solving a linear equation model	4.7 ± 2.65	4.8 ± 2.5	3.37 ± 1.94	3.3 ± 2
Gradient processing method	2.7 ± 2.1	1.9 ± 1.5	2.4 ± 1.8	1.6 ± 1.3
Fitting using the HS model	0.89 ± 0.65	0.9 ± 0.67	0.64 ± 0.44	0.64 ± 0.45
Fitting using the E-based model	0.88 ± 0.65	0.81 ± 0.6	0.62 ± 0.45	0.62 ± 0.45

^a R_{1nm}: reflectance spectra with resolution of 1 nm

^b R_{0.5nm}: reflectance spectra with resolution of 0.5 nm

^c T_{1nm}: transmittance spectra with resolution of 1 nm

^d T_{0.5nm}: transmittance spectra with resolution of 0.5 nm

6.8 Discussion

Fig. 6.5 and Fig. 6.6 show that the simultaneous solution of wavelength dependent MLBL (i.e. solving a linear equation model) has the highest overall error in the SO₂ values estimated based on signals measured from wavelength dependent scattering-absorbing media in both of the measurement modes. This error is due to the selection of wavelengths when there is an expensive tradeoff between sensitivity of the estimated value towards noise and accuracy of the estimated SO₂. The combination of wavelengths 469 nm, 593 nm and 600 nm used in this demonstration was chosen in Chapter 4 based on reflectance data for the medium shown in Fig. 6.4, thus they might not be the optimal combination for the transmittance measurements in terms of accuracy and robustness of the estimated value to noise. This is because the accurate estimation of SO₂ value requires μ_a and A of the selected wavelengths to comply with either one of the wavelength selection strategies

discussed in section 4.4.2. So even though a wavelength combination chosen based on the reflectance data may have the same α (or their α are as shown in Eq. (4.4.21)), their attenuation measured from the transmission measurements may not satisfy Eq. (4.4.18), so giving an inaccurate estimation of SO_2 value. This can be seen from the error plots shown in Fig. 6.6 and Fig. 6.8, where the estimated SO_2 value exceeding the analytical limit of -2 to 102% was observed at certain SO_2 range (i.e. shown as discontinuity of the line at SO_2 of about and beyond 95% and 80% using the noiseless and noisy data, respectively), when the data at these selected wavelengths are used to give an estimation of SO_2 value. This shows that a different wavelength combination should be chosen when one of the measurement parameters is changed. However, it was found in this work that this method has the fastest processing speed compared to other employed analytical methods as it considered only the data at the selected three wavelengths.

The accuracy of the value estimated via the analysis of the gradient value of different wavelength pairs (in A versus wavelength space) collected in pre-measurement stage is shown in Fig. 6.5 and Fig. 6.6 to improve with a decrease in sampling interval of the employed spectra. This is due to the increase in the number of data points considered during the estimation of SO_2 as explained in section 5.4.3. On the contrary, the simultaneous solution of wavelength dependent MLBL shown in Eq. (4.4.1), and the fitting of the attenuation spectra using the HS model and E-based model do not show any significant improvement in their calculated ΔSO_2 with the decrease in the spectral sampling interval. This is because solving for SO_2 via wavelength dependent MLBL uses only the attenuation and absorbers' extinction coefficients of the selected three wavelengths, while the curve fitting models rely on the SO_2 dependent variation in the attenuation spectrum during the estimation of SO_2 .

A similar trend is observed when these techniques are used on the noisy signals. Fig. 6.7, Fig. 6.8 and Table 6.2 show that errors given by the Gradient processing technique are considerably large and these errors are comparable (at certain SO_2 values) to that given by the wavelength dependent MLBL when spectra with a resolution of 1 nm are used. However, the error of the estimated value reduced by about 30% with a decrease in the spectral sampling interval to 0.5 nm as more data points are taken into consideration during the estimation of SO_2 value. Other techniques do not show any noticeable change in their performance with the improved sampling resolution.

The accuracy of the value estimated by curve fitting models shown in Eq. (6.2.1) and Eq. (6.4.6) is consistent for different measurement schemes and spectral resolution. Their performance are similar even in the presence of noise shown Fig. 6.7, Fig. 6.8 and Table 6.2, where it is shown that these fitting models produce an overall lowest error with the least variation compared to other techniques. This implies that both of these fitting models have sufficiently reflected the true underlying processes (i.e. scattering and absorption processes) that give the measured attenuation spectrum. Additionally, the curve fitting method considers all the data points and depends on the SO_2 dependent variation in the attenuation spectrum in the estimation of SO_2 ; as long as the measured data are sufficiently sampled (in terms of number of data points), these fitting models would work reasonably well even with noisy data. But these fitting models failed to produce an estimated value within the limit chosen in this work (i.e. analytical range of -2% to 102%) when the set SO_2 is at about and beyond 98% shown in Fig. 6.7 and Fig. 6.8. An explanation of this is that the employed optimisation method does not apply bound to the estimated SO_2 value. This is also the reason for the discontinuity in the error line produced by the simultaneous solution of wavelength dependent MLBL shown in Fig. 6.6

and Fig. 6.8 when no constraint is imposed on the value estimated using this method. This problem, however, is not observed in the values given by the Gradient processing method because the estimated value is given by the analytical value when the selected wavelength pairs are stored in pre-measurement stage. Hence, the estimated value can only be within the analytical range considered in this work.

6.9 Conclusion

This chapter established the link between the terms in the HS model shown in Eq. (6.2.1) and that in cumulant based model shown in Eq. (6.3.1). It is shown that cumulant can be associated with the coefficients in the model, but they are not equivalent. In addition, the HS model is better than the truncated cumulant based model at reproducing the measured attenuation spectrum as it accounts for a non-zero infinite term. The developed E-based model to account for the variation in each term in the model (associated with higher-order cumulants) with wavelength has, although not to a great degree, improved the accuracy of the estimated values. Besides, with the decrease in the number of fitting parameters in the E-based model, a shorter computation time is expected during the estimation of the f_a .

Based on a comparison of the techniques described in Chapters 4 & 5 and this chapter in section 6.7, it is reasonable to conclude that the processing of gradient value of pre-measurement selected wavelength pairs in the A versus wavelength space (i.e. Gradient processing method) is a preferable quantification technique considering the accuracy of the estimated value and computing time. This is because this technique has intermediate performance in terms of accuracy of value, noise performance and processing time as compared to simultaneous solution of a linear equation model and fitting method. This

technique may require working with high sampling resolution spectra to improve the accuracy of the estimated values but its performance is consistent for both transmission and reflection data in comparison to that of the wavelength dependent MLBL. Besides this technique works with certain wavelengths, so is also theoretically more time efficient than by fitting the HS model and E-based model to the attenuation spectrum in recovering the medium's f_a . Nonetheless, the fitting of the measured attenuation spectrum using HS model and E-based models is of preference when accuracy (of estimated value) is the prior concern. This is due to the high accuracy of their estimated values and they are also more robust to noise.

Chapter 7

Conclusions and Future work

7.1 Conclusion

In view of the fact that problems in accurately determining the concentration value of an absorber in a medium arise when the medium is scattering and the Lambert-Beer law cannot be applied, this thesis aimed to determine different approaches to predict the fractional concentration value of an absorber in a scattering-absorbing medium.

This work began in Chapter 3 with a goal to solve this problem by minimising the effects of scattering on the signals and to linearise the A versus μ_a plot, which can then be approximated by the Modified Lambert-Beer law or any other developed attenuation model. This work has experimentally demonstrated and verified the performance of polarisation subtraction techniques following recommendations by Lu²⁴ and Stockford *et al.*¹⁵² whose discussions and observations were based on the simulation results. This chapter showed that the polarisation subtraction technique removed the scattering components on the signals, producing a more linear A versus μ_a relationship, but several issues concern-

ing the implementation of polarisation subtraction techniques for practical use have also been identified in this work. These issues include the poor signal to noise ratio of the polarisation subtracted signals, the restrictions polarisation subtraction technique has placed on the experimental system and the limitation of its application. For these reasons, it was decided that the remaining work in this thesis would focus on finding different analytical approaches to extract the true fractional concentration value of an absorber using the nonpolarised data measured from a scattering medium.

In Chapter 4, it was shown that for the case of a medium with wavelength invariant μ'_s , the fractional concentration value of an absorber can be recovered using the Modified Lambert-Beer law when μ_a of the either two of the selected wavelengths are the same. These wavelengths can be identified as those which measured the same attenuation. However if changes in a medium's μ'_s with wavelength is a monotonic function, the wavelength dependent MLBL is more suitably used to approximate the variation in the measured attenuation with μ_a and μ'_s . Only the data at a combination of three wavelengths are needed in the estimation of the absorber's fractional concentration value, but a new wavelength combination needs to be identified when either the measurement subject or one of the measurement parameters changes. Based on the error derivations, this chapter identified the strategies of optimal wavelength selection, thus removing the need of using brute force method. The optimal wavelength combination for a range of SO_2 values, a considered measurement medium, wavelength range and experiment system was determined by examining the mean and standard deviation of error in the value given by all the wavelength combinations using the wavelength dependent MLBL. This process, however, is time consuming and it required all measurement parameters to be known precisely. This chapter concluded that wavelengths which are closely spaced on the A versus wavelength

plot are more likely to satisfy the conditions outlined in this work and produced low error (typically about less than 2 %) in their estimated value but they are susceptible to noise on the signals.

Chapter 5 extended the knowledge of the selection of wavelengths for the quantification of f_a value in a scattering medium to the next level. Instead of having to re-identify a new wavelength combination when one of the measurement parameters changes, the estimation of an absorber's fractional concentration value is based on the understanding of how changes in a medium's optical properties modify the attenuation value. This technique is derived based on the known behaviour of wavelength dependent μ'_s and μ_a values. The relationship between α and attenuation response of different wavelength pairs (in A versus wavelength space) is approximated using the cumulant based function and this approach relied on this relationship in identifying the optimal set of wavelength pairs. It was shown that a large number of wavelength pairs used in the analysis improves the accuracy of the estimated value, so interpolation of the employed spectra may be needed. It was also concluded that the wavelength region where changes in μ_a with SO_2 are pronounced is suitable for the analysis.

In Chapter 6, the physical meaning of parameters in the Heuristic search-based model (HS model) are understood and they are linked to that of the cumulant based model. This work attempted to improve the performance of this curve fitting model by including the wavelength dependent higher order cumulants terms, which are lacking in the HS model, without increasing the complexity of the fitting model. Based on the results obtained from the quantification works involving the approaches discussed in Chapter 4 - 6, it was concluded that data processing using wavelength dependent MLBL is fast but it has the worst performance. The Gradient processing approach has a better performance in terms

of the accuracy of the estimated value (compared to the wavelength dependent MLBL), while medium characterisation using the curve fitting models is more resilient to noise in the system and their performance are consistent for spectra with different sampling resolution.

The tradeoffs in using the techniques discussed in this work are summarised in Table 7.1.

Table 7.1: The tradeoffs in using the experimental and analytical techniques used in this work.

Experimental/Analytical technique	Limitations	Advantages
Polarisation subtraction technique	<ul style="list-style-type: none"> • its performance depends on the quality of polarisers and detector's sensitivity • produces signals with poor SNR 	<ul style="list-style-type: none"> • produce a more linear A versus μ_a relationship that can be represented by MLBL
Solving a linear equation model	<ul style="list-style-type: none"> • requires a strict knowledge of all the measurement parameters • requires intensive processing prior to experiment 	<ul style="list-style-type: none"> • fast processing time • analysis using only data at three wavelengths
Gradient processing method	<ul style="list-style-type: none"> • its performance depends on resolution of the employed spectra • derivation based on the monotonical variation in μ'_s with wavelength • works well only in region where changes in μ_a with SO_2 are large 	<ul style="list-style-type: none"> • does not require an attenuation model to give an estimate of f_a • does not depend critically on the experimental parameters
Curve fitting method	<ul style="list-style-type: none"> • requires an attenuation model • valid when changes in a medium's μ'_s with wavelength is monotonic 	<ul style="list-style-type: none"> • the performance is robust to noise • has the best performance in terms of accuracy of the estimated value • does not depend critically on the experiment parameters

7.2 Future work

The steps involved in determining an absorber's fractional concentration value in the case of a wavelength dependent scattering-absorbing medium using the Gradient processing approach described in Chapter 5 are valid only when the variation in the medium's μ'_s with wavelength is approximately linear. This is also the case when the wavelength dependent MLBL and curve fitting models described in Chapter 4 and Chapter 6, respectively, are used for quantification work. This study considered only the monotonic variation in a medium's μ'_s with wavelength because this variation is similar to those found in human skin, hence findings obtained from this study can be applied to oximetry. The next line of this research is to examine the types of modification that can be made on these models and techniques to account for other variation of μ'_s , or to develop a technique or model that can suitably be used for analytical work when changes in the medium's μ'_s with the measurement wavelength is a random function, which is found in most of the microsphere phantoms.

The experimental investigation of the performance of different approaches used in this work remains a challenge. There is a need to extend this study so that the developed algorithms can be applied on volunteers of diverse backgrounds. But this validation work is possible only if the mean SO_2 across veins, arteries, and capillaries of the human volunteers are known. Several ways have been proposed by other workers such as Sæbø *et al.*¹⁵³ who is reported to be able to prepare blood samples of different SO_2 with a chemical agent.

Appendix A

Simultaneous solution to the parameters in Modified Lambert Beer law

Duling and Pittman modified the equation deduced by Twersky and referred it as the Modified Lambert Beer Law (MLBL) as follows:³

$$A(\lambda) = G + \mu_a(\lambda)d \quad (\text{A.0.1})$$

If two absorbing species (i.e. absorber A and B) are present in the medium to give the medium absorption as

$$\mu_a(\lambda) = C_A \varepsilon_A(\lambda) + C_B \varepsilon_B(\lambda) \quad (\text{A.0.2})$$

where subscripts A and B denote that of the corresponding absorbers. Substituting Eq. (A.0.2) into Eq. (A.0.1) so that the MLBL becomes

$$A(\lambda) = G + (C_A \varepsilon_A(\lambda) + C_B \varepsilon_B(\lambda_1))d \quad (\text{A.0.3})$$

It is not possible to find the absolute concentration of these absorbers (i.e. C_A and C_B) using the continuous intensity measurements because the photon mean pathlength is unknown, but the fractional concentration value of an absorber can be determined. The fractional concentration of absorber A in this medium is given by

$$f_a = \frac{C_A}{C_A + C_B} \quad (\text{A.0.4})$$

Rearranging Eq. (A.0.3) provides

$$A = G + (\varepsilon_A C_a + \varepsilon_B (T_a - C_a))d \quad (\text{A.0.5})$$

where $T_a = C_A + C_B$ is the total concentration of absorber A and B. Using Eq. (A.0.4) so that Eq. (A.0.5) becomes

$$A = G + ((\varepsilon_A - \varepsilon_B)C_a + \varepsilon_B T_a)d \quad (\text{A.0.6})$$

$$= G + ((\varepsilon_A - \varepsilon_B)f_a + \varepsilon_B)dT_a \quad (\text{A.0.7})$$

The value of G , d , T_a and f_a are generally unknown, but Duling and Pittman assumed that these values are invariant with wavelength. The light attenuation measured using two wavelengths, λ_1 and λ_2 , are approximated by the MLBL as

$$A(\lambda_1) = G + ((\varepsilon_A(\lambda_1) - \varepsilon_B(\lambda_1))f_a + \varepsilon_B(\lambda_1))dT_a \quad (\text{A.0.8})$$

$$A(\lambda_2) = G + ((\varepsilon_A(\lambda_2) - \varepsilon_B(\lambda_2))f_a + \varepsilon_B(\lambda_2))dT_a \quad (\text{A.0.9})$$

Eq. (A.0.8) and Eq. (A.0.9) giving a pair of simultaneous equations, using which the parameter G can be solved and is given by

$$G = \frac{A_1(\varepsilon_{AB_2}f_a + \varepsilon_{B_2}) - A_2(\varepsilon_{AB_1}f_a + \varepsilon_{B_1})}{\varepsilon_{AB_2}f_a + \varepsilon_{B_2} - \varepsilon_{AB_1}f_a - \varepsilon_{B_1}} \quad (\text{A.0.10})$$

where ε_{AB_1} denote $\varepsilon_A(\lambda_1) - \varepsilon_B(\lambda_1)$. The measurement at the third wavelength, λ_3 gives the solution of f_a described as follows. The attenuation measured at λ_3 can be expressed using the MLBL as

$$A(\lambda_3) = G + ((\varepsilon_A(\lambda_3) - \varepsilon_B(\lambda_3))f_a + \varepsilon_B(\lambda_3))dT_a \quad (\text{A.0.11})$$

Rearranging the simultaneous equation of Eq. (A.0.9) and Eq. (A.0.11) gives

$$\frac{A_2 - G}{\varepsilon_{AB_2}f_a + \varepsilon_{B_2}} = \frac{A_3 - G}{\varepsilon_{AB_3}f_a + \varepsilon_{B_3}} \quad (\text{A.0.12})$$

and solving for f_a in Eq. (A.0.12) yields

$$f_a = \frac{(A_3 - G)\varepsilon_{B_2} - (A_2 - G)\varepsilon_{B_3}}{(A_2 - G)\varepsilon_{AB_3} - (A_3 - G)\varepsilon_{AB_2}} \quad (\text{A.0.13})$$

Substituting Eq. (A.0.10) into Eq. (A.0.13) to eliminate G in the equation produces

$$f_a = \frac{A_1(\varepsilon_{B_3} - \varepsilon_{B_2}) + A_2(\varepsilon_{B_1} - \varepsilon_{B_3}) + A_3(\varepsilon_{B_2} - \varepsilon_{B_1})}{A_1(\varepsilon_{AB_2} - \varepsilon_{AB_3}) + A_2(\varepsilon_{AB_3} - \varepsilon_{AB_1}) + A_3(\varepsilon_{AB_1} - \varepsilon_{AB_2})} \quad (\text{A.0.14})$$

Substituting Eq. (A.0.14) into Eq. (A.0.10) gives

$$G = \frac{A_1(\varepsilon_{AB_3}\varepsilon_{B_2} - \varepsilon_{AB_2}\varepsilon_{B_3}) + A_2(\varepsilon_{AB_1}\varepsilon_{B_3} - \varepsilon_{AB_3}\varepsilon_{B_1}) + A_3(\varepsilon_{AB_2}\varepsilon_{B_1} - \varepsilon_{AB_1}\varepsilon_{B_2})}{\varepsilon_{AB_1}(\varepsilon_{B_3} - \varepsilon_{B_2}) + \varepsilon_{AB_2}(\varepsilon_{B_1} - \varepsilon_{B_3}) + \varepsilon_{AB_3}(\varepsilon_{B_2} - \varepsilon_{B_1})} \quad (\text{A.0.15})$$

The value of T_a in Eq. (A.0.7) is incorporated into the parameter d , so it cannot be determined from the MLBL. The parameter dT_a is simply referred to in the following as d , and can be solved by substituting Eq. (A.0.14) and Eq. (A.0.15) into Eq. (A.0.11) to give

$$d = \frac{A_1(\varepsilon_{AB_3} - \varepsilon_{AB_2}) + A_2(\varepsilon_{AB_1} - \varepsilon_{AB_3}) + A_3(\varepsilon_{AB_2} - \varepsilon_{AB_1})}{\varepsilon_{AB_1}(\varepsilon_{B_2} - \varepsilon_{B_3}) + \varepsilon_{AB_2}(\varepsilon_{B_3} - \varepsilon_{B_1}) + \varepsilon_{AB_3}(\varepsilon_{B_1} - \varepsilon_{B_2})} \quad (\text{A.0.16})$$

In the case when λ_1 and λ_2 are isobestic wavelengths, the difference between the extinction coefficient of the absorbers at these wavelengths become zero as these values are given by

$$\varepsilon_A(\lambda_1) = \varepsilon_B(\lambda_1) \quad (\text{A.0.17})$$

$$\varepsilon_A(\lambda_2) = \varepsilon_B(\lambda_2) \quad (\text{A.0.18})$$

Substituting Eq. (A.0.17) and Eq. (A.0.18) into Eq. (A.0.14) reduces the expression of f_a to

$$f_a = \frac{A_1(\varepsilon_{B_3} - \varepsilon_{B_2}) + A_2(\varepsilon_{B_1} - \varepsilon_{B_3}) + A_3(\varepsilon_{B_2} - \varepsilon_{B_1})}{(A_2 - A_1)\varepsilon_{AB_3}} \quad (\text{A.0.19})$$

Appendix B

Preparing a scattering phantom

The polystyrene microspheres used in this work have the following properties:

Table B.1: Properties of a microsphere.

Properties	Value
Diameter	1.4 μm
Refractive index (n_{sph})	1.59
Density (ρ)	1.003 mg mm^{-3}

Based on the properties listed in Table B.1, the volume of each sphere (V_{sph}) is calculated as:

$$V_{\text{sph}} = \frac{4}{3}\pi a^3 \quad (\text{B.0.1})$$

where a is the radius of the spheres, so that $V_{\text{sph}} = 1.43694 \times 10^{-9} \text{mm}^{-3}$. The mass of each sphere, $M_{\text{sph}} = 1.44125 \times 10^{-12} \text{g}$, is given from:

$$M_{\text{sphere}} = \rho V_{\text{sph}} \quad (\text{B.0.2})$$

The scattering coefficient, μ_s , of a sample can be determined by

$$\mu_s = N\sigma_{\text{sca}} \quad (\text{B.0.3})$$

where N is the sphere density and σ_{sca} is the scattering cross section given by,¹⁵⁴

$$\sigma_{\text{sca}} = \frac{\lambda_m^2}{2\pi n_m^2} \sum_{n=1}^{\infty} (2n+1)(|a_n|^2 + |b_n|^2) \quad (\text{B.0.4})$$

The a_n and b_n are Mie coefficients expressed as,¹⁵⁴

$$a_n = \frac{\Psi_n(x)\Psi'_n(mx) - m\Psi_n(mx)\Psi'_n(x)}{\xi(x)\Psi'_n(mx) - m\Psi_n(mx)\xi'_n(x)} \quad (\text{B.0.5})$$

$$b_n = \frac{m\Psi_n(x)\Psi'_n(mx) - \Psi_n(mx)\Psi'_n(x)}{m\xi(x)\Psi'_n(mx) - \Psi_n(mx)\xi'_n(x)} \quad (\text{B.0.6})$$

where,

$$\Psi(z) = S_n(z) \quad (\text{B.0.7})$$

$$\xi(z) = S_n(z) + iC_n(z) \quad (\text{B.0.8})$$

Both of the parameter S_n and C_n denote the Riccati-Bessel function, while x and m in Eq. (B.0.4) represent scatterer size parameter and the mismatched refractive index be-

tween scatterers and the medium.

In the experiments, these microspheres were immersed in the water $n_m = 1.33$ to produce a mismatched refractive index of $m = 1.195$. If $\lambda_m = 671$ nm is employed as the measurement wavelength, the size parameter of the scatterers, $x = 8.7178$, is calculated from.¹⁵⁵

$$x = \frac{2\pi a}{\lambda_m/n_m} \quad (\text{B.0.9})$$

Thus σ_{sca} is calculated as $5.2959 \times 10^{-12} \text{mm}^2$. If $\mu_s = 5 \text{mm}^{-1}$ is required, using the calculated σ_{sca} value and the relationship given in Eq. (B.0.3), N is calculated as $9.44 \times 10^5 \text{mm}^{-3}$. The mass of spheres per unit volume required to achieve this μ_s value is calculated using the following equation:

$$M_{\text{cal}} = M_{\text{sphere}} \times N \quad (\text{B.0.10})$$

which give $M_{\text{cal}} = 1.36 \text{mg mm}^{-3}$.

In addition, using Eq. (B.0.5) - Eq. (B.0.8), $g = 0.92$ is calculated from:²⁸

$$g = \frac{\lambda^2}{\pi^2 n_m^2 \sigma_{\text{sca}}} \left\{ \sum_{n=1}^{\infty} \frac{2n+1}{n(n+1)} \text{Re}\{a_n b_n^*\} + \sum_{n=1}^{\infty} \frac{n(n+2)}{n+1} \text{Re}\{a_n a_{n+1}^* + b_n b_{n+1}^*\} \right\} \quad (\text{B.0.11})$$

Appendix C

Monte Carlo simulation of photon propagation direction and polarisation state

The parameters in the Monte Carlo simulation which determine the position, propagation direction and polarisation state of a photon in a scattering medium are listed in the following sections.

C.1 Photon propagation direction

The photon propagating direction is determined by longitudinal angle θ and azimuthal angle ϕ . The scattering angle decides the angle between the incoming and outgoing light and has a value from within the range of $\theta \in [0, \pi)$, while the azimuthal angle describes the rotation angle around the incident light and it is in the range of $\phi \in [0, 2\pi)$.

C.2 Polarisation state of a photon

In the simulations, the polarisation states of the photons in a scattering medium are derived from the Stokes vectors. The scattering angle θ and azimuthal angle ϕ are given by the random number generator in Polarised Monte Carlo model (PMC), both of the Mueller matrix and Stokes vector are updated at each scattering event to produce the polarisation state of a photon. The polarisation state of a scattered photon is described by the Stokes parameters, $S_s = [I_s, Q_s, U_s, V_s]$, as

$$S_s = \mathbf{M}(\theta) \mathbf{R}(\phi) S$$

Here, $\mathbf{M}(\theta)$ and $\mathbf{R}(\phi)$ are the Mueller matrix and the rotation matrix, respectively, while $S = [I_i, Q_i, U_i, V_i]$ is the polarisation state of the incoming light. The Mueller matrix described the interaction of polarised photons with medium.

For spherical scatterers with symmetrical properties, the Mueller matrix is reduced from 16 components down to just four parameters and it is given by:^{28,154,156}

$$\mathbf{M}(\theta) = \begin{pmatrix} m_{11}(\theta) & m_{12}(\theta) & 0 & 0 \\ m_{12}(\theta) & m_{11}(\theta) & 0 & 0 \\ 0 & 0 & m_{33}(\theta) & m_{34}(\theta) \\ 0 & 0 & -m_{34}(\theta) & m_{33}(\theta) \end{pmatrix}$$

where

$$\begin{aligned}
m_{11} &= \frac{1}{2} (|S_2|^2 + |S_1|^2) \\
m_{12} &= \frac{1}{2} (|S_2|^2 - |S_1|^2) \\
m_{33} &= \frac{1}{2} (S_1 S_2^* + S_2 S_1^*) \\
m_{34} &= \frac{i}{2} (S_1 S_2^* - S_2 S_1^*)
\end{aligned}$$

Here, S_x is the amplitude of the scattering matrix given from the scattering coefficients, scattering angle θ and azimuthal angle ϕ .¹⁵⁶ The rotation matrix $\mathbf{R}(\phi)$ provides the photon's position, and it transforms the global coordinate of the scattered photon from the local coordinate of light incident on the scatterers. These coordinate systems of the Monte Carlo model are presented elsewhere,^{24,156} and \mathbf{R} is expressed as:¹⁵⁶

$$\mathbf{R}(\phi) = \begin{pmatrix} 1 & 0 & 0 & 0 \\ 0 & \cos(2\phi) & \sin(2\phi) & 0 \\ 0 & -\sin(2\phi) & \cos(2\phi) & 0 \\ 0 & 0 & 0 & 1 \end{pmatrix}$$

It is important to note here that for the nonpolarised light, $Q_i = U_i = V_i = 0$, so the Stokes parameters of the scattered light are:

$$I_s = m_{11}I_i, \quad Q_s = m_{12}I_i, \quad U_s = 0, \quad V_s = 0 \quad (\text{C.2.1})$$

The photons' position and their polarisation properties are tracked and stored each time

the Stokes parameters are updated. The summation of the Stokes parameters of a collection of single scatterer is to produce the Stokes parameters of the scattered light.¹⁵⁶

Appendix D

Grouping of wavelength combinations for the analysis of a medium with three absorbers

The diagram describing the process of grouping and storing different combinations of three wavelengths for the spectroscopy analysis of a scattering medium containing three absorbers is summarised in Fig. D.1.

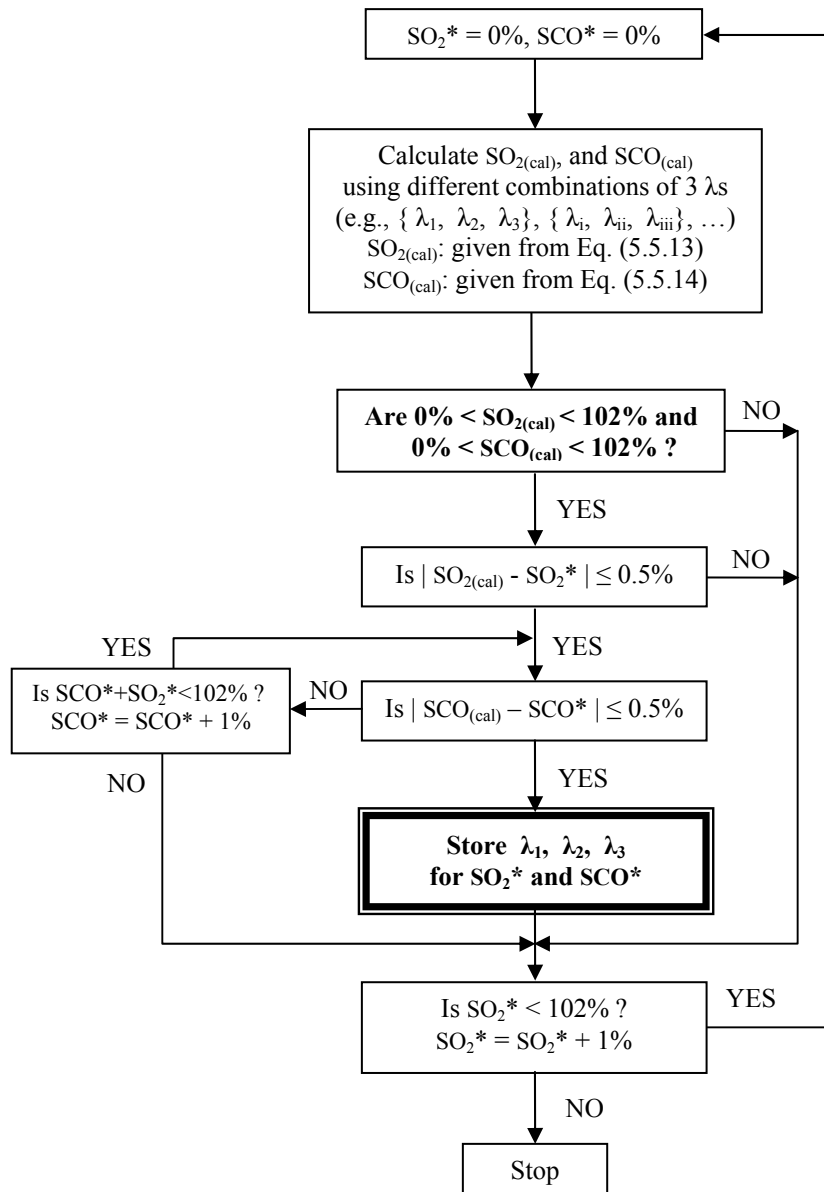


Figure D.1: The process of grouping and storing three wavelength combinations for different SO_2^* and SCO^* levels.

Appendix E

Solving for the value of fitting parameters using TPSF cumulants

To demonstrate how the value of parameters in a fitting model can be solved using a finite number of cumulants, taking Eq. (E.0.1) as an example of curve fitting model. Expanding the exponential term in Eq. (E.0.1) as a Taylor series and rearranging the equation provides Eq. (E.0.2):

$$A = g' - a \exp(-b\mu_a) \quad (\text{E.0.1})$$

$$= \underbrace{(g' - a)}_{\kappa_0} + \underbrace{(ab)}_{\kappa_1} \mu_a - \underbrace{(ab^2)}_{\kappa_2} \frac{\mu_a^2}{2!} + \underbrace{(ab^3)}_{\kappa_3} \frac{\mu_a^3}{3!} - \dots \quad (\text{E.0.2})$$

where g' , a and b are fitting parameters and they are the unknowns in Eq. (E.0.1). To solve these unknowns using the simultaneous equations, at least an equal amount of cumulants are required (i.e., only κ_0 to κ_2 will be needed).

$$A = \underbrace{(g' - a)}_{\kappa_0} + \underbrace{(ab)}_{\kappa_1} \mu_a - \underbrace{(ab^2)}_{\kappa_2} \frac{\mu_a^2}{2!} + \underbrace{(ab^3)}_{\kappa_3} \frac{\mu_a^3}{3!} - \dots \quad (\text{E.0.3})$$

Note that

$$\kappa_2 = ab^2 \quad (\text{E.0.4})$$

$$\kappa_1 = ab \quad (\text{E.0.5})$$

Substituting $\kappa_1 = ab$ into Eq. (E.0.4) gives

$$\kappa_2 = \kappa_1 b \quad (\text{E.0.6})$$

$$b = \frac{\kappa_2}{\kappa_1} \quad (\text{E.0.7})$$

Replacing Eq. (E.0.7) into Eq. (E.0.5) produces

$$a = \frac{\kappa_1}{b} \quad (\text{E.0.8})$$

$$= \frac{\kappa_1^2}{\kappa_2} \quad (\text{E.0.9})$$

and

$$g - a = \kappa_0 \quad (\text{E.0.10})$$

$$g = \kappa_0 + \frac{\kappa_1^2}{\kappa_2} \quad (\text{E.0.11})$$

Bibliography

- [1] I. F. Duarte, A. Barros, I. Delgadillo, C. Almeida, and A. M. Gil. Application of ftir spectroscopy for the quantification of sugars in mango juice as a function of ripening. *Journal of Agricultural and Food Chemistry*, 50(11):3104–3111, May 2002.
- [2] F. C. Delori. Noninvasive technique for oximetry of blood in retinal vessels. *Appl. Opt.*, 27:1113–1125, March 1988.
- [3] R. N. Pittman and B. R. Duling. A new method for the measurement of percent oxyhemoglobin. *J Appl Physiol*, 38(2):315–320, February 1975.
- [4] M. H. Smith. Optimum wavelength combinations for retinal vessel oximetry. *Appl. Opt.*, 38(1):258–267, January 1999.
- [5] J. B. Fishkin, O. Coquoz, E. R. Anderson, M. Brenner, and B. J. Tromberg. Frequency-domain photon migration measurements of normal and malignant tissue optical properties in a human subject. *Appl. Opt.*, 36(1):10–20, January 1997.
- [6] M. Oda, Y. Yamashita, G. Nishimura, and M. Tamura. A simple and novel algorithm for time-resolved multiwavelength oximetry. *Physics in Medicine and Biology*, 41(3):551, March 1996.
- [7] I.P. Stanley, C. Mei, K. John, O. Rebecca, S. Robert, G. Stephan, M. Jeffrey, L. Joseph, and Subcommittee O. Hyperbilirubinemia. An evidence-based review of important issues concerning neonatal hyperbilirubinemia. *Pediatrics*, 114(1):e130–153, July 2004.
- [8] G. Reich. Near-infrared spectroscopy and imaging: Basic principles and pharmaceutical applications. *Advanced Drug Delivery Reviews*, 57(8):1109–1143, June 2005.

- [9] M. Blanco, J. Coello, H. Iturriaga, S. Maspoch, and Pezuela. Near-infrared spectroscopy in the pharmaceutical industry . critical review. *Analyst*, 123(8):135–150, 1998.
- [10] R. H. Stavn. Lambert-beer law in ocean waters: optical properties of water and of dissolved/suspended material, optical energy budgets. *Appl. Opt.*, 27(2):222–231, January 1988.
- [11] T. Upile, W. Jerjes, H. Sterenborg, A. E. Naggar, A. Sandison, and et al. Head and neck optical diagnostics: vision of the future of surgery. *Head & Neck Oncology*, 1(1):25, 2009.
- [12] A. Vogel, V. V. Chernomordik, J. D. Riley, M. Hassan, F. Amyot, B. Dasgeb, S. G. Demos, R. Pursley, R. F. Little, R. Yarchoan, Y. Tao, and A. H. Gandjbakhche. Using noninvasive multispectral imaging to quantitatively assess tissue vasculature. *Journal of biomedical optics*, 12(5), 2007.
- [13] E. Okada, M. Schweiger, S. R. Arridge, M. Firbank, and D. T. Delpy. Experimental validation of monte carlo and finite-element methods for the estimation of the optical path length in inhomogeneous tissue. *Appl. Opt.*, 35(19):3362–3371, July 1996.
- [14] J. Hoffmann, D. W. Lübbers, and H. M. Heise. Applicability of the kubelka-munk theory for the evaluation of reflectance spectra demonstrated for haemoglobin-free perfused heart tissue. *Physics in Medicine and Biology*, 43(12):3571, December 1998.
- [15] S. R. Arridge, M. Cope, and D. T. Delpy. The theoretical basis for the determination of optical pathlengths in tissue: temporal and frequency analysis. *Physics in medicine and biology*, 37(7):1531–1560, July 1992.
- [16] A. Pifferi, P. Taroni, G. Valentini, and S. Andersson-Engels. Real-time method for fitting time-resolved reflectance and transmittance measurements with a monte carlo model. *Appl. Opt.*, 37(13):2774–2780, May 1998.
- [17] A. Kienle and M. S. Patterson. Determination of the optical properties of turbid media from a single monte carlo simulation. *Physics in Medicine and Biology*, 41(10):2221, October 1996.
- [18] J. B. Fishkin, P. T. C. So, A. E. Cerussi, S. Fantini, M. A. Franceschini, and E. Gratton. Frequency-domain method for measuring spectral properties in multiple-scattering media: methemoglobin absorption spectrum in a tissuelike phantom. *Appl. Opt.*, 34(7):1143–1155, March 1995.

- [19] D. T. Delpy, M. Cope, P. van der Zee, S. Arridge, S. Wray, and J. Wyatt. Estimation of optical pathlength through tissue from direct time of flight measurement. *Physics in medicine and biology*, 33(12):1433–1442, December 1988.
- [20] E. L. Heffer and S. Fantini. Quantitative oximetry of breast tumors: A near-infrared method that identifies two optimal wavelengths for each tumor. *Appl. Opt.*, 41(19):3827–3839, July 2002.
- [21] J. Tiedeman, S. Kirk, S. Srinivas, and J. Beach. Retinal oxygen consumption during hyperglycemia in patients with diabetes without retinopathy. *Ophthalmology*, 105(1):31–36, January 1998.
- [22] L. M. Schnapp and N. H. Cohen. Pulse oximetry. uses and abuses. *Chest* 98, pages 1244–1250, 1990.
- [23] Y. Tsuchiya. Photon path distribution and optical responses of turbid media: theoretical analysis based on the microscopic beer-lambert law. *Physics in medicine and biology*, 46(8):2067–2084, August 2001.
- [24] B. Lu. Theoretical examination of scattering media by temporal analysis. *Thesis (University of Nottingham)*, 2007.
- [25] I. M. Stockford, B. Lu, J. A. Crowe, S. P. Morgan, and D. E. Morris. Reduction of error in spectrophotometry of scattering media using polarization techniques. *Applied spectroscopy*, 61(12):1379–1389, December 2007.
- [26] I. Alabboud. Human retinal oximetry using hyperspectral imaging. *Thesis (Heriot Watt University)*, 2009.
- [27] P. I. Rodmell. Novel pulse oximeter. *Thesis (University of Nottingham)*, 2005.
- [28] V. Tuchin. *Tissue Optics: Light Scattering Methods and Instruments for Medical Diagnosis, Second Edition (SPIE Press Monograph Vol. PM166)*. SPIE Publications, 2nd edition, September 2007.
- [29] S. Fantini, M. A. Franceschini, J. S. Maier, S. A. Walker, B. B. Barbieri, and E. Gratton. Frequency-domain multichannel optical detector for noninvasive tissue spectroscopy and oximetry. *Optical Engineering*, 34(1):32–42, 1995.
- [30] W. G. Zijlstra, A. Buursma, and O. W. Van Assendelft. *Visible and near infrared absorption spectra of human and animal haemoglobin: Determination and application*. VSP Books, October 2000.

- [31] B. Chance, J. S. Leigh, H. Miyake, D. S. Smith, S. Nioka, R. Greenfeld, M. Finander, K. Kaufmann, W. Levy, and M. Young. Comparison of time-resolved and -unresolved measurements of deoxyhemoglobin in brain. *Proceedings of the National Academy of Sciences*, 85(14):4971–4975, July 1988.
- [32] S. A. Prahl, M. Keijzer, S. L. Jacques, and A. J. Welch. A Monte Carlo model of light propagation in tissue. In G. J. Müller and D. H. Sliney, editors, *SPIE Proceedings of Dosimetry of Laser Radiation in Medicine and Biology*, volume IS 5, pages 102–111, 1989. monte carlo.
- [33] G. Müller, B. Chance, R. Alfano, S. Arridge, and et al. Medical optical tomography : functional imaging and monitoring. *SPIE institutes for advanced optical technologies*, 11, 1993.
- [34] M. Hammer, D. Schweitzer, B. Michel, E. Thamm, and A. Kolb. Single scattering by red blood cells. *Appl. Opt.*, 37(31):7410–7418, November 1998.
- [35] F. Bevilacqua, D. Piguet, P. Marquet, J. D. Gross, B. J. Tromberg, and C. Depeursinge. In vivo local determination of tissue optical properties: Applications to human brain. *Appl. Opt.*, 38(22):4939–4950, August 1999.
- [36] Y. Du, X. H. Hu, M. Cariveau, X. Ma, G. W. Kalmus, and J. Q. Lu. Optical properties of porcine skin dermis between 900 nm and 1500 nm. *Physics in Medicine and Biology*, 46(1):167+, January 2001.
- [37] P. Van der Zee and D. T. Delpy. Simulation of the point spread function for light in tissue by a monte carlo method. *Advances in experimental medicine and biology*, 215:179–191, 1987.
- [38] G. Alexandrakis, T. J. Farrell, and M. S. Patterson. Monte carlo diffusion hybrid model for photon migration in a two-layer turbid medium in the frequency domain. *Appl. Opt.*, 39(13):2235–2244, May 2000.
- [39] Y. Tsuchiya and T. Urakami. Quantitation of absorbing substances in turbid media such as human tissues based on the microscopic beer-lambert law. *Optics Communications*, pages 269–280, December 1997.
- [40] H. Zhang, M. Miwa, Y. Yamashita, and Y. Tsuchiya. Quantitation of absorbers in turbid media using time-integrated spectroscopy based on microscopic beer-lambert law. *Japanese Journal of Applied Physics*, 37(Part 1, No. 5A):2724–2727, 1998.

- [41] D. E. Morris. Quantitative spectrophotometry on scattering media. *Thesis (University of Nottingham)*, 2009.
- [42] J. Crowe, D. Morris, M. Woolfson, P. Rodmell, and J. Walker. Quantitative spectrophotometry of scattering media via frequency-domain and constant-intensity measurements. *J. Opt. Soc. Am. A*, 24(7):1969–1974, July 2007.
- [43] J. M. Schmitt, A. H. Gandjbakhche, and R. F. Bonner. Use of polarized light to discriminate short-path photons in a multiply scattering medium. *Appl. Opt.*, 31(30):6535–6546, October 1992.
- [44] B. Lu, S. P. Morgan, J. A. Crowe, and I. M. Stockford. Comparison of methods for reducing the effects of scattering in spectrophotometry. *Appl. Spectrosc.*, 60(10):1157–1166, October 2006.
- [45] M. S. Patterson, B. Chance, and B. C. Wilson. Time resolved reflectance and transmittance for the non-invasive measurement of tissue optical properties. *Appl. Opt.*, 28(12):2331–2336, June 1989.
- [46] W. F. Cheong, S. A. Prahl, and A. J. Welch. A review of the optical properties of biological tissues. *IEEE Journal of Quantum Electronics*, 26(12):2166–2185, Dec 1990.
- [47] S. R. Arridge and J. C. Hebden. Optical imaging in medicine :ii modelling and reconstruction. *Physics in Medicine and Biology*, 42(5):841, May 1997.
- [48] A. Ishimaru. *Wave propagation and scattering in random media. Vol 1: Single scattering and transport theory*. Academic Press.
- [49] S. L. Jacques and B. W. Pogue. Tutorial on diffuse light transport. *Journal of Biomedical Optics*, 13(4), 2008.
- [50] N. Metropolis and S. Ulam. The monte carlo method. *Journal of the American Statistical Association*, 44(247):335, September 1949.
- [51] S. T. Flock, M. S. Patterson, B. C. Wilson, and D. R. Wyman. Monte carlo modeling of light propagation in highly scattering tissue–i: Model predictions and comparison with diffusion theory. *IEEE transactions on bio-medical engineering*, 36(12):1162–1168, December 1989.
- [52] Y. Nomura, O. Hazeki, and M. Tamura. Relationship between time-resolved and non-time-resolved beer - lambert law in turbid media. *Physics in Medicine and Biology*, 42(6):1009, June 1997.

- [53] L. Wang. Monte carlo modeling of light transport in multi-layered tissues. *Computer Methods and Programs in Biomedicine*, 47(2):131–146, July 1995.
- [54] C. Dunsby and P. M. W. French. Techniques for depth-resolved imaging through turbid media including coherence-gated imaging. *Journal of Physics D: Applied Physics*, 36(14):207, July 2003.
- [55] S. Jun, L. Ling, N. Masatsugu, K. Nobuki, and Y. Katsuyuki. Determination of a quantitative algorithm for the measurement of muscle oxygenation using cw near-infrared spectroscopy mean optical pathlength without the influence of adipose tissue. *Proceedings of SPIE*, 4082:76, 2000.
- [56] S. L. Jacques. Spectral imaging and analysis to yield tissue optical properties. *Journal of Innovative Optical Health Sciences (JIOHS)*, 2(2):123–129, 2009.
- [57] C. Yang, J. H. Everitt, M. R. Davis, and C. Mao. A ccd camera-based hyperspectral imaging system for stationary and airborne applications. *Geocarto International*, 18(2):71–80, 2003.
- [58] D. T. Delpy and M. Cope. Quantification in tissue near-infrared spectroscopy. *Royal Society of London Philosophical Transactions Series B*, 352:649–659, June 1997.
- [59] J. C. Hebden, R. A. Kruger, and K. S. Wong. Time resolved imaging through a highly scattering medium. *Appl. Opt.*, 30(7):788–794, March 1991.
- [60] D. Comelli, A. Bassi, A. Pifferi, P. Taroni, A. Torricelli, R. Cubeddu, F. Martelli, and G. Zaccanti. In vivo time-resolved reflectance spectroscopy of the human forehead. *Appl. Opt.*, 46(10):1717–1725, April 2007.
- [61] D. R. Kirkby and D. T. Delpy. Measurement of tissue temporal point spread function (tpsf) by use of a gain-modulated avalanche photodiode detector. *Physics in medicine and biology*, 41(5):939–949, May 1996.
- [62] A. Duncan, J. H. Meek, M. Clemence, C. E. Elwell, L. Tyszczyk, M. Cope, and D. Delpy. Optical pathlength measurements on adult head, calf and forearm and the head of the newborn infant using phase resolved optical spectroscopy. *Physics in Medicine and Biology*, 40(2):295–304, February 1995.
- [63] S. P. Morgan and K. Y. Yong. Elimination of amplitude-phase crosstalk in frequency domain near-infrared spectroscopy. *Review of Scientific Instruments*, 72(4):1984–1987, 2001.

- [64] E. M. Sevick, J. K. Frisoli, C. L. Burch, and J. R. Lakowicz. Localization of absorbers in scattering media by use of frequency-domain measurements of time-dependent photon migration. *Appl. Opt.*, 33(16):3562–3570, June 1994.
- [65] B. J. Tromberg, L. O. Svaasand, T. Tsay, and R. C. Haskell. Properties of photon density waves in multiple-scattering media. *Appl. Opt.*, 32(4):607–616, February 1993.
- [66] V. Twersky. Interface effects in multiple scattering by large, low-refracting, absorbing particles. *J. Opt. Soc. Am.*, 60(7):908, July 1970.
- [67] J. Mayhew. Spectroscopic analysis of changes in remitted illumination: The response to increased neural activity in brain. *NeuroImage*, 10(3):304–326, September 1999.
- [68] M. Meinke, G. Müller, J. Helfmann, and M. Friebel. Empirical model functions to calculate hematocrit-dependent optical properties of human blood. *Appl. Opt.*, 46(10):1742–1753, April 2007.
- [69] D. M. Hueber, M. A. Franceschini, H. Y. Ma, Q. Zhang, J. R. Ballesteros, S. Fantini, D. Wallace, V. Ntziachristos, and B. Chance. Non-invasive and quantitative near-infrared haemoglobin spectrometry in the piglet brain during hypoxic stress, using a frequency-domain multidistance instrument. *Physics in Medicine and Biology*, 46(1):41, January 2001.
- [70] S. J. Madsen, B. C. Wilson, M. S. Patterson, Y. D. Park, S. L. Jacques, and Y. Hefetz. Experimental tests of a simple diffusion model for the estimation of scattering and absorption coefficients of turbid media from time-resolved diffuse reflectance measurements. *Appl. Opt.*, 31(18):3509–3517, June 1992.
- [71] M. Kohl, R. Watson, and M. Cope. Optical properties of highly scattering media determined from changes in attenuation, phase, and modulation depth. *Appl. Opt.*, 36(1):105–115, January 1997.
- [72] B. W. Pogue and M. S. Patterson. Frequency-domain optical absorption spectroscopy of finite tissue volumes using diffusion theory. *Physics in medicine and biology*, 39(7):1157–1180, July 1994.
- [73] N. Naghavi and M. H. Miran Baygi. Modeling of optical properties of normal and tumor tissue using reflectance spectra for appropriate dosimetry in photodynamic therapy. *Journal of Applied Sciences*, 9(3):583–587, 2009.

- [74] R. Zhang, W. Verkruyse, B. Choi, J. A. Viator, B. Jung, L. O. Svaasand, G. Aguilar, and J. S. Nelson. Determination of human skin optical properties from spectrophotometric measurements based on optimization by genetic algorithms. *Journal of biomedical optics*, 10(2), 2005.
- [75] J. Qin and R. Lu. Determination of the optical properties of turbid materials by hyperspectral diffuse reflectance. July 2005.
- [76] M. R. Ostermeyer and S. L. Jacques. Perturbation theory for diffuse light transport in complex biological tissues. *J. Opt. Soc. Am. A*, 14(1):255–261, January 1997.
- [77] A. Sassaroli, F. Martelli, and S. Fantini. Perturbation theory for the diffusion equation by use of the moments of the generalized temporal point-spread function. i. theory. *Journal of the Optical Society of America. A, Optics, image science, and vision*, 23(9):2105–2118, September 2006.
- [78] M. N. Santos. Computation of one-sided probability density functions from their cumulants. *Journal of Mathematical Chemistry*, 41(1):71–77–77, January 2007.
- [79] D. E. Morris, I. M. Stockford, and J. A. Crowe. Determination of the validity of spectrophotometric measurements based upon cumulants of the temporal point-spread function. *Opt. Lett.*, 33(12):1339–1341, June 2008.
- [80] D. W. Lübbers and R. Wodick. The examination of multicomponent systems in biological materials by means of a rapid scanning photometer. *Appl. Opt.*, 8(5):1055–1062, May 1969.
- [81] P. J. Smith. A recursive formulation of the old problem of obtaining moments from cumulants and vice versa. *The American Statistician*, 49, May 1995.
- [82] F. Lehner. Cumulants in noncommutative probability theory i. noncommutative exchangeability systems. *Mathematische Zeitschrift*, pages 67–100, September 2004.
- [83] M. Kobayashi, Y. Ito, N. Sakauchi, I. Oda, I. Konishi, and Y. Tsunazawa. Analysis of nonlinear relation for skin hemoglobin imaging. *Opt. Express*, 9(13):802–812, December 2001.
- [84] S. P. Morgan and M. Ridgway. Polarization properties of light backscattered from a two layer scattering medium. *Opt. Express*, 7(12):395–402, December 2000.
- [85] F. C. MacKintosh and S. John. Diffusing-wave spectroscopy and multiple scattering of light in correlated random media. *Physical Review B*, 40(4):2383–2406, Aug 1989.

- [86] F. C. MacKintosh, J. X. Zhu, D. J. Pine, and D. A. Weitz. Polarization memory of multiply scattered light. *Physical Review B*, 40(13):9342–9345, Nov 1989.
- [87] I. M. Stockford. Characterisation of layered scattering media using polarised light. *Thesis (University of Nottingham)*, 2004.
- [88] X. Gan, S. P. Schilders, and M. Gu. Image enhancement through turbid media under a microscope by use of polarization gating methods. *J. Opt. Soc. Am. A*, 16(9):2177–2184, September 1999.
- [89] S. P. Morgan, M. P. Khong, and M. G. Somekh. Effects of polarization state and scatterer concentration on optical imaging through scattering media. *Appl. Opt.*, 36(7):1560–1565, March 1997.
- [90] P. Chang, J. Walker, K. Hopcraft, B. Ablitt, and E. Jakeman. Polarization discrimination for active imaging in scattering media. *Optics Communications*, 159(1-3):1–6, January 1999.
- [91] M. P. Siegel, Y. L. Kim, H. K. Roy, R. K. Wali, and V. Backman. Assessment of blood supply in superficial tissue by polarization-gated elastic light-scattering spectroscopy. *Appl. Opt.*, 45(2):335–342, January 2006.
- [92] M. Kohl, M. Cope, M. Essenpreis, and D. Böcker. Influence of glucose concentration on light scattering in tissue-simulating phantoms. *Opt. Lett.*, 19(24):2170–2172, December 1994.
- [93] G. Vargas, E. K. Chan, J. K. Barton, H. G. Rylander, and A. J. Welch. Use of an agent to reduce scattering in skin. *Lasers in Surgery and Medicine*, 24(2):133–141, 1999.
- [94] E. K. Chan, B. Sorg, D. Protsenko, M. O’Neil, M. Motamedi, and A. J. Welch. Effects of compression on soft tissue optical properties. *IEEE Journal of Selected Topics in Quantum Electronics*, 2(4):943–950, Dec 1996.
- [95] L. Wang, P. P. Ho, C. Liu, G. Zhang, and R. R. Alfano. Ballistic 2-d imaging through scattering walls using an ultrafast optical kerr gate. *Science*, August 1991.
- [96] J. O’Doherty, J. Henricson, C. Anderson, M. J. Leahy, G. E. Nilsson, and F. Sjöberg. Sub-epidermal imaging using polarized light spectroscopy for assessment of skin microcirculation. *Skin Research and Technology*, 13(4):472–484, November 2007.

- [97] Y. Yamashita, F. Kawaguchi, Y. Ito, N. Shinohara, M. Haida, S. Takagi, and Y. Shinohara. Concentration measurements of a light absorber localized in a scattering medium. *Appl. Opt.*, 33(31):7541–7546, November 1994.
- [98] A. Lesuffleur, H. Im, N. C. Lindquist, K. S. Lim, and S. H. Oh. Laser-illuminated nanohole arrays for multiplex plasmonic microarray sensing. *Opt. Express*, 16(1):219–224, January 2008.
- [99] T. Nishita, Y. Dobashi, and E. Nakamae. Display of clouds taking into account multiple anisotropic scattering and sky light. In *SIGGRAPH '96: Proceedings of the 23rd annual conference on Computer graphics and interactive techniques*, pages 379–386, New York, NY, USA, 1996.
- [100] R. M. Pope and E. S. Fry. Absorption spectrum (380-700 nm) of pure water. ii. integrating cavity measurements. *Appl. Opt.*, 36(33):8710–8723, November 1997.
- [101] E. Hecht. *Optics (Third ed.)*. Addison Wesley Longman, Inc., 1998.
- [102] A. K. C. Huong, I. M. Stockford, J. A. Crowe, and S. P. Morgan. Optical monitoring of tissue using differential polarization spectroscopy. *IOP Photon08*, 2008.
- [103] I. Vitkin, R. Laszlo, and C. Whyman. Effects of molecular asymmetry of optically active molecules on the polarization properties of multiply scattered light. *Opt. Express*, 10(4):222–229, February 2002.
- [104] V. Sankaran, J. T. Walsh, and D. J. Maitland. Polarized light propagation through tissue phantoms containing densely packed scatterers. *Opt. Lett.*, 25(4):239–241, February 2000.
- [105] T. G. Spence, C. C. Harb, B. A. Paldus, R. N. Zare, B. Willke, and R. L. Byer. A laser-locked cavity ring-down spectrometer employing an analog detection scheme. *Review of Scientific Instruments*, 71:347–353, February 2000.
- [106] S. L. Jacques, J. C. Ramella-Roman, and K. Lee. Imaging skin pathology with polarized light. *Journal of Biomedical Optics*, 7(3):329–340, July 2002.
- [107] I. Meglinsky and S. Matcher. Modelling the sampling volume for skin blood oxygenation measurements. *Medical and Biological Engineering and Computing*, 39(1):44–50, January 2001.
- [108] I. V. Meglinsky and S. J. Matcher. *The reflected spectrum of complex multi-layered inhomogeneous highly scattering medium*, chapter 5. Professional Engineering Publishing Limited.

- [109] A. K. C. Huong, I. M. Stockford, J. A. Crowe, and S. P. Morgan. Investigation of optimum wavelengths for oximetry. volume 7368, page 736811. SPIE, 2009.
- [110] H. Sato, M. Kiguchi, F. Kawaguchi, and A. Maki. Practicality of wavelength selection to improve signal-to-noise ratio in near-infrared spectroscopy. *NeuroImage*, 21(4):1554–1562, April 2004.
- [111] W. T. Baxter, J. M. Davidenko, L. M. Loew, J. P. Wuskell, and J. Jalife. Technical features of a CCD video camera system to record cardiac fluorescence data. *Annals of biomedical engineering*, 25(4):713–725, 1997.
- [112] A. N. Bashkatov, E. A. Genina, V. I. Kochubey, and V. V. Tuchin. Optical properties of human skin, subcutaneous and mucous tissues in the wavelength range from 400 to 2000 nm. *Journal of Physics D Applied Physics*, 38:2543–2555, August 2005.
- [113] R. Graaff, A. C. M. Dassel, M. H. Koelink, F. F. M. de Mul, J. G. Aarnoudse, and W. G. Zijistra. Optical properties of human dermis in vitro and in vivo. *Appl. Opt.*, 32(4):435–447, February 1993.
- [114] N. Ahlquist and R. Charlson. Measurement of the wavelength dependence of atmospheric extinction due to scatter. *Atmospheric Environment (1967)*, 3(5):551–564, September 1969.
- [115] P. P. Taroni, A. Torricelli, and R. Cubeddu. Time-resolved optical spectroscopy and imaging of breast. *Optoelectronics Review*, 12:249–253, 2004.
- [116] R. R. Anderson and J. A. Parrish. The optics of human skin. *The Journal of investigative dermatology*, 77(1):13–19, July 1981.
- [117] E. H. Wood. Normal oxygen saturation of arterial blood during inhalation of air and oxygen. *Journal of applied physiology*, 1(8):567–574, February 1949.
- [118] H. J. Van Staveren, C. J. M. Moes, J. Van Marle, M. J. C. Van Gemert, and S. A. Prahl. Light scattering in intralipid-10 in the wavelength range of 400-1100 nm. *Appl. Opt.*, 30:4507–4514, November 1991.
- [119] G. B. Cordon and M. G. Lagorio. Absorption and scattering coefficients: A biophysical-chemistry experiment using reflectance spectroscopy. *Journal of Chemical Education*, 84(7):1167, July 2007.

- [120] N. Shah, A. Cerussi, C. Eker, J. Espinoza, J. Butler, J. Fishkin, R. Hornung, and B. Tromberg. Noninvasive functional optical spectroscopy of human breast tissue. *Proceedings of the National Academy of Sciences of the United States of America*, 98(8):4420–4425, April 2001.
- [121] C. E. Thorn, S. J. Matcher, I. V. Meglinski, and A. C. Shore. Is mean blood saturation a useful marker of tissue oxygenation? *Am J Physiol Heart Circ Physiol*, 296(5):H1289–1295, May 2009.
- [122] L. Caspary, J. Thum, A. Creutzig, D. W. Lübbers, and K. Alexander. Quantitative reflection spectrophotometry: spatial and temporal variation of hb oxygenation in human skin. *International journal of microcirculation, clinical and experimental / sponsored by the European Society for Microcirculation*, 15(3):131–136, 1995.
- [123] J. R. Taylor. *An introduction to error analysis: The study of uncertainties in physical*. University Science Books, second edition, 1997.
- [124] H. Zhao, F. E. Kruis, and C. Zheng. Reducing Statistical Noise and Extending the Size Spectrum by Applying Weighted Simulation Particles in Monte Carlo Simulation of Coagulation. *Aerosol Science and Technology*, 43(8):781–793, 2009.
- [125] T. Oggier, M. Lehmann, R. Kaufmann, M. Schweizer, M. Richter, P. Metzler, G. Lang, F. Lustenberger, and N. Blanc. An all-solid-state optical range camera for 3d real-time imaging with sub-centimeter depth resolution (swissranger). In L. Mazuray, P. J. Rogers, & R. Wartmann, editor, *Society of Photo-Optical Instrumentation Engineers (SPIE) Conference Series*, volume 5249 of *Presented at the Society of Photo-Optical Instrumentation Engineers (SPIE) Conference*, pages 534–545, February 2004.
- [126] G. E. Healey and R. Kondepudy. Radiometric CCD camera calibration and noise estimation. *IEEE Transactions on Pattern Analysis and Machine Intelligence*, 16(3):267–276, March 1994.
- [127] O. A. Skydan, F. Lilley, M. J. Lalor, and D. R. Burton. Quantization error of ccd cameras and their influence on phase calculation in fringe pattern analysis. *Appl. Opt.*, 42(26):5302–5307, September 2003.
- [128] B. W. Rice, M. D. Cable, and M. B. Nelson. In vivo imaging of light-emitting probes. *Journal of Biomedical Optics*, 6(4):432–440, 2001.
- [129] B. Meyer, C. Schaller, C. Frenkel, B. Ebeling, and J. Schramm. Distributions of local oxygen saturation and its response to changes of mean arterial blood pressure in

- the cerebral cortex adjacent to arteriovenous malformations. *Stroke*, 30(12):2623–2630, December 1999.
- [130] W. Rath, R. Reichle, W. Hartmann, K. Frank, and J. Christiansen. A fabry-perot interferometer/grating monochromator combination for high resolution optical spectroscopy. *Measurement Science and Technology*, 1(7):611–614, 1990.
- [131] I. Djermanov, S. Iordanova, and I. Koleva. Spectrograph coupled with ccd module for high resolution spectroscopy measurements. *Journal of Physics: Conference Series*, 63(1):012029, 2007.
- [132] T. M. Lehmann, C. Gnner, and K. Spitzer. Survey: Interpolation methods in medical image processing. *IEEE Transactions on Medical Imaging*, 18:1049–1075, 1999.
- [133] G. Papakostas, Y. Boutalis, C. Papaodysseus, and D. Fragoulis. Numerical error analysis in Zernike moments computation. *Image and Vision Computing*, 24(9):960–969, September 2006.
- [134] C. C. Steven and C. Raymond. *Numerical Methods for Engineers: With Software and Programming Applications*. McGraw-Hill Science/Engineering/Math, 4 edition, July 2001.
- [135] F. Paolo, M. Francesca, and S. Andrea. On the cumulant analysis of EXAFS in crystalline solids. *Journal of Synchrotron Radiation*, 8(6):1214–1220, Nov 2001.
- [136] A. Stuart, C. R. Marie-Cécile, D. A. Ross, G. Igor, B. Edouard, and D. B. Jean. Processivity and coupling in messenger rna transcription. *PloS one*, 5(1), 2010.
- [137] J. Swait and J. Louviere. The role of the scale parameter in the estimation and comparison of multinomial logit models. *Journal of Marketing Research*, 30(3), 1993.
- [138] R. H. Kraichnan. Realizability inequalities and closed moment equations. *Annals of the New York Academy of Sciences*, 357:37–46, December 1980.
- [139] I. Myung. The importance of complexity in model selection. *Journal of Mathematical Psychology*, 44(1):190–204, March 2000.
- [140] K. Z. Mohsen and B. Yaser. Target transform fitting in a voltammetric study of metal complexation. *Analytica chimica acta*, 621(2):163–170, July 2008.

- [141] T. F. Coleman and Y. Li. An interior trust region approach for nonlinear minimization subject to bounds. Technical report, Ithaca, NY, USA, 1993.
- [142] M. Yaqub, R. Boellaard, M. A. Kropholler, M. Lubberink, and A. A. Lammertsma. Simulated Annealing in pharmacokinetic modeling of PET neuroreceptor studies: accuracy and precision compared with other optimization algorithms. pages 3222–3225.
- [143] S. S. Skiena. *The algorithm design manual*. Springer, 2 edition, 2008.
- [144] I. M. Robert and N. Palmerston. Discrete Mechanics and Optimal Control for Image Registration. *Anziam Journal*, 48:1–16, 2007.
- [145] A. Geletu. Solving optimization problems using the matlab optimization toolbox - a tutorial. December 2007.
- [146] W. Zhao, R. Wu, C. Ma, and G. Casella. A fast algorithm for functional mapping of complex traits. *Genetics*, 167(4):2133–2137, August 2004.
- [147] T. Homma. Importance measures in global sensitivity analysis of nonlinear models. *Reliability Engineering & System Safety*, 52(1):1–17, April 1996.
- [148] J. C. Lagarias, J. A. Reeds, M. H. Wright, and P. E. Wright. Convergence properties of the nelder–mead simplex method in low dimensions. *SIAM J. on Optimization*, 9(1):112–147, 1998.
- [149] E. Magid, D. Keren, E. Rivlin, and I. Yavneh. Spline-Based Robot Navigation. pages 2296–2301, October 2006.
- [150] B. C. Wilson and S. L. Jacques. Optical reflectance and transmittance of tissues: principles and applications. *IEEE Journal of Quantum Electronics*, 26(12):2186–2199, Dec 1990.
- [151] A. J. Welch and M. Gemert. *Optical-Thermal Response of Laser-Irradiated Tissue(Lasers, Photonics, and Electro-Optics)*. Plenum Press, August 1995.
- [152] I. M. Stockford, B. Lu, J. A. Crowe, S. P. Morgan, and D. E. Morris. Reduction of error in spectrophotometry of scattering media using polarization techniques. *Appl. Spectrosc.*, 61(12):1379–1389, December 2007.
- [153] K. B. Sæbø and A. Bjørnerud. Accurate de-oxygenation of ex vivo whole blood using sodium dithionite. *Proc. Intl. Soc. Mag. Reson. Med.*, 8, 2000.

- [154] L. V. Wang and H. Wu. *Biomedical Optics: Principles and Imaging*. Wiley-Interscience, 1 edition, May 2007.
- [155] M. I. Mishchenko. Light scattering by size-shape distributions of randomly oriented axially symmetric particles of a size comparable to a wavelength. *Appl. Opt.*, 32(24):4652–4666, August 1993.
- [156] C. F. Bohren and D. R. Huffman. *Absorption and scattering of light by small particles*. Wiley-Interscience, April 1983.